UNIVERSIDADE FEDERAL DO RIO GRANDE DO SUL
ESCOLA DE ENGENHARIA
DEPARTAMENTO DE ENGENHARIA QUÍMICA
PROGRAMA DE PÓS-GRADUAÇÃO EM ENGENHARIA QUÍMICA

Geração de gás de síntese sobre catalisadores baseados em óxidos mistos

TESE DE DOUTORADO

Guilherme de Souza

Porto Alegre
2014

UNIVERSIDADE FEDERAL DO RIO GRANDE DO SUL

ESCOLA DE ENGENHARIA

DEPARTAMENTO DE ENGENHARIA QUÍMICA

PROGRAMA DE PÓS-GRADUAÇÃO EM ENGENHARIA QUÍMICA

Geração de gás de síntese sobre catalisadores baseados em óxidos mistos

Guilherme de Souza

Tese de Doutorado apresentado como requisito parcial para obtenção do título de Doutor em Engenharia.

Área de concentração: Cinética Aplicada, Catálise e Reatores Químicos e Biorreatores

Orientadores:

Prof. Nilson Romeu Marcilio, D.Sc.

Prof. Oscar William Perez-Lopez, D.Sc.

Porto Alegre

2014

UNIVERSIDADE FEDERAL DO RIO GRANDE DO SUL

ESCOLA DE ENGENHARIA

DEPARTAMENTO DE ENGENHARIA QUÍMICA

PROGRAMA DE PÓS-GRADUAÇÃO EM ENGENHARIA QUÍMICA

A Comissão Examinadora, abaixo assinada, aprova a Tese de Doutorado *Geração de gás de síntese sobre catalisadores baseados em óxidos mistos*, elaborada por Guilherme de Souza, como requisito parcial para obtenção do Grau de Doutor em Engenharia.

Comissão Examinadora:

Profª Elisa Barbosa Coutinho, D.Sc.
Instituto de Química, UFRGS

Profº Gabriel Meneghetti Faé Gomes, D.Sc.
Fundação de Ciência e Tecnologia - CIENTEC

Profº João Henrique Zimnoch dos Santos, D.Sc.
Instituto de Química, UFRGS

Profª Maria do Carmo Rangel Santos Varela, D.Sc.
Instituto de Química, UFBA

Agradecimentos

Aos meus pais, Jair e Lilian, e aos meus irmãos Fernando e Luiza, pelo amor e apoio, estando sempre presentes.

Ao Programa de Pós-Graduação em Engenharia Química da Universidade Federal do Rio Grande do Sul, aos seus professores e demais funcionários, pelos recursos disponibilizados e auxílio para a realização deste trabalho.

Aos orientadores, Prof. Dr. Oscar William Perez-Lopez e Prof. Dr. Nilson Romeu Marcilio, pelos ensinamentos, confiança e dedicação prestada ao longo da composição do trabalho. Os agradecimentos se estendem aos colegas de laboratório e do curso, especialmente aos bolsistas de iniciação científica, Vinícius da Costa Ávila e Cássia Ruoso, pelo companheirismo e valiosas colaborações.

Aos professores, Dr. Andrei Khodakov, Drª. Marla Azário Lansarin, Drª. Naira Maria Balzaretti, Drª. Michèle Oberson de Souza e Dr. Roberto Fernando de Souza, pela amizade, incentivo e contribuições na minha formação. Igualmente, sou grato pela disponibilidade e contribuições dos membros da banca examinadora da tese.

À CAPES, CNPq e FAPERGS, pela concessão da bolsa de doutorado, de treinamento no exterior e fomento de recursos financeiros.

Aos demais familiares, amigos e colegas que contribuíram para a concretização deste trabalho, muito obrigado, *ex toto corde*.

Resumo

A tecnologia *Coal, Gas or Biomass-To-Liquids* (*XTL*) permite a obtenção de combustíveis líquidos a partir de biomassa, carvão mineral ou gás natural. A síntese de catalisadores otimizados constitui um desafio para aumentar a viabilidade desses processos. Neste contexto, por exibirem propriedades catalíticas interessantes para diferentes processos químicos, os óxidos mistos apresentam-se como alternativas promissoras. Entretanto, a sua aplicação nesta tecnologia ainda requer maior investigação. A proposta da tese foi a de avaliar catalisadores baseados em óxidos mistos para a geração de gás de síntese a partir da decomposição do etanol e da reforma do etanol ou do metano. Foram preparadas amostras Fe-Al, Co-Al e Ni-Al pelo método da co-precipitação, sendo caracterizadas por diferentes técnicas. As reações foram conduzidas em reatores tubulares de leito fixo, com alimentação contínua dos reagentes gasosos e líquidos e com análise por cromatografia gasosa. Um melhor compromisso entre propriedades e desempenho catalítico na reação de decomposição do etanol foi observado para amostras com razões molares Ni^{2+}/Al^{3+} entre 1 e 3, pois esta composição favoreceu a formação dos óxidos mistos. Para materiais baseados em Fe, Co ou Ni, houve a formação de materiais do tipo hidrotalcita nos precursores dos catalisadores Co-Al e Ni-Al, formando óxidos mistos após o tratamento térmico. Foram observadas conversões de etanol e seletividade para H_2 e CO mais altas na reação de decomposição do etanol sobre estas amostras. Catalisadores à base de ferro conduziram à maior formação de eteno e acetaldeído e menor deposição de coque. A substituição parcial de Ni por um terceiro elemento modificou o perfil de redução e diminuiu a acidez das amostras. Nas amostras Ni-Al, os catalisadores contendo Zn, Mo ou Co apresentaram maior atividade na reação de reforma a vapor do etanol nas temperaturas de 400 e 450°C. Um aumento na redutibilidade e na área específica foi verificado com a substituição parcial de ferro por cobre ou cobalto nas amostras Fe-Al. A melhoria nas propriedades do material resultou em desempenho superior nos testes de reforma a vapor do etanol, especialmente para o catalisador Co-Fe-Al. Em relação à reforma do metano, foram investigadas amostras Co-Al modificadas com um terceiro elemento. A substituição parcial de Co por um elemento de maior alcalinidade

propiciou um incremento na área específica e modificações no perfil de redução, na força ou quantidade de sítios alcalinos e na cristalinidade do material. As alterações nas propriedades do material proporcionaram menor formação de coque, sendo mantidas ou elevadas as conversões de CH_4 e CO_2. O catalisador Mg-Co-Al apresentou os melhores resultados de atividade, especialmente para o catalisador com razão molar Mg/Co = 0,5 e para ativação na temperatura de 500°C. Desta forma, foi possível avaliar as diferenças entre óxidos mistos contendo diferentes metais ativos para a geração do gás de síntese, bem como a otimização destes catalisadores por meio da adição de promotores. Os óxidos mistos exibiram alta área específica, elevada estabilidade térmica e moderada acidez que conduziram a melhores desempenhos nos diferentes processos estudados.

Palavras-chave: Gás de síntese; decomposição; reforma; óxidos mistos.

Abstract

The Coal or Gas or Biomass-To-Liquids (XTL) technology allows the production of liquid fuels from biomass, mineral coal or natural gas. The synthesis of optimized catalysts is a great challenge for improving the feasibility of these processes. In this context, mixed oxides are promising alternatives as they exhibit interesting catalytic properties for different chemical processes. However, its application for XTL processes still requires further investigation. The purpose of this thesis was to evaluate catalysts based on mixed oxides for the generation of synthesis gas through the decomposition of ethanol and the reforming of ethanol or methane. Fe-Al, Co-Al and Ni-Al samples were prepared by the co-precipitation method and characterized by different techniques. The reactions were conducted using tubular fixed bed reactors. The gaseous and liquid feedstocks were fed continuously and the analysis was performed by gas chromatography. A better commitment between the properties and catalytic performance for the decomposition of ethanol was observed for samples with Ni^{2+}/Al^{3+} molar ratios between 1 and 3 because this composition favored the formation of the mixed oxides. For the Fe-, Co- or Ni-based materials, the formation of hydrotalcite-type materials was identified in the precursors of the Co-Al and Ni-Al catalysts and thus yielding mixed oxides after thermal treatment. Higher conversion of ethanol and selectivity towards H_2 and CO for the decomposition of ethanol was observed for these samples. The iron-based catalysts led to higher formation of ethylene and acetaldehyde and a decrease on the coke deposition. The partial substitution of Ni by a third element modified the reduction profile and decreased the acidity of samples. For the Ni-Al samples, the catalysts containing Zn, Mo or Co showed higher activity for the steam reforming of ethanol at 400 and 450°C. An increase in the reducibility and in the specific surface area was verified when iron is partly substituted by copper or cobalt in the Fe-Al samples. The improvement in the properties of the material resulted in a better performance for the steam reforming of ethanol, especially for the Co-Fe-Al catalyst. Regarding the reforming of methane, different Co-Al samples modified with a third element were investigated. The partial substitution of Co by an element with higher basicity provided an increase in the specific surface area and modifications on the

reduction profile, in the strength or quantity of the alkalinity sites and in the overall crystallinity of the material. The changes in the properties provided smaller coke formation while maintaining or even increasing the CO_2 and CH_4 conversions. The Mg-Co-Al catalyst exhibited the best activity results, especially for the catalyst with Mg/Co molar ratio of 0.5 and for activation at 500°C. Therefore, it was possible to evaluate the differences between the mixed oxides based on different active metals for the generation of the synthesis gas, as well as the optimization of these catalysts through the addition of promoters. The mixed oxides exhibited high specific surface area, high thermal stability and moderate acidity that led to better performance for the different studied processes.

Keywords: Synthesis gas, decomposition, reforming, mixed oxides.

Sumário

Lista de figuras

Lista de tabelas

Lista de símbolos

β	Largura à meia altura do máximo do pico
λ	Comprimento de onda da radiação
θ	Ângulo de Bragg
[ ]	Concentração molar
A	Ânion da intercamada
D	Tamanho médio dos cristalitos das fases óxida e metálica
d_p	Diâmetro médio de partícula
F_i	Vazão de alimentação do componente *i*
I_D	Intensidade da banda D (espectros Raman)
I_G	Intensidade da banda G (espectros Raman)
M^{II}, M^{2+}	Metal divalente
M^{III}, M^{3+}	Metal trivalente
M, Me	Metal
N	Número de átomos de H ou C das espécies
S_{BET}	Área específica estimada pelo método dinâmico de B.E.T.
S_{Ci}	Seletividade para os produtos contendo carbono

S_{H2}	Seletividade para hidrogênio
T_{max}	Temperatura máxima
T_{REA}	Temperatura de reação
T_{red}	Temperatura de redução
X_{ET}	Conversão de etanol
X_{REA}	Conversão dos reagentes
W_{CAT}	Massa de catalisador

Siglas

2D	2 dimensões
ATM	Atmosfera
B.E.T.	Brunauer, Emmett e Teller
BTL	*Biomass-to-liquids*
BTX	Benzeno, tolueno e xileno
CCD	*Charge coupled device*
CCS	*Carbon capture and storage*
CME	Centro de Microscopia Eletrônica
CNF	*Carbon nanofibers*
CNT	*Carbon nanotubes*
CSTR	*Continuous stirred tank reactor*
CTL	*Coal-to-liquids*
DTA	*Differential thermal analysis*
DTG	*Derivative thermogravimetric analysis*
FID	*Flame Ionisation Detector*
FT	Fischer-Tropsch
GC	*Gas chromatograph*

GHSV	*Gas hourly space velocity*
GTL	*Gas-to-liquids*
HCC	Hidrocraqueamento catalítico
HIDW	Hidroisomerização
HT	Materiais do tipo hidrotalcitas
MEV, *SEM*	Microscopia eletrônica de varredura
MWCNT	*Multi walled carbon nanotubes*
pH	Potencial hidrogeniônico
R&D	*Research and Development*
SWCNT	*Single walled carbon nanotubes*
Syngas	*Synthesis gas*
Tar	Alcatrão
TCD	*Thermal conductivity detector*
TG, TGA	*Thermal gravimetric analysis*
TPD	*Temperature-programmed desorption*
TPO	*Temperature-programmed oxidation*
TPR	*Temperature-programmed reduction*
WGS	*Water-gas shift*
XRD	*X-ray diffraction*
XTL	*X-to-liquids*

Capítulo 1

Introdução

O esgotamento das reservas de petróleo e a consequente oscilação no preço do barril tem incentivado a busca por fontes alternativas que possam suprir a demanda mundial de energia. Entre elas, a tecnologia genericamente designada por *X-To-Liquids* ou *XTL* (*X = B, C* ou *G,* onde *B = Biomass, C = Coal* e *G = Gas*) possibilita a obtenção de um substituto sintético do petróleo. Esta tecnologia conduz à formação de hidrocarbonetos líquidos e outros produtos químicos a partir do gás de síntese (*syngas*), uma mistura contendo monóxido de carbono e hidrogênio que pode ser gerada a partir de diferentes recursos. As fontes alternativas incluem o gás natural e o carvão mineral, os quais, embora também tenham origem fóssil, apresentam reservas conhecidas que superam as de petróleo crú em 1,5 e 25 vezes, respectivamente (DRY, 2002). A energia obtida a partir da biomassa constitui-se em alternativa igualmente promissora em função de esta fonte ser renovável.

Independentemente da fonte empregada, a tecnologia *XTL* possui três principais etapas, ou seja: geração do gás de síntese, conversão do gás via síntese de Fischer-Tropsch (FT) e hidroprocessamento. Embora as três etapas estejam relativamente bem estabelecidas, Vosloo (2001) destaca que um dos maiores desafios consiste em desenvolvê-las de forma combinada, ou seja, buscar melhorias e inovações advindas de uma análise integrada e que possam conduzir ao melhor custo-benefício da tecnologia como um todo.

Nesta proposta, algumas características deste processo apresentam-se como oportunidades promissoras a serem exploradas para a otimização da tecnologia. Por exemplo, os metais Ru, Ni, Fe e Co são ativos em ambas as etapas de geração e de conversão do *syngas*, embora tipicamente apenas o cobalto e o ferro apresentem viabilidade para emprego na síntese de Fischer-Tropsch (DRY, 2004a; DRY, 2004b). A avaliação energética indica que as reações de gaseificação e reforma são endotérmicas, enquanto que a síntese FT é fortemente exotérmica. Por outro lado, a maior diferença entre os processos parece ser nas condições operacionais. A gaseificação ou reforma requer elevadas temperaturas, enquanto que temperaturas moderadas são adequadas para a síntese FT. As condições operacionais variam com a rota empregada. Entretanto, para a geração do gás de síntese, são utilizadas temperaturas da ordem de 1000°C, enquanto que temperaturas entre 200 e 350°C são empregadas na síntese FT. Em ambos os processos, pressões elevadas (normalmente acima de 20 bar) são utilizadas de forma a aumentar as taxas de reação e favorecer o rendimento nos produtos de interesse.

Devido a esses desafios, constata-se uma evolução significativa nas últimas décadas, no projeto dos reatores e nos catalisadores utilizados neste processo (ESPINOZA *et al*., 1999; STEYNBERG *et al*., 1999). Entretanto, em face às muitas possibilidades e à contínua busca por torná-la ainda mais viável economicamente, esta tecnologia continua recebendo grande atenção, especialmente no desenvolvimento de catalisadores com melhor desempenho e maior vida útil.

A geração do gás de síntese é a etapa mais onerosa da tecnologia *XTL* (DRY, 2004b). Os metais de transição do grupo VIII da tabela periódica apresentam atividade nos processos de reforma. Dentre os referidos elementos, a literatura aponta para Ru e Rh como os metais mais ativos, seguido por Ni, Ir, Pt, Pd e Co (ROSTRUP-NIELSEN e HANSEN, 1993; JONES *et al*., 2008). A taxa de formação de carbono sobre as partículas dos catalisadores baseados em metais nobres é inferior ao observado sobre Ni e Co (ROSTRUP-NIELSEN e HANSEN, 1993), o que representa uma menor tendência à desativação por este mecanismo sobre os metais nobres. Entretanto, o menor custo destes últimos é um incentivo para a sua utilização como metal ativo nos catalisadores destes processos.

A maioria dos catalisadores utilizados em processos de geração do *syngas* das tecnologias *BTL* e *GTL* é preparada pelo método da impregnação. Esta técnica requer um menor número de etapas, sendo a mais utilizada para preparar catalisadores contendo metais nobres por resultar na sua elevada dispersão sobre um suporte. Os percentuais dos metais nobres utilizados normalmente se limita a 1 wt.% do total, sendo de 5-15 wt.% a composição de outros metais utilizados (SATTERFIELD, 1991; HAGEN, 2006).

Por outro lado, no caso dos componentes ativos com menor custo, o método da precipitação mostra-se adequado (HAGEN, 2006). Este método é normalmente utilizado quando se deseja um teor mais alto do metal ativo (acima de 20 wt.%), propiciando uma mistura mais homogênea dos componentes do catalisador, com distribuição da fase ativa mais uniforme e permitindo morfologias diferentes daqueles que o suporte oferece. Outra vantagem, em relação à impregnação, se relaciona ao tamanho de poros e à distribuição de tamanhos de poro, o qual é possível se controlar com este método (LEE, 1985; SATTERFIELD, 1991). Apesar do teor mais alto do metal ativo que pode ser empregado no método da precipitação, em comparação às amostras sintetizadas por impregnação, é possível obter cristais com pequenos tamanhos, especialmente em se tratando em materiais do tipo óxidos mistos. O método de precipitação é uma das técnicas mais práticas e reprodutíveis na preparação de catalisadores baseados em óxidos mistos (COELHO, 1994).

Os óxidos mistos possuem aplicações em diversas áreas. Na indústria química, estes materiais são empregados como catalisadores heterogêneos por possuírem propriedades desejadas tais como elevada área específica, alta estabilidade térmica e cristais do metal ativo com pequenos diâmetros (TRIFIRÓ e VACCARI, 1996; VACCARI, 1998; ABELLÓ *et al.*, 2013; RÃCIULETE *et al.*, 2014). Como catalisadores heterogêneos, as propriedades físico-químicas e catalíticas dos óxidos mistos dependem consideravelmente do grau de não-estequiometria dos componentes (COELHO, 1994). Como mostraram Bhatthacharyya, Chang e Schumacher (1998), o fato de o metal ativo estar aleatoriamente disperso nas camadas da estrutura dos materiais do tipo óxidos mistos, leva à tendência de minimizar o fenômeno de agregação dos cristais deste metal e, desta forma, o crescimento do diâmetro no decorrer dos processos. Consequentemente, os óxidos mistos são promissores para evitar a perda de atividade através do mecanismo de sinterização e crescimento dos cristais, bem como pela deposição de coque. Estes dois mecanismos de desativação são críticos na tecnologia *XTL*.

Apesar da sua versatilidade e das propriedades promissoras apresentadas, os estudos envolvendo o desenvolvimento e a aplicação de óxidos mistos em processos relacionados à geração do gás de síntese são escassos. Alguns trabalhos preliminares envolvendo os processos de decomposição e de reforma sobre óxidos mistos à base de Co, Fe e Ni sugeriram a viabilidade do emprego destes materiais para a geração do *syngas* (LI *et al*., 2008; MEZALIRA *et al*., 2011; BUDIMAN *et al*., 2012; ESPINAL *et al*., 2012a; SERRANO-LOTINA *et al*., 2012; CAI *et al*., 2013). Entretanto, uma investigação mais ampla destes materiais e o seu desempenho nas diferentes rotas é necessária para uma avaliação mais precisa quanto à sua viabilidade.

1.1 Objetivos

O objetivo geral da presente tese consiste na avaliação de diferentes catalisadores tipo óxidos mistos, preparados pelo método da precipitação, para a geração do gás de síntese pelos processos de decomposição do etanol e de reforma a vapor do etanol e reforma do metano com dióxido de carbono.

Como objetivos específicos da tese, tem-se:

(i) a determinação da composição, ou, mais especificamente, a relação entre metal divalente e metal trivalente que proporcione propriedades e desempenho catalítico mais adequado aos óxidos mistos;

(ii) o estudo de catalisadores baseados em diferentes metais ativos, ou seja, em ferro, cobalto ou níquel, incluindo o seu desempenho na reação de decomposição do etanol;

(iii) a caracterização e a avaliação do desempenho dos catalisadores de níquel modificados com terceiro elemento na geração de *syngas* a partir da reforma a vapor do etanol;

(iv) a investigação de catalisadores Fe-Al, com diferentes razões Fe/Al e com a substituição parcial de Fe por Cu ou Co, e o seu desempenho para a reforma a vapor do etanol;

(v) a investigação de catalisadores M-Co-Al (M = Ca, La, Li ou Mg) para a reforma do metano com dióxido de carbono. Para o sistema catalítico com melhor desempenho, o estudo de amostras com diferentes razões M/Co e das condições de ativação na reação de reforma do metano.

A tese divide-se em diferentes capítulos que expõem o estado atual da arte das tecnologias investigadas, a metodologia empregada e os resultados atingidos, discutidos em face às referências mencionadas.

O capítulo 1 introduz o tema que será desenvolvido e a contribuição que a tese pretende oferecer. O segundo capítulo é dedicado à revisão do estado da arte das diferentes etapas constitutivas da tecnologia *XTL*, focando especialmente nos catalisadores heterogêneos existentes para a geração do gás de síntese através dos processos expressos no objetivo geral da tese. A metodologia experimental empregada na preparação e na caracterização dos catalisadores estudados é apresentada no capítulo 3. Este também informa os procedimentos e a parte analítica dos testes de atividade catalítica.

Os principais resultados da parte experimental são apresentados e discutidos a partir do quarto capítulo. Nestes, há a preocupação de explicar os resultados dos ensaios de atividade obtidos com base nos dados de caracterização e nas informações disponíveis na literatura. O capítulo 4 explora a relação entre propriedades e desempenho catalítico na decomposição do etanol sobre amostras com diferentes razões Ni/Al. No capítulo 5 são investigados catalisadores baseados em diferentes metais ativos, ou seja, em níquel, cobalto ou ferro. A reação de decomposição do etanol é utilizada para comparar o desempenho catalítico dos diferentes metais ativos. A reação de reforma a vapor do etanol sobre catalisadores Ni-Al ou Fe-Al modificados é estudada nos capítulos 6 e 7, respectivamente. A obtenção do gás de síntese por reforma do metano sobre catalisadores Co-Al modificados com um terceiro elemento é abordada no capítulo 8. A partir dos resultados deste, a composição do sistema catalítico com melhor desempenho é modificada visando à sua otimização.

No capítulo 10 é elaborada a conclusão da tese a partir dos principais resultados observados. Também são propostas sugestões de trabalhos futuros na área. Ao final, são apresentadas as referências bibliográficas citadas no trabalho.

Capítulo 2

Revisão bibliográfica

O processo de obtenção de hidrocarbonetos e compostos oxigenados a partir de gás de síntese envolve etapas bem estabelecidas. Entretanto, os avanços no projeto e desenvolvimento de reatores e dos catalisadores, bem como os fatores ambientais e econômicos, revelam que muitos desafios perduram quanto à busca pela otimização das tecnologias envolvidas. Nos tópicos que seguem, serão mostrados aspectos gerais da tecnologia *Biomass, Coal* e *Gas-To-Liquids* (*XTL*) e fatores que incentivam a sua utilização para fins de atendimento às demandas globais de energia. Adicionalmente, serão mostrados os esforços recentemente desprendidos e resultados mais significativos no desenvolvimento de novos catalisadores para os processos de geração do gás de síntese.

2.1 Importância da tecnologia XTL

A tecnologia designada por *XTL* envolve a obtenção de hidrocarbonetos e produtos oxigenados a partir da conversão de um gás de síntese (*syngas*), sendo este gerado pelo processamento de diferentes recursos. A tecnologia também pode ser expressa especificamente em função da fonte de que provém o gás de síntese. Desta forma, pode ser chamada *CTL* (*Coal-To-Liquids*), *GTL* (*Gas-To-Liquids*) ou *BTL* (*Biomass-To-Liquids*) quando a mistura gasosa é obtida respectivamente a partir do carvão mineral, do gás natural ou de biomassa.

De forma genérica, as etapas componentes da tecnologia *XTL* podem ser vistas no esquema mostrado na Figura 2.1.

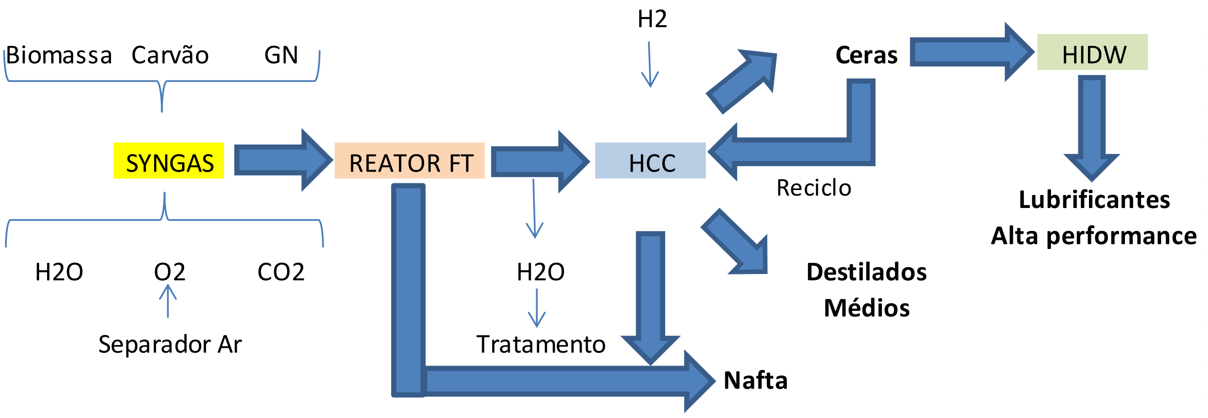

Figura 2.1: Esquema representativo da tecnologia *XTL*.
Fonte: Adaptado de SOUSA-AGUIAR (2010).

Conforme ilustrado na Figura 2.1, o *syngas* pode ser gerado por diferentes rotas envolvendo as três fontes supramencionadas. Após a purificação do gás efluente e ajuste da razão H_2/CO através de reator de deslocamento ou *water-gas shift* (*WGS*), o gás de síntese alimenta o reator Fischer-Tropsch. Após a síntese de Fischer-Tropsch, os hidrocarbonetos e compostos oxigenados na faixa desejada são recolhidos diretamente do reator para serem armazenados e comercializados. A água formada neste processo é enviada para a unidade de remoção de contaminantes orgânicos para posterior descarte ou reuso, enquanto que as frações mais pesadas são encaminhadas para o hidrocraqueamento catalítico (*HCC*). No hidrocraqueamento, os hidrocarbonetos de cadeia muito longa são fracionados em compostos de menor cadeia em presença de H_2. Os produtos que permanecem com cadeias pesadas neste processo podem ser submetidos ao processo de hidroisomerização (*HIDW*) para a obtenção de lubrificantes, ou podem, ainda, ser realimentados ao reator de hidrocraqueamento. Os lubrificantes obtidos por esta tecnologia são de alta qualidade, apresentando a menor razão custo/benefício disponível quando comparados com lubrificantes obtidos por outras rotas (SOUSA-AGUIAR, 2010).

Há muitos fatores que incentivam a exploração desta tecnologia. Ao proporcionar combustíveis sintéticos, a tecnologia *XTL* oferece uma alternativa promissora e conveniente para suprir as demandas energéticas globais face ao esgotamento das reservas de petróleo e à consequente flutuação do preço do barril. A Figura 2.2 mostra a oscilação do seu preço nos últimos anos, mantendo-se atualmente em um elevado patamar.

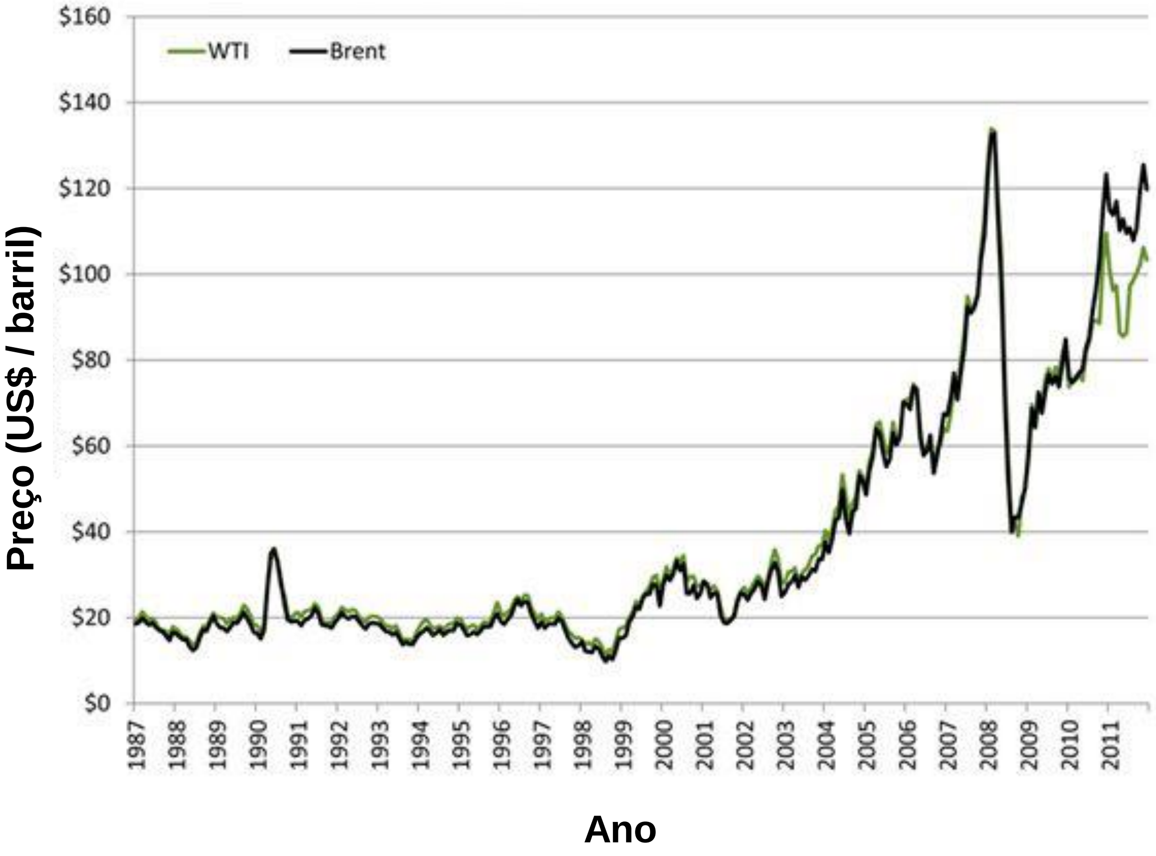

Figura 2.2: Variação do preço do barril de petróleo com os anos a partir de 1987
Fonte: CASEY RESEARCH (2011).

Essas oscilações podem decorrer das mais variadas causas, sejam elas relacionadas a políticas públicas internas de países exportadores de petróleo, a política externa, a conflitos armados, a crises econômicas e à variação cambial. O investimento em tecnologias alternativas permite amenizar a variabilidade da cotação ao se diversificar os recursos empregados e as localidades que desenvolveriam as referidas *commodities*.

Tratando mais especificamente dos recursos, a tecnologia *XTL* possui grande apelo em função das reservas conhecidas dos demais recursos fósseis comparadas as de petróleo crú. De acordo com Dry (2002), as reservas conhecidas de gás natural e de carvão mineral superam às de petróleo por fatores de 1,5 e 25 vezes, respectivamente. Os dados mais recentes podem ser vistos na Figura 2.3, que revelam a distribuição das reservas fósseis conhecidas em diferentes regiões e explicitam o predomínio do carvão mineral frente às duas outras fontes. A China, Índia, Rússia, Austrália e Estados Unidos da América possuem vastas reservas de carvão. Por este motivo, constata-se a existência de inúmeras plantas *CTL* nestes países, estando grande parte delas operando a partir da formação e conversão do gás de síntese (MOHANTY, KUNZRU e SARAF, 1990).

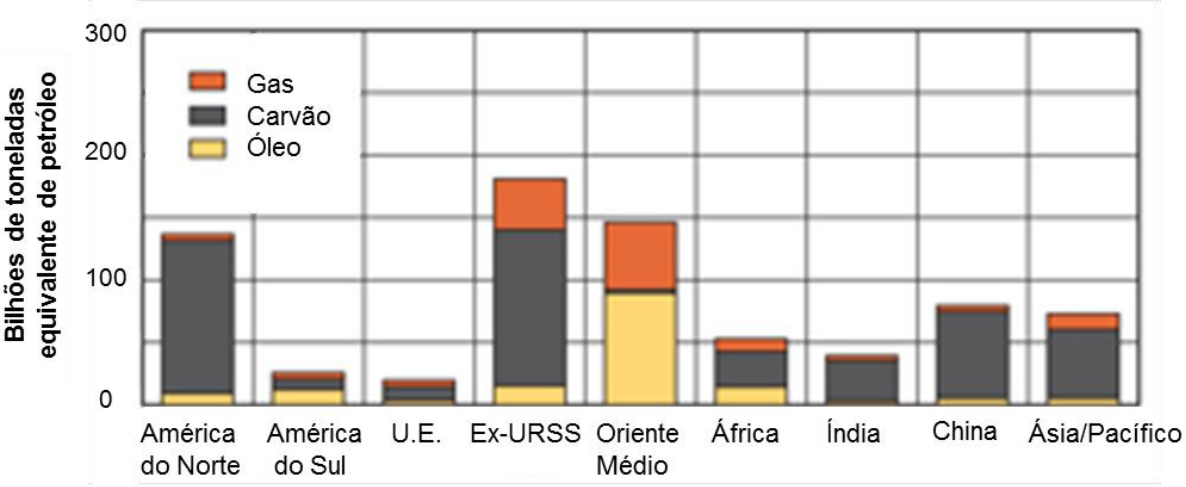

Figura 2.3: Distribuição das reservas de recursos fósseis.

Fonte: WORLD COAL ASSOCIATION (2011).

Em relação ao gás natural, a Tabela 2.1 indica o grande investimento que vem sendo feito na tecnologia *GTL*. O Catar possui duas unidades de grande capacidade com operação iniciada recentemente. A unidade Pearl iniciou a produção em 2011 e possui capacidade equivalente que se aproxima da exibida pela maior planta *CTL* disponível (Secunda, na África do Sul). Também se percebe a inserção da China neste mercado, com quatro unidades *GTL*.

Tabela 2.1: Relação de unidades *GTL* de grande capacidade.

Nome da planta	Capacidade (bpd)	Proprietário	Início
Secunda (CTL) *	160000	Sasol	Sasol 2 - 1980 Sasol 3 - 1984
Oryx GTL	34000	Qatar Petroleum (51%) Sasol (49%)	2007
Escravos GTL	34000	Chevron (75%) Nigerian National Petroleum Co. (15%) Sasol (10%)	2013
Ordos (China)	24000	Shenhua Sasol	2008
Pearl GTL	140000	Qatar Petroleum Shell	2011
Bintulu GTL (Malásia)	15000	Shell	1993
Mossgas, Mossel Bay (África do Sul)	47000	PetroSA (37,5%) Statoil (37,5%) Lurgi (35%)	1992
Jincheng (China)	2500	Jinmei	Em operação
Changzhi (China)	4000	Lu'an	Em construção
Ordos 2 (China)	4000	Yitai	Em operação

* Planta *CTL*, referência para comparação.

Fonte: HYDROCARBON PROCESSING (2011).

Além das reservas disponíveis e da viabilidade econômica do processo, outros autores apontam outros incentivos para a exploração do gás natural por estas tecnologias. A tecnologia *GTL* é uma alternativa promissora para a redução das emissões de NO_x e SO_x para a atmosfera, uma vez que o combustível obtido é praticamente isento de compostos nitrogenados, aromáticos e sulfurados (FEIO *et al.*, 2008; LIRA *et al.*, 2008). Além disso, o diesel obtido pelo processo *GTL* possui um número de cetano próximo do ideal para a boa performance deste combustível.

As reservas de gás natural geralmente se encontram em áreas remotas ou em pequenas quantidades, sendo difícil explorá-las por meio de tecnologias convencionais que envolvam o transporte por tubovias ou por liquefação do gás. Segundo Velasco *et al.* (2010), aproximadamente 40% das reservas encontram-se muito afastadas dos grandes mercados, o que acaba inviabilizando o transporte por tubovias. A restrição no envio do gás natural advindo da prospecção do petróleo em plataformas *offshore* para *flare* também é um fator incentivador para a sua exploração. Esse parece ser o motivo pelo qual o Cenpes/Petrobras iniciou, em 2012, a operação de uma planta *GTL* de pequena capacidade (20 bpd) desenvolvida junto à empresa CompactGTL® (COMPACTGTL, 2013), ou seja, essas restrições e a adequação à tecnologia *GTL* tornam a conversão do gás natural via Fischer-Tropsch atrativa em muitos cenários.

A possibilidade de obtenção de combustíveis sintéticos pelo processamento de recursos renováveis (biomassa), através da tecnologia *BTL,* é igualmente de grande interesse. Esta tecnologia encontra-se em fase de implementação comercial. Há algumas unidades de pequeno porte (demonstração) já construídas e em fase inicial de operação, utilizando resíduos de agricultura e madeira. Entretanto, há muitos incentivos financeiros para a instalação de novas unidades, sobretudo na União Europeia (EUROPEAN BIOFUELS, 2013).

Independentemente da fonte do gás de síntese, Vosloo (2001) destaca que a tecnologia *XTL* passou a apresentar maior viabilidade econômica com o aumento do custo-benefício da tecnologia FT. Este avanço resultou do desenvolvimento de catalisadores com melhor desempenho, bem como da otimização do projeto dos reatores, conforme mostrado em alguns trabalhos (ESPINOZA *et al.*, 1999; STEYNBERG *et al.*, 1999). Uma das maiores oportunidades para este processo consiste na integração energética entre as seções de geração e de conversão do gás de síntese (VOSLOO, 2001).

Além da conversão do gás de síntese pela síntese FT, outras alternativas comerciais para obtenção de combustíveis de valor agregado a partir do *syngas* incluem a produção de dimetil éter (*DME*), de gás natural sintético (*SNG*), de hidrogênio e de metanol. Este último pode ser utilizado para a síntese de outros produtos, como, por exemplo, o processo *Methanol-To-Gasoline* (*MTG*), o qual possibilita a obtenção de gasolina por meio de um processo altamente seletivo a este produto.

2.2 Processos de geração do gás de síntese

A etapa de geração do gás de síntese, incluindo a sua purificação, é a mais onerosa da tecnologia *XTL*, representando custos de instalação e operação na ordem de 60 - 70% dos custos totais da planta (DRY, 2002). Em função da sua maior eficiência, o processo *GTL* possibilita a redução significativa do capital total. Entretanto, o carvão mineral possui reservas nacionais estimadas que superam as de petróleo por um fator de 3,5 vezes, em termos de tonelada equivalente de petróleo (MME, 2014).

2.2.1 Carvão mineral

A conversão indireta de carvão mineral em hidrocarbonetos envolve a formação de gás de síntese a partir da sua gaseificação, conforme mostrado na Equação termoquímica 2.1. A Equação 2.1 não considera outras reações que ocorrem na gaseificação do carvão, especialmente envolvendo outros componentes presentes no carvão mineral (*e.g.*, enxofre e nitrogênio).

$$C_{(s)} + H_2O \rightarrow CO + H_2 \qquad \Delta H_{298K} = 131\ kJ \cdot gmol^{-1} \qquad (2.1)$$

Embora a literatura aponte para uma menor eficiência energética e produtividade em óleo (Kabe *et al.,* 2004), o processo *CTL* indireto apresenta algumas vantagens frente à liquefação direta do carvão mineral. O principal aspecto é justamente a pureza (sem nitrogênio e enxofre), obtida com a possibilidade da purificação do gás gerado em etapa anterior aos processos de conversão do gás, e a grande variedade dos produtos obtidos, sobretudo, a partir da reação de Fischer-Tropsch.

A razão H_2/CO resultante da gaseificação do carvão é inferior ao valor ótimo para as reações de Fischer-Tropsch. Normalmente, a razão obtida por esta rota não excede 0,7 $mol \cdot mol^{-1}$, embora testes em planta piloto para gaseificação do carvão mineral gaúcho já tenham fornecido razão molar H_2/CO de até 2,0 (TOSCANI *et al*., 1984). Para obter um valor mais apropriado para o processo seguinte, é possível efetuar o reciclo de uma fração gasosa efluente do gaseificador. Lu e Lee (2007) mostraram que é possível alcançar eficiências de 50% (base carbono) para o processo *CTL* indireto pelo ajuste do gás de síntese de 0,5 para 1,4 através do reciclo parcial da corrente gasosa. Além disso, a composição do gás pode ser modificada por meio da reação de deslocamento (*WGS*). A reação, mostrada na Equação 2.2, propicia o enriquecimento em hidrogênio a partir do consumo de monóxido de carbono.

$$H_2O + CO \leftrightarrow H_2 + CO_2 \qquad \Delta H_{298K} = -41\ kJ\cdot gmol^{-1} \qquad (2.2)$$

Conforme mostrado na Figura 2.3, as reservas de carvão mineral são significativamente maiores quando comparadas às conhecidas de gás natural. Todavia, Rostrup-Nielsen (1993) destaca que o investimento inicial necessário para uma planta para a obtenção de hidrocarbonetos pela conversão de *syngas* gerado pelo carvão é três vezes maior do que o requerido para a instalação de uma unidade *GTL*. Por outro lado, a literatura também ressalta que unidades *CTL* deste tipo podem apresentar boa rentabilidade para a condição de baixos preços praticados para o carvão e se eletricidade e hidrocarbonetos de alto valor são produzidos em complemento aos combustíveis líquidos em alta escala (AASBERG-PETERSEN *et al.*, 2004; LIU *et al.*, 2011; MANTRIPRAGADA e RUBIN, 2011).

Entretanto, uma grande preocupação das plantas *CTL* é a emissão de CO_2, advinda do excesso de átomos de carbono em relação ao hidrogênio. Conforme Dry e Steynberg (2004), a corrente enriquecida em CO_2 gerada pelo tratamento do gás de síntese é enviada para a atmosfera. Se somada à emissão subsequente associada à queima dos combustíveis líquidos, para o ciclo completo, estima-se que o combustível gerado a partir do carvão emitiria o dobro de dióxido de carbono se comparado aos combustíveis líquidos convencionais, ou seja, obtidos a partir do petróleo crú (FARRELL e BRANDT, 2006).

Neste contexto, algumas alternativas para evitar a emissão atmosférica de CO_2 incluem a sua captura e armazenamento (*CCS*) e a conversão deste gás por meio da sua aplicação em outros processos. Para a estratégia *CCS* convencional, Liu *et al*. (2011) indicam que as emissões seriam reduzidas apenas até níveis comparáveis aos da cadeia de produção dos combustíveis a partir do petróleo crú. Por outro lado, a conversão do gás em bio-óleo por microalgas ou em produtos de valor via processos catalíticos são propostas com um maior apelo. Neste último, uma promissora rota é a sua utilização para a reforma do metano. Por meio dela, gás de síntese seria obtido a partir do CO_2, o qual é justamente o produto de interesse da primeira etapa do processo *CTL* indireto.

2.2.2 Biomassa

Genericamente, a obtenção de gás de síntese a partir da gaseificação de biomassa pode ser representada pela Equação 2.3.

$$C_xH_yO_z + (x - z)H_2O \rightarrow xCO + (x + y/2 - z)H_2 \qquad \Delta H > 0 \qquad (2.3)$$

Uma ilustração do processo de gaseificação de biomassa pode ser vista na Figura 2.4.

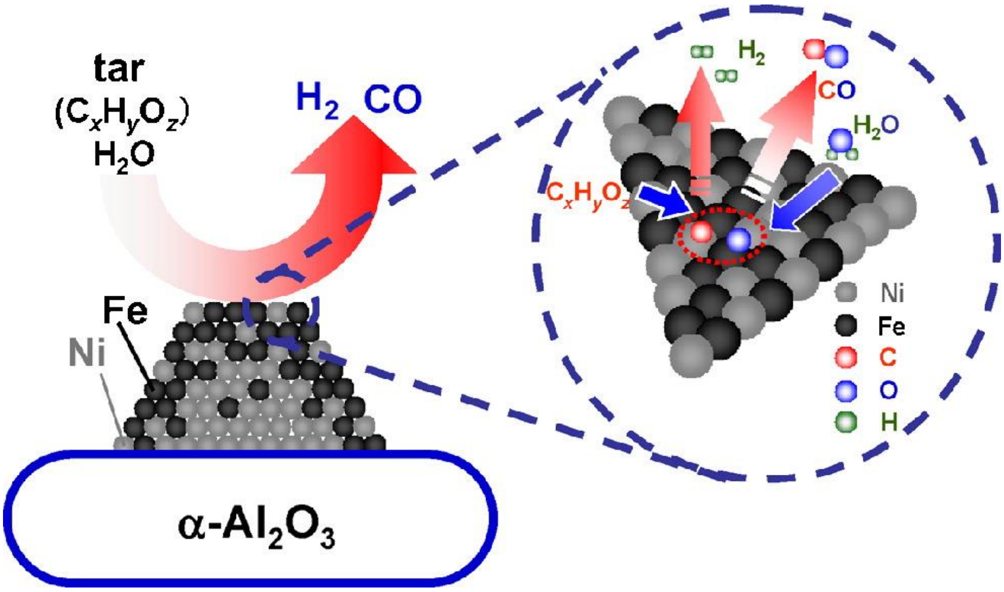

Figura 2.4: Representação da obtenção de gás de síntese através da gaseificação de alcatrão (*tar*) sobre catalisadores Ni-Fe/α-Al_2O_3.
Fonte: WANG, L. *et al.* (2011).

O esquema indica, macroscopicamente, a difusão dos reagentes do interior da fase fluida para a superfície das partículas e, de forma reversa, a difusão dos produtos H_2 e CO do leito para o interior da fase fluida de forma simplificada. Microscopicamente, a molécula do reagente orgânico ($C_xH_yO_z$) é adsorvida no sítio ativo da partícula de catalisador. Ao reagir com a molécula de água, os produtos H_2 e CO dessorvem do sítio ativo.

O gás de síntese também pode ser obtido por outros processos além da gaseificação com vapor d'água mencionada. Outras rotas incluem a pirólise (PEÑA, GÓMEZ e FIERRO, 1996; DUFOUR *et al.*, 2009), a oxidação parcial (MIYAZAWA *et al.*, 2005; DAUENHAUER *et al.*, 2007; RENNARD *et al.*, 2008; RENNARD, KRUGER e SCHMIDT, 2009; RENNARD *et al.*, 2010) e a reforma com dióxido de carbono (HU e LU, 2009; PACHECO, PESSOA e FALCÃO, 2009; DA SILVA *et al.*, 2011).

Em relação à oxidação parcial, algumas vantagens são apontadas como incentivadores desta rota por Rennard *et al.* (2010). As duas principais reações que ocorrem são indicadas nas Equações 2.4 e 2.5, em que a primeira pode ser moderadamente exotérmica ou endotérmica. Dependendo da quantidade de oxigênio empregado e de outras condições do processo, este pode se dar de forma autotérmica, em que a energia demandada pela reação de oxidação parcial seria fornecida pela de oxidação completa (Equação 2.5).

$$C_xH_yO_z + (x/2 - z/2)O_2 \rightarrow xCO + (y/2)H_2 \qquad (2.4)$$

$$C_xH_yO_z + (x + y/4 - z/2)O_2 \rightarrow xCO_2 + (y/2)H_2O \qquad \Delta H < 0 \qquad (2.5)$$

Outras vantagens incluiriam a disponibilidade de O_2 para remoção de coque, as elevadas taxas de transferência de calor e eficiência térmica, tempos de contato mínimos e altas conversões.

Uma proposta inovadora consiste na co-gaseificação de carvão e biomassa integrada com captura do CO_2 de forma a reduzir a emissão de gases do efeito estufa na síntese de combustíveis FT sintéticos. A análise global do processo indica viabilidade econômica e menores emissões do combustível sintético comparado ao ciclo envolvendo o refino tradicional do petróleo crú (LIU *et al.*, 2011). Entretanto, outros estudos ainda precisam ser conduzidos para melhor desenvolver o conceito da co-gaseificação de carvão e biomassa.

Artigos recentes tratando da conversão do gás de síntese obtido a partir de biomassa pela síntese de Fischer-Tropsch são um claro indicativo do interesse comercial no processo *BTL*, apontando para a tendência de expansão nessa tecnologia (JUN *et al.*, 2004; DEMIRBAS, 2007; LÖGDBERG *et al.*, 2009; ZHANG, 2010; BORG *et al.*, 2011). Além do etanol, outros principais recursos renováveis desta natureza investigados incluem o glicerol, resíduos sólidos urbanos e industriais (WANG *et al.*, 2013; MIYAZAWA *et al.*, 2005; RENNARD *et al.*, 2010; ZHANG, 2010; WANG, L. *et al.*, 2011; KOIKE *et al.*, 2013; MANFRO & SOUZA, 2014) e materiais ricos em lignocelulose como cavacos de madeira e resíduos agrícolas (DI BLASI *et al.*, 1999; RAPAGNÁ *et al.*, 2002; DUFOUR *et al.*, 2009).

Conforme destacaram Hamelinck *et al*. (2004), em acréscimo aos produtos principais H_2, CO e CO_2, o gás de síntese obtido neste processo frequentemente contém uma série de contaminantes indesejáveis ao processo. Dentre eles, mencionam-se alcatrão (*tar*), BTX (benzeno, tolueno e xileno), impurezas como NH_3, HCN, H_2S, COS, HCl, além de metais voláteis, particulados e fuligem. Por consequência, a purificação do gás de síntese prévia à síntese de FT requer diversas etapas. Estas também se relacionam com a tecnologia empregada na geração do gás e nas suas condições operacionais. Precisamente, a dificuldade na produção e, sobretudo, na limpeza do gás de síntese é apontada como sendo a principal causa de unidades industriais ainda não terem sido estabelecidas (ZHANG, 2010).

2.2.3 Gás natural

Assim como ocorre no processo *BTL*, a transformação de gás natural em gás de síntese possui diferentes alternativas. Há três principais rotas disponíveis, indicadas sempre em função do maior componente da mistura gasosa (metano), as quais são: reforma a vapor do metano (Equação 2.6), reforma do metano com dióxido de carbono (Equação 2.7) e oxidação parcial do metano (Equação 2.8).

$$CH_4 + H_2O \rightarrow 3H_2 + CO \qquad \Delta H_{298K} = 206\ kJ \cdot gmol^{-1} \qquad (2.6)$$

$$CH_4 + CO_2 \rightarrow 2H_2 + 2CO \qquad \Delta H_{298K} = 246\ kJ \cdot gmol^{-1} \qquad (2.7)$$

$$CH_4 + ½O_2 \rightarrow 2H_2 + CO \qquad \Delta H_{298K} = -36\ kJ \cdot gmol^{-1} \qquad (2.8)$$

Comercialmente, a reforma a vapor do metano (Equação 2.6) é a tecnologia mais amplamente utilizada para produção de gás de síntese no processo *GTL*.

Entretanto, algumas desvantagens recorrentemente apontadas para a reforma a vapor do gás natural incluem (PEÑA, GÓMEZ e FIERRO, 1996; LUNSFORD, 2000; VOSLOO, 2001):

- razão H_2/CO obtida é maior do que a necessária para a síntese FT;
- equipamento para reforma é de alto custo;
- reação demanda muita energia (fortemente endotérmica);
- não é compatível com plantas em regiões áridas;
- conversão mais baixa de metano devido a uma temperatura máxima de operação (T_{max} = 900°C).

Por outro lado, as demais alternativas podem ser atrativas e viáveis à reforma a vapor. Dentre alguns fatores incentivadores desta escolha, Peña, Gómez e Fierro (1996) destacam: a razão H_2/CO; a destinação do gás de síntese; a pureza do produto; a presença de CO_2, N_2, H_2O e CH_4; a capacidade da planta; a disponibilidade, pureza e custo das matérias-primas.

Como já fora mencionado, a reforma pode ser conduzida sem a alimentação de vapor d’água (a seco), utilizando, neste caso, dióxido de carbono. Como sugerido pela Equação 2.7, a razão molar H_2/CO resultante é menor, se aproximando da unidade. Essa rota possui grande apelo ambiental, uma vez que consome dois gases responsáveis pelo efeito estufa. De acordo com Chattanathan, Adhikari e Taylor (2012), a contribuição individual de CO_2 e de CH_4 para o efeito estufa total seria de, respectivamente, 9 - 26% e 4 - 9%. Entretanto, a formação de coque é ainda mais acentuada neste processo, uma vez que a ausência de água impede que o carbono formado seja gaseificado.

Para a oxidação parcial catalítica, a literatura aponta para vantagens e desvantagens (LUNSFORD, 2000; VOSLOO, 2001; SANTOS, 2005; AASBERG-PETERSEN *et al.*, 2011). Aspectos que incentivam a oxidação parcial do metano incluem:

- razão molar H_2/CO se aproxima de 2, que é o valor ideal para a síntese FT;

- reação moderadamente exotérmica;

- reação é mais rápida quando comparada à reforma a vapor.

Por outro lado, são desvantagens desta rota:

- reação de oxidação total difícil de ser controlada;

- necessidade de planta que forneça O_2;

- ocorrência de *hot spots*, pontos de superaquecimento no leito que conduzem à sinterização do catalisador ou mesmo ao rompimento das paredes do equipamento de reforma;

- Maior periculosidade devido à mistura CH_4/O_2.

Uma revisão completa da literatura, focando os mecanismos da reação de oxidação parcial do metano sobre catalisadores à base de metais de transição, foi realizada por Enger, Lødeng e Holmen (2008). A maior parte dos trabalhos envolve níquel e cobalto, seguidos por ródio e rutênio. Embora os catalisadores de cobalto reduzidos tipicamente conduzam à conversão de equilíbrio, diversas pesquisas mostraram que a sua desativação ocorre em temperaturas superiores quando comparada ao níquel (SLAGTERN *et al.*, 1998; WANG e RUCKENSTEIN, 2001). Enger, Lødeng e Holmen (2009) mostraram que a principal causa é a reoxidação do cobalto metálico. Ainda relacionado às fases envolvendo cobalto, Sokolovskii *et al.* (1997) mostraram que o cobalto na forma cúbica conduz às atividades mais elevadas na oxidação parcial do metano, enquanto que a desativação é acompanhada pela perda de sítios de cobalto metálico e formação da fase $CoAl_2O_4$. Em função destes fenômenos, normalmente são adicionados promotores visando à maior redutibilidade em temperaturas mais baixas.

Além das rotas abordadas, é de particular interesse realizar reações de reforma combinadas. A principal opção é a reforma autotérmica. O nome advém do fato de o processo ser feito com a minimização da energia fornecida ao reformador. Mais precisamente, o conceito envolve o fornecimento da energia requerida para a gaseificação do metano com vapor d'água a partir da oxidação do metano em um mesmo reator. Como ilustra a Figura 2.6, o reator de reforma autotérmica consiste em um queimador, uma câmara de combustão e um leito catalítico em um mesmo casco pressurizado.

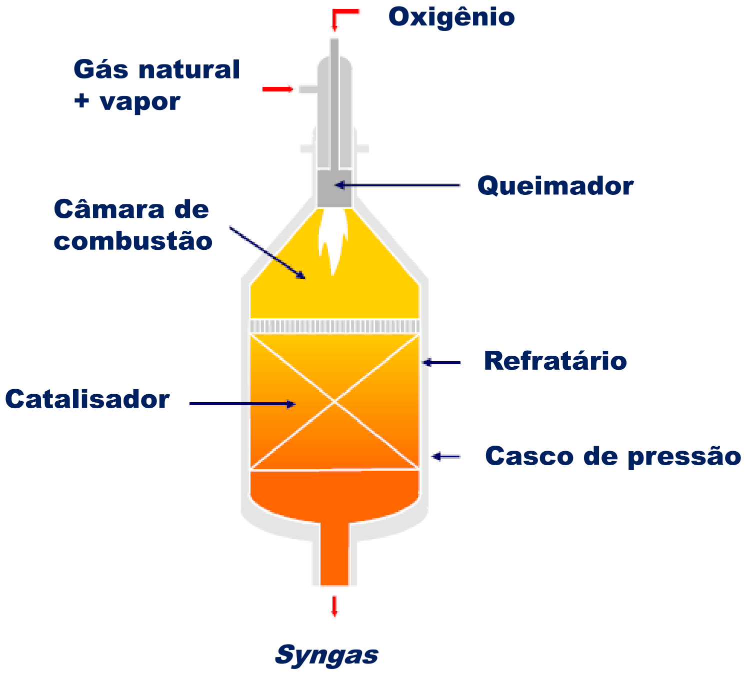

Figura 2.5: Ilustração do reator para reforma autotérmica.

Fonte: AASBERG-PETERSEN *et al.* (2011)

Embora ocorra um incremento no investimento em equipamentos e a razão H_2/CO resultante seja maior do que a desejável para a síntese FT, há alguns benefícios ao se conduzir este processo combinado. Em especial, além da integração energética, esses benefícios incluem as condições de operação mais brandas do que a reforma a vapor, a menor quantidade de *hot spots* e a menor deposição de coque sobre o catalisador quando comparados à oxidação parcial (ARMOR, 1999; VOSLOO, 2001; SANTOS, 2005).

Ainda são encontradas reformas combinadas além da autotérmica. Os principais objetivos consistem na minimização do coque formado, da energia requerida pelo processo e ou no ajuste da razão H_2/CO. A maioria dos artigos científicos sobre este assunto envolve a combinação da reforma do metano, com CO_2, com vapor d'água ou com oxigênio. Armor (1999) destaca que, no caso da reforma com $CO_2 + H_2O$, a razão H_2/CO não é inferior a 1,3/1 $mol \cdot mol^{-1}$. Neste caso, a reação global é dada pela Equação 2.9.

$$2CH_4 + H_2O + CO_2 \rightarrow 5H_2 + 3CO \qquad (2.9)$$

Outros aspectos relacionados à aplicação em larga escala e ao projeto dos equipamentos especificamente para cada rota também podem ser obtidos na literatura (ARMOR, 1999; AASBERG-PETERSEN *et al.*, 2011).

2.3 Catalisadores para a geração de gás de síntese

Os catalisadores utilizados nos processos de geração de gás de síntese baseiam-se em metais de transição do grupo VIII da tabela periódica. Dentre estes, a literatura refere-se, em sua maioria, a materiais que possuem níquel ou metais nobres como metais ativos no processo. Além destes, em menor quantidade, as pesquisas incluem catalisadores à base de cobalto e ferro. A literatura também indica que as plantas comerciais para reforma do metano operam utilizando catalisadores de níquel suportados em óxidos tais como Al_2O_3, ZrO_2, $MgAl_2O_4$, $CaO\text{-}Al_2O_3$ e MgO (ROSTRUP-NIELSEN, 1993; AASBERG-PETERSEN *et al.*, 2011).

Em artigos recentes, que revisaram o estado da arte atual dos processos de reforma do etanol (BSHISH *et al.*, 2011) e do metano (BUDIMAN *et al.*, 2012), é possível observar o predomínio de catalisadores preparados pelo método da impregnação à umidade incipiente ou à seco. Neste método, uma solução contendo o precursor do metal ativo, com volume necessário para preencher o volume dos poros do suporte, é aspergida sobre um óxido poroso (DAVIDSON, SUN e WANG, 2013). As principais vantagens deste método consistem na ausência da etapa de filtração, na inserção de praticamente todos os átomos do metal sobre o suporte e na minimização da geração de efluentes líquidos. Entretanto, sucessivas impregnações são necessárias se teores mais altos do metal são desejados (DE JONG, 2009). A deposição do precursor do metal ocorre por precipitação durante a secagem dos sólidos, conduzindo a fracas interações do metal com o suporte, além de dificultar o controle sobre a deposição do metal e, desta forma, sobre a dispersão (REGALBUTO, 2006; EWBANK *et al*., 2014).

Para a síntese de materiais com elevados teores dos metais ativos, o método da precipitação possibilita a obtenção de uma mistura mais homogênea dos componentes e materiais com diferentes morfologias (SATTERFIELD, 1991; HAGEN, 2006). A co-precipitação de diferentes componentes é uma das técnicas mais práticas e reprodutíveis na preparação de catalisadores baseados em óxidos mistos. Neste método, ocorre a precipitação simultânea de íons metálicos no seio de uma solução geralmente aquosa (COELHO, 1994; CHEN *et al*., 2013). O processo pode resultar na formação de materiais do tipo hidrotalcitas (HT). Estes materiais são argilas aniônicas sintéticas cuja preparação é simples e de baixo custo, embora raramente possam ser obtidas diretamente na natureza. Conforme mostrado na Figura 2.7, estes materiais consistem em hidróxidos mistos lamelares em que há a presença de ânions e moléculas de água nas intercamadas da estrutura. A sua composição química pode ser descrita em termos dos metais (M) e do ânion da intercamada (A) pela fórmula genérica $[M^{2+}_{1-x}M^{3+}_{x}(OH)_2]^{b+}[A^{n-}]_{b/n}{\cdot}mH_2O$ (VACCARI, 1998; MACHEJ *et al*., 2014).

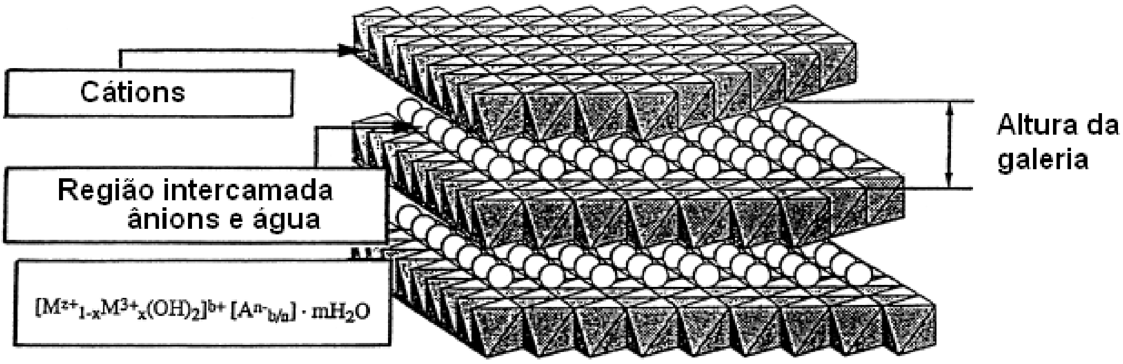

Figura 2.6: Representação da estrutura de material do tipo hidrotalcita (VACCARI, 1998).

Estes compostos constituem uma classe especial de materiais inorgânicos que atualmente vêm chamando a atenção pelo seu potencial de aplicação na medicina, como condutores iônicos. Mas o principal interesse consiste na sua aplicação na catálise, utilizando estes compostos como catalisadores, como suportes e como precursores. A calcinação conduzida em condições adequadas resulta na formação dos óxidos mistos ao promover a destruição da estrutura da hidrotalcita, a qual normalmente ocorre a temperaturas inferiores a 400°C (LÓPEZ-SALINAS *et al.*, 1996; HOLGADO, RIVES e SAN ROMÁN, 2001; TZOMPANTZI *et al*., 2013).

As propriedades físico-químicas e catalíticas dos óxidos mistos dependem do grau de não-estequiometria dos seus componentes (CHEN *et al*., 2013). Segundo Thevenot, Szymanski e Chaumette (1989, *apud* VACCARI, 1999), o valor de x da fórmula geral necessário para formar estruturas do tipo hidrotalcitas é de 0,1 – 0,5, correspondendo a valores para a razão molar M^{II}/M^{III} no intervalo 1 – 9. No entanto, há indícios de que a formação de compostos do tipo hidrotalcitas puros ocorra em um intervalo mais estreito ($0,20 < x < 0,34$), ou seja, em um valor da razão M^{II}/M^{III} entre 2 e 4 (VACCARI, 1999; RÃCIULETE *et al*., 2014).

Assim, as propriedades extraordinárias que apresentam, tais como alta área específica obtida pela elevada dispersão dos óxidos mistos, controle das propriedades ácido/base e elevada estabilidade térmica (VACCARI, 1998; ABELLÓ *et al.*, 2013; RÃCIULETE *et al*., 2014), fazem com que seja de interesse investigar a aplicação de catalisadores do tipo óxidos mistos para diferentes processos. Para exemplificar, há referências da utilização de diferentes óxidos mistos nos processos de oxidação total do metano (URDÃ *et al*., 2013), de decomposição do metano (ESCOBAR e PEREZ-LOPEZ, 2014), de síntese de *n*-butanol a partir do etanol (CARVALHO *et al*., 2012), de deslocamento água-gás (POGGIO-FRACCARI *et al*., 2014), dentre outras. Apesar disso, ainda são necessárias investigações mais aprofundadas sobre a utilização destes materiais em processos de geração do gás de síntese.

2.3.1 Reforma do metano

Os metais de transição do grupo VIII são ativos na reforma a vapor de hidrocarbonetos. Destes, as revisões na literatura elencam Ru e Rh como os metais mais ativos para a reforma, seguidos por Ni, Ir, Pt, Pd e Re (ROSTRUP-NIELSEN e HANSEN, 1993; JONES *et al.*, 2008). Os elementos Co e Fe também são ativos, mas tipicamente oxidam em condições normais de reforma (ROSTRUP-NIELSEN, 1973). A Figura 2.8 reproduz a frequência de *turnover* em função da energia de adsorção de C e O, fornecendo uma ideia qualitativa da atividade dos diferentes metais ativos.

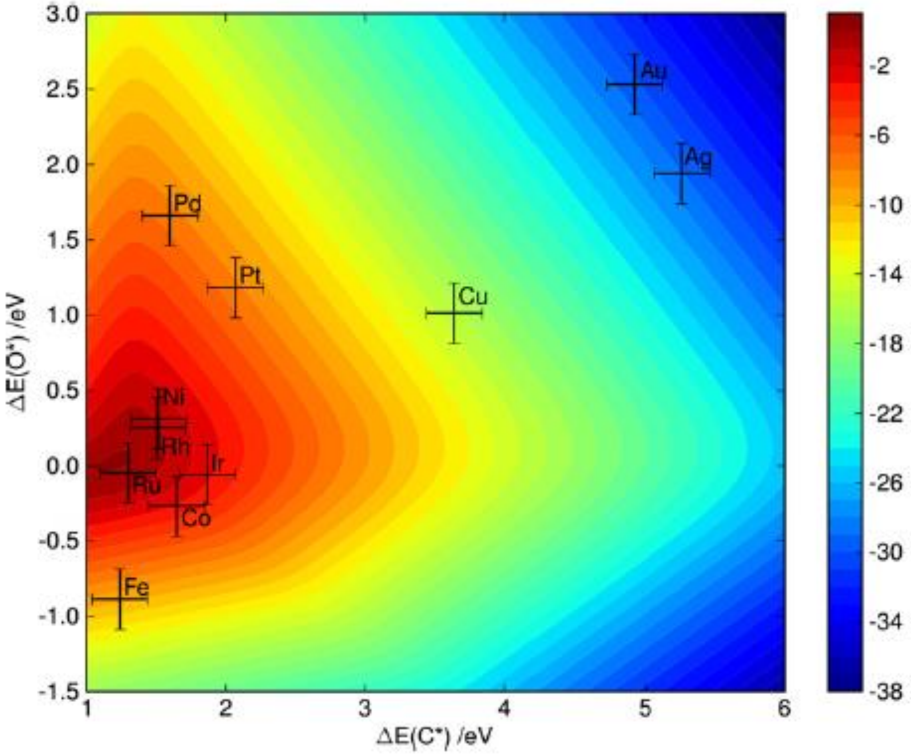

Figura 2.7: Gráfico 2D da frequência de *turnover* ($\log_{10}$) em função das energias de adsorção de C e O. Cálculos realizados considerando, como condições da reação de reforma, 773 K, 1 bar e 10% de conversão de CH_4. Fonte: JONES *et al.* (2008).

Além disso, a taxa de formação de carbono é sensivelmente menor sobre catalisadores à base de metais nobres comparada ao exibido pelo Ni, atribuído à menor dissolução de carbono nestes metais (ROSTRUP-NIELSEN, 1993). Entretanto, o elevado custo dos metais nobres incentiva a utilização do Ni, assim como pesquisas que visem a potencial aplicação de catalisadores à base de Co e Fe. Neste contexto, alguns trabalhos para reforma com CO_2 sobre catalisadores de Co suportados mostraram que a formação de coque e a reoxidação do cobalto podem ser diminuídas pela adição de promotores tais como álcalis e metais nobres (NAGAOKA, TAKANABE e AIKA, 2003; BOUARAB *et al.*, 2004; NAGAOKA, TAKANABE e AIKA, 2004).

Como já fora mencionado, a reforma pode ser conduzida sem a alimentação de vapor d'água (a seco), utilizando, neste caso, dióxido de carbono. Como sugerido pela Equação 2.7, a razão molar H_2/CO resultante é menor, se aproximando da unidade. Essa rota possui grande apelo ambiental, uma vez que consome dois gases responsáveis pelo efeito estufa. De acordo com Chattanathan, Adhikari e Taylor (2012), a contribuição individual de CO_2 e de CH_4 para o efeito estufa total seria de, respectivamente, 9 - 26% e 4 - 9%. Rostrup-Nielsen e Hansen (1993) mostraram que o mecanismo envolvido na reforma de hidrocarbonetos com CO_2 não se modifica significativamente com a substituição de CO_2 por H_2O. Desta forma, o desempenho dos metais ativos para reforma mencionados anteriormente possui a tendência de ser similar em ambos os processos, embora a atividade de Rh e Ru não seja tão superior aos demais como verificada para a reforma a vapor. Entretanto, a formação de coque é ainda mais acentuada neste processo, uma vez que a ausência de água impede a gaseificação do carbono através da equação 2.18.

Para evitar a desativação por deposição de coque sobre catalisadores baseados em Ni ou Co, algumas alternativas incluem a utilização de diferentes suportes como Al_2O_3, CeO_2, La_2O_3, SiO_2, ZrO_2, etc. (WANG, LU e MILLAR, 1996; ROH, POTDAR e JUN, 2004; POMPEO *et al.*, 2005; BARROSO-QUIROGA e CASTRO-LUNA, 2010). A adição de pequenas quantidades de metais nobres como promotores é outra estratégia frequentemente adotada, os quais incluem Ru (CRISAFULLI *et al.*, 2002; NAGAOKA, TAKANABE e AIKA, 2004), Pt (NAGAOKA, TAKANABE e AIKA, 2004; PAWELEC *et al.*, 2007), Pd (STEINHAUER *et al.*, 2009). Além dos metais nobres, outros promotores também podem ser adicionados para melhoria do desempenho destes catalisadores, sendo que a maioria dos autores investiga a modificação com óxidos de metais alcalinos. Estes frequentemente conduzem a menores taxas de deposição de coque, mantendo similares conversões de metano. Os metais com maior alcalinidade investigados como promotores, em sua maior parte, são adicionados por co-impregnação. Estes promotores incluem K, Li, La, Mg, Ba, Ca dentre outros (RUCKENSTEIN e HU, 1995; QUINCOCES *et al.*, 2001; DIAS e ASSAF, 2003; HOU *et al.*, 2003; BOUARAB *et al.*, 2004; JING *et al.*, 2004; JUAN-JUAN, ROMÁN-MARTÍNEZ e ILLÁN-GÓMEZ, 2006; BARROSO-QUIROGA e CASTRO-LUNA, 2010). Além da adição por co-impregnação, outros autores propuseram a modificação do material mediante a síntese por outros métodos, dando origem a diferentes materiais. Neste caso, são destacados materiais precipitados do tipo óxidos mistos (BHATTACHARYYA, CHANG e SCHUMACHER, 1998; CRISAFULLI *et al.*, 2002; GUO *et al.*, 2004; HOU e YASHIMA, 2004; MARTINEZ *et al.*, 2004; KIM *et al.*, 2007; DAZA *et al.*, 2008; DAZA *et al.*, 2010) e do tipo perovsquita (GOLDWASSER *et al.*, 2005; CHOUDHARY e MONDAL, 2006).

Em relação aos materiais do tipo óxidos mistos, Bhattacharyya, Chang e Schumacher (1998) compararam o desempenho de óxidos mistos Ni-Al e Ni-Mg-Al com catalisadores NiO suportados para a reação de reforma a seco do metano. Os autores observaram maior atividade para os óxidos mistos, a qual foi atribuída à dispersão uniforme e menor tamanho de cristais de Ni^0 formados, bem como à menor formação de coque. A distribuição aleatória dos íons de níquel nas intercamadas da estrutura desacelera o fenômeno de crescimento dos cristais e, desta forma, minimiza a agregação do níquel metálico que conduz à diminuição da área metálica e consequente menor atividade.

Trabalhos recentes envolvendo óxidos mistos baseados em níquel para a reforma do metano com dióxido de carbono incluíram sistemas catalíticos do tipo Ni-Co-Al, Ni-Al, Ce-Ni-Al (DE SOUSA *et al*., 2012), La-Mg-Ni-Al (SERRANO-LOTINA *et al*., 2012; SERRANO-LOTINA & DAZA, 2013), Ni-Fe (CARVALHO *et al*., 2014), dentre outros.

Em relação aos óxidos mistos que possuem o cobalto como metal ativo, a maioria dos trabalhos baseia-se em materiais do tipo Co-Al (GENNEQUIN *et al*., 2011; BUDIMAN *et al*., 2012; CAI *et al*., 2013; FAKEEHA *et al*., 2014). Destes, o sistema Mg-Co-Al tem sido apontado como o mais promissor, em decorrência da minimização da formação de coque, em função da presença do álcali, a qual é acompanhada da manutenção de alta atividade para a reação de reforma. Entretanto, não foi realizado um estudo comparativo com diferentes elementos alcalinos, para avaliar o seu efeito sobre as propriedades estruturais e catalíticas para a reação de reforma do metano com CO_2.

2.3.2 Decomposição e reforma do etanol

Os processos envolvendo a transformação catalítica do etanol permitem a obtenção de diversos produtos. Estes incluem hidrogênio, gás de síntese, metano, eteno e acetaldeído.

Para exemplificar a sua complexidade, são destacadas reações que podem ocorrer simultaneamente durante a transformação do etanol. Estas são favorecidas ou desfavorecidas conforme as condições operacionais e os catalisadores empregados.

A reforma a vapor do etanol produz gás de síntese (Equação 2.10) ou, quando em excesso de água, hidrogênio e CO_2 (Equação 2.11).

$$C_2H_5OH + H_2O \rightarrow 2CO + 4H_2 \qquad \Delta H_{298K} = 256\ kJ{\cdot}mol^{-1} \qquad (2.10)$$

$$C_2H_5OH + 3H_2O \rightarrow 2CO_2 + 6H_2 \qquad \Delta H_{298K} = 174\ kJ{\cdot}mol^{-1} \qquad (2.11)$$

Entretanto, outras possíveis reações que podem ocorrer incluem a desidratação (Equação 2.12) e desidrogenação (Equação 2.13) do etanol, assim como também a subsequente decomposição do acetaldeído (Equação 2.14). Essas reações são favorecidas quando há a ausência da co-alimentação de água no sistema, ou seja, no processo de decomposição do etanol.

$$C_2H_5OH \rightarrow C_2H_4 + H_2O \qquad \Delta H_{298K} = 45\ kJ{\cdot}mol^{-1} \qquad (2.12)$$

$$C_2H_5OH \rightarrow CH_3CHO + H_2 \qquad \Delta H_{298K} = 68\ kJ{\cdot}mol^{-1} \qquad (2.13)$$

$$CH_3CHO \rightarrow CH_4 + CO \qquad \Delta H_{298K} = -19\ kJ{\cdot}mol^{-1} \qquad (2.14)$$

O gás de síntese também pode ser obtido a partir de reações envolvendo o metano gerado na Equação 2.14, bem como pela reação *WGS* (Equação 2.2).

$H_2O + CO \rightarrow CO_2 + H_2$ $\Delta H_{298K} = -41\ kJ \cdot mol^{-1}$ (2.2)

Material carbonáceo (coque) pode ser formado durante este processo. Além de ser formado a partir da decomposição do metano (Equação 2.15), o coque também pode ser formado pela reação de Boudouard (Equação 2.16) e polimerização do eteno formado (Equação 2.17). Entretanto, o coque também pode ser consumido em elevadas temperaturas pela reação de Boudouard reversa e pela gaseificação com vapor d'água, expressa na Equação 2.18.

$CH_4 \rightarrow C_{(s)} + 2H_2$ $\Delta H_{298K} = 75\ kJ \cdot mol^{-1}$ (2.15)

$2CO \leftrightarrow CO_2 + C_{(s)}$ $\Delta H_{298K} = -172\ kJ \cdot mol^{-1}$ (2.16)

$nC_2H_4 \rightarrow$ polímero $\rightarrow$ coque (2.17)

$C_{(s)} + H_2O \rightarrow CO + H_2$ $\Delta H_{298K} = 131\ kJ \cdot mol^{-1}$ (2.18)

Outra reação significativa que pode ser favorecida em temperaturas de reação amenas consiste na decomposição do etanol para gerar CO_2 e CH_4 (Equação 2.19).

$C_2H_5OH \rightarrow ½CO_2 + 3/2CH_4$ $\Delta H_{298K} = -74\ kJ \cdot gmol^{-1}$ (2.19)

Trabalhos recentes mostraram que a força da interação do metal ativo com o suporte é fundamental para o bom desempenho dos catalisadores para a reforma do etanol (BAYRAM *et al.*, 2011; ILGAZ-SOYKAL *et al.*, 2012; MARTONO & VOHS, 2012; TRANE-RESTRUP *et al.*, 2013). Desta forma, o incremento dessas interações que os óxidos mistos oferecem é um incentivo para a sua aplicação neste processo.

Os trabalhos envolvendo os catalisadores do tipo óxidos mistos para reforma a vapor do etanol, em sua maioria, voltam-se à obtenção de hidrogênio. Alguns resultados promissores observados pelo grupo do Prof. Laborde (MAS *et al.*, 2008a; MAS *et al.*, 2008b) para óxidos mistos do tipo $NiAl_2O_4$ foram sucedidos por outras pesquisas envolvendo óxidos mistos baseados no mesmo metal ativo (COLEMAN *et al.*, 2009; MUROYAMA *et al.*, 2010), além de materiais à base de cobalto (BUSCA *et al.*, 2010; ESPINAL *et al.*, 2012a; ESPINAL *et al.*, 2012b).

Abelló e colaboradores (2013) investigaram óxidos mistos do tipo Ni/Fe derivados de hidrotalcitas para a reforma a vapor do etanol. Os autores encontraram forte relação das propriedades do material com a razão Ni/Fe. Para razões Ni/Fe moderadas, os autores obtiveram o melhor compromisso entre atividade catalítica e propriedades estruturais e eletrônicas, sobretudo por proporcionar menores diâmetros dos cristais de Ni^0 e menor formação de coque. Em trabalho complementar do mesmo grupo, foi observado que, para razões Ni/Fe muito baixas, ou seja, para elevados teores de ferro, os óxidos mistos apresentam decréscimo na estabilidade térmica, sendo mais suscetíveis a desativar por sinterização da fase metálica (BOLSHAK, ABELLÓ e MONTANÉ, 2013).

De forma similar, óxidos mistos do tipo Ni-Mg-Al exibiram propriedades fortemente dependentes da razão entre os diferentes elementos (COLEMAN *et al*., 2009; ROMERO *et al*., 2014). A adição de magnésio, por ser um álcali, minimiza a formação de coque sobre as partículas do catalisador. Entretanto, elevados teores do elemento alcalino podem resultar na queda de atividade catalítica para a reação de reforma ao modificar as interações do Ni^0 com a matriz do catalisador. No caso de trabalho recentemente publicado, que avaliou o efeito da razão Mg/Ni sobre catalisadores para a reforma do etanol (ROMERO *et al*., 2014), foi determinada a razão molar ótima de Mg/Ni = 0.33.

No caso de óxidos mistos do tipo Co-Fe (ABDELKADER *et al*., 2013), foi observado um efeito sinergético entre ambos os metais. Enquanto os catalisadores óxidos simples, Co_3O_4 ou Fe_2O_3, embora com elevada atividade inicial, desativaram rapidamente durante a reação de reforma do etanol, foi observado um aumento significativo na estabilidade térmica e no rendimento a hidrogênio na reação sobre o óxido misto Co-Fe.

Outros catalisadores do tipo óxidos mistos avaliados recentemente na reforma a vapor do etanol incluem Ni-Cu-La-Zr, os quais apresentaram propriedades igualmente promissoras quando comparados a materiais suportados com composição similar (BUSSI *et al*., 2013).

As pesquisas na reação de decomposição do etanol são em número significativamente menor comparada à reação de reforma do etanol e se concentram em catalisadores similares aos reportados para as reações de reforma deste insumo. Neste processo, a ausência de vapor d'água conduz à maior formação de coque. Assim, além da produção de hidrogênio, este processo pode conduzir à formação de nanotubos (*CNT*) e/ou nanofibras de carbono (*CNF*), conforme as condições da reação e dos catalisadores utilizados. Os filamentos de carbono que podem ser obtidos por esta rota possuem propriedades mecânicas, óticas e térmicas únicas, com aplicações em diversas áreas (GALLEGO *et al*., 2013).

Assim como ocorre na reforma do etanol, a maioria dos catalisadores para a decomposição do etanol é do tipo suportado. Os principais materiais possuem níquel (WANG, G. *et al*. 2009; MEZALIRA *et al*. 2011 GALLEGO *et al*., 2011; GALLEGO, MONDRAGON e BATIOT-DUPEYRAT, 2013), ferro (IGARASHI *et al.* 2004; LI *et al*. 2008; LIU *et al*. 2009; GAO *et al*. 2010; WANG, G. *et al*.,. 2011a), cobalto (IGARASHI *et al*. 2004; WANG, G. *et al*.,. 2011b) ou molibdênio (BARTHOS *et al*. 2007; LIU *et al.* 2009; GAO *et al.* 2010) como metais ativos.

Wang, G. *et al.* (2009) e Mezalira *et al.* (2011) investigaram catalisadores contendo diferentes teores de níquel suportado em alumina. Os autores mostraram que teores mais altos do metal ativo são necessários para aumentar o rendimento em hidrogênio e a quantidade e qualidade dos filamentos de carbono. Entretanto, não são encontrados estudos similares para outros tipos de materiais voltados a este processo, bem como estudos comparativos entre os principais metais ativos utilizados para a decomposição do etanol, nas mesmas condições operacionais.

Capítulo 3

Materiais e métodos

O presente capítulo dedica-se à descrição do procedimento experimental relacionado à síntese das amostras, à sua caracterização e aos testes de avaliação dos catalisadores nas diferentes reações investigadas na tese.

3.1 Reagentes

A relação dos reagentes utilizados na preparação dos catalisadores e nos testes de atividade catalítica é apresentada na Tabela 3.1.

Tabela 3.1: Relação dos reagentes utilizados na preparação das amostras e nos testes de atividade catalítica.

Reagente	Fórmula	Pureza (%)	Fornecedor
Álcool etílico absoluto	C_2H_5OH	99,5	Synth
Carbonato de sódio anidro	Na_2CO_3	99,5	Synth
Hidróxido de sódio	$NaOH$	97,0	Synth
Molibdato de amônio	$(NH_4)_6Mo_7O_{24}\cdot 4H_2O$	99,0	Vetec
Nitrato de alumínio nonahidratado	$Al(NO_3)_3\cdot 9H_2O$	98,0	Synth
Nitrato de cálcio tetrahidratado	$Ca(NO_3)_2\cdot 4H_2O$	99,0	Synth
Nitrato de cobalto hexahidratado	$Co(NO_3)_2\cdot 6H_2O$	98,0	Synth
Nitrato de cobre trihidratado	$Cu(NO_3)_2\cdot 3H_2O$	98,0	Synth
Nitrato de ferro (III) nonahidratado	$Fe(NO_3)_3\cdot 9H_2O$	98,0	Vetec
Nitrato de lantânio hexahidratado	$La(NO_3)_3\cdot 6H_2O$	99,0	Vetec
Nitrato de lítio	$LiNO_3$	95,0	Vetec
Nitrato de magnésio hexahidratado	$Mg(NO_3)_2\cdot 6H_2O$	98,0	Vetec
Nitrato de níquel hexahidratado	$Ni(NO_3)_2\cdot 6H_2O$	97,0	Vetec
Nitrato de zinco hexahidratado	$Zn(NO_3)_2\cdot 6H_2O$	96,0	Synth
Oxicloreto de zircônio IV octahidratado	$ZrOCl_2\cdot 8H_2O$	99,5	Vetec

OBS: Todos os reagentes são grau analítico P.A.

Os catalisadores foram preparados utilizando água destilada (destilador marca Biomatic), sendo posteriormente deionizada em coluna de deionização Permution. Similarmente, a mesma qualidade foi usada no preparo das soluções líquidas empregadas nas reações envolvendo etanol.

Nos testes de atividade, adicionalmente aos reagentes líquidos relacionados na Tabela 3.1, foram utilizados os gases especiais indicados na Tabela 3.2.

Tabela 3.2: Relação dos gases utilizados na calcinação das amostras e nos testes de atividade.

Gás	Pureza
Ar sintético	99,997%
Dióxido de carbono	99,995%
Hélio	99,995%
Hidrogênio	99,999%
Metano	99,5%
Mistura amônia/hélio	5,0 ± 0,2 mol% He
Nitrogênio	99,999%

3.2 Síntese dos catalisadores

Os catalisadores foram preparados através do método da co-precipitação contínua. O método foi apresentado em trabalhos anteriores (HERMES, 2010; SOUZA, 2010), porém será sucintamente destacado nos parágrafos que seguem, explicitando as particularidades aplicadas aos diferentes materiais sintetizados.

Foram preparadas amostras baseadas em níquel, ferro e cobalto contendo dopantes. A relação dos catalisadores sintetizados é mostrada na Tabela 3.3.

Tabela 3.3: Relação dos catalisadores preparados.

Amostra	Composição nominal molar (%)										
	Ca	Cu	La	Li	Mg	Mo	Zn	Co	Fe	Ni	Al
Ni33	-	-	-	-	-	-	-	-	-	33,3	66,7
Ni50	-	-	-	-	-	-	-	-	-	50,0	50,0
Ni66[#]	-	-	-	-	-	-	-	-	-	66,7	33,3
Ni75	-	-	-	-	-	-	-	-	-	75,0	25,0
Ni90	-	-	-	-	-	-	-	-	-	90,0	10,0
MgNA	-	-	-	-	11,1	-	-	-	-	55,6	33,3
ZnNA	-	-	-	-	-	-	11,1	-	-	55,6	33,3
CoNA	-	-	-	-	-	-	-	11,1	-	55,6	33,3
MoNA	-	-	-	-	-	11,1	-	-	-	55,6	33,3
Fe66	-	-	-	-	-	-	-	-	66,7	-	33,3
Fe75	-	-	-	-	-	-	-	-	75,0	-	25,0
Fe80	-	-	-	-	-	-	-	-	80,0	-	20,0
CuFe70	-	11,1	-	-	-	-	-	-	70,0	-	33,3
CoFe70	-	-	-	-	-	-	-	11,1	70,0	-	33,3
Co66[##]	-	-	-	-	-	-	-	66,7	-	-	33,3
CaCoAl	11,1	-	-	-	-	-	-	55,6	-	-	33,3
LaCoAl	-	-	11,1	-	-	-	-	55,6	-	-	33,3
LiCoAl	-	-	-	11,1	-	-	-	55,6	-	-	33,3
MgCoAl[###]	-	-	-	-	11,1	-	-	55,6	-	-	33,3
Mg22CA	-	-	-	-	22,2	-	-	44,5	-	-	33,3
Mg33CA	-	-	-	-	33,3	-	-	33,4	-	-	33,3

[#] A amostra Ni66 também foi designada por NA.
[##] A amostra Co66 também foi designada por CoAl.
[###] A amostra MgCoAl também foi designada por Mg11CA.

A Figura 3.1 apresenta as etapas da síntese dos catalisadores.

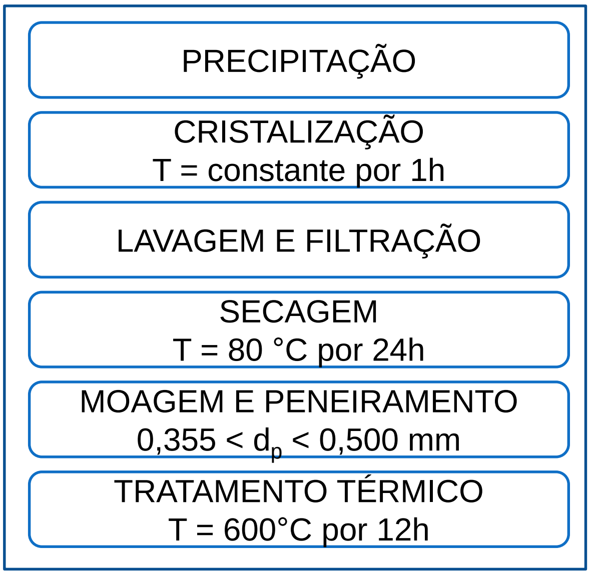

Figura 3.1: Etapas de preparação das amostras**.**

O processo de co-precipitação foi conduzido em reator tanque agitado contínuo (*CSTR*) encamisado de vidro contendo, inicialmente, aproximadamente 100 mL de água destilada e deionizada. A temperatura foi mantida constante pelo emprego de um banho termostatizado (Lauda, tipo E-100). O sistema foi submetido à agitação contínua (agitador mecânico Fisatom, modelo 710) e a pH constante (pHmetro Digimed , tipo DM 20). No caso das amostras à base de níquel e cobalto, os valores de temperatura e de pH foram mantidos em 50°C ± 0,5°C e 8,0 ± 0,1, respectivamente. No caso dos catalisadores à base de ferro, os valores adotados foram de 60°C ± 0,5°C e 9,0 ± 0,1, respectivamente.

A solução aquosa contendo os nitratos dos metais foi preparada com volume de 100 mL com concentração de 1 M. Em relação ao agente precipitante, as amostras foram preparadas utilizando solução aquosa de carbonato de sódio com volume de 125 mL com concentração de 2 M. A alimentação das duas soluções foi feita continuamente mediante a utilização de duas bombas peristálticas (Flex Flo, modelo A-1830-4N), em que a vazão do agente precipitante foi ajustada de forma a manter o valor de pH desejado. A vazão de saída da solução do reator foi ajustada de forma a fornecer um tempo de residência médio no reator *CSTR* de 6 min.

A Figura 3.2 mostra a unidade utilizada na etapa de precipitação da síntese dos materiais.

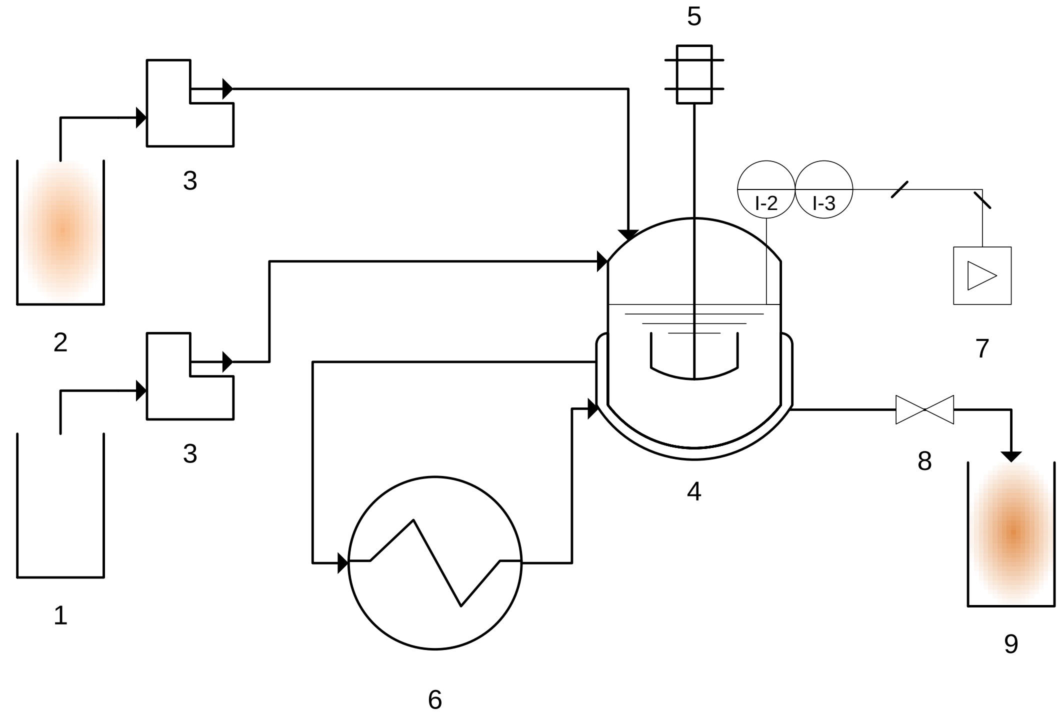

Figura 3.2: Representação esquemática do sistema de co-precipitação utilizado na síntese dos catalisadores. (1) Solução contendo o agente precipitante; (2) Solução contendo os sais metálicos; (3) Bombas peristálticas; (4) Reator *CSTR* encamisado; (5) Agitador mecânico; (6) Banho termostatizado; (7) pHmetro; (8) Válvula de saída e (9) Coleta do precipitado.

Após a etapa de precipitação, foi realizada a etapa de cristalização do efluente. Nesta etapa, a solução foi submetida à agitação magnética (Fisatom, modelo 752A) na mesma temperatura da etapa anterior por 1 h. Após o processo de cristalização, foi feita a filtração a vácuo e a lavagem com água deionizada. Para garantir a remoção dos íons advindos do material de partida, a condutividade da água residual foi monitorada (condutivímetro Digimed, tipo DM 31). A lavagem foi encerrada quando a condutividade detectada na água residual foi inferior a 100 $\mu S.cm^{-1}$.

A torta coletada foi seca a 80˚C em estufa (DeLéo, controlador TTL057N). Após 24 h, o sólido foi moído e peneirado. A faixa granulométrica 0,355 mm < d_p < 0,500 mm foi reservada e encaminhada para tratamento térmico.

A calcinação foi realizada em reator tubular de quartzo conectado a um forno elétrico com controle digital de temperatura. Após estabelecer-se um fluxo contínuo de 50 $mL \cdot min^{-1}$ de ar sintético, a temperatura do forno foi elevada a 600˚C com uma taxa de aquecimento de $10˚C \cdot min^{-1}$, sendo mantida nesta temperatura por 6 h.

Ressalta-se que, no caso das amostras à base de ferro (*i.e.*, Fe66, Fe75, Fe80, CuFe70 e CoFe70), o processo de precipitação foi realizado utilizando uma solução contendo os nitratos com concentração de 0,5 M, enquanto que uma mistura equimolar de hidróxido de sódio e carbonato de sódio (2 M) foi usada como agente precipitante. Essa condição foi empregada em função da maior acidez das amostras baseadas em ferro, requerendo uma base mais forte para melhor controle da precipitação do material.

3.3 Caracterização das amostras

As amostras em suas diferentes formas, quais sejam frescas, calcinadas, reduzidas e após reação, foram investigadas por diferentes técnicas de caracterização. A caracterização do material é fundamental para conseguir explicar os resultados obtidos nos testes de atividade quanto à conversão dos reagentes, à seletividade e à estabilidade. Desta forma, complementa os dados dos testes catalíticos, conduzindo a uma melhor compreensão das propriedades do material, suas modificações durante as reações e influência no desempenho em um determinado processo. O procedimento analítico de cada uma das técnicas é descrito a seguir.

3.3.1 Termogravimetria e análise térmica diferencial (*TG-DTA*)

A termogravimetria (*TG*) permite a avaliação qualitativa e quantitativa da decomposição térmica de uma amostra. Por meio desta técnica, a variação de massa, devido a uma transformação física ou química, é medida sob atmosfera controlada, a qual pode ser medida em função do tempo (método isotérmico) ou da temperatura (método dinâmico). Para explicitar as principais etapas constituintes da decomposição, o comportamento térmico também pode ser expresso na forma diferencial (*DTG*).

O estudo termogravimétrico foi conduzido em uma termobalança modelo SDT Q600 (TA Instruments) através do método dinâmico. O equipamento utilizado também permite avaliar a natureza dos efeitos térmicos associados às perdas de massa e aos fenômenos físicos de forma simultânea. A análise térmica diferencial (*DTA*) fornece informações relevantes para identificar os diferentes fenômenos e a respectiva faixa de temperatura em que ocorrem.

Nas medidas realizadas, aproximadamente 10 mg de amostra não calcinada foram dispostas em um cadinho de alumina. Um disco de safira foi inserido no cadinho de referência, para fins de avaliação da natureza térmica das transformações (*DTA*). Após 10 min de purga com 1000 $mL \cdot min^{-1}$ de N_2, a amostra foi submetida a aquecimento sob 100 $mL \cdot min^{-1}$ de ar sintético. A temperatura foi elevada até 850˚C a uma taxa de aquecimento de $10˚C \cdot min^{-1}$. Os dados foram coletados continuamente.

3.3.2 Medida de área específica

A área específica de um material pode ser estimada pela utilização do método de B.E.T. (Brunauer, Emmett e Teller). Neste método, a área é estimada a partir do volume de adsorbato condensado necessário para recobrir a superfície da monocamada de um sólido.

Foi utilizado o método dinâmico de B.E.T. (ponto único) por adsorção de N_2 a -196˚C em um equipamento multipropósito na determinação da área específica ($m^2 \cdot g^{-1}$) dos catalisadores preparados neste trabalho. Antes das medidas de fisissorção, 100 mg de amostra foram inseridas em um reator de leito fixo de quartzo e submetidas a tratamento térmico a 250˚C por 1 h. Essa etapa visa à eliminação da umidade e de outros componentes eventualmente presentes nas amostras após a calcinação. Após o pré-tratamento, foram ajustadas vazões de 30 $mL\cdot min^{-1}$ de uma mistura N_2:He (30% v/v) e de 30 $mL\cdot min^{-1}$ de He, usado como referência. O valor da a área específica foi obtido a partir da média de quatro medidas de adsorção de N_2.

3.3.3 Redução à temperatura programada (*TPR*)

Através da redução à temperatura programada (*TPR*), pode-se estudar a reação de hidrogenação ou redução do material submetido a uma taxa de aquecimento linear, sob fluxo de uma mistura redutora (normalmente hidrogênio diluído). Desta forma, é obtido um perfil de redução do material, cujo comportamento varia conforme as quantidades e tipos de elementos constituintes, bem como o seu estado de oxidação. Em óxidos metálicos (MeO_x), a reação pode ser arbitrariamente expressa pela Equação 3.1.

$$MeO_x + xH_2 \rightarrow Me + xH_2O \qquad (3.1)$$

Os ensaios de *TPR* foram conduzidos em um equipamento multipropósito também utilizado nos experimentos de determinação da área específica. O sistema é dotado de um *trap* para evitar a entrada de água produzida na redução dos óxidos, no detector. Após o pré-tratamento convencional, foi admitido 30 $mL\cdot min^{-1}$ de uma mistura redutora H_2:N_2 (10% v/v) e 30 $mL\cdot min^{-1}$ de N_2 puro, usado como referência. Aproximadamente 100 mg de catalisador foi submetido ao aquecimento a uma taxa de 10˚$C\cdot min^{-1}$ até 880˚C, sendo o consumo de hidrogênio monitorado continuamente pelo detector

.

3.3.4 Dessorção à temperatura programada (*TPD*)

A dessorção à temperatura programada permite avaliar a acidez ou basicidade total, assim como os tipos e a força dos sítios presentes em um determinado material. Essa avaliação é possibilitada a partir da saturação do material por uma molécula sonda, escolhida convenientemente conforme a natureza do sítio que se deseja investigar.

TPD de dióxido de carbono

A caracterização da natureza dos sítios básicos dos catalisadores foi conduzida por dessorção à temperatura programada utilizando dióxido de carbono (*TPD-*CO_2). Pelo fato de a molécula ser um ácido de Brönsted-Lowry, os picos em temperaturas baixas se relacionam à dessorção de sítios com baixa alcalinidade, com os quais o gás utilizado possui uma fraca interação. Por outro lado, os picos em temperaturas mais altas associam-se a sítios alcalinos ou com baixa acidez. A intensidade dos picos representa a quantidade de sítios deste tipo presentes na amostra.

As medidas de *TPD-*CO_2 foram realizadas no mesmo sistema multipropósito utilizado nas análises *TPR* e de área específica. Após a etapa de pré-tratamento, 100 mg de catalisador foi saturado com o gás mediante fluxo de 30 $mL\cdot min^{-1}$ de uma corrente pura de CO_2, na temperatura de 100˚C, mantido por 30 min. A saturação foi sucedida por etapa de purga com 30 $mL\cdot min^{-1}$ de N_2 puro durante 30 min. Após a etapa de adsorção, a temperatura foi elevada a 600˚C (10˚C$\cdot min^{-1}$) sob fluxo de 30 $mL\cdot min^{-1}$ de N_2.

TPD de amônia

A dessorção de amônia à temperatura programada (*TPD-NH₃*) foi utilizada para a caracterização da natureza dos sítios predominantemente ácidos dos materiais. Na curva *TPD-NH₃*, pelo fato de a amônia ser uma base, os picos em temperaturas inferiores representam sítios com fraca acidez, enquanto que picos deslocados em temperaturas mais altas, sítios ácidos fortes.

O sistema e metodologia utilizada na análise de *TPD-NH₃* assemelham-se ao empregado nas medidas de *TPD-CO₂*. Entretanto, nos experimentos de *TPD-NH₃*, a saturação do catalisador foi realizada utilizando 30 $mL \cdot min^{-1}$ de uma mistura NH_3/He (5 mol%). A saturação foi sucedida por etapa de purga com 30 $mL \cdot min^{-1}$ de He puro durante 30 min. O aquecimento para dessorção da amônia foi realizada nas mesmas condições do procedimento utilizado na análise de *TPD-CO₂*, porém utilizando 30 $mL \cdot min^{-1}$ de He.

3.3.5 Difração de raios X (*XRD*)

A técnica de difração de raios X (*XRD*) foi utilizada para obter informações sobre a estrutura e as fases cristalinas presentes nos materiais a partir da detecção do feixe difratado após incidência de radiação sobre a amostra.

Os espectros das amostras não calcinadas, calcinadas, reduzidas e desativadas foram obtidos em um difratômetro Bruker D2 Phaser, utilizando radiação CuKα. A fonte operava a 30 kV e 15 mA e o porta-amostras era rotacionado a 15 rpm. Os difratogramas foram obtidos em temperatura ambiente no intervalo de 2θ de 10 a 70°, com passo de 0,05° e com tempo de 1 s por passo.

Nas análises das amostras reduzidas, os catalisadores foram ativados nas mesmas condições empregadas antes dos testes de atividade. Depois de finalizado o tempo da fase isotérmica, os catalisadores foram resfriados até temperaturas inferiores a 50°C e passivados com corrente de O_2:N_2 (1,4% v/v) por 30 min. O tamanho médio dos cristais das fases óxida e metálica de Fe, Ni e Co (*D*) foi estimado pela equação de Scherrer (Equação 3.2) em função do ângulo de Bragg, da largura à meia altura do máximo do pico (β) e do comprimento de onda da radiação (λ).

$$D = \frac{0{,}9 \cdot \lambda}{\beta \cdot \cos\theta} \tag{3.2}$$

3.3.6 Oxidação à temperatura programada (*TPO-DTA*)

Após a reação, os catalisadores foram submetidos à oxidação à temperatura programada. Os ensaios foram conduzidos para investigar a formação de coque sobre o catalisador, durante a reação, avaliando, desta forma, a tendência à desativação por deposição de coque. A quantidade de coque formada nos testes foi obtida a partir da diferença entre a massa inicial e final da amostra referentes à perda de massa decorrente da sua combustão.

Os ensaios de *TPO-DTA* foram realizados em termobalança (TA Instruments, modelo SDT Q600). O procedimento experimental é o mesmo descrito nas análises *TGA-DTA*. Entretanto, foram utilizadas 20 mg de catalisador desativado nos testes de oxidação.

3.3.7 Microscopia eletrônica de varredura (MEV)

A microscopia eletrônica de varredura (MEV) fornece imagens sobre as primeiras camadas da superfície dos materiais. Os catalisadores após as reações foram moídos e metalizados com ouro com 24 h de antecedência à realização das medidas de microscopia. As amostras foram analisadas utilizando um equipamento JEOL JSM-6060 operando com voltagem de aceleração de 20 kV sob vácuo. Para aquisição das imagens, foram utilizados aumentos entre 10.000 e 30.000 x. O equipamento utilizado é disponibilizado no Centro de Microscopia Eletrônica da UFRGS (CME).

3.3.8 Espectroscopia Raman

A espectroscopia Raman é uma técnica de alta resolução que também permite obter informações sobre composição química e estrutural de materiais. Ela se baseia no espalhamento de um feixe de luz monocromática após a sua incidência sobre o material que se deseja investigar. Neste trabalho, foi utilizado um microespectrômetro Raman desenvolvido em laboratório. O aparato experimental é constituído por um microscópio, um monocromador e um dispositivo de carga acoplada (*CCD*) resfriado por nitrogênio líquido. Maiores detalhes sobre as análises podem ser conferidas na literatura (BALZARETTI *et al.*, 2003).

3.4 Testes Catalíticos

O desempenho dos catalisadores foi avaliado mediante testes de atividade em unidades de bancada disponíveis no Laboratório de Processos Catalíticos (ProCat/DEQUI/UFRGS). Os reagentes não convertidos e os produtos foram analisados por cromatografia gasosa, através de dois equipamentos: *GC* Varian, modelo Star 3600cx, conectado em linha com as unidades catalíticas e *GC* Perkin Elmer, AutoSystem XL, disponível para análise *off-line*. Os cromatogramas eram obtidos pela comunicação direta entre o cromatógrafo gasoso e o computador, com os dados sendo processados por *softwares* adequados. Os componentes obtidos eram identificados com base nos tempos de retenção e quantificados pelas medidas de área integrada a partir dos cromatogramas.

3.4.1 Testes de atividade envolvendo o etanol

Os testes catalíticos envolvendo a transformação do etanol foram feitos em unidade representada na Figura 3.3. Os ensaios envolvendo a transformação do etanol foram conduzidos em um reator tubular de leito fixo de quartzo, com 630 mm de comprimento e 8 mm de diâmetro interno. O reator foi aquecido em um forno tubular (marca Sanchis) controlado por dispositivo Novus, modelo N1100. A temperatura central do leito foi medida por um termopar do tipo K. A leitura do valor de temperatura do leito era feita em indicador conectado ao termopar (Novus, modelo N1500), sendo a temperatura do forno ajustada em função da temperatura deste dispositivo. A vazão dos gases era estabelecida por controladores digitais de fluxo mássico (fabricantes Sierra Instruments Inc. e Cole Parmer). Os reagentes líquidos eram alimentados por meio de bombas dosadoras (Cole Parmer, Modelo 74900), sendo a seringa conectada ao septo localizado na extremidade superior do reator. A pressão era verificada por um manômetro localizado na entrada do reator (Casa dos Manômetros). Dois *traps* foram instalados no *by-pass* da unidade, a montante do cromatógrafo *GC* Varian, para análise *offline*. As linhas que faziam a comunicação da saída do reator com os *traps* e com o *GC* Varian eram mantidas em aproximadamente 120°C por resistores flexíveis (Pan Electric), a fim de evitar a condensação de produtos na tubulação.

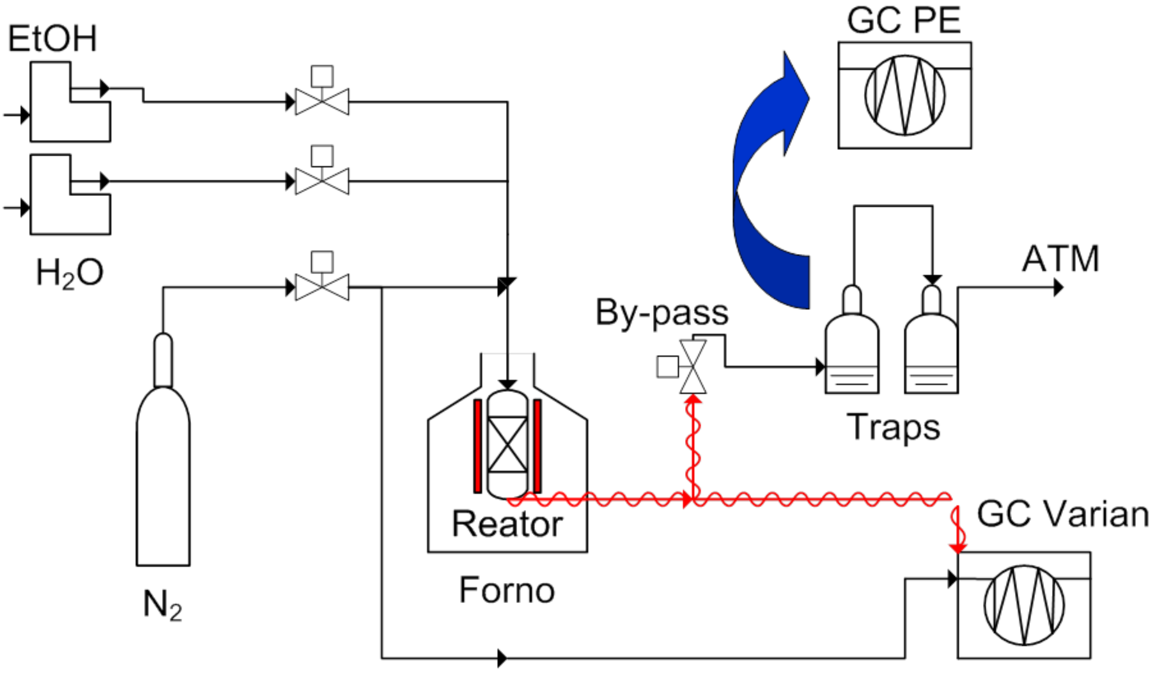

Figura 3.3: Representação da unidade utilizada nos testes catalíticos envolvendo o etanol**.**

Os testes foram precedidos pela redução *in situ* do catalisador à pressão ambiente. A massa de catalisador usada nos testes foi de 100 mg, sendo diluída em quartzo (1 v/v). Após o teste de estanqueidade do sistema, as extremidades do reator foram isoladas com lã de rocha e foi admitido hidrogênio a uma vazão de 100 $mL \cdot min^{-1}$. O reator foi aquecido a uma taxa de 5˚$C \cdot min^{-1}$ até temperaturas entre 400 e 600˚C, sendo mantido nesta temperatura por períodos entre 1 e 2 h. Após esta etapa, o sistema era levado à temperatura de reação, sendo então cortado o fluxo de H_2 e alimentado nitrogênio a uma vazão de 100 $mL \cdot min^{-1}$. A injeção do reagente líquido era feita simultaneamente à troca do gás, sendo alimentada na vazão de 0,5 $mL \cdot h^{-1}$. Para a reação de decomposição do etanol, foi utilizado etanol puro. Para os testes de reforma a vapor do etanol, foi utilizada a razão $EtOH/H_2O$ de 1 $mol \cdot mol^{-1}$. Após 15 min de alimentação dos reagentes, foram iniciadas as injeções cromatográficas, usando-se colunas Porapak Q e Molecular Sieve 13x. A temperatura da reação foi mantida constante nos testes de estabilidade, em que se acompanhava a(s) conversão(ões) do(s) reagente(s) com o tempo. Nas reações com diferentes temperaturas, as medidas, em uma determinada condição, foram obtidas a partir da média de cinco injeções. Na transição entre as condições operacionais, aguardava-se 10 min na nova condição antes que os dados fossem registrados.

3.4.2 Testes de atividade na reação de reforma do metano

Os testes catalíticos de reforma a seco do metano foram feitos em unidade representada na Figura 3.4. Os ensaios de reforma do CH_4 foram realizados em um reator tubular de leito fixo de quartzo. As dimensões do reator eram 370 mm de comprimento e 9 mm de diâmetro interno. A carga de catalisador diluída em igual volume de quartzo era posicionada no reator de forma que o centro do leito fosse posicionado junto à extremidade do termopar (tipo K) que media e controlava a temperatura do forno. Para esta função, foi usado um controlador digital de temperatura (Therma, modelo TH90 DP201-300). A vazão dos gases era estabelecida por controladores digitais de fluxo mássico (Sierra Instruments Inc., modelo C100-L). A pressão era verificada em manômetro (Wika) posicionado na tubulação à entrada do reator.

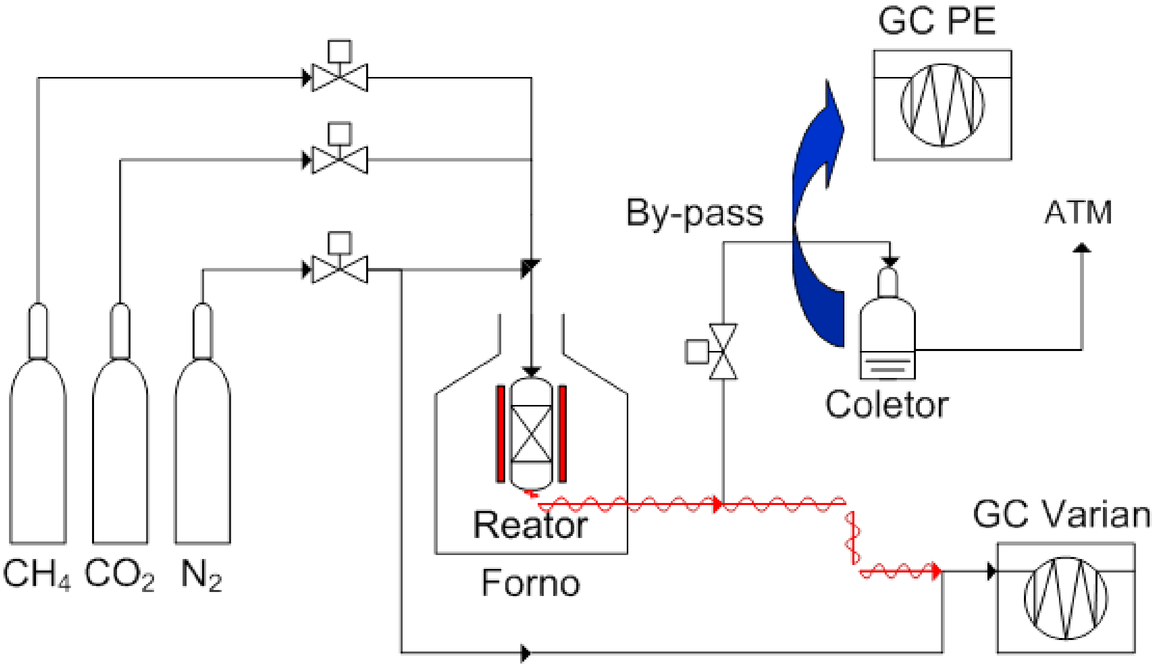

Figura 3.4: Representação da unidade utilizada nos testes catalíticos envolvendo metano.

Os experimentos de avaliação catalítica foram precedidos de ativação *in situ* utilizando uma mistura redutora 10%H_2/N_2 (v/v) a uma vazão de 50 mL·min^{-1} e à pressão ambiente. Após alimentada a mistura gasosa, o forno foi aquecido a 5˚C·min^{-1} até a temperatura de redução de 700˚C, sendo mantido nesta temperatura por 1 h. Após esta etapa, a amostra foi resfriada até a temperatura inicial da reação. A alimentação da mistura redutora foi interrompida, sendo admitida a mistura reacional. À exceção dos testes de estabilidade, as reações foram conduzidas utilizando 100 mg de catalisador e 100 mL·min^{-1} de mistura $CH_4/CO_2/N_2$ (10:10:80 v/v). Nestas condições, a velocidade espacial (*GHSV*) foi mantida em 6 NL CH_4·g^{-1}·h^{-1}. Adicionalmente, foi realizado um ensaio em que o catalisador foi reduzido a 500°C por 4 h. As temperaturas variaram entre 400 e 550°C. O procedimento de análise foi similar ao adotado nos testes envolvendo a transformação de etanol. Foram anotados os valores obtidos pela média de cinco a seis injeções, as quais iniciavam quando eram decorridos 5 min após atingir a nova condição.

A conversão dos reagentes (X_{REA}) foi calculada de acordo com a Equação 3.1, com base nas suas concentrações na entrada e saída do reator ([*REA*]).

$$X_{REA} = \frac{[REA]_{ENTRADA} - [REA]_{SAÍDA}}{[REA]_{ENTRADA}} \qquad (3.1)$$

As seletividades a hidrogênio (S_{H2}) e aos produtos contendo carbono (S_{Ci}) foram calculadas em função da concentração da espécie *i* e do número de átomos de H ou C das espécies (*N*) e são mostradas nas Equações 3.2 e 3.3, respectivamente.

$$S_{H2} = \frac{[H_2]}{\sum N.[H_{2N}]} \qquad (3.2)$$

$$S_{Ci} = \frac{N.[C_N]}{\sum N.[C_N]} \qquad (3.3)$$

Capítulo 4

Influence of the Ni/Al ratio on Ni-Al mixed oxides and their catalytic properties for ethanol decomposition

Artigo a ser submetido ao periódico: *Applied Clay Science*.

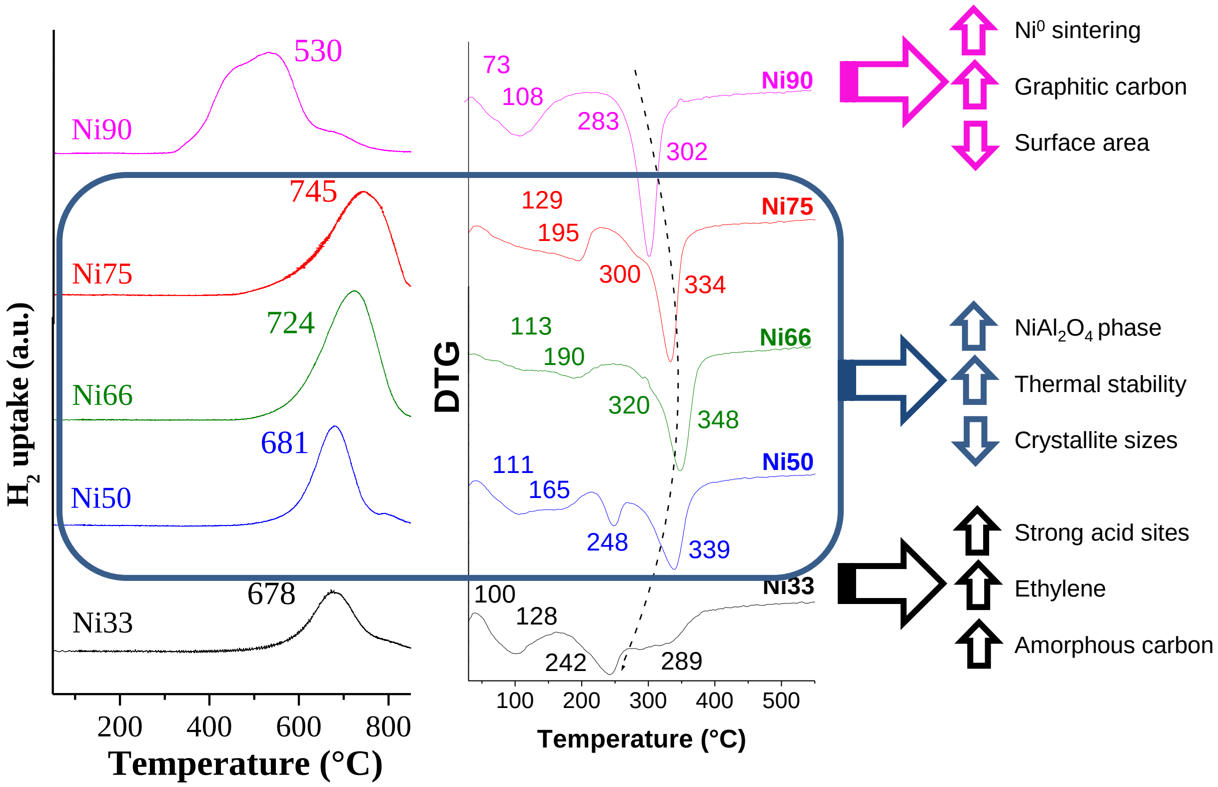

Influence of the Ni/Al ratio on Ni-Al mixed oxides and their catalytic properties for ethanol decomposition

Guilherme de Souza[1,2], Nilson R. Marcilio[1] and Oscar W. Perez-Lopez[1,*]

[1] Department of Chemical Engineering, Federal University of Rio Grande do Sul - UFRGS, R. Eng. Luiz Englert S/N°, Build. 12204. 90040-040 Porto Alegre-RS, Brazil

[2] Fundação de Ciência e Tecnologia do Estado do Rio Grande do Sul - CIENTEC, Av. das Indústrias, 2270, Distrito Industrial, 94930-230 Cachoeirinha-RS, Brazil.

* Corresponding author: O. W. Perez-Lopez. UFRGS, Rua Eng. Luiz Englert S/N°, Build. 12204. Zip Code: 90040-040 - Porto Alegre, Brazil. Phone: +55 51 3308 3953. Fax: +55 51 3308 3277. Email: perez@enq.ufrgs.br

Abstract

The relationship between the structural and catalytic properties with the composition of nickel-aluminium mixed oxides was investigated in this work. For this purpose, a series of Ni-Al materials was synthesised by the precipitation method with Ni/Al molar ratios between 0.5 and 9. Samples were characterized by the following techniques: TG/DTA, XRD, H_2-TPR, NH_3-TPD and TPO/DTA. The samples with Ni/Al ratio = 0.5 formed mostly the Al_2O_3 phase, while the Ni/Al ratio = 9 led mainly to the bulk NiO phase. On the other hand, the Ni/Al ratio between 1 and 3 favoured the formation of the mixed oxide phase. These intermediate compositions provided an enhancement in the thermal stability and specific surface area and a decrease in the crystallite sizes. The lower Ni/Al ratios led to the production of ethylene, which should be mostly related to the higher amount of sites with stronger acidity. The samples with the Ni/Al ratio = 2 and 3 promoted the selectivity towards synthesis gas. However, for higher Ni/Al ratios, low thermal stability that led to sintering and deactivation due to coke formation was found for this sample.

Keywords: Nickel catalyst; mixed oxides; characterization, decomposition of ethanol; carbon.

4.1. Introduction

Among the biomass technologies available, the chemical transformation of ethanol is an interesting option for supplying the global demands for energy, fine chemicals and materials with outstanding properties. The steam reforming and the decomposition of ethanol provide a wide range of products that are feedstock for several industrial applications. Hydrogen, synthesis gas, methane, ethylene and acetaldehyde are some products that can be obtained through these routes. The distribution of products depends on the catalyst and the operational conditions. The steam reforming of ethanol favours the production of high-purity hydrogen for fuel cells application, especially when carried out at high temperatures and in excess water. Several works highlighted the feasibility of such process recently [1-4]. On the other hand, the decomposition of ethanol can originate a broader range of chemicals. For example, ethanol can be dehydrated to form ethylene that can undergo to the so-called “green” polyethylene, as produced by the petrochemical Braskem in Brazil. This route also originates synthesis gas (or syngas), that is a mixture of H_2 and CO that can produce electricity, hydrocarbons or oxygenates. Furthermore, the carbon deposited on the catalyst’s particles by the decomposition of ethanol can present interesting properties. Indeed, several works have demonstrated that this material often is constituted by carbon nanotubes (CNT) or carbon nanofibres (CNF) [5-7]. These structures have impressive electrical, thermal and mechanical properties that attract its application for several fields [8].

Nickel is one of the most active metals for the reforming and the decomposition processes [9, 10]. According to observations of Rostrup-Nielsen (1993) for the reforming catalysts, the nickel crystals sinter rapidly above the Tammann temperature, that is ca. 600°C for nickel [11]. Therefore, when it is possible, operation at temperatures lower than this value are desirable in order to prevent sintering of nickel. For example, Wang et al. (2009) observed the sintering of the Ni0 particles for ethanol decomposition at 700°C and 800°C. This phenomenon affected the reaction and the quality of the CNT and CNF structures [12]. Different authors explored a series of alumina-supported catalysts with different contents of nickel [6, 12]. The referred authors showed that higher loads of the active metal are required in order to maximise the hydrogen yield and the amount and quality of the carbon filaments. Other papers reported data for the decomposition of ethanol over catalysts based on molybdenum [7, 13, 14], iron [5, 7, 14-16] and cobalt [16, 17]. However, the high activity and the low cost exhibited by nickel is an incentive for the Ni-catalysts.

The nickel catalysts for the decomposition of ethanol are mostly prepared by the impregnation of the nickel precursor on an oxide support. However, mixed oxides usually present very interesting properties for application as heterogeneous catalysts. These structures usually exhibit high thermal stability, large specific surface area, memory effect and homogeneous interdispersion [18-21]. This uniform dispersion conducts to the formation of smaller crystallites that normally lead to higher activity. Moreover, homogeneous interdispersion contributes to the minimisation of the carbon deposition, because larger crystallites of nickel promote coking. For clay-derived catalysts, it is believed that the randomly distribution of the Ni ions in the layered structure slow down the crystal growth phenomenon by minimising the aggregation of the active metal particles [22]. Interesting results for nickel-based mixed oxides were found for the steam reforming of ethanol [23-26]. Notwithstanding the characteristics of such materials, data for the decomposition of ethanol over Ni-mixed oxides is scarce. Thereof, the aim of this work is the investigation of the effect of the Ni/Al ratio on the catalytic properties of Ni-Al materials. For this purpose, a series of samples with different compositions was prepared and characterised with comprehensive techniques. The decomposition of ethanol was adopted as a model reaction.

4.2. Materials and Methods

4.2.1 Preparation of samples

The Ni-Al samples were prepared adopting Ni/Al molar ratios between 0.5 and 9 through the continuous co-precipitation method earlier described [21]. The Ni-Al samples were synthesised by mixing an aqueous solution containing Ni(II) and Al(III) nitrates (1 M) with an aqueous solution containing Na_2CO_3 (2 M) in a continuous stirred tank reactor (CSTR). The precipitation procedure was carried out at constant temperature (50°C) and pH (8± 0.1) values. The precipitate was crystallised at 50°C for 1 h and then filtered and washed thoroughly with distilled and deionised water. After drying at 80°C for 24 h, the samples were crushed and sieved. The fraction with particle sizes between 355 and 500 µm was taken. The thermal treatment was conducted under air flow of 50 $mL \cdot min^{-1}$ at 600°C for 6 h. The samples were identified according to the content of nickel.

4.2.2 Characterisation

The fresh samples were characterised by thermogravimetry with differential thermal analyses (TG/DTA). BET surface area measurements (S_{BET}), X-ray diffraction (XRD), NH_3 temperature-programmed desorption (NH_3-TPD) and temperature-programmed reduction (H_2-TPR) data were collected for calcined samples. The spent catalysts were investigated by the temperature-programmed oxidation (TPO/DTA) and X-ray diffraction (XRD).

The TG/DTA and TPO/DTA experiments were conducted using TA thermobalance equipment (Model SDT600). Approximately 10 mg each of fresh (TG/DTA) or spent sample (TPO/DTA) was purged with 1000 $mL \cdot min^{-1}$ of N_2 at 30°C for 10 min before the tests. The samples were heated to 850°C (10°C·min^{-1}) under a synthetic air flow rate of 100 mL·min^{-1}.

The S_{BET}, NH_3-TPD and H_2-TPR data were obtained using a multipurpose system equipped with a thermal conductivity detector (TCD). A quartz tube was loaded with 100 mg of the calcined sample and placed in a temperature-controlled oven. The pretreatment step was conducted under a N_2 flow at 250°C for 1 h and then cooled to room temperature. The samples were saturated with ammonia at 100°C and heated to 600°C at a rate of 10°C·min^{-1} under 30 mL·min^{-1} of He for NH_3-TPD. For the H_2-TPR analysis, the temperature was increased up to 900°C (10°C·min^{-1}) under 30 mL·min^{-1} of a 10% H_2/N_2 (v/v) mixture flow. The S_{BET} was carried out by the N_2 dynamic adsorption method at -196°C.

The powder XRD patterns were recorded for calcined and spent catalysts. The patterns were collected for 2θ between 10 and 70° using a Bruker D2 Phaser X-ray diffractometer at ambient temperature using CuKα radiation

4.2.3 Catalytic evaluation

The catalysts were first reduced *in situ* under 100 mL·min^{-1} of pure H_2 flow for 1 h at 500°C. The reactions were carried out in a quartz tubular fixed bed reactor (6 mm i.d.) loaded with 100 mg of catalyst diluted with quartz (1:1 v/v). The tests were performed under atmospheric pressure at 500°C. The flow rate of nitrogen was adjusted to 100 mL·min^{-1} through a mass flow controller. The ethanol was fed through syringe-type micropump at a flow rate of 0.5 mL·h^{-1}. The products were analysed by gas chromatography. The ethanol conversion (X_{ET}) was 100% during the reaction time evaluated. The distribution of products was measured after a pseudo steady-state condition was observed, which occurred between 1 and 2 h. The selectivity for hydrogen (S_{H2}) and C-containing products (S_{Ci}) was evaluated as follows:

$$S_{H2} = \frac{[H_2]}{\sum \nu_j.[H_{2j}]} \tag{4.1}$$

$$S_{Ci} = \frac{\nu_i.[C_i]}{\sum \nu_j.[C_j]} \tag{4.2}$$

Where $[C_j]$ and $[H_{2j}]$ is respectively the number of moles of C-containing and H_2-containing *j* product in the outlet stream and v_j is the ratio of stoichiometric reaction coefficients.

4.3 Results and discussion

4.3.1 Characterisation of the fresh and calcined Ni-Al samples

The nominal molar composition and S_{BET} values are displayed in Table 4.1, while the XRD patterns for the calcined samples are displayed in Figure 4.1.

Table 4.1. Nominal composition and S_{BET} values for the calcined samples.

Sample	Composition (mol. %)		Ni/Al ratio	S_{BET} ($m^2 \cdot g^{-1}$)
	Ni	Al		
Ni33	33.3	66.7	0.5	135
Ni50	50	50	1	107
Ni66	66.7	33.3	2	143
Ni75	75	25	3	122
Ni90	90	10	9	70

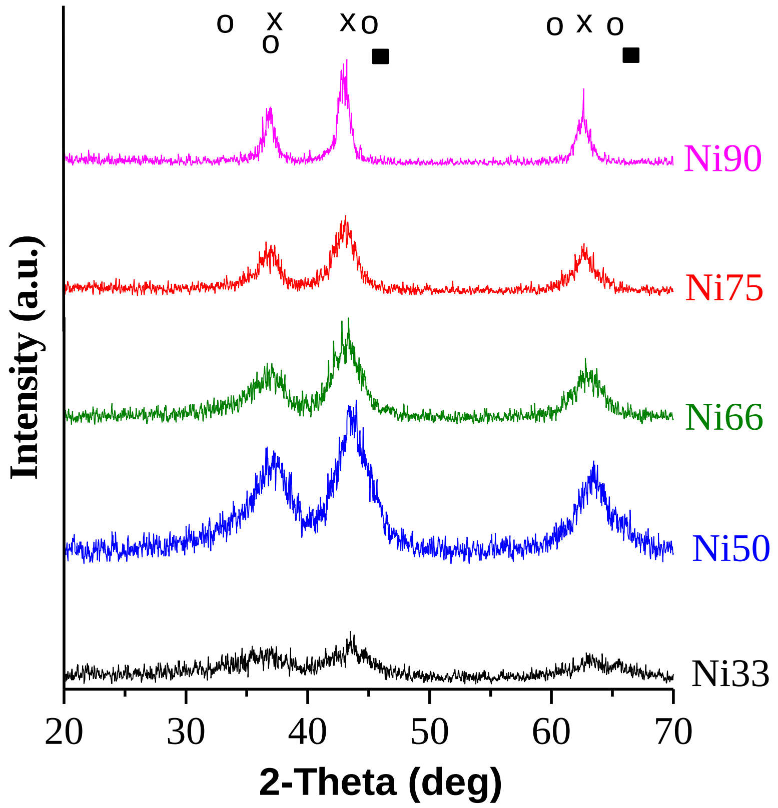

Figure 4.1. XRD patterns for calcined samples.
Identified crystalline phases: (x) NiO; (O) $NiAl_2O_4$; (■) γ-Al_2O_3.

The XRD patterns in Figure 4.1 present diffraction peaks that can be ascribed to the NiO, $NiAl_2O_4$ and Al_2O_3 phases. All the catalysts display the diffraction reflections assigned to the NiO phase. Although the Ni33 catalyst exhibits very broad peaks, it can be seen that the width of the peak of NiO at $2\theta = 43.4°$ decreases with increasing Ni content. It suggests the formation of smaller crystallites for decreasing the Ni/Al ratio on samples. Indeed, the homogeneous interdispersion of the elements is a typical characteristic of the mixed oxides [19]. The Ni33 and Ni50 samples possess reflections that can be related to the Al_2O_3 phase. The formation of the $NiAl_2O_4$ is clear for the Ni50, Ni66 and Ni75 catalysts. The thinnest peak at $2\theta = 43.4°$ for the Ni90 sample reveals the formation of larger and less stable crystallites for this catalyst.

Regarding the S_{BET} data (Table 4.1), the high specific surface area of the Ni33 sample might be related to the formation of Al_2O_3 provided by the low content of Ni, as suggested by its XRD pattern (Figure 4.1). The NiO phase might be well dispersed or possessing a strong interaction with the alumina for this sample. For the samples with the Ni/Al molar ratio of 1, 2 and 3, the S_{BET} increases for the Ni66 sample and decreases for the Ni75 sample. Actually, the Ni66 sample exhibits the highest S_{BET} value (143 $m^2 \cdot g^{-1}$). This value is similar to the specific surface area reported for nickel co-precipitated catalyst that was calcined at lower temperatures [27]. The mixed oxides are typically favoured for M^{2+}/M^{3+} molar ratios between 2 and 4 [28]. These results indicate that the formation of the Ni-Al mixed oxides is favoured for the Ni/Al ratio = 2. The decrease in the S_{BET} for the Ni75 sample can be attributed to the excess of Ni compared to Al. For higher contents of Ni (i.e., the Ni90 sample), it was observed the lowest specific surface area. This result is associated to the high content of Ni that form preferentially the NiO phase because the $NiAl_2O_4$ mixed oxides have higher surface area compared to Ni oxides. Therefore, the results are in agreement with the XRD analysis (Figure 4.1), which showed the formation of the $NiAl_2O_4$ phase for the samples with intermediate Ni/Al ratios.

Figure 4.2-a and Figure 4.2-b exhibit respectively the DTA and DTG curves from the thermal decomposition of the uncalcined samples.

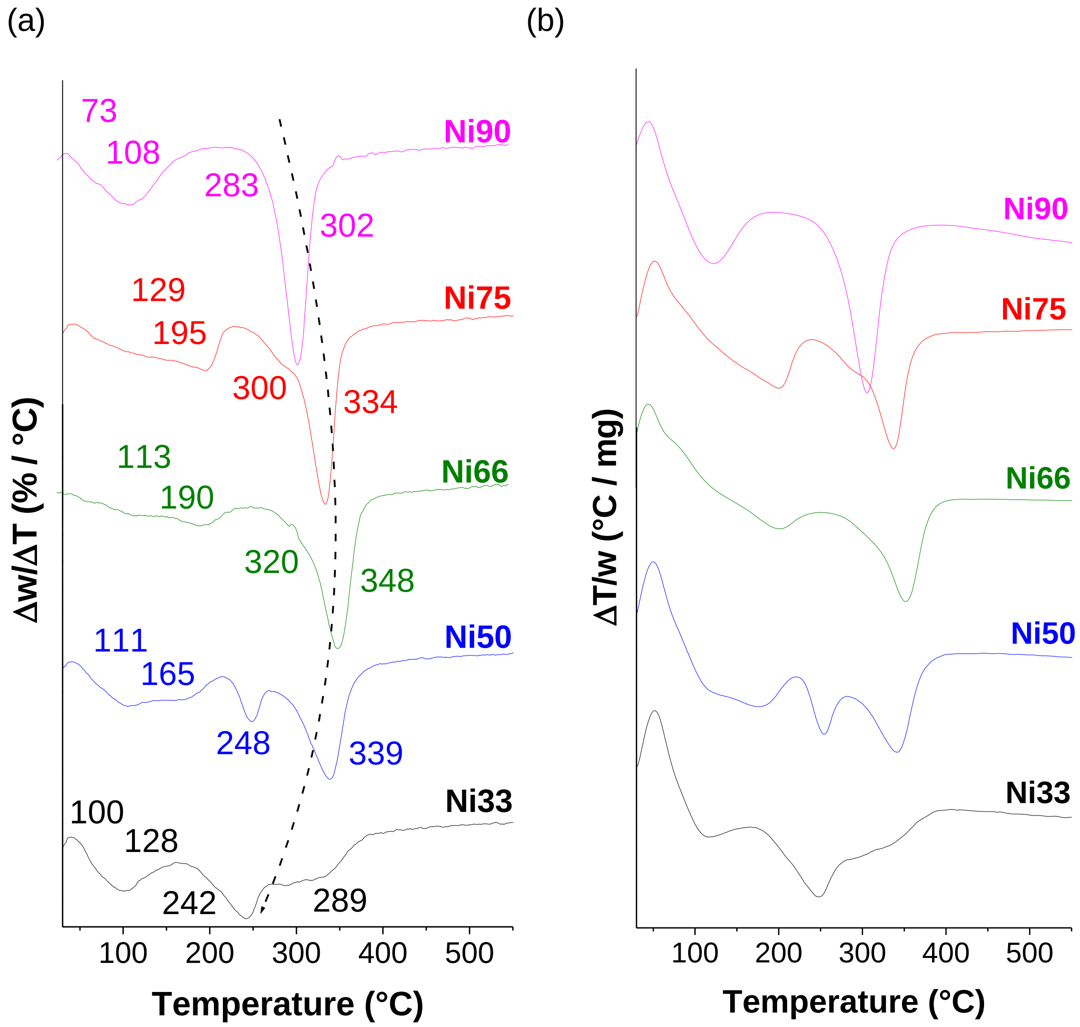

Figure 4.2. (a) DTG and (b) DTA curves for uncalcined samples.

Figure 4.2-a shows DTG peaks associated to the decomposition of the precursors. The corresponding DTA peaks (in Figure 4.2-b) reveal that these weight losses are endothermic events. The weight losses at temperatures below 200°C are usually ascribed to the removal of humidity and interlayer water from the structure [29-31]. The peaks centred at temperatures between 242 – 348°C are associated to the release of the NO_x, OH^- and CO_3^{2-} compounds from the decomposition of the precursors [21, 32]. As expected for these materials, the structure collapses at temperatures below 400°C and the mixed oxides are formed [18, 33]. The same decomposition behaviour was observed for other samples prepared by the precipitation method with similar precursors [21, 34].

In general, the DTG peaks are shifted towards higher temperatures for the Ni66 sample. The weight losses take place at lower temperatures as the Ni/Al molar ratio deviates from 2. Indeed, the samples loaded with the lowest and the highest Ni content (the Ni33 and Ni90 samples, respectively) exhibit the thermogravimetric events at the lowest temperatures. Consequently, Figure 4.2-a and 4.2-b suggest that the Ni66 sample possesses the highest thermal stability, which is significantly lower for the Ni33 and Ni90 samples. This result is in agreement with the S_{BET} analysis (Table 4.1) because the mixed oxides generally exhibit high thermal stability [19, 28].

The thermogravimetric curves (Figure 4.2) are in agreement with the S_{BET} (Table 4.1) and XRD analyses (Figure 4.1). The pure NiO phase was preferentially formed for the Ni90 sample, while the samples with lower Ni/Al ratios also formed the $NiAl_2O_4$ and γ-Al_2O_3 phases. Among these materials, the Ni33 sample exhibited evidences that the alumina phase was formed for this sample.

The H_2-TPR profiles are presented in Figure 4.3.

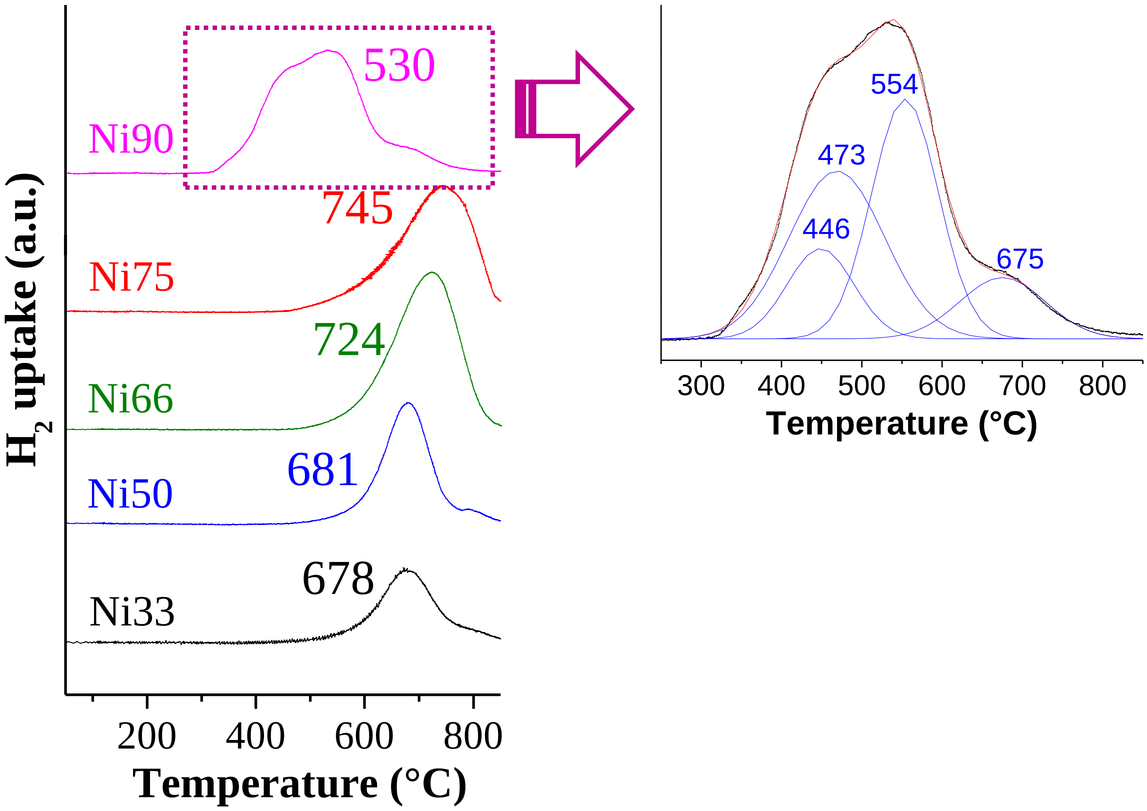

Figure 4.3. H_2-TPR profiles for calcined samples.

The H_2-TPR profiles shown in Figure 4.3 exhibit reduction peaks centred at temperatures in the range 530 - 745°C. The reduction peaks are shifted towards higher temperatures with increasing Ni content, except for the Ni90 catalyst. This broad peak can be assigned mostly to the reduction of Ni in the $NiAl_2O_4$ spinel phase identified in the XRD patterns (Figure 4.1) because the reduction of the bulk phase of NiO occurs at lower temperatures [35, 36]. The reduction at higher temperatures compared to the pure NiO is a typical feature of catalysts derived from hydrotalcite-type materials [37, 38]. Aside the Ni90 sample, this behaviour indicates that higher quantity of the $NiAl_2O_4$ phase is formed with increasing the nickel content on samples.

The H_2-TPR curve obtained for the Ni33 sample shows the strong interaction between the NiO with the support (Al_2O_3) because the reduction peak is located at similar temperature compared to the samples with Ni/Al ratio between 1 and 3.

The broad peak at lower temperatures for the Ni90 sample indicates the formation of the bulk or segregated nickel oxide phases rather than the Ni spinel phase. The deconvolution of this peak suggests several peaks centred at 446 – 554°C and related to the NiO crystallites with non-homogeneous sizes. The small peak centred at 675°C reveals the presence of lesser Ni-Al mixed oxides in the Ni90 catalyst. The peaks located at lower temperatures for the latter sample also highlight the formation of the bulk NiO phase and larger particles suggested by the XRD patterns (Figure 4.1). For this catalyst composition, there are fewer Al^{3+} cations available to surround the Ni ions in the layered structure that could be expected from mixed oxide structures. Hence, it cannot isolate the active metal ions from each other and prevent the aggregation process. In addition to the XRD reflections, the TPR curves provides further insights on the crystalline phases that explain well the lowest specific surface area (Table 4.1) and thermal stability (Figure 4.2) obtained for the Ni90 sample.

Figure 4.4 displays the ammonia desorption profile for the calcined catalysts.

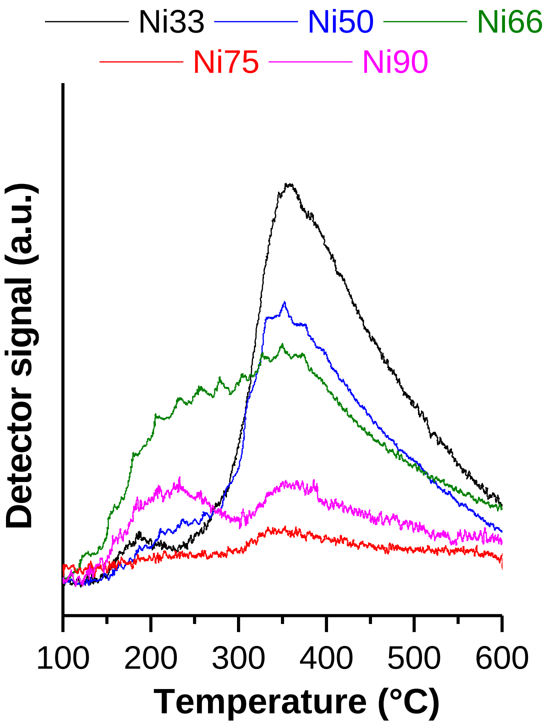

Figure 4.4. NH_3-TPD curves for the calcined samples.

It can be identified two major desorption peaks for all the samples in Figure 4.4. The peak at lower temperature denotes sites with weak acidity, while the peak centred at ca. 360°C is ascribed to moderate acid sites. Aside the Ni75 sample, the Figure 4.4 shows a clear trend for the relation between the number and quality of sites and the Ni/Al ratio on samples. Indeed, increasing the Ni/Al ratio leads to an increase in the number of sites with weaker acidity and decrease the amount of stronger acid sites. For samples with Ni/Al molar ratio > 2, the overall acidity decreases significantly. The total acidity varied in the following order: Ni33 (100%) > Ni66 (86%) > Ni50 (74%) > Ni90 (36%) > Ni75 (16%).

4.3.2 Decomposition of ethanol

The results of ethanol decomposition after 1-h time on stream (TOS) are summarised in Table 4.2. The conversion of ethanol was 100% for all runs.

Table 4.2. Results for the ethanol decomposition.

Sample	S_{H2} (%)	S_{Ci} (%)			
		CO	CH_4	CO_2	C_2H_4+ C_2H_6
Ni33	28	10	4	14	72
Ni50	25	7	2	14	77
Ni66	52	29	26	45	0
Ni75	51	27	31	39	3
Ni90	49	22	39	39	0

Table 4.2 reveals that the dehydration of ethanol (eq. 4.4.3) is favoured for the Ni33 and Ni50 catalysts because of its high selectivity for ethylene. This result is expected due to the highest amount of stronger acid sites revealed for these samples by NH_3-TPD (Figure 4.4). The same behaviour was reported for nickel supported on alumina [6]. The increase in the Ni/Al ratio decreases the quantity of stronger acid sites and thus promotes the dehydrogenation of ethanol (eq. 4.4), where acetaldehyde undergoes to carbon monoxide and methane (eq. 4.5). Based on the high amount of CO_2, the Boudouard (eq. 4.6) and the water-gas shift (eq. 4.7) reactions are also favoured for high contents of nickel.

$$C_2H_5OH \rightarrow C_2H_4 + H_2O \qquad \Delta H_{298K}= 45\ kJ\cdot mol^{-1} \qquad (4.3)$$

$$C_2H_5OH \rightarrow CH_3CHO + H_2 \qquad \Delta H_{298K} = 68\ kJ\cdot mol^{-1} \qquad (4.4)$$

$$CH_3CHO \rightarrow CH_4 + CO \qquad \Delta H_{298K} = -19\ kJ\cdot mol^{-1} \qquad (4.5)$$

$$2CO \rightarrow CO_2 + C_{(S)} \qquad \Delta H_{298K}= -172\ kJ\cdot mol^{-1} \qquad (4.6)$$

$$H_2O + CO \rightarrow CO_2 + H_2 \qquad \Delta H_{298K}= -41\ kJ\cdot mol^{-1} \qquad (4.7)$$

For samples with Ni/Al ratio 2, the selectivity for methane increases and the selectivity towards hydrogen and carbon monoxide decreases with increasing Ni/Al ratio. This trend suggests that the mixed oxides could easily promote the decomposition (eq. 4.8) or the conversion of methane by the steam reforming reaction (eq. 4.9).

$$CH_4 \rightarrow C_{(S)} + 2H_2 \qquad \Delta H_{298K}= 75\ kJ\cdot mol^{-1} \qquad (4.8)$$

$$CH_4 + H_2O \rightarrow CO + 3H_2 \qquad \Delta H_{298K}= 206\ kJ\cdot mol^{-1} \qquad (4.9)$$

4.3.3 Characterisation of the spent catalysts

Figure 4.5 exhibits the DTA curves related to combustion of carbon deposited on the spent catalysts. The number expressed in brackets denotes the amount of carbon formed per mass of catalyst per hour ($g_C \cdot g_{cat}^{-1} \cdot h^{-1}$).

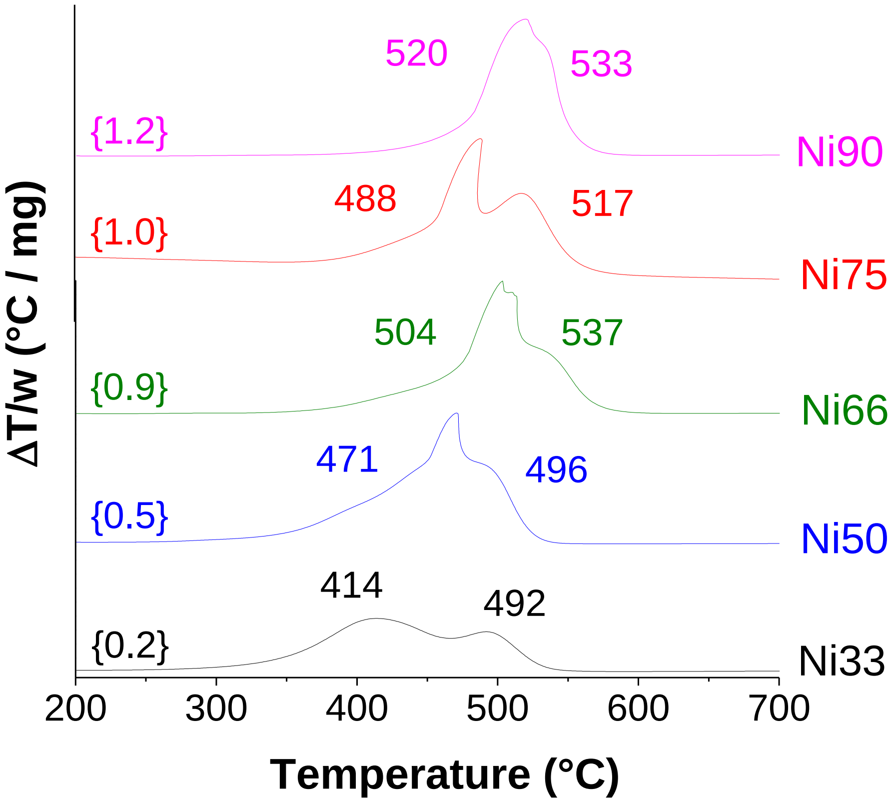

Figure 4.5. TPO-DTA curves for the spent catalysts.

The TPO-DTA data collected for the different catalysts revealed that the amount of carbon increased with increasing Ni/Al ratio. The same trend was observed by Mezalira et al. (2011) for decomposition of ethanol over supported Ni/Al_2O_3 samples [6]. It is generally accepted that larger crystallites of nickel promote coke formation for reforming and decomposition processes [22, 39], thus the greater amount of carbon for samples with higher Ni/Al ratio. The XRD patterns for calcined catalysts (Figure 4.1) previously showed crystallites with larger sizes for samples with higher Ni/Al, in which the Ni90 catalyst revealed much larger diameters ascribed to the formation of segregated Ni oxide rather than the mixed oxide phases (see the TPR curves in Figure 4.3).

The DTA curves associated to the carbon combustion present overlapped peaks at temperature in the range 300 – 570°C. Moreover, the position of peaks varies according to the composition of samples. Thus, the DTA analysis suggests that different types of carbon are generated according to the Ni/Al ratio. In general, the increase in the Ni/Al ratio generates carbon deposits that are oxidised at higher temperatures. According to the literature, amorphous carbon is told to cover the active metal sites and leads to deactivation, whereas filamentous carbon can grow without blocking completely the access of reactants to the metal surface [40]. It was also shown that the diameter and the shape of the carbon filaments obtained from decomposition processes change with the content of the active metal [21].

The amorphous carbon oxidises at approximately 400°C, while carbon nanotubes and carbon nanofibres are usually burned at temperatures in the range 450 - 500°C and graphitic carbon at temperatures above 500°C [21, 41, 42]. Therefore, the Ni33 sample might exhibit mostly amorphous carbon that would conduct easier for deactivation by coking. The shoulder displayed by the Ni50 sample probably indicates the presence of amorphous carbon, although in lesser quantities compared to the Ni33 sample. For catalysts with Ni/Al ≥ 2, the filamentous and graphitic structures are the predominant types of carbon. Based on the aforementioned reports, increasing the Ni/Al ratio (from 2 to 9) minimises the production of the carbon nanotubes and promotes the formation of the graphitic carbon.

Figure 4.6 shows X-ray diffraction spectra collected for the spent catalysts. The spectra show reflections at $2\theta = 44.5°$ and 51.8° ascribed to metallic nickel. Furthermore, a broad reflection can be identified at 2θ in the range 20 – 30° assigned to carbon.

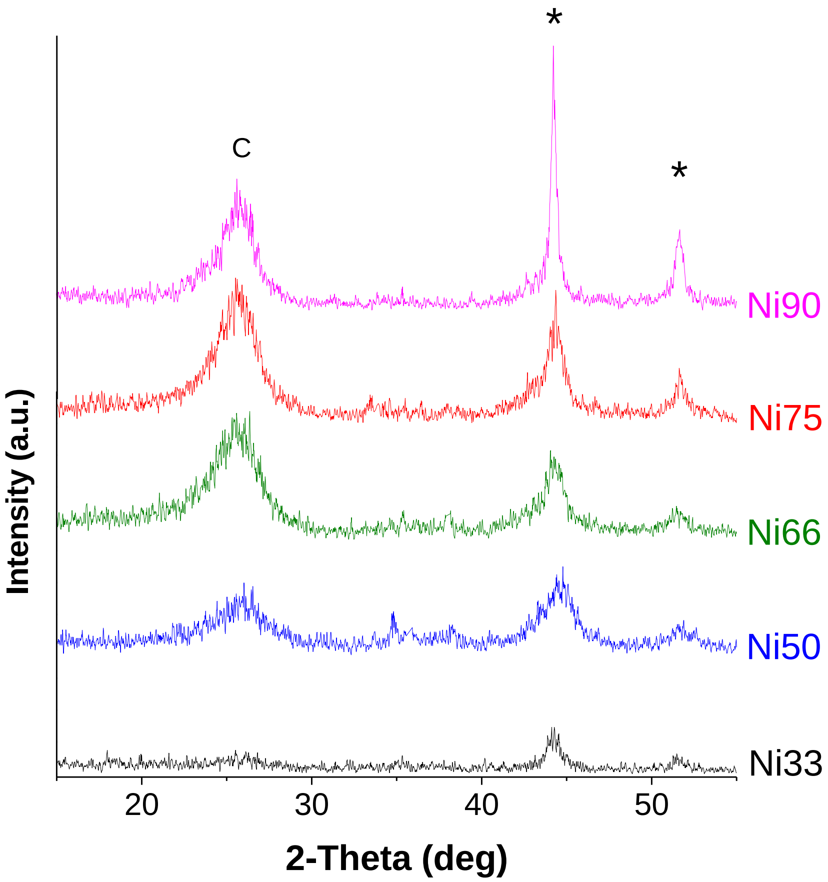

Figure 4.6. XRD patterns for the spent samples. Identified crystalline phases: (*) Ni^0; (C) carbon.

From the width at half the maximum intensity peak at 2θ = 44.5°, it can be seen that the Ni^0 crystallite size follows the behaviour for the Ni oxide phase for calcined samples (shown in Figure 4.1). The diameter for the metallic nickel crystallites decreases with decreasing Ni/Al ratio for samples with Ni/Al molar ratio ≥ 1. Additionally, the strongest intensity for the reflection exhibited by the Ni90 sample suggest that sintering might occur easily for this sample, which is expected from its lowest thermal stability highlighted by the DTA (Figure 4.2) and H_2-TPR (Figure 4.3) analyses. Apparently, the Ni^0 crystallites for the Ni33 sample are larger than those formed for the samples with intermediate Ni/Al ratios (i.e., the Ni50, Ni66 and Ni75 samples).

The intensity of the broad peak between 20° and 30° is proportional to the amount of carbon formed measured by TPO/DTA (Figure 4.5). Indeed, the peak is very short for the Ni33 sample and significantly smaller for the Ni50 catalyst compared to the samples with Ni/Al ≥ 2.

4.3.4 Discussion

The results showed a strong influence of the composition on the characteristics of the Ni-Al oxides and their catalytic properties for the decomposition of ethanol. The variation of the Ni/Al ratio between 0.5 and 9 led to materials with different morphology and catalytic properties. Although the sample with Ni/Al molar ratio = 0.5 (i.e., Ni33) would correspond to the stoichiometric $NiAl_2O_4$ mixed oxide, the XRD patterns (Figure 4.1) evidenced that the Ni is well dispersed as NiO on the Al_2O_3 oxide because this sample is poorly crystallised and exhibited reflections assigned to the alumina phase. The Al-rich sample showed behaviour similar to the alumina-supported Ni catalysts (Ni/Al_2O_3). The S_{BET} data (Table 4.1) corroborate this feature because the specific surface area exhibited by the Ni33 sample (135 $m^2 \cdot g^{-1}$) is close to the alumina materials calcined at similar conditions [6, 43, 44]. The H_2-TPR results for the Ni33 sample (Figure 4.3) revealed a peak centred at 678°C that indicates the Ni well dispersed and with strong interaction with the alumina because this temperature is much higher than the temperature required for the reduction of the bulk NiO phase [35, 36]. Moreover, the DTA curves (Figure 4.2-b) exhibited an endothermic peak ascribed to dehydroxylation at much lesser temperatures.

The increase in the Ni/Al ratio provided significantly changes in the characteristics (S_{BET}, XRD and TPR) and in the catalytic properties (NH_3-TPD and selectivity). The S_{BET} data (Table 4.1) varied in the following order: Ni33 > Ni50 < Ni66 > Ni75 >> Ni90. These results suggest that the formation of the mixed oxides occurs starting from the Ni/Al molar ratio = 1 (Ni50), whereas the highest S_{BET} value is achieved by the sample with Ni/Al molar ratio = 2. However, the mixed oxide structure collapses for samples with Ni/Al molar ratio > 3, which forms mainly the segregated bulk NiO phase. This behaviour is consistent with the information given by the different characterisation techniques employed in this work (S_{BET}, DTG, DTA, XRD and H_2-TPR).

The sample with the higher content of Al (i.e., Ni33) presented characteristics of pure alumina (Al_2O_3) not only in terms of specific surface area (Table 4.1), crystallinity (Figure 4.1) and acid character of its surface (Figure 4.4). These properties result in high selectivity towards ethylene due to dehydration of ethanol, which is expected from acid catalysts, as well as amorphous carbon.

Despite decreasing the S_{BET} area, the increase of the Ni/Al molar ratio to 1 (Ni50) might provide the formation of the $NiAl_2O_4$ mixed oxide. The reflections at 2θ = 37.0, 45.2 and 65.8° in the XRD patterns suggest the presence of this mixed oxide phase in addition to the NiO phase (2θ = 37.4, 43.4 and 63.1°). Although a shift in the XRD reflections of the NiO phase could be related to the temperature of the thermal treatment, this is not the case for the trend observed in Figure 4.1, where only the Ni/Al ratio varied. The H_2-TPR profile showed a small increase in the reduction temperature, but the degree of reduction was proportionally to the Ni content on this sample. On the other hand, the NH_3-TPD result showed a decrease in the total acidity (quantitative), while the maximum at 350°C revealed that the strength of the acid sites is similar to the Ni33 sample. This trend is important for understanding the similarity between the distribution of products displayed by both the Ni33 and Ni50 samples during the catalytic evaluation (Table 4.2).

The further increment on the Ni/Al molar ratio to 2 and 3 increases the degree of non-stoichiometry due to the excess of nickel on samples. However, the S_{BET} value and crystallinity did not change significantly. The most remarkable effect was noted in the reduction profile (Figure 4.3), because a significantly increase at the reduction temperature. The maxima reduction temperature is located at 725 and 745°C for the Ni66 (Ni/Al = 2) and Ni75 (Ni/Al = 3) samples, respectively. The H_2-TPR results showed no segregation of the NiO phase on this samples, since the reduction of the bulk NiO phase takes place at much lower temperatures than the reduction temperature range displayed in Figure 4.3 (at approximately 400°C). This means that the excess f Ni was accommodated in the mixed oxide structure formed. This can be possible if the Ni that normally occupies tetrahedral sites (in the standard spinel phase) changed its position towards octahedral sites firstly filled by Al. This would lead the the formation of an inversed spinel phase [$Ni_{tet}(Ni_{oct}Al_{oct})O_4$], where the subscripts “tet” and “oct” refer to tetrahedral and octahedral sites, respectively. The formation of inversed spinel phases are reported in literature for materials prepared by different methods [45] and temperatures [46].

Another explanation is that the excess of NiO could be well dispersed on the surface of the spinel phase, where the mixed oxide would act as a support of the NiO. This hypothesis can also be found in the literature [47, 48]. Therefore, the mixed oxide phase would be responsible for the thermal properties of the catalysts, presenting improved resistance to sintering [47].

It could be seen in the NH_3-TPD analysis (Figure 4.4) that increasing the Ni/Al ratio changes the amount and the strength of the acid sites. The Ni66 sample exhibit similar proportion of weak and intermediate acid sites, while the sample with the ratio Ni/Al = 3 exhibit much lesser amount of both the acid sites. The difference in the acidity is greater when compared to the Ni33 and Ni50 samples. The impact of these characteristics on the catalytic properties is clear because the Ni66 and Ni75 samples exhibited almost no selectivity towards ethylene (see Eq. 3) and high selectivity towards hydrogen (Table 4.2).

For the sample with the ratio Ni/Al = 9, both the characterization and the catalytic results were quite different from the others (from the rest). From the S_{BET} (Table 4.1), XRD (Figure 4.1) and NH_3-TPD (Figure 4.4) results, it could be noted that the mixed oxide structure collapsed because the amount of Ni available in the Ni90 sample was much higher than the amount that could be accommodated in the mixed oxide. As a consequence, apparently the excess of nickel (in relation to the stoichiometric $NiAl_2O_4$ phase) stayed as segregated NiO phase.

This hypothesis is supported mainly by the H_2-TPR results (Figure 4.3), which showed that the reduction of most of the oxide phases takes place at temperatures below 600°C. The deconvolution of the broad reduction peak revealed three major peaks centred in the range 450 – 550°C, which is expected for the NiO phase. Only a small fraction (ca. 10%) reduced at higher temperatures that was associated to the mixed oxide phase (675°C). This maximum temperature is the same observed for the Ni33 sample, thus indicating that this small content form the stoichiometric mixed oxide phase. The values obtained for the area of the peaks from the deconvolution of the broad TPR peak indicate that all the aluminum is presented as mixed oxide and then only 5% of the nickel would be in this stoichiometric mixed oxide phase ($NiAl_2O_4$). It can be told that the remaining Ni (85%) would be as bulk NiO in the structure of the Ni90 sample.

The lowest S_{BET} area for the Ni90 sample (70 $m^2 \cdot g^{-1}$) also corroborates the hypothesis given above. Moreover, the X-ray diffractogram (Figure 4.1) revealed only reflections assigned to the NiO. The NH_3-TPD curves (Figure 4.4) revealed low acidity for the surface of the Ni90 sample, related to the excess of NiO. These characteristics led to low selectivity for the products related to dehydration of ethanol (eq. 3). Finally, the XRD patterns for the spent samples (Figure 4.6) showed that a strong sintering takes place for the Ni90 catalyst. This happens because the NiO possesses lower thermal stability compared to the mixed oxides, thus the lower resistance for sintering and coke deposition displayed by the sample with the highest Ni/Al ratio. Therefore, both the deactivation mechanisms showed in Figure 4.5 and Figure 4.6 (sintering and coking) might be more critical for the Ni90 catalyst.

4.4 Conclusions

A series of Ni-Al samples with Ni/Al molar ratios between 0.5 and 9 was prepared by the precipitation method.

The S_{BET} and thermogravimetric results showed that the Ni/Al ratio strongly changes the characteristics of the materials. The samples exhibited behaviour or properties varying from the Al_2O_3 (for the Ni/Al < 1) to the bulk NiO phase (Ni/Al > 3). For the samples with intermediate Ni/Al ratios (i.e., $1 \leq \text{Ni/Al} \leq 3$), mixed oxides with high specific surface area, moderate acidity, improved thermal stability and high resistance to coking were obtained.

The sample with the lowest Ni content (Ni33) showed S_{BET} and XRD pattern typically assigned to Al_2O_3. These data indicate that the nickel is well dispersed on the alumina phase, which is suggested by the high reduction temperature. This Al-rich sample exhibited high acidity and thus produced ethylene as the major product during the ethanol reaction. This high acidity also formed amorphous carbon that leads to deactivation by coking.

On the other hand, the Ni-rich sample (Ni90) presented characteristics of the bulk NiO phase. This sample showed low S_{BET} and XRD pattern and reduction profile assigned to the NiO phase. The excess of Ni led to the collapse of the spinel phase, whereas most of the Ni was accommodated as segregated NiO phase. Despite possessing low acidity, this catalyst exhibited low thermal stability (lower reduction temperatures). This feature promoted sintering, which was revealed by the XRD pattern of the spent catalyst.

The samples with Ni/Al molar ratio = 2 and 3 presented the most promising characteristics for the decomposition of ethanol because it provided high selectivity towards H_2 and CO and low quantity of ethylene and carbon. The catalytic data could be attributed to the formation of the $NiAl_2O_4$ mixed oxide phase with moderate acidity and improved thermal stability for these samples.

ACKNOWLEDGEMENTS

The authors wish to thank the financial support and scholarships granted by the “Conselho Nacional de Desenvolvimento Científico e Tecnológico – CNPq” and by the “Coordenação de Aperfeiçoamento de Pessoal de Nível Superior – CAPES”.

References

[1] W. Wang, Y. Wang, International Journal of Energy Research 34 (2010) 1285-1290.

[2] W. Wang, Y.Q. Wang, International Journal of Energy Research 32 (2008) 1432-1443.

[3] P.D. Vaidya, A.E. Rodrigues, Chemical Engineering Journal 117 (2006) 39-49.

[4] H. Fajardo, E. Longo, D. Mezalira, G. Nuernberg, G. Almerindo, A. Collasiol, L.D. Probst, I.S. Garcia, N.V. Carreño, Environmental Chemistry Letters 8 (2010) 79-85.

[5] G. Wang, H. Wang, W. Li, Z. Ren, J. Bai, J. Bai, Fuel Processing Technology 92 (2011) 531-540.

[6] D.Z. Mezalira, L.D. Probst, S. Pronier, Y. Batonneau, C. Batiot-Dupeyrat, Journal of Molecular Catalysis a-Chemical 340 (2011) 15-23.

[7] Q. Liu, Y. Ouyang, L. Zhang, Y. Xu, Y. Fang, Physica E: Low-dimensional Systems and Nanostructures 41 (2009) 1204-1209.

[8] R. Tian, X. Wang, M. Li, H. Hu, R. Chen, F. Liu, H. Zheng, L. Wan, Applied Surface Science 255 (2008) 3294-3299.

[9] G. Jones, J.G. Jakobsen, S.S. Shim, J. Kleis, M.P. Andersson, J. Rossmeisl, F. Abild-Pedersen, T. Bligaard, S. Helveg, B. Hinnemann, J.R. Rostrup-Nielsen, I. Chorkendorff, J. Sehested, J.K. Nørskov, Journal of Catalysis 259 (2008) 147-160.

[10] J.R. Rostrup-Nielsen, J.H.B. Hansen, Journal of Catalysis 144 (1993) 38-49.

[11] J.R. Rostrup-Nielsen, Catalysis Today 18 (1993) 305-324.

[12] G. Wang, H. Wang, Z. Tang, W. Li, J. Bai, Applied Catalysis B: Environmental 88 (2009) 142-151.

[13] R. Barthos, A. Széchenyi, Á. Koós, F. Solymosi, Applied Catalysis A: General 327 (2007) 95-105.

[14] F. Gao, L. Zhang, Y. Yang, S. Huang, Applied Surface Science 256 (2010) 3357-3360.

[15] W. Li, H. Wang, Z. Ren, G. Wang, J. Bai, Applied Catalysis B-Environmental 84 (2008) 433-439.

[16] H. Igarashi, H. Murakami, Y. Murakami, S. Maruyama, N. Nakashima, Chemical Physics Letters 392 (2004) 529-532.

[17] G. Wang, H. Wang, W. Li, J. Bai, Rsc Advances 1 (2011) 1585-1592.

[18] M.J. Holgado, V. Rives, M.S. San Roman, Applied Catalysis a-General 214 (2001) 219-228.

[19] A. Vaccari, Catalysis Today 41 (1998) 53-71.

[20] F. Trifiró, A. Vaccari, Comprehensive Supramolecular Chemistry, Pergamon, Oxford, 1996, pp. 251, vol. 257.

[21] N.A. Hermes, M.A. Lansarin, O.W. Perez-Lopez, Catalysis Letters 141 (2011) 1018-1025.

[22] A. Bhattacharyya, V.W. Chang, D.J. Schumacher, Applied Clay Science 13 (1998) 317-328.

[23] V. Mas, M.L. Dieuzeide, M. Jobbagy, G. Baronetti, N. Amadeo, M. Laborde, Catalysis Today 133 (2008) 319-323.

[24] H. Muroyama, R. Nakase, T. Matsui, K. Eguchi, International Journal of Hydrogen Energy 35 (2010) 1575-1581.

[25] C. Resini, T. Montanari, L. Barattini, G. Ramis, G. Busca, S. Presto, P. Riani, R. Marazza, M. Sisani, F. Marmottini, U. Costantino, Applied Catalysis a-General 355 (2009) 83-93.

[26] G. Busca, U. Costantino, T. Montanari, G. Ramis, C. Resini, M. Sisani, International Journal of Hydrogen Energy 35 (2010) 5356-5366.

[27] F. Kovanda, T. Rojka, P. Bezdicka, K. Jiratova, L. Obalova, K. Pacultova, Z. Bastl, T. Grygar, Journal of Solid State Chemistry 182 (2009) 27-36.

[28] A. Vaccari, Applied Clay Science 14 (1999) 161-198.

[29] J.I. Di Cosimo, V.K. Díez, M. Xu, E. Iglesia, C.R. Apesteguía, Journal of Catalysis 178 (1998) 499-510.

[30] R.L. Frost, A.W. Musumeci, T. Bostrom, M.O. Adebajo, M.L. Weier, W. Martens, Thermochimica Acta 429 (2005) 179-187.

[31] E.L. Crepaldi, P.C. Pavan, J.B. Valim, Journal of the Brazilian Chemical Society 11 (2000) 64-70.

[32] S.J. Palmer, H.J. Spratt, R.L. Frost, Journal of Thermal Analysis and Calorimetry 95 (2009) 123-129.

[33] G. de Souza, V.C. Ávila, N.R. Marcílio, O.W. Perez-Lopez, Procedia Engineering 42 (2012) 1805-1815.

[34] L.H. Zhang, X. Xiang, L. Zhang, F. Li, J. Zhu, D.G. Evans, X. Duan, Journal of Physics and Chemistry of Solids 69 (2008) 1098-1101.

[35] J.A. Montoya, E. Romero-Pascual, C. Gimon, P. Del Angel, A. Monzon, Catalysis Today 63 (2000) 71-85.

[36] J.J. Guo, H. Lou, H. Zhao, D.F. Chai, X.M. Zheng, Applied Catalysis a-General 273 (2004) 75-82.

[37] F. Cavani, F. Trifiro, A. Vaccari, Catalysis Today 11 (1991) 173-301.

[38] O.W. Perez-Lopez, A. Senger, N.R. Marcilio, M.A. Lansarin, Applied Catalysis a-General 303 (2006) 234-244.

[39] K. Aasberg-Petersen, I. Dybkjær, C.V. Ovesen, N.C. Schjødt, J. Sehested, S.G. Thomsen, Journal of Natural Gas Science and Engineering 3 (2011) 423-459.

[40] J.L. Ewbank, L. Kovarik, C.C. Kenvin, C. Sievers, Green Chemistry 16 (2014) 885-896.

[41] F.F. de Sousa, H.S.A. de Sousa, A.C. Oliveira, M.C.C. Junior, A.P. Ayala, E.B. Barros, B.C. Viana, J.M. Filho, A.C. Oliveira, International Journal of Hydrogen Energy 37 (2012) 3201-3212.

[42] C. Escobar, O. Perez-Lopez, Catalysis Letters 144 (2014) 796-804.

[43] Z. Xu, Y. Li, J. Zhang, L. Chang, R. Zhou, Z. Duan, Applied Catalysis A: General 210 (2001) 45-53.

[44] G. Li, L. Hu, J.M. Hill, Applied Catalysis A: General 301 (2006) 16-24.

[45] Z. Boukha, C. Jiménez-González, B. de Rivas, J.R. González-Velasco, J.I. Gutiérrez-Ortiz, R. López-Fonseca, Applied Catalysis B: Environmental 158–159 (2014) 190-201.

[46] Y.S. Han, J.B. Li, X.S. Ning, B. Chi, Journal of the American Ceramic Society 87 (2004) 1347-1349.

[47] O. Clause, B. Rebours, E. Merlen, F. Trifiró, A. Vaccari, Journal of Catalysis 133 (1992) 231-246.

[48] Y. Cesteros, P. Salagre, F. Medina, J.E. Sueiras, Chemistry of Materials 12 (2000) 331-335.

Capítulo 5

Synthesis and characterisation of the structural and catalytic properties of Fe-, Co- and Ni-based co-precipitated catalysts

Artigo a ser submetido ao periódico: *Journal of Thermal Analysis and Calorimetry*.

Synthesis and characterisation of the structural and catalytic properties of Fe-, Co- and Ni-based co-precipitated catalysts

Guilherme de Souza[1,2], Cássia Ruoso[1]; Nilson R. Marcilio[1] and Oscar W. Perez-Lopez[1,*]

[1] Department of Chemical Engineering, Federal University of Rio Grande do Sul - UFRGS, R. Eng. Luiz Englert S/N°, Build. 12204. 90040-040 Porto Alegre-RS, Brazil

[2] Fundação de Ciência e Tecnologia do Estado do Rio Grande do Sul - CIENTEC, Av. das Indústrias, 2270, Distrito Industrial, 94930-230 Cachoeirinha-RS, Brazil.

* Corresponding author: O. W. Perez-Lopez. UFRGS, Rua Eng. Luiz Englert S/N°, Build. 12204. Zip Code: 90040-040 - Porto Alegre, Brazil. Phone: +55 51 3308 3953. Fax: +55 51 3308 3277. Email: perez@enq.ufrgs.br

Abstract

This paper reports the structural and catalytic properties of Ni-, Co- and Fe-Al co-precipitated catalysts. The decomposition of ethanol was chosen as the model reaction in order to evaluate the catalytic performance of the samples. The samples were studied by thermogravimetry (TG/DTA), X-ray diffraction (XRD), specific surface area (S_{BET}), temperature-programmed reduction (H_2-TPR) and oxidation (TPO/DTA), scanning electron microscopy (SEM) and Raman spectroscopy. The TG/DTA, XRD and H_2-TPR analyses point to the formation of mixed oxide structures for the Ni- and Co-samples. The Co-catalyst exhibited higher selectivity towards H_2 and CO and better H_2/CO molar ratio for the use in Fischer-Tropsch Synthesis. The Fe-catalyst presented higher selectivity towards ethylene and acetaldehyde. The increase in the reaction temperature enhances the selectivity towards H_2 and CO and decreases the H_2/CO ratio and the formation of CO_2 and carbon on samples. In general, the TPO/DTA, SEM and Raman analyses of the spent catalysts suggest that the carbon deposits on the samples are mainly filamentous or graphitic carbon. These structures do not encapsulate the active metal, thus minimising the deactivation by coking compared to the amorphous carbon.

Keywords: Mixed oxides; characterisation; thermal analyses; decomposition of ethanol; carbon.

5.1. Introduction

The depletion of crude petroleum reserves challenges researchers to find feasible and environmentally friendly alternative resources. Among them, fuels derived from biomass are particularly desirable, especially because they are generated from renewable resources. In this context, the catalytic conversion of biomass sources to hydrogen is currently been widely investigated. The steam reforming of ethanol with excess water appears to be a very interesting route for the production of hydrogen. Nevertheless, questions regarding the expensive new infrastructure and efficiency matters that would be required for a future hydrogen society could lead to the production of synthetic liquid fuels instead of only hydrogen [1, 2].

Alternatively, hydrocarbons and a wide range of different chemicals can be obtained from the conversion of synthesis gas (H_2 and CO mixture). The synthesis gas can be originated from biomass resources (such as wastes and effluents) through the Fischer-Tropsch Synthesis (FTS) and through the synthesis and conversion of methanol. The decomposition processes provide a more suitable H_2/CO ratio for the further processes than the steam reforming with excess water.

The decomposition of rich ethanol wastes is an interesting route because it can generate other oxygenates, ethylene, hydrogen and synthesis gas, depending on the process operation conditions and the catalyst used. Also, this process can produce carbon nanotubes (CNT) or nanofibres (CNF) that exhibit outstanding properties, with potential application in many fields and high value in the market [3-5]. For this purpose, supported catalysts based on iron, nickel or cobalt have been investigated [3-7]. However, results for decomposition of ethanol over co-precipitated samples are rarely reported. The co-precipitation method can originate mixed oxides, which have desirable properties such as high surface area, high thermal stability and small crystallite sizes [8, 9]. These are key parameters for the performance of a catalytic system. According to Bhattacharyya et al., the divalent metal ions (M^{2+}) are randomly distributed in the layered structure of mixed oxides derived from hydrotalcite-type materials (HT). For these materials, the active metal ions should be surrounded by other ions that might minimise aggregation and thus prevent sintering and coke formation [10].

In order to develop catalysts suitable for these decomposition processes, Ni-Al, Fe-Al and Co-Al co-precipitated catalysts were characterised and evaluated for the decomposition of ethanol at moderate temperatures.

5.2. Materials and Methods

5.2.1 Preparation of samples

The samples were prepared through the continuous co-precipitation method described previously [11]. The samples were synthesised adopting the same M/Al molar ratio of 2. The Co66 and Ni66 samples were synthesised by mixing an aqueous solution containing metal nitrates (1 M) with another aqueous solution of precipitating agent (Na_2CO_3, 2 M) in a continuous stirred tank reactor (CSTR) at constant temperature (50°C) and pH (8± 0.1). The co-precipitation procedure for the Fe66 sample was carried out using an aqueous solution containing the metal nitrates (0.5 M) and a solution of NaOH and Na_2CO_3 (1:1 molar ratio, 2 M) at 60°C and at a pH value of 9. The precipitate was crystallised for 1 h at the same temperature adopted for the co-precipitation step. Then, the precipitate was filtered and washed thoroughly with distilled and deionised water. After drying at 80°C for 24 h, the samples were crushed and sieved. The fraction with particle sizes between 355 and 500 µm was taken. The thermal treatment was conducted under air flow of 50 mL·min^{-1} at 600°C for 6 h.

5.2.2 Catalytic evaluation

The catalysts were reduced *in situ* under 100 mL·min^{-1} of pure H_2 flow for 1 h at the same reaction temperature prior to the reaction. The catalytic evaluations were carried out in a quartz tubular fixed bed reactor (6 mm i.d.) loaded with 100 mg of catalyst diluted with quartz (1:1 v/v). The tests were performed under atmospheric pressure at 500°C or 600°C. The flow rate of nitrogen was adjusted to 100 mL·min^{-1} through a mass flow controller. The ethanol was fed through syringe-type micropump at a flow rate of 0.5 mL·h^{-1}. The products were analysed by gas chromatography. The ethanol conversion (X_{ET}) was estimated according to equation 5.1.

$$X_{ET}(\%) = \frac{[EtOH]_{IN} - [EtOH]_{OUT}}{[EtOH]_{IN}} x100\% \tag{5.1}$$

The selectivity for hydrogen (S_{H2}) and C-containing products (S_{Ci}) was evaluated as follows:

$$S_{H2} = \frac{[H_2]}{\sum \nu_j . [H_{2j}]} \tag{5.2}$$

$$S_{Ci} = \frac{\nu_i . [C_i]}{\sum \nu_j . [C_j]} \tag{5.3}$$

Where [C_j] and [H_{2j}] is respectively the number of moles of C-containing and H_2-containing *j* product in the outlet stream and *uj* is the ratio of stoichiometric reaction coefficients

5.2.3 Characterisation

The samples were characterised by the BET specific surface area (S_{BET}), thermogravimetry coupled with differential thermal analyses (TG/DTA), X-ray diffraction (XRD), temperature-programmed reduction (H_2-TPR), temperature-programmed oxidation (TPO/DTA), scanning electron microscopy (SEM) and Raman spectroscopy.

The TG/DTA and TPO/DTA analyses were performed using TA thermobalance equipment (Model SDT600). In these experiments, approximately 10 mg each of the uncalcined (TG/DTA) or the reduced or spent catalyst (TPO/DTA) was firstly purged with 1000 $mL \cdot min^{-1}$ of N_2 at 30°C for 10 min. After this pretreatment, the samples were heated to 850°C (10°$C \cdot min^{-1}$) under a synthetic air flow rate of 100 $mL \cdot min^{-1}$.

The S_{BET} and H_2-TPR data were obtained using a multipurpose system (SAMP3) equipped with a thermal conductivity detector (TCD). A quartz tube was loaded with 100 mg of the calcined sample and placed in a temperature-controlled oven. The pretreatment step was conducted under a N_2 flow at 250°C for 1 h. For the H_2-TPR analysis, the temperature was increased up to 900°C (10°$C \cdot min^{-1}$) under 30 $mL \cdot min^{-1}$ of a 10% H_2/N_2 (v/v) mixture flow. The S_{BET} was carried out by the N_2 dynamic adsorption method at -196°C.

Aside the experiments conducted using the SAMP3 system, additional H_2-TPR analyses were performed in the TA thermobalance equipment (Model SDT600) adopting the same procedure used for the reduction step prior to the catalytic runs, where the hydrogen uptake was estimated by means of weight change. The same heating ramp (5°$C \cdot min^{-1}$), reduction temperature (500°C or 600°C) and GHSV for the hydrogen flow (60 L $H_2 \cdot g^{-1} \cdot h^{-1}$) were employed. For the TPO-DTA analysis for spent catalysts, additional tests were made in order to ensure that the reoxidation of the metallic phases did not influence the weight loss that was attributed to the combustion of coke. The calcined catalysts that were reduced in the TA thermobalance, after ending the isothermal step at the reduction temperature, were immediately cooled and then reoxidised following the same procedure stablished for the standard TPO-DTA tests.

The powder XRD patterns of calcined catalysts were collected for 2θ between 10 and 70° with a Bruker D2 Phaser X-ray diffractometer at ambient temperature using CuKα radiation.

The scanning electron microscopy (SEM) images were obtained in a JEOL JSM-6060 equipment at 20 kV under vacuum. The Raman spectra were recorded using a laboratory-built micro-Raman spectrometer described elsewhere [12].

5.3 Results

5.3.1 Characterisation

The nominal molar composition and S_{BET} data of the three samples is displayed in Table 5.1.

Table 5.1. Nominal composition and S_{BET} values for the calcined samples.

Sample	Composition (mol. %)		M	S_{BET} ($m^2 \cdot g^{-1}$)
	M	Al		
Ni66	66.7	33.3	Ni	143
Co66	66.7	33.3	Co	54
Fe66	66.7	33.3	Fe	79

The samples were prepared maintaining the M/Al molar ratio at 2. In the case of the Ni66 and Co66 samples, this composition might favour the formation of mixed oxides from the decomposition of the precursors. It is known that these phases are favoured for M^{2+}/M^{3+} molar ratios between 2 and 4 [8]. The Ni66 material exhibits the highest S_{BET} value (143 m²·g^{-1}). This value is similar to the specific surface area reported elsewhere for nickel co-precipitated catalyst that was calcined at 450°C (145 m²·g^{-1}) [13].

The thermal decomposition behaviour of the uncalcined samples can be evaluated from Figure 5.1.

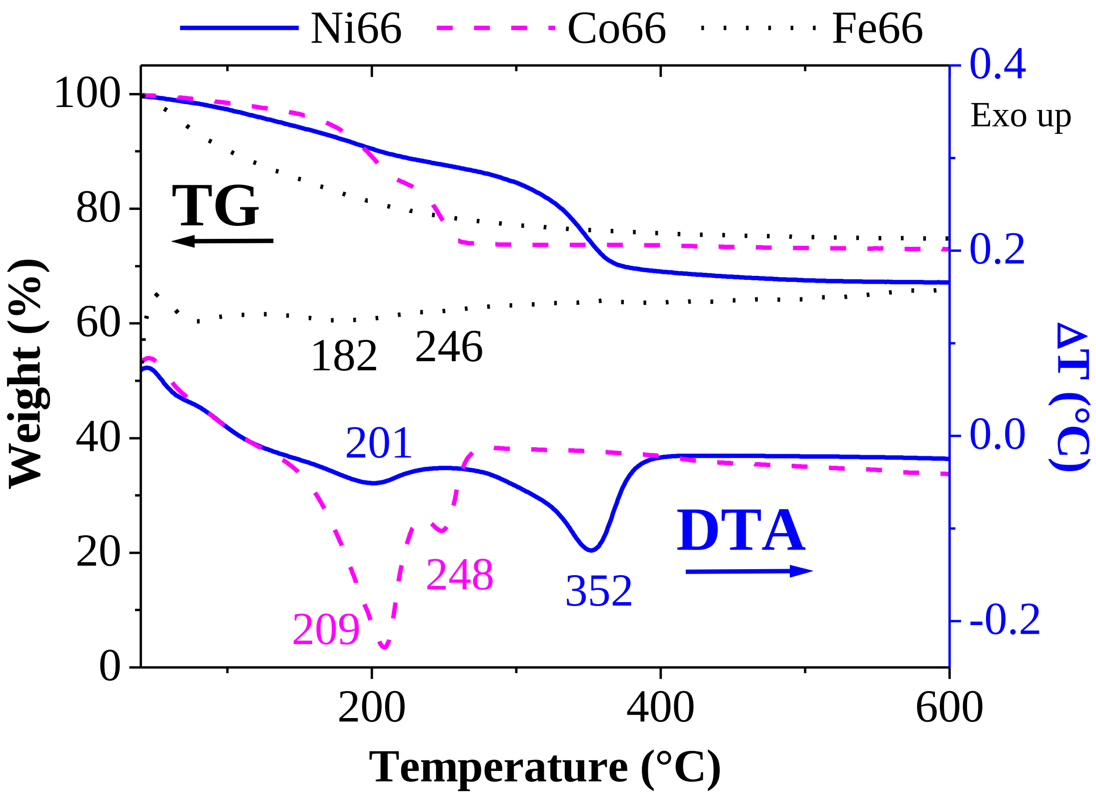

Figure 5.1. .TG/DTA curves for uncalcined Ni66 (solid line), Co66 (dashed line) and Fe66 (dotted line) samples.

The DTA peaks reveal that the weight losses associated to the decomposition of the precursors are endothermic events. The thermogravimetric events in the range 182-209°C are usually attributed to the removal of humidity and interlayer water from the structure [14-16]. The release of the NO, OH^- and CO_3^{2-} compounds from the decomposition of the precursors are expected to occur at higher temperatures (246 – 352°C) [17, 18]. The well dispersed mixed oxides are usually obtained upon calcination of the layered double hydroxides materials at temperatures below 400°C [11, 19]. Other samples prepared by the precipitation method with similar precursors exhibited the same decomposition trend [17, 20]. The DTA peaks related to the weight losses for the Fe66 sample are lesser endothermic compared to the Co66 and Ni66 samples, which might be related to the precursors that included NaOH. The Ni66 sample presents the DTA peak at the highest temperature (352°C), which indicates higher thermal stability for this sample. It also can point to the formation of Ni-Al mixed oxides, because mixed oxides are known to exhibit high thermal stability [21].

The XRD patterns for the uncalcined and calcined samples are displayed in Figure 5.2.

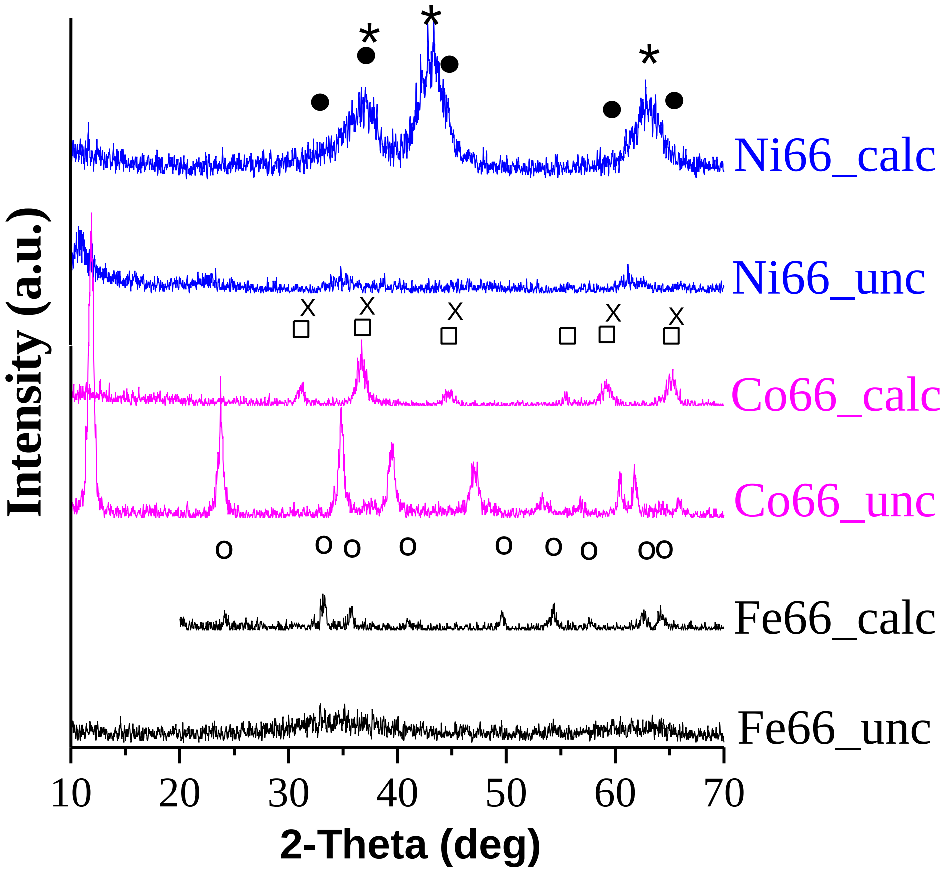

Figure 5.2. XRD patterns for the calcined (calc) and uncalcined (unc) samples. Identified phases: (*) NiO; (●) $NiAl_2O_4$; (x) Co_3O_4; (□) $CoAl_2O_4$; (O) Fe_2O_3.

For the calcined Ni66 sample, the XRD patterns exhibit diffraction reflections at 2θ = 37.4, 43.4 and 63.1° and at 2θ = 37.0, 45.0 and 65.6°. These reflections reveal the presence of the NiO and $NiAl_2O_4$ phases, respectively. As reported elsewhere for other Fe-Al materials [22], the diffraction reflections located at 2θ = 24.2, 33.2, 35.6, 40.9, 49.5, 54.0, 62.4 and 64.0° were found for the Fe66 calcined sample. The reflections can be ascribed solely to the hematite phase (Fe_2O_3). The X-ray diffraction patterns did not point to the formation of the hercynite phase ($FeAl_2O_4$). Regarding the calcined Co66 sample, the diffraction reflections assigned to the Co_3O_4 and the $CoAl_2O_4$ crystalline phases can be identified. Among the calcined samples, the Ni66 sample exhibits peaks with broader width that could suggest the formation of crystallites with smaller diameters for this sample. Regarding the uncalcined samples, the Co66 sample showed diffraction peaks that could be clearly attributed to hydrotalcite-type phase [23]. The major reflections were also identified for the Ni66 uncalcined sample. As seen for the calcined material, the Ni66 uncalcined sample displays broader peaks compared to the uncalcined Co66 sample. The hydrotalcite-type phase could not be found for the fresh Fe66 sample.

The H_2-TPR curves are shown in Figure 5.3.

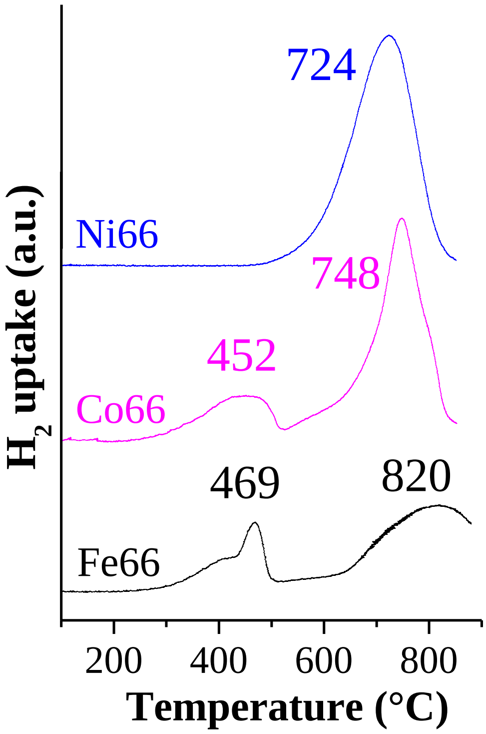

Figure 5.3. H_2-TPR profiles for calcined samples.

The H_2-TPR curves are displayed in Figure 5.3. The Ni66 catalyst shows a major hydrogen uptake that starts at ca. 500°C and ends at 900°C. The peak is assigned to the reduction of Ni in the $NiAl_2O_4$ spinel phase identified in the XRD patterns (Figure 5.2). The reduction of the segregated phase NiO is known to occur at significantly lower temperatures [24, 25].

Regarding the Co66 catalyst, the overlapped reduction peaks centred at 452°C corresponds to the reduction of the bulk cobalt oxide that was identified by the XRD analysis in Figure 5.2 ($Co_3O_4 \rightarrow CoO \rightarrow Co^0$)[26-28]. The TPR peak in the temperature range 550-850°C can be ascribed to the reduction of the $CoAl_2O_4$ mixed oxide phase [26, 29].

For the Fe66 catalyst, the peaks at temperatures in the range 300 - 550°C are typically ascribed to the reduction $Fe_2O_3 \rightarrow Fe_3O_4$ and possibly its subsequent reduction to FeO. The following peaks that start at 600°C are related to further transformations of the iron oxides to metallic iron. On the contrary to the other catalysts, this peak at higher temperatures might not be related to the reduction involving mixed oxides, because the $FeAl_2O_4$ spinel phase was not identified on the corresponding XRD pattern (Figure 5.2).

The reduction at higher temperatures compared to the pure metal oxides is a typical feature of catalysts derived from hydrotalcite-type materials [30, 31]. Therefore, the TPR curves is in agreement with the XRD patterns for the uncalcined samples (Figure 5.2), because both the analyses point to the formation of mixed oxides derived from the hydrotalcite-type compounds for the Ni66 and Co66 samples.

Figure 5.4 shows the weight losses due to the reduction of the nickel oxide species for the Ni66 catalyst reduced under hydrogen flow at different activation procedures. As mentioned above, the reduction procedures are the same applied before the catalytic evaluation. The Δ value is the difference between the weight measured at 400°C and at the end of the experiment.

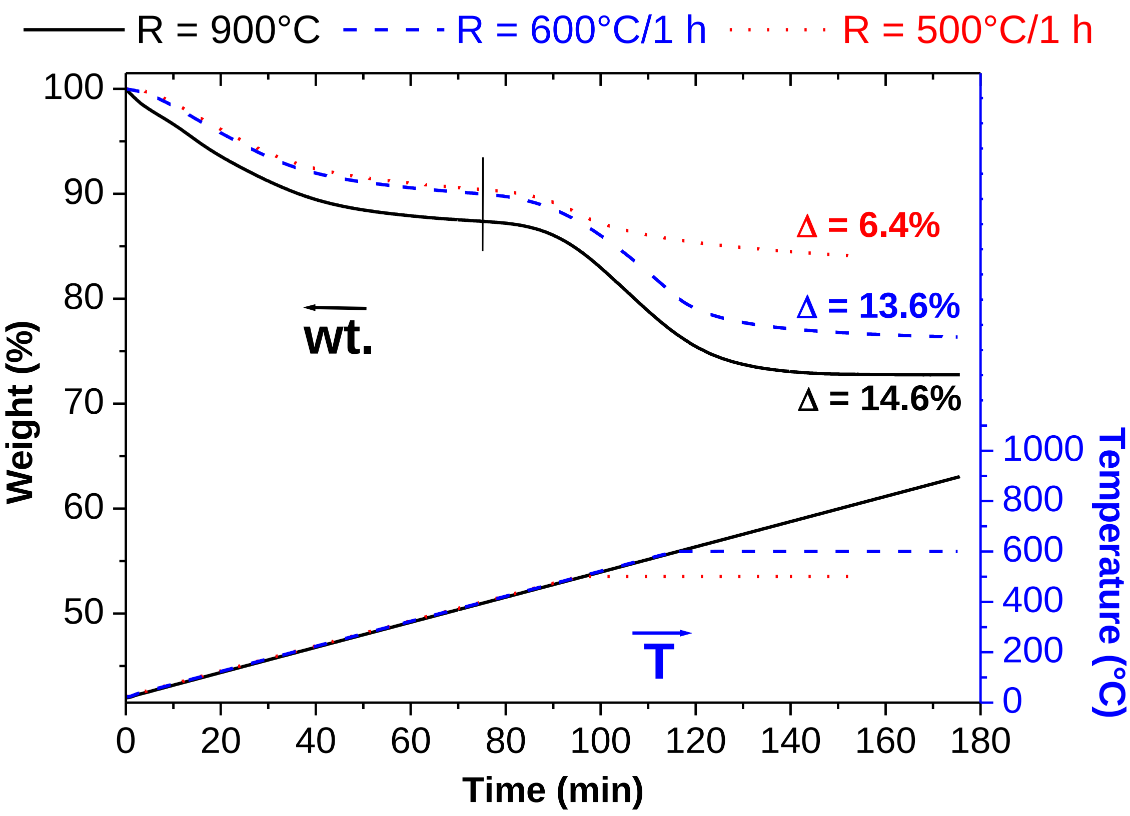

Figure 5.4. Weight losses related to the reduction of the Ni66 catalyst at different reduction procedures: 900°C (solid line), 600°C for 1 h (dashed line) and 500°C for 1 h (dotted line).

The analysis of the H_2-TPR profile for the Ni66 in Figure 5.3 could lead to misjudge regarding the total reduction of the Ni species for the different activation methods. Apparently, the reduction at 500°C or 600°C could be considered as completely inadequate for reducing the oxide phases revealed by the XRD patterns (Figure 5.2). However, the comparison of the weight losses associated to the different reduction procedures for the Ni66 catalyst in Figure 5.4 provides an estimative about the degree of reduction of each activation procedure. It can be seen that the degree of reduction for the activation conducted at 600°C for 1 h is higher than 90%, while the total reduction for the process at 500°C for 1 h is approximately 50%. Therefore, the reduction at 600°C is appropriate for the Ni66 catalyst. The other samples, Co66 and Fe66, showed reduction peaks ending at higher temperatures in Figure 5.3. The degree of reduction at the condition 600°C/1 h was approximately 70% for the Co66 catalyst and 50% for the Fe66 catalyst.

Figure 5.5 shows the curves regarding reduction at 600°C and reoxidation cycles for the three catalysts. Aside the removal of humidity that takes place at lower temperatures, it can be seen that the samples are oxidised at temperatures below 400°C, because the weight gain due to the reoxidation phenomenon is equivalent to the weight loss associated to the reduction of the oxides. Therefore, Figure 5.5 highlights that the phenomena takes place at different temperatures. The reoxidation of the reduced metal oxides finishes at significantly lower temperatures compared to the reduction of the oxides. The reoxidation for the Ni66, Co66 and Fe66 finishes respectively at 350°C, 340°C and 400°C.

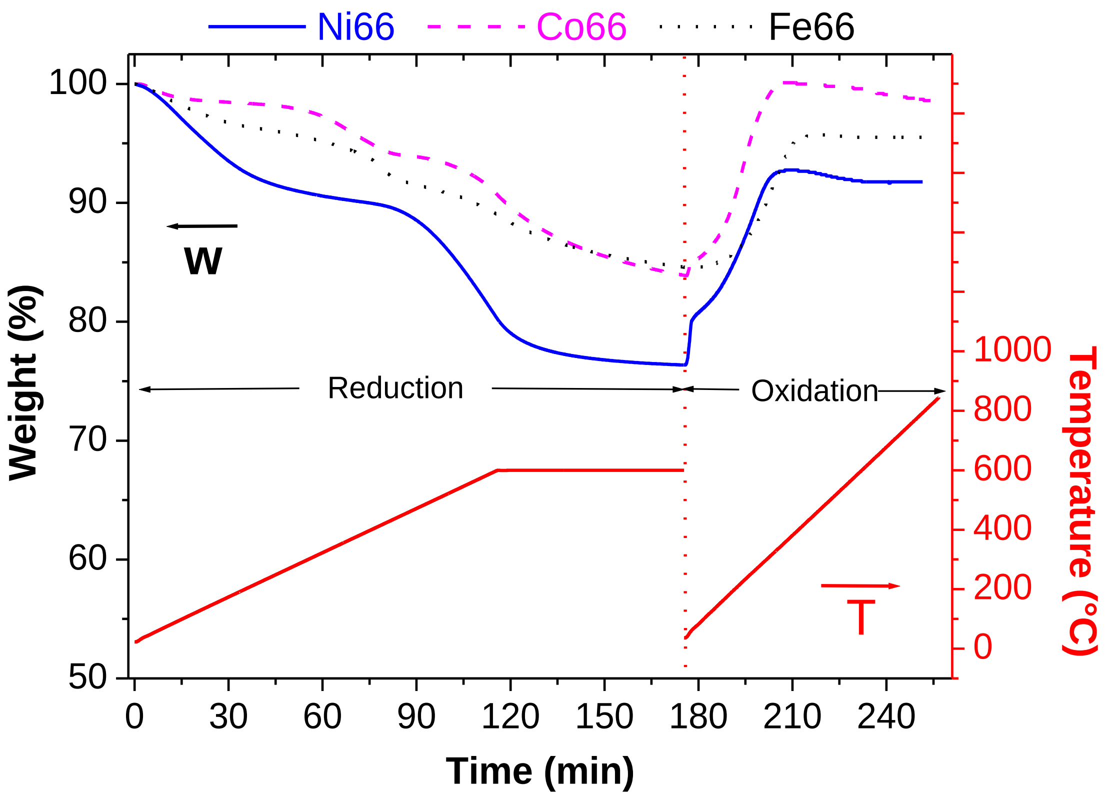

Figure 5.5. Reduction and oxidation curves for the Ni66 (solid line), Co66 (dashed line) and Fe66 (dotted line) catalysts.

5.3.2 Decomposition of ethanol

Table 5.2 summarises the conversion of ethanol and the distribution of products collected after 2 h of time on stream of the decomposition of ethanol runs.

Table 5.2. Ethanol decomposition results after 2 h of time on stream.

Sample	T_{REA} (°C)	X_{ET} (%)	S_{H2} (%)	Selectivity to C-containing products (%)					H_2/CO ratio
				CO	CH_4	CO_2	$C_2H_4 + C_2H_6$	CH_3CHO	
Ni66	500	100	61	34	30	32	4	0	2.5
	600	100	70	55	20	8	17	0	1.7
Fe66	500	43	35	20	1	11	37	31	2.3
	600	100	47	35	3	2	44	16	1.7
Co66	500	100	71	53	17	30	0	0	1.9
	600	100	83	75	20	5	0	0	1.8

Table 5.2 reveals higher selectivity towards hydrogen and carbon monoxide and lower formation of carbon dioxide with increasing reaction temperature. This feature is expected because the decomposition of ethanol to light gases (eq. 5.4) is favoured for higher temperatures. The further decomposition of methane provides hydrogen and carbon (eq. 5.5). The ethylene and acetaldehyde products are formed by this process through the dehydration (eq. 5.6) and dehydrogenation (eq. 5.7) of ethanol reactions, respectively. The carbon dioxide might be formed by the Boudouard (eq. 5.8) and the water-gas shift (eq. 5.9) reactions. The endothermic nature of these later reactions explains the decrease in the selectivity towards CO_2 with increasing the reaction temperature.

$$C_2H_5OH \rightarrow CH_4 + CO + H_2 \qquad \Delta H_{298K} = 49\ kJ\cdot mol^{-1} \qquad (5.4)$$

$$CH_4 \rightarrow C_{(S)} + 2H_2 \qquad \Delta H_{298K} = 75\ kJ\cdot mol^{-1} \qquad (5.5)$$

$C_2H_5OH \rightarrow C_2H_4 + H_2O$ ΔH_{298K}= 45 kJ·mol^{-1} (5.6)

$C_2H_5OH \rightarrow CH_3CHO + H_2$ ΔH_{298K} = 68 kJ·mol^{-1} (5.7)

$2CO \rightarrow CO_2 + C_{(S)}$ ΔH_{298K}= -172 kJ·mol^{-1} (5.8)

$H_2O + CO \rightarrow CO_2 + H_2$ ΔH_{298K}= -41 kJ·mol^{-1} (5.9)

It can be seen different distribution of products according to the catalyst used for the decomposition of ethanol. The Fe66 catalyst promotes the formation of ethylene and acetaldehyde (eq. 5.6 and 5.7) rather than the light gases. Furthermore, the conversion of ethanol is not complete for the decomposition o ethanol over the Fe66 catalyst at 500°C. Regarding the Co66 sample, higher selectivity towards H_2 and CO is observed for the reaction at both the reaction temperatures. Moreover, there was no formation of the C_2 products for the Co66 sample.

Regarding the H_2/CO ratio, Table 5.2 shows the synthesis gas with higher content of H_2 for the decomposition of ethanol at 500°C. This result is expected because the reactions that produce hydrogen (*e.g.*, eq. 5.5, 5.7 and 5.9) occur even at lower temperatures. On the other hand, most of the reactions that originates CO is favoured only at high temperatures. This compound can be formed through reactions such as the steam reforming of ethanol (eq. 5.10) and the steam (eq. 5.11) and the dry (eq. 5.12) reforming of methane. The Ni66 and Fe66 catalysts present higher variation in the H_2/CO ratio according to the reaction temperature, while the Co66 sample shows similar values for both the reaction temperatures. Furthermore, the H_2/CO ratio provided by this process is close to the optimal ratio for the FTS technology [32], especially those for the Co66 catalyst. Considering this feature, the decomposition of ethanol over the Co66 catalyst at 500°C provided the best results.

$C_2H_5OH + H_2O \rightarrow 2CO + 4H_2$ ΔH_{298K} = 256 kJ·mol^{-1} (5.10)

$CH_4 + H_2O \rightarrow 3H_2 + CO$ ΔH_{298K} = 209 kJ·mol^{-1} (5.11)

$CH_4 + CO_2 \rightarrow 2H_2 + 2CO$ ΔH_{298K} = 246 kJ·mol^{-1} (5.12)

5.3.3 Characterisation of the spent catalysts

Figure 5.6 exhibits the DTA curves related to the combustion of carbon deposited on the spent catalysts. The number expressed in brackets denotes the amount of carbon formed per mass of catalyst per hour ($g_C \cdot g_{cat}^{-1} \cdot h^{-1}$).

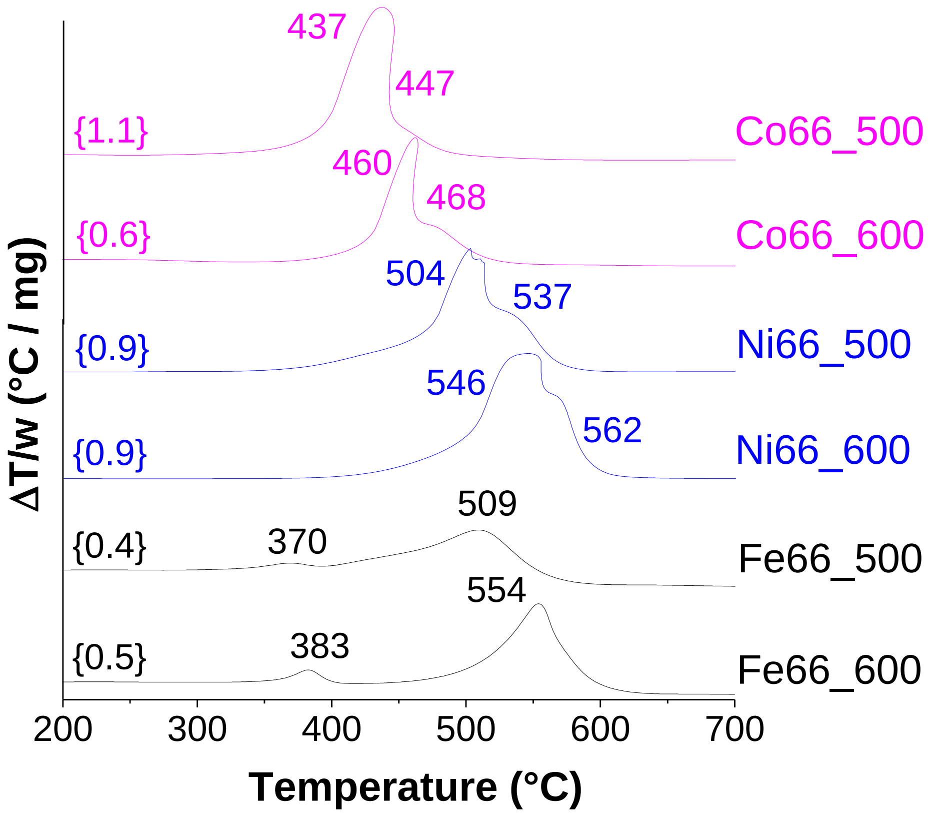

Figure 5.6. TPO-DTA curves for the spent catalysts.

The DTA curves associated to the combustion of carbon exhibit overlapped peaks at temperature in the range 350 – 650°C. The measurement of coke might not be significantly affected by the reoxidation of the metallic phase because the DTA peaks related to the combustion of carbon starts at temperatures in which the reoxidation phenomenon is ending (as shown in Figure 5.5).

The position of the peaks varies according to the active metal and the reaction temperature. The TPO-DTA data reveal higher formation of carbon on the Co66 catalyst after the decomposition of ethanol conducted at the lower temperature (500°C). The opposite trend is observed for the Fe66 catalyst regarding the reaction temperature. However, this catalyst exhibited much lower activity at 500°C compared to the other samples. The lower amount of coke on the catalysts is accompanied by its oxidation at higher temperatures for the reaction at 600°C.

Figure 5.6 indicates that the regeneration process might be conducted at milder conditions for the Co66 catalyst because the carbon is burned at significantly lower temperatures. The combustion is finished at similar temperatures for both the Ni66 and Fe66 samples, hence suggesting similar conditions for the regeneration step of these spent catalysts.

The overlapped DTA peaks suggest that different types of carbon are generated for each reaction temperature and active metal. The amorphous carbon is told to cover the active metal sites and conducts to deactivation. The filamentous carbon can grow without blocking completely the metal surface [29]. The amorphous carbon is known to be burned at approximately 400°C. The carbon nanotubes and carbon nanofibres are usually oxidised in the range 450 - 500°C and the graphitic carbon at temperatures above 500°C [17, 33, 34].

The small peaks or the shoulder at *ca.* 400°C for the Co66 and Fe66 spent samples at 500°C and the Fe66 after reaction at 600°C suggests that amorphous carbon might be formed on these samples. The overlapped peaks at temperatures higher than 400°C observed for all the samples suggest that filamentous and graphitic carbon structures are preferentially formed for the studied samples. This is an interesting result because it indicates that these samples exhibit increased resistance to deactivation by coking.

The SEM images in Figure 5.7 support the discussion above. The images show carbon filaments deposited on the spent Ni66 and Fe66 catalysts after reaction at 600°C. While the filaments displayed in Figure 5.7-a appear to cover the Ni66 catalyst surface, Figure 5.7-b shows lower amounts of these structures on the Fe66 catalyst. Although lower quantity of carbon is expected for Fe66 based on TPO-DTA analysis (Figure 5.6), the SEM image also points to the formation of amorphous carbon, as suggested by the DTA peak centred at 383°C. These data could explain the stable activity the studied catalysts (Table 5.2) because filamentous carbon are formed preferentially to amorphous carbon. The Fe66 catalyst showed a decrease in the conversion of ethanol that is possibly related to the amorphous carbon suggested by both the TPO/DTA (Figure 5.6) and SEM (Figure 5.7) experiments.

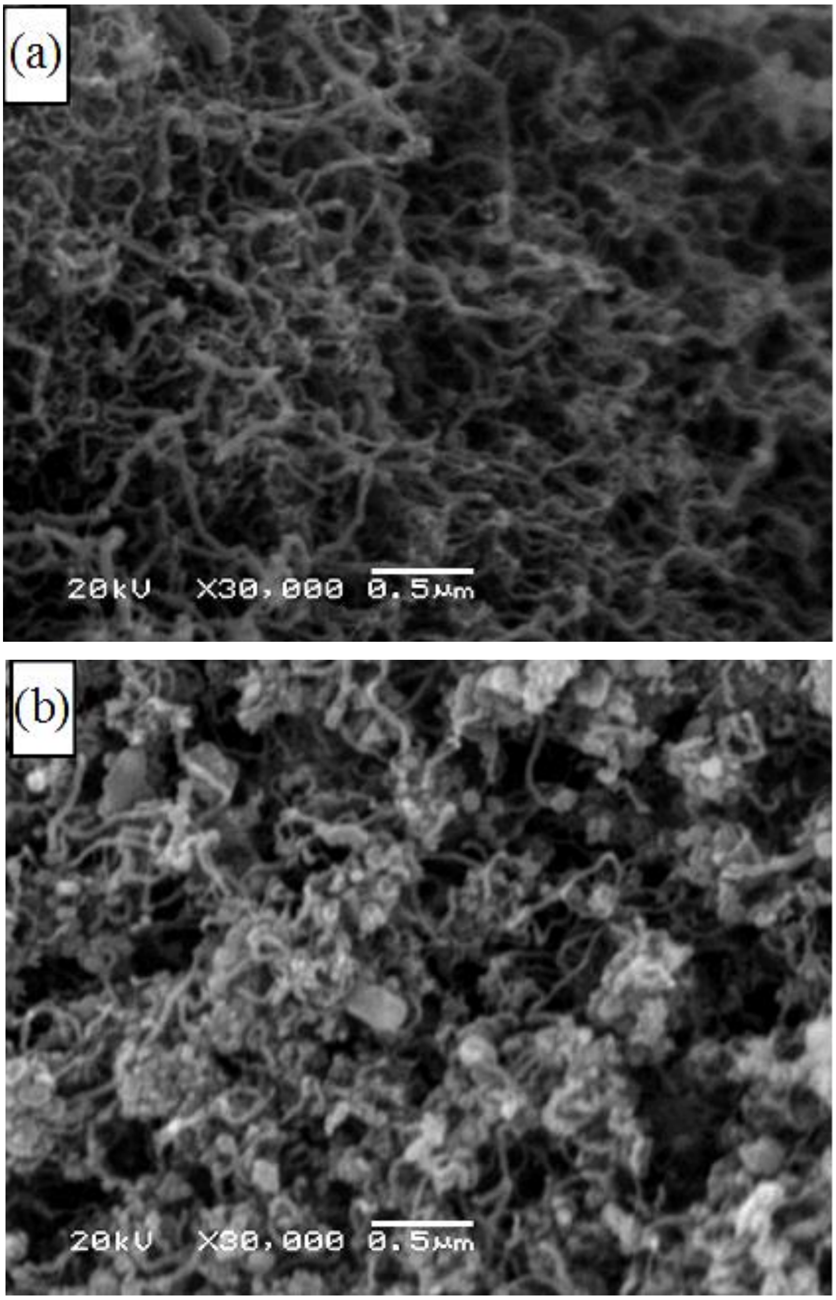

Figure 5.7. SEM images for the (a) Ni66 and (b) Fe66 spent catalysts after the decomposition of ethanol runs at 600°C.

The Raman spectra for the spent catalysts are displayed in Figure 5.8.

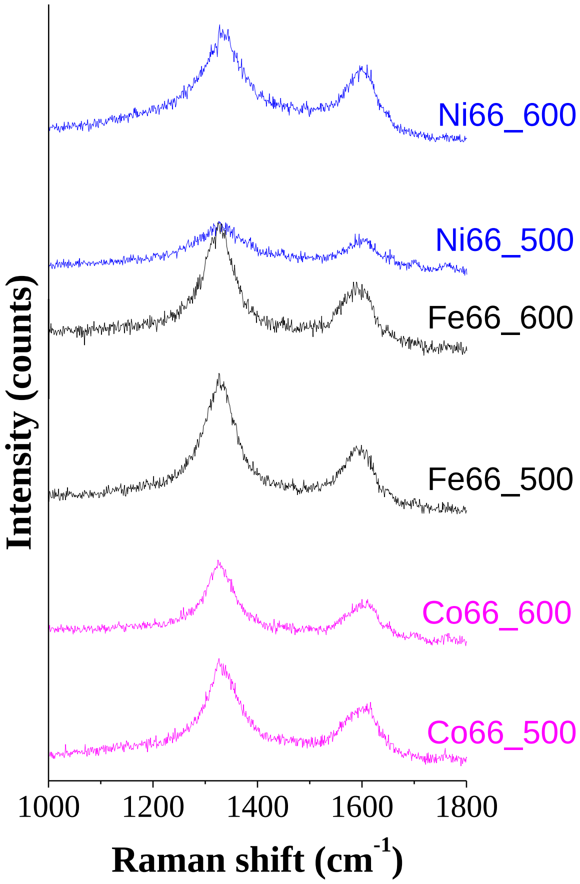

Figure 5.8. Raman spectra of the spent catalysts.

The Raman spectra in Figure 5.8 exhibit two major peaks for all catalysts. The first peak (known as D band) is located at 1325-1335 cm^{-1} and provides information regarding defects and impurities in the carbon forms [35]. The G band is located at 1590-1615 cm^{-1} and indicates ordered structures. The ratio between the intensity of the peaks of the D band and G band (I_D/I_G ratio) indicates the perfection of the structure and purity of the carbon filaments, whereas lower I_D/I_G ratio values are associated with higher crystallinity and fewer defects on their walls [36, 37]. The I_D/I_G ratio values increased in the following order: Ni66_500 (1.3) < Ni66_600 (1.5) < Co66_500 (1.7) < Co66_600 (1.8) ≤ Fe66_600 (1.8) < Fe66_500 (2.0). The high I_D/I_G ratio values observed suggest that multi-walled carbon nanotubes (MWCNT) and or carbon nanofibers are formed rather than single-walled carbon nanotubes (SWCNT). Moreover, the I_D/I_G results indicate that the CNT and CNF formed over Ni66 catalyst present lower defects and impurities, while the carbon filaments synthesized over Fe66 samples are expected to present lower purity and higher defects. Additionally, as reported elsewhere [4], ethanol decomposition carried out at lower temperatures lead to lower I_D/I_G ratios and hence the formation of nanotubes and or nanofibers with higher purities and lower defects for Ni66 and Co66 catalysts. On the contrary, the Fe66 catalyst shows higher I_D/I_G ratio for ethanol decomposition at 600°C. The same behaviour for MWCNT formed from decomposition of ethanol over Fe/Al_2O_3 catalysts was reported by Li et al. (2008), although it was not explained by the authors [3]. In the case of the Fe66 catalyst, it could be related to the interaction of carbon with the ethylene and acetaldehyde compounds produced by this sample (Table 5.2).

5.4 Discussion

The characterisation of uncalcined samples revealed that different structures are formed for the samples prepared. The Ni- and Co-precursors revealed XRD reflections that point to the formation of hydrotalcite-type materials (Figure 5.2). These compounds are expected from the M^{II}/M^{III} molar ratio adopted for these samples [8, 9]. The thermal decomposition behaviour of these precursors (Figure 5.1) also confirms the formation of the referred structures, which are known to collapse and yield the mixed oxides at temperatures below 400°C [38].

The formation of the mixed oxides could be verified by both the XRD patterns and H_2-TPR (Figure 5.3) analyses of the calcined Ni66 and Co66 catalysts. Indeed, the $NiAl_2O_4$ and $CoAl_2O_4$ phases were identified by XRD. The formation of these phases could be verified by H_2-TPR because most of the hydrogen uptake occurs at temperatures higher than those required for the reduction of the pure metal oxides (*ca.* 400°C) [24-28]. Specially, the Ni66 sample exhibited only the reduction peak at higher temperatures, revealing the absence of the NiO phase. The solely formation of the mixed oxide phase for the Ni66 sample is in agreement with the smaller crystallite sizes and the increased thermal stability revealed by the X-ray pattern for the calcined Ni66 sample (Figure 5.2) and by the TG/DTA curves (Figure 5.1). The mixed oxides derived from the hydrotalcite-type materials are known to present crystallites with small diameters that would prevent the aggregation and crystal growth phenomenon. This would lead to an enhancement in the thermal stability [8, 10].

On the contrary, the hydrotalcite-type compound was not identified in Figure 5.2 for the uncalcined Fe66 material, whose thermal decomposition profile was different from the observed for the Co66 and Ni66 samples (Figure 5.1). The XRD patterns (Figure 5.2) and the reduction profile (Figure 5.3) for the calcined Fe66 catalyst corroborated this hypothesis because this sample exhibited only the segregated Fe_2O_3 phase.

Aside the differences of the metals in terms of activity, the catalysts that formed mixed oxides (i.e., Ni66 and Co66) exhibited better performance for the formation of synthesis gas and stable conversion of ethanol. On the other hand, the Fe66 catalyst showed higher selectivity towards compounds with higher chain length (ethylene and acetaldehyde). Moreover, the Fe66 sample exhibited a decrease in the conversion of ethanol at 500°C. This can be related to the aforementioned lower thermal stability and higher crystallite diameters expected for the Fe66 catalyst. This result can also be related to the amorphous carbon that was suggested by TPO/DTA for this sample (see peaks at 370-383°C in Figure 5.6). This type of carbon is known to encapsulate the active metal sites and leads to deactivation [29]. However, the TPO/DTA and the SEM images (Figure 5.7) shows that filamentous and graphitic carbon is the predominant type of carbon deposited on the spent samples, thus the complete conversion of ethanol during all the reaction for almost all the tests.

5.5 Conclusions

In this work, Ni-, Co- and Fe-Al co-precipitated samples were synthesised and characterised by several techniques. The thermal decomposition of the precursors showed that the structure collapses at temperatures below 400°C. The XRD patterns indicate the formation of hydrotalcite-type structures and metal aluminates for the Ni- and Co-precursors and calcined samples, respectively. The H_2-TPR curves are in agreement to the XRD data because it exhibits barely reducible metal oxide species that are predominant for the Ni- and Co-samples. For the decomposition of ethanol reaction, higher temperatures favoured the generation of synthesis gas and minimised the formation of CO_2, the H_2/CO ratio and coke. The Co-catalyst showed the highest selectivity towards H_2 and CO and better H_2/CO molar ratio for the use in Fischer-Tropsch Synthesis. The Fe-catalyst produced mainly ethylene and acetaldehyde rather than the light gases. According to the characterisation of the spent catalysts, filamentous and graphitic carbon are formed rather that amorphous carbon.

ACKNOWLEDGEMENTS

The authors wish to thank the financial support and scholarships granted by the “Conselho Nacional de Desenvolvimento Científico e Tecnológico – CNPq” and by the “Coordenação de Aperfeiçoamento de Pessoal de Nível Superior – CAPES”. The authors are grateful for the Raman analyses performed by N.M. Balzaretti (UFRGS).

References

[1] G.W. Huber, J.N. Chheda, C.J. Barrett, J.A. Dumesic. Production of liquid alkanes by aqueous-phase processing of biomass-derived carbohydrates. Science 308 (2005) 1446-50.

[2] J.R. Rostrup-Nielsen. Making fuels from biomass. Science 308 (2005) 1421-2.

[3] W. Li, H. Wang, Z. Ren, G. Wang, J. Bai. Co-production of hydrogen and multi-wall carbon nanotubes from ethanol decomposition over Fe/Al_2O_3 catalysts. Applied Catalysis B-Environmental 84 (2008) 433-9.

[4] D.Z. Mezalira, L.D. Probst, S. Pronier, Y. Batonneau, C. Batiot-Dupeyrat. Decomposition of ethanol over Ni/Al_2O_3 catalysts to produce hydrogen and carbon nanostructured materials. Journal of Molecular Catalysis a-Chemical 340 (2011) 15-23.

[5] G. Wang, H. Wang, W. Li, Z. Ren, J. Bai, J. Bai. Efficient production of hydrogen and multi-walled carbon nanotubes from ethanol over Fe/Al_2O_3 catalysts. Fuel Processing Technology 92 (2011) 531-40.

[6] R. Chen, Y. Xie, Y. Zhou, J. Wang, H. Wang. Production of hydrogen-rich gas and multi-walled carbon nanotubes from ethanol decomposition over molybdenum modified Ni/MgO catalysts. Journal of Energy Chemistry 23 (2014) 244-50.

[7] G. Wang, J. Wang, H. Wang, J. Bai. Preparation and evaluation of molybdenum modified Fe/MgO catalysts for the production of single-walled carbon nanotubes and hydrogen-rich gas by ethanol decomposition. Journal of Environmental Chemical Engineering.

[8] A. Vaccari. Clays and catalysis: a promising future. Applied Clay Science 14 (1999) 161-98.

[9] F. Trifiró, A. Vaccari. Hydrotalcite-like anionic clays (layer double hydroxides). Comprehensive Supramolecular Chemistry. Oxford: Pergamon; 1996, p. 251, vol. 7.

[10] A. Bhattacharyya, V.W. Chang, D.J. Schumacher. CO_2 reforming of methane to syngas: I: evaluation of hydrotalcite clay-derived catalysts. Applied Clay Science 13 (1998) 317-28.

[11] G. de Souza, V.C. Ávila, N.R. Marcílio, O.W. Perez-Lopez. Synthesis Gas Production by Steam Reforming of Ethanol over M-Ni-Al Hydrotalcite-type Catalysts; M = Mg, Zn, Mo, Co. Procedia Engineering 42 (2012) 1805-15.

[12] N.M. Balzaretti, M.R. Gallas, T.M.H. Costa, V. Stefani, C.A. Perottoni, J.A.H. da Jornada. Raman investigation of 2,5-bis(benzoxazol-2 '-yl)4-methoxyphenol under high pressure. Journal of Raman Spectroscopy 34 (2003) 244-7.

[13] F. Kovanda, T. Rojka, P. Bezdicka, K. Jiratova, L. Obalova, K. Pacultova, et al. Effect of hydrothermal treatment on properties of Ni-Al layered double hydroxides and related mixed oxides. Journal of Solid State Chemistry 182 (2009) 27-36.

[14] J.I. Di Cosimo, V.K. Díez, M. Xu, E. Iglesia, C.R. Apesteguía. Structure and Surface and Catalytic Properties of Mg-Al Basic Oxides. Journal of Catalysis 178 (1998) 499-510.

[15] R.L. Frost, A.W. Musumeci, T. Bostrom, M.O. Adebajo, M.L. Weier, W. Martens. Thermal decomposition of hydrotalcite with chromate, molybdate or sulphate in the interlayer. Thermochimica Acta 429 (2005) 179-87.

[16] E.L. Crepaldi, P.C. Pavan, J.B. Valim. Comparative study of the coprecipitation methods for the preparation of Layered Double Hydroxides. Journal of the Brazilian Chemical Society 11 (2000) 64-70.

[17] N.A. Hermes, M.A. Lansarin, O.W. Perez-Lopez. Catalytic Decomposition of Methane Over M-Co-Al Catalysts (M = Mg, Ni, Zn, Cu). Catalysis Letters 141 (2011) 1018-25.

[18] S.J. Palmer, H.J. Spratt, R.L. Frost. Thermal decomposition of hydrotalcites with variable cationic ratios. Journal of Thermal Analysis and Calorimetry 95 (2009) 123-9.

[19] M.J. Holgado, V. Rives, M.S. San Roman. Characterization of Ni-Mg-Al mixed oxides and their catalytic activity in oxidative dehydrogenation of n-butane and propene. Applied Catalysis A-General 214 (2001) 219-28.

[20] L.H. Zhang, X. Xiang, L. Zhang, F. Li, J. Zhu, D.G. Evans, et al. Influence of iron substitution on formation and structure of Cu-based mixed oxides derived from layered double hydroxides. Journal of Physics and Chemistry of Solids 69 (2008) 1098-101.

[21] A. Vaccari. Preparation and catalytic properties of cationic and anionic clays. Catalysis Today 41 (1998) 53-71.

[22] L. Zhang, J.-M.M. Millet, U.S. Ozkan. Effect of Cu loading on the catalytic performance of Fe-Al-Cu for water-gas shift reaction. Applied Catalysis A-General 357 (2009) 66-72.

[23] R. Allmann, H.P. Jepsen. Die struktur des hydrotalkits. Neues Jahrbuch für Mineralogie, Monatshefte (1969).

[24] J.A. Montoya, E. Romero-Pascual, C. Gimon, P. Del Angel, A. Monzon. Methane reforming with CO_2 over Ni/ZrO_2-CeO_2 catalysts prepared by sol-gel. Catalysis Today 63 (2000) 71-85.

[25] J.J. Guo, H. Lou, H. Zhao, D.F. Chai, X.M. Zheng. Dry reforming of methane over nickel catalysts supported on magnesium aluminate spinels. Applied Catalysis A-General 273 (2004) 75-82.

[26] A.A. Khassin, T.M. Yurieva, G.N. Kustova, I.S. Itenberg, M.P. Demeshkina, T.A. Krieger, et al. Cobalt-aluminum co-precipitated catalysts and their performance in the Fischer-Tropsch synthesis. Journal of Molecular Catalysis A-Chemical 168 (2001).

[27] S. Ribet, D. Tichit, B. Coq, B. Ducourant, F. Morato. Synthesis and activation of Co-Mg-Al layered double hydroxides. Journal of Solid State Chemistry 142 (1999).

[28] M. Gabrovska, R. Edreva-Kardjieva, K. Tenchev, P. Tzvetkov, A. Spojakina, L. Petrov. Effect of Co-content on the structure and activity of Co–Al hydrotalcite-like materials as catalyst precursors for CO oxidation. Applied Catalysis A: General 399 (2011) 242-51.

[29] J.L. Ewbank, L. Kovarik, C.C. Kenvin, C. Sievers. Effect of preparation methods on the performance of Co/Al_2O_3 catalysts for dry reforming of methane. Green Chemistry 16 (2014) 885-96.

[30] F. Cavani, F. Trifiro, A. Vaccari. HYDROTALCITE-TYPE ANIONIC CLAYS: PREPARATION, PROPERTIES AND APPLICATIONS. Catalysis Today 11 (1991) 173-301.

[31] O.W. Perez-Lopez, A. Senger, N.R. Marcilio, M.A. Lansarin. Effect of composition and thermal pretreatment on properties of Ni-Mg-Al catalysts for CO_2 reforming of methane. Applied Catalysis A-General 303 (2006) 234-44.

[32] M.E. Dry. The Fischer-Tropsch process: 1950-2000. Catalysis Today 71 (2002) 227-41.

[33] F.F. de Sousa, H.S.A. de Sousa, A.C. Oliveira, M.C.C. Junior, A.P. Ayala, E.B. Barros, et al. Nanostructured Ni-containing spinel oxides for the dry reforming of methane: Effect of the presence of cobalt and nickel on the deactivation behaviour of catalysts. International Journal of Hydrogen Energy 37 (2012) 3201-12.

[34] C. Escobar, O. Perez-Lopez. Hydrogen Production by Methane Decomposition Over Cu–Co–Al Mixed Oxides Activated Under Reaction Conditions. Catalysis Letters 144 (2014) 796-804.

[35] W.Z. Li, H. Zhang, C.Y. Wang, Y. Zhang, L.W. Xu, K. Zhu, et al. Raman characterization of aligned carbon nanotubes produced by thermal decomposition of hydrocarbon vapor. Applied Physics Letters 70 (1997) 2684-6.

[36] K. Nakamura, M. Fujitsuka, M. Kitajima. DISORDER-INDUCED LINE BROADENING IN 1ST-ORDER RAMAN-SCATTERING FROM GRAPHITE. Physical Review B 41 (1990) 12260-3.

[37] G. Wang, H. Wang, Z. Tang, W. Li, J. Bai. Simultaneous production of hydrogen and multi-walled carbon nanotubes by ethanol decomposition over Ni/Al_2O_3 catalysts. Applied Catalysis B: Environmental 88 (2009) 142-51.

[38] E. Lopez-Salinas, M. Garcia-Sanchez, M. Luisa Ramon-Garcia, I. Schifter. New Gallium-Substituted Hydrotalcites: $Mg_{1-x}Ga_x(OH)_2\ (CO_3)_{x/2}\cdot mH_2O$. Journal of Porous Materials 3 (1996) 169-74.

Capítulo 6

Synthesis gas production by steam reforming of ethanol over M-Ni-Al hydrotalcite-type catalysts; M = Mg, Zn, Mo, Co

Artigo publicado no periódico: *Procedia Engineering*, em agosto de 2012.

Synthesis gas production by steam reforming of ethanol over M-Ni-Al hydrotalcite-type catalysts; M = Mg, Zn, Mo, Co

Guilherme de Souza[a], Vinícius C. Ávila[a], Nilson R. Marcílio[a], Oscar W. Perez-Lopez[a]

[a] *Department of Chemical Engineering, Federal University of Rio Grande do Sul,*
Eng. Luiz Englert St. s/n, 90040-040 Porto Alegre, RS, Brazil

* Corresponding author: Tel.: +55(51)3308.3953; fax: +55(51)3308.3277. E-mail address: perez@enq.ufrgs.br.

Abstract

This paper presents the investigation of nickel-based hydrotalcite-type materials for the steam reforming of ethanol for synthesis gas production. The partial substitution of Ni by a third element leads to changes in terms of surface area, crystallinity, acidic sites and reduction profile. Lower reaction temperatures favored the dehydration and dehydrogenation of ethanol, while synthesis gas was produced mainly at higher temperatures. Samples modified with Co, Mo and Zn exhibited higher activity at intermediate temperatures, while Co-, Mo- and unmodified samples presented higher selectivity towards H_2 and CO at higher temperatures.

Keywords: Steam reforming of ethanol; synthesis gas; Ni-based catalysts; hydrotalcite-type materials.

6.1. Introduction

The depletion of crude petroleum reserves has led to the investigation of alternative fuels and energy sources. Among these alternative sources, bio-ethanol derived from biomass feedstocks presents some advantages such as high hydrogen content, good availability, low production cost, non-toxicity and easy handling, transportation and storage [1, 2]. In this context, the steam reforming of ethanol process is a promising route because H_2 and synthesis gas can be obtained from a renewable resource. Despite having outstanding potential, the use of H_2 in fuel cells still requires advancement in R&D before large scale application of this technology is possible. Moreover, a future hydrogen society would require an expensive new infrastructure [3, 4], whereas modern diesel engines are almost as efficient as fuel cell-driven cars that use hydrogen fuel appear to be [5]. On the other hand, ethanol reforming could also produce synthesis gas instead of H_2 generation. Technologies for synthesis gas conversion for ammonia and methanol production are very well established. Furthermore, synthesis gas can produce gasoline, diesel, lubricants and other oxygenates through the very well-known Fischer-Tropsch process.

The desired reactions in ethanol steam reforming result in synthesis gas (eq. *6.1*) or H_2 and CO_2 (eq. *6.2*), depending on the amount of water in the feed stream.

$$C_2H_5OH + H_2O \rightarrow 2CO + 4H_2 \qquad \Delta H_{298K} = 256\ kJ\cdot mol^{-1} \tag{6.1}$$

$$C_2H_5OH + 3H_2O \rightarrow 2CO_2 + 6H_2 \qquad \Delta H_{298K} = 174\ kJ\cdot mol^{-1} \tag{6.2}$$

However, there are other possible reactions that can occur, which may include the dehydration (eq. *6.3*) and the dehydrogenation (eq. *6.4*) of ethanol, as well as the further decomposition of acetaldehyde (eq. *6.5*).

$$C_2H_5OH \rightarrow C_2H_4 + H_2O \qquad \Delta H_{298K} = 45\ kJ\cdot mol^{-1} \tag{6.3}$$

$$C_2H_5OH \rightarrow CH_3CHO + H_2 \qquad \Delta H_{298K} = 68\ kJ\cdot mol^{-1} \tag{6.4}$$

$CH_3CHO \rightarrow CH_4 + CO \qquad \Delta H_{298K} = -19\ kJ \cdot mol^{-1}$ (6.5)

Synthesis gas can also be obtained from the steam reforming (eq. *6.6*) and dry reforming (eq. *6.7*) of methane, while hydrogen can be produced by the decomposition of methane (eq. *6.8*) and the water-gas shift (eq. *6.9*) reactions.

$CH_4 + H_2O \rightarrow CO + 3H_2 \qquad \Delta H_{298K} = 206\ kJ \cdot mol^{-1}$ (6.6)

$CH_4 + CO_2 \rightarrow 2CO + 2H_2 \qquad \Delta H_{298K} = 246\ kJ \cdot mol^{-1}$ (6.7)

$CH_4 \rightarrow C_{(s)} + 2H_2 \qquad \Delta H_{298K} = 75\ kJ \cdot mol^{-1}$ (6.8)

$H_2O + CO \rightarrow CO_2 + H_2 \qquad \Delta H_{298K} = -41\ kJ \cdot mol^{-1}$ (6.9)

As eq. *6.8* indicates, carbonaceous materials (coke) are formed during this process. In addition to being formed through the decomposition of methane, coke is also produced from the Boudouard reaction (eq. *6.10*) and polymerization of ethylene (eq. *6.11*). However, coke can be gasified at high temperatures through the reverse of the Boudouard reaction expressed in eq. *6.10* and by steam reforming (eq. *6.12*).

$2CO \rightarrow CO_2 + C_{(s)} \qquad \Delta H_{298K} = -172\ kJ \cdot mol^{-1}$ (6.10)

$n.C_2H_4 \rightarrow polymer \rightarrow coke$ (6.11)

$C_{(s)} + H_2O \rightarrow CO + H_2 \qquad \Delta H_{298K} = 131\ kJ \cdot mol^{-1}$ (6.12)

Although investigations using catalysts based on Ir [6], Rh [7], Pd [8] and Co [9, 10] for the steam reforming of ethanol have been carried out, the high cost of these metals would limit their application at the industrial scale. Therefore, Ni-based catalysts have been widely investigated for this process [11, 12]. Among the nickel catalysts, promising results were found for hydrotalcite-type (HT) materials [13-15]. Although they have interesting properties such as a high surface area and high thermal stability [16, 17], further investigations of these materials for steam reforming of ethanol are still scarce.

In the context of the above discussion, the present work aims to better understand the relation between reaction temperature and product distribution, as well as to improve the performance of nickel-based HT materials for the steam reforming of ethanol by the partial substitution of Ni by a third element such as Mg, Zn, Mo or Co.

6.2. Experimental

6.2.1 Preparation of samples

The samples employed in this work were prepared with the continuous co-precipitation method using two aqueous solutions. The first solution contained an aqueous mixture of aluminium nitrate and nickel nitrate, and Zn nitrate, Mg nitrate, Co nitrate or ammonium molybdate were added for some samples. An aqueous solution of Na_2CO_3 was used as the precipitating agent. The co-precipitation process was conducted in a CSTR at a constant temperature (50°C). The solution containing the nitrates was added at a constant flow rate, while the flow rate of the precipitant was continuously adjusted to maintain the pH at a constant value (8 ± 0.1).

After the co-precipitation process, the effluent was collected and stirred at 50°C for 1 h. After this crystallisation step, the precipitate was filtered and washed thoroughly with distilled and deionised water. The slurry was dried at 80°C for 24 h in an oven. All samples were crushed and sieved to the desired particle sizes (500–355 µm) and calcined under an air flow (50 $mL\cdot min^{-1}$) at 600°C for 6 h.

6.2.2 Characterisation

The materials were characterised by BET surface area measurements, thermogravimetric coupled with differential thermal analyses (TG/DTA), temperature-programmed reduction (H_2-TPR), temperature-programmed desorption of ammonia (NH_3-TPD), temperature-programmed oxidation (TPO/DTA) and X-ray diffraction (XRD) patterns.

The NH_3-TPD profiles were collected using a multipurpose system (SAMP3). A quartz tube was loaded with 100 mg of the calcined sample and placed in a temperature-controlled oven. The sample was first outgassed at 250°C under N_2 flow over 1 h, then cooled to 100°C and saturated with NH_3. After adsorption, the sample was purged with a flow of pure helium for 30 min to remove weakly adsorbed species. The desorption curves were recorded with a thermal conductivity detector (TCD) by increasing the temperature to 600°C at a heating rate of $10°C\cdot min^{-1}$ with a $30\ mL\cdot min^{-1}$ helium flow.

The H_2-TPR analysis was carried out in the same multipurpose system (SAMP3). After pretreatment at 250°C, the temperature was increased to 880°C ($10°C\cdot min^{-1}$) using $30\ mL\cdot min^{-1}$ of a 10% H_2/N_2 (v/v) reduction mixture.

In the same apparatus, the BET surface area measurements (S_{BET}) were obtained by the N_2 dynamic adsorption method at the normal boiling point of N_2 (-196°C). As in the TPD and TPR experiments, the samples were preheated from room temperature to 250°C for 1 h before the BET measurements.

Thermogravimetric (TG/DTA) and temperature-programmed oxidation (TPO/DTA) coupled with differential thermal analysis were performed in a TA thermobalance (Model SDT600). In these experiments, approximately 10 mg of fresh sample (TG/DTA) or the sample after reaction (TPO/DTA) was first purged with N_2 at room temperature. The samples were then heated to approximately 850°C at a rate of $10°C\cdot min^{-1}$ under an air flow rate of $100\ mL\cdot min^{-1}$.

The powder X-ray diffraction (XRD) patterns were collected with a Bruker D2 Phaser X-ray diffractometer using CuKα radiation.

6.2.3 Activity evaluation

The catalytic evaluations were performed in a 6-mm inner diameter fixed-bed quartz reactor loaded with 100 mg of catalyst and using quartz wool as support for the catalytic bed. The samples were heated in a programmable electric oven, and the temperature was measured by a K-type thermocouple set in the middle of the bed. The samples were reduced in situ with a 100 mL·min^{-1} H_2 flow at 400°C for 2 h prior to the reactions. The runs were carried out under atmospheric pressure, at temperatures between 400 and 600°C. The flow rate of N_2 (100 mL·min^{-1}) was adjusted through a mass flow controller (Cole Parmer), and the ethanol-water mixture (1:1 molar ratio) was fed by a syringe-type micro-pump (KD Scientific) at a flow rate of 0.5 mL·h^{-1}. The gas hourly space velocity (GHSV) was approximately 30,000 mL·g^{-1}·h^{-1}.

The products were analysed using an on-line Varian 3600CX gas chromatograph equipped with a flame ionisation detector (FID) and a thermal conductivity detector (TCD). The ethanol conversion and the water consumption were defined as

$$X_{react}(\%) = \frac{[\mathrm{Re}\,act]_{IN} - [\mathrm{Re}\,act]_{OUT}}{[\mathrm{Re}\,act]_{IN}} x100 \qquad (6.13)$$

Additionally, the selectivity for hydrogen and towards C-containing products was evaluated as follows:

$$S_{H2} = \frac{[H_2]}{\sum \nu_j . [H_{2j}]} \tag{6.14}$$

$$S_{Ci} = \frac{\nu_i . [C_i]}{\sum \nu_j . [C_j]} \tag{6.15}$$

6.3 Results and discussion

Table 6.1 shows the nomenclature, the nominal composition and the BET specific surface area results for the samples. The surface area of 143 $m^2 \cdot g^{-1}$ found for NA is ascribed to the mixed oxides resulting from the decomposition of hydrotalcites [18] and is close to those reported for similar Ni-Al materials, although the temperature used for thermal treatment is not the same as in other cases [15, 19]. In addition, the substitution of 11.1 mol% of Ni by a third metal results in a small influence in the surface area, except for MoNA (with a surface area as large as 168 $m^2 \cdot g^{-1}$), which indicates the formation of smaller crystallites associated with the presence of MoO_x in the structure.

Table 6.1. Sample nominal composition and BET surface area.

Sample	Composition (atomic ratio)						S_{BET}
	Mg	Zn	Mo	Co	Ni	Al	(m^2/g)
NA	0.0	0.0	0.0	0.0	66.7	33.3	143
MgNA	11.1	0.0	0.0	0.0	55.6	33.3	140
ZnNA	0.0	11.1	0.0	0.0	55.6	33.3	141
MoNA	0.0	0.0	11.1	0.0	55.6	33.3	168
CoNA	0.0	0.0	0.0	11.1	55.6	33.3	138

The thermal decomposition characteristics of uncalcined samples obtained by thermal analysis (TGA/DTA) are summarised in Table 6.2. The partial substitution of

Ni by another metal results in materials that exhibit a higher total weight loss, which ranges from 32.9% (for NA) to 44.6% (for MoNA). The endothermic peaks are related to the loss of interlayer water and the subsequent removal of OH^- and the decomposition of interlayer anions in the structures, leading to the formation of the mixed oxide structure. These peaks are commonly observed for hydrotalcite-type materials [16, 17, 19]. Nevertheless, MoNA exhibits a peak located at higher temperatures (415°C), probably related to NH_4^+ ions from the precursor materials, which decompose at higher temperatures.

Table 6.2. Weight loss and DTA data obtained from TG analysis.

Sample	Total weight loss (%)	DTA peak temperature (°C)		
		1st peak (endo)	2nd peak (endo)	3rd peak (endo)
NA	32.9	201	352	-
MgNA	35.5	217	307	355
ZnNA	33.3	168	344	-
MoNA	44.6	173	343	415
CoNA	42.3	177	342	-

Fig. 6.1 shows the X-ray diffraction patterns of the calcined samples. The XRD patterns show a poor crystalline structure, which is in agreement with BET results (Tab. 6.1). Although it is difficult to identify the crystalline phases due to the low intensity of peaks, the diffraction reflections exhibited by NA at $2\theta = 37.0$, 45.0 and 65.6° can be attributed to $NiAl_2O_4$, while the diffraction peaks at 37.4, 43.4 and 63.1° can be ascribed to NiO. Both phases were also reported elsewhere for coprecipitated Ni-Al materials [20]. While MgNA displays a similar XRD pattern, it can be observed in Fig. 6.1 that the partial replacement of Ni by Zn, Mo or Co results in a decrease in the crystallinity, which could indicate the formation of smaller crystallites.

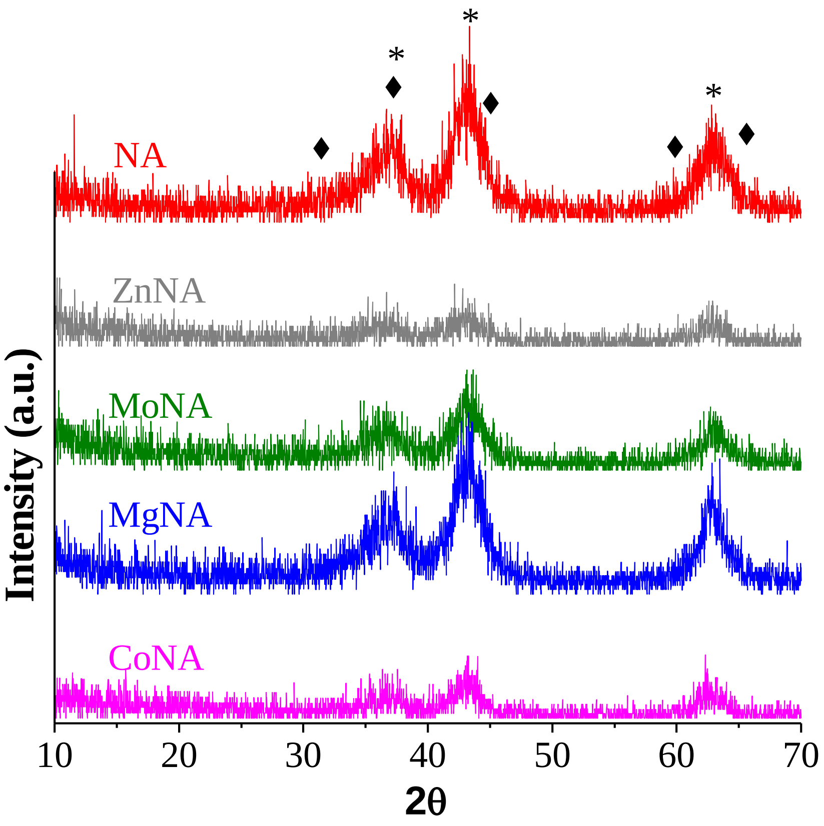

Figure 6.1. . X-ray diffraction (XRD) patterns of the calcined materials: (*) NiO; (♦) $NiAl_2O_4$.

The H_2-TPR profiles displayed in Fig. 6.2-a reveal the presence of broad reduction peaks at temperatures between 600 and 800°C for all samples. The peaks exhibit a “shoulder” that begins at approximately 450°C for ZnNA, MoNA and CoNA. It should be noted that the reduction peak is centred at higher temperatures for the NA and MgNA samples (726-764°C), while the maxima for ZnNA, MoNA and CoNA are located between 680 and 720°C. For the NA sample, the peak is centred at 726°C and can be assigned to the reduction of Ni in $NiAl_2O_4$ because the reduction temperature for pure NiO takes place at temperatures between 360-400°C [21, 22]. Therefore, despite having been identified as NiO by XRD (Fig. 6.1), the TPR profile suggests the absence of a segregated NiO phase. Furthermore, the “shoulder” indicates that the reduction of NiO occurs with a strong interaction of the support.

These TPR results are in agreement with reports by other authors for coprecipitated Ni-Al materials [14, 20]. The reduction peak is shifted towards higher temperatures for MgNA, which indicates the formation of a more stable phase in spite of the stronger interaction of NiO with magnesium, as reported by Daza et al. [23]. The significantly lower temperatures for the reduction peaks displayed by ZnNA and MoNA are probably related to the synergetic effect between Zn or Mo and Ni.

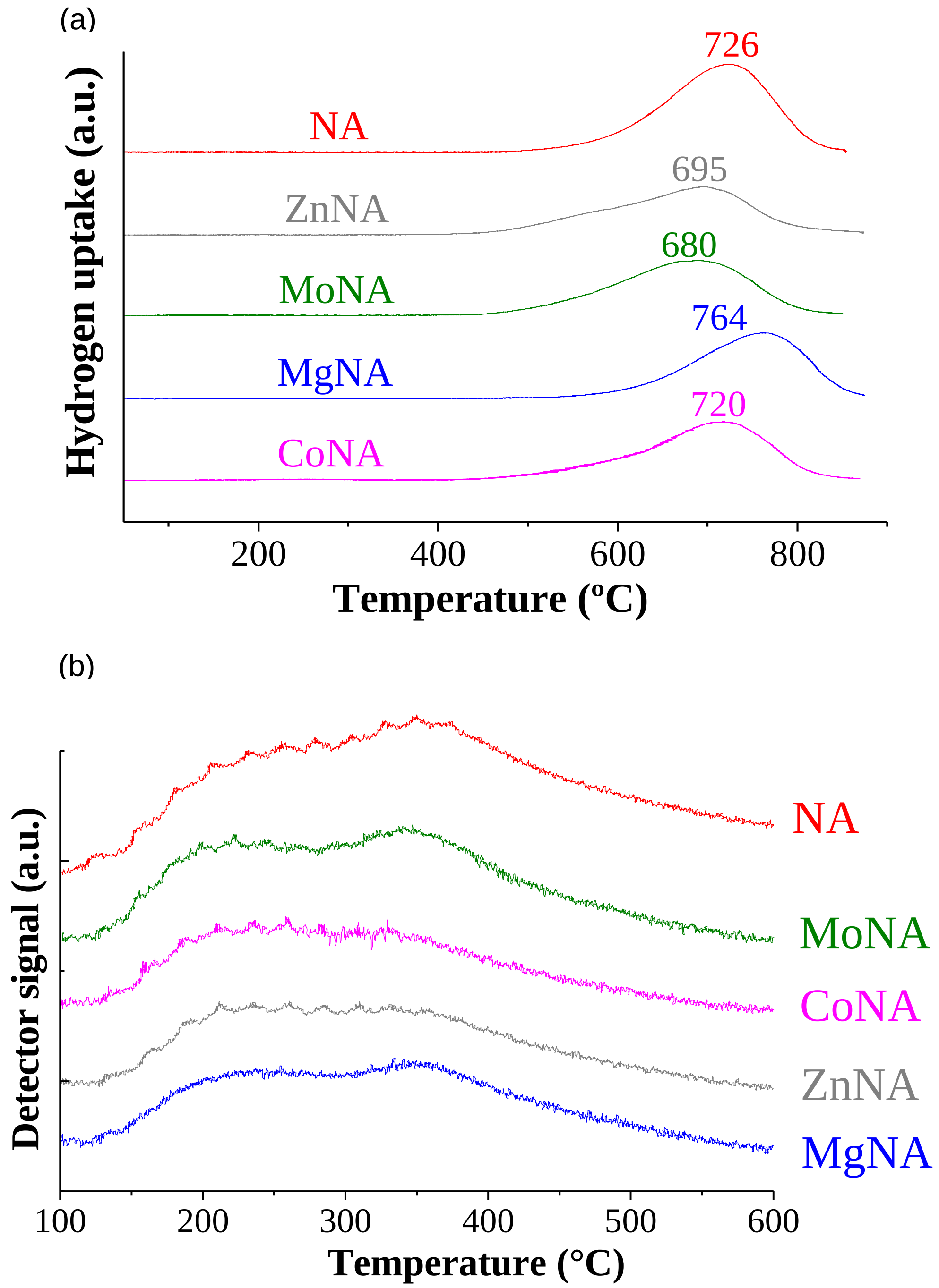

Figure 6.2. (a) H_2-TPR profiles for calcined samples; (b) NH_3-TPD profiles for calcined samples.

The NH_3-TPD profiles are shown in Figure 6.2-b. The possibility of ammonia dissociation was not taken into account in the analysis. The desorption curves display two overlapping peaks for all samples. The first peak is located at a temperature of approximately 200°C and is ascribed to weakly acidic sites. The second peak at 350°C corresponds to sites with stronger acidity. The larger intensity of desorption peaks presented by NA reveals a higher acidity for this sample. The samples with Ni partially substituted for a third element display weaker interactions with NH_3 at both the weak and the moderately acidic sites. As expected from the higher alkalinity of Mg and Zn, MgNA and ZnNA show the lowest amount of acidic sites.

Ethanol conversion and products distribution as a function of reaction temperature obtained for NA catalytic evaluation are displayed in Fig. 6.3-a. The NA sample achieves complete ethanol conversion at temperatures above 500°C under reaction conditions. Between 400 and 450°C, although H_2 and CO_2 are identified as the major products, significant amounts of acetaldehyde, ethylene and methane (approximately 20 mol% each) are observed, indicating that the dehydrogenation (eq. 6.4) and dehydration (eq. 6.3) of ethanol have occurred appreciably in this temperature range, as well as acetaldehyde decomposition to methane (eq. 6.5). A significant decrease in selectivity for these primary ethanol decomposition compounds (i.e., C_2H_4 and CH_3CHO) is noted for temperatures between 450 and 500°C, followed by an increase in selectivity for H_2, CO_2 and CO. These results are expected from the thermodynamics because the steam reforming of ethanol reactions (eq. 6.1 and 6.2) are strongly endothermic, while the ethanol decomposition reactions (eq. 6.3 and 6.4) have only a moderately endothermic nature. At temperatures higher than 500°C, the selectivity for methane and carbon dioxide continuously decreases. In the temperature range of 550-600°C, higher formation of both synthesis gas components can be observed, while the formation of C_2H_4 and CH_3CHO is negligible. Again, thermodynamics dictate that reactions that form synthesis gas from ethanol (eq. 6.1) and from methane (eq. 6.6 and 6.7) are favoured at higher temperatures compared to the steam reforming of ethanol in the presence of excess water, which results in the production of H_2 and CO_2 (eq. 6.2). The higher selectivity towards H_2 and CO for higher temperatures was also observed for a Ni-based hydrotalcite-type catalyst in a recent report [24].

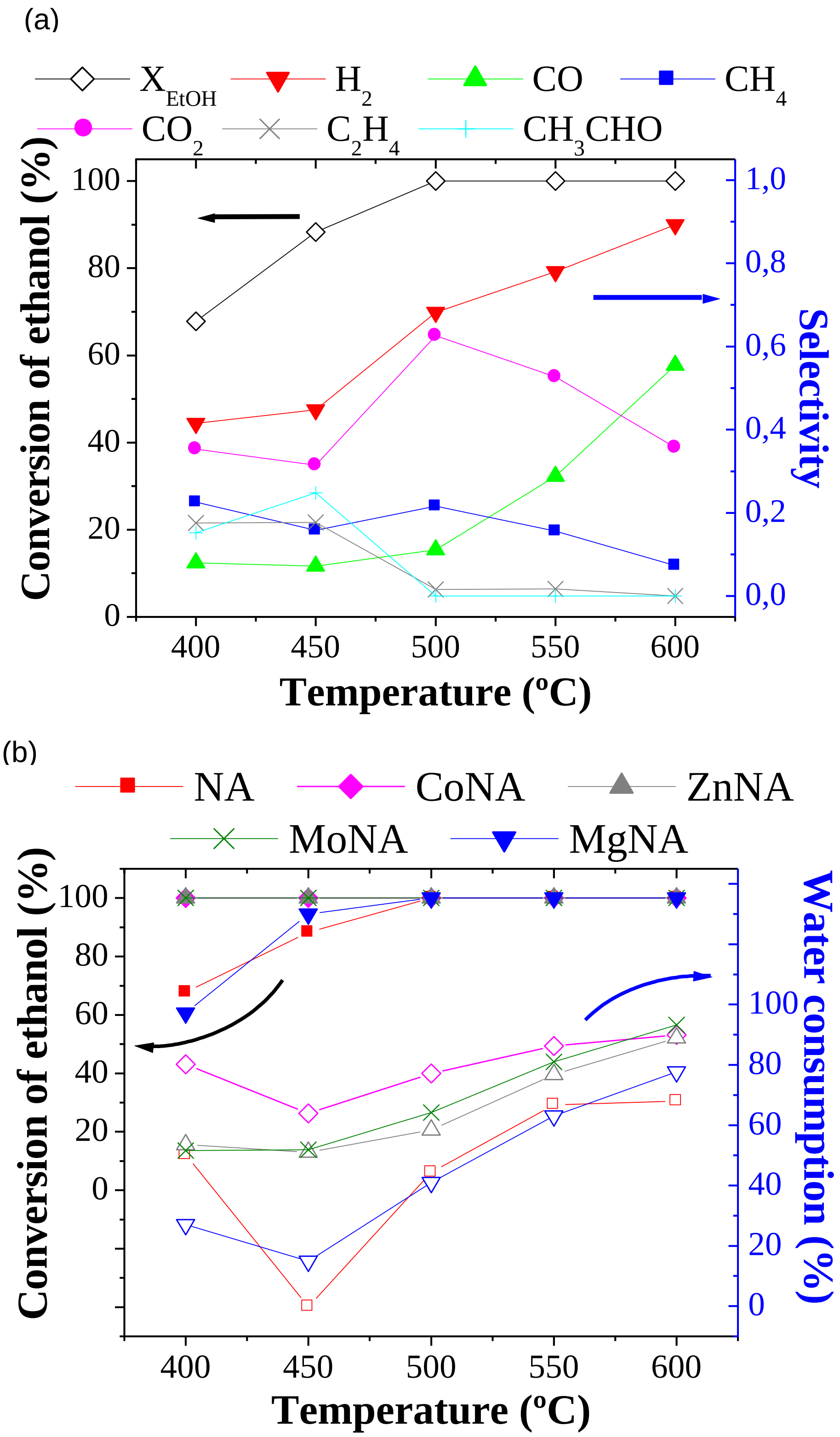

Figure 6.3. (a) Conversion of ethanol and product selectivity versus reaction temperature of ethanol steam reforming over NA; (b) Conversion of ethanol (closed symbols) and water consumption (open symbols) as a function of the reaction temperature for ethanol steam reforming over modified Ni-Al samples (W_{CAT} = 0.1 g; F_{N2} = 100 mL·min^{-1}; F_{LIQ} = 0.5 mL·h^{-1}; H_2O/C_2H_5OH = 1).

Fig. 6.3-b shows the variation of ethanol conversion and water consumption with reaction temperature for the modified materials. Ethanol conversion is complete at all reaction temperatures for all materials except for NA and MgNA; thus, it was not possible to establish a correlation between ethanol conversion and the surface area measurements (Tab. 6.1). However, this result could be related to the smaller particles of ZnNA, MoNA and CoNA suggested by XRD patterns (Fig. 6.1). Moreover, an induction period is observed at the beginning of the reaction for NA and MgNA catalysts, which is because the complete reduction of metal oxides occurs in higher temperatures for both of these materials (as shown by TPR in Fig. 6.2-a).

As expected by the reaction behaviour shown in Fig. 6.3-a, Fig. 6.3-b shows that the modified NA materials also exhibit a decrease in water consumption at 450°C. Although water is consumed by the steam reforming of ethanol (eq. 6.1 and 6.2) and the water gas shift (eq. 6.9) reactions, the higher incidence of reactions that produce water as a co-product, such as the dehydration of ethanol (eq. 6.3) (indeed, the selectivity for C_2H_4 reaches 20% at this temperature), results in a decrease in water consumption. This phenomenon may be associated with the activation temperature, suggesting that the complete reduction of nickel oxide occurs during the reaction through the hydrogen produced in the process. Although the preactivation step was conducted at a lower temperature than that required for the complete reduction of oxides (Fig. 6.1), the XRD pattern of NA after the reaction shown in Fig. 6.4-a depicts the formation of metallic nickel (and carbon). Above 450°C, water consumption increases with the increase of reaction temperature because steam reforming reactions are favoured at higher temperatures.

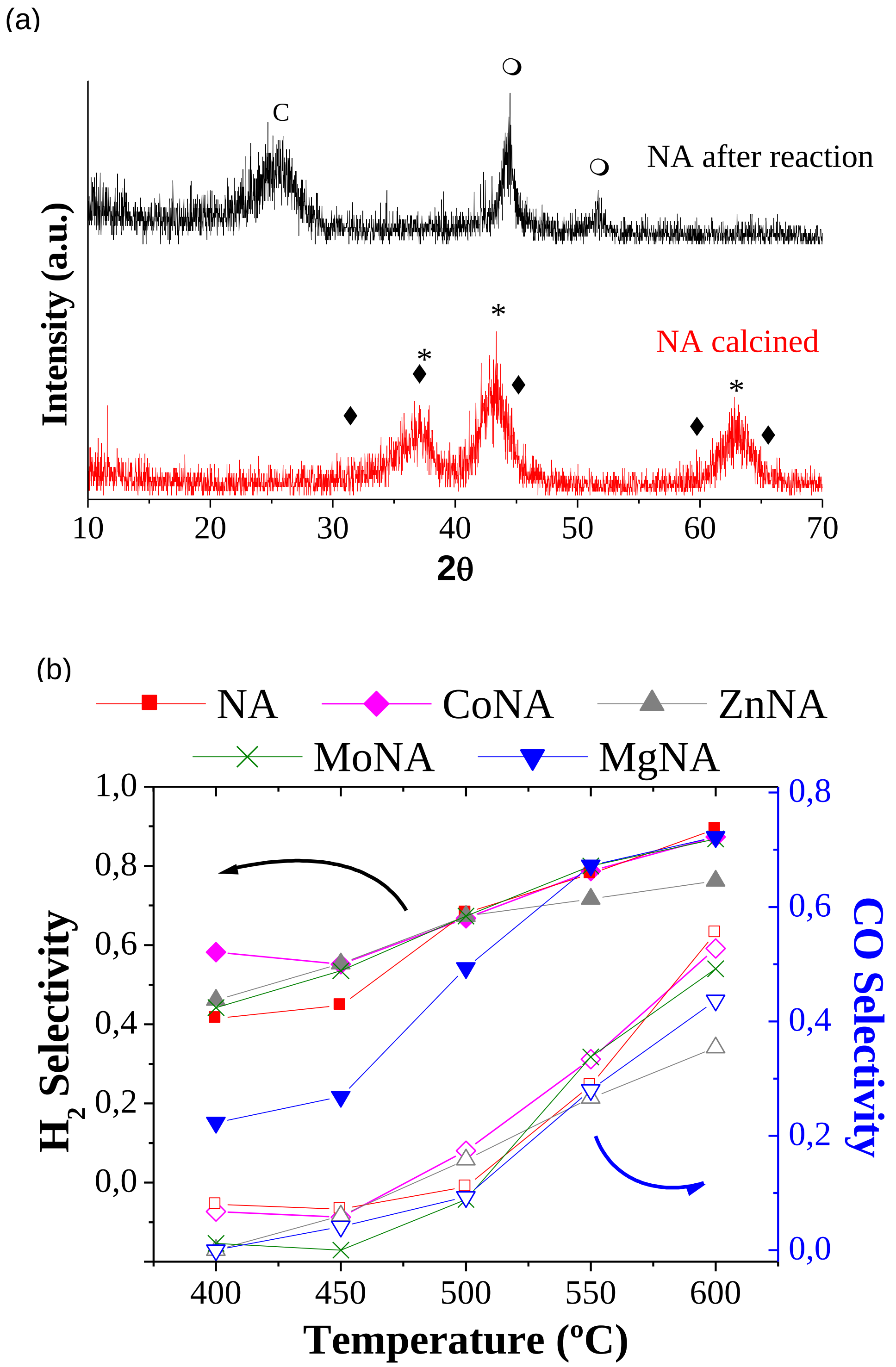

Figure 6.4. (a) X-ray diffraction (XRD) patterns of calcined NA and NA after reaction: (C) carbon; (❍) Ni^0; (*) NiO; (♦) $NiAl_2O_4$; (b) Hydrogen selectivity (closed symbols) and CO selectivity (open symbols) as a function of the reaction temperature of ethanol steam reforming over modified Ni-Al samples (W_{CAT} = 0.1 g; F_{N2} = 100 mL•min^{-1}; F_{LIQ} = 0.5 mL•h^{-1}; H_2O/C_2H_5OH = 1).

The reaction selectivity for H_2 and CO for modified samples is presented in Fig.6. 4-b. Higher selectivity for synthesis gas is observed as temperature increases. The same behaviour was observed in other published papers [11, 13], but the selectivity found for carbon monoxide is higher in this study because a lower H_2O/EtOH ratio was used. The selectivity towards H_2 at higher temperatures is very similar for all samples except ZnNA. Additionally, MgNA presented the largest variation in H_2 selectivity over the temperature range. Concerning the selectivity for CO, Fig. 6.4-b shows that NA and CoNA display the highest selectivity for CO at higher temperatures. The selectivity for CO exhibited by ZnNA followed the lower H_2 formation at 600°C.

Table 6.3. TPO/DTA analysis of catalysts after reaction.

Sample	Total weight loss (%)	DTA peak temperature (°C)
NA	59.8	510
MgNA	33.0	568
ZnNA	64.0	510
MoNA	49.0	510
CoNA	58.9	467

The XRD patterns of NA after the reaction (Fig. 6.4-a) exhibited diffraction peaks associated with the formation of carbon on the catalyst surface. To verify the deactivation tendency due to coke formation, the TPO-DTA analysis shown in Tab. 6.3 was performed on samples after catalytic runs. Interestingly, NA exhibits a high amount of coke formation, despite having shown lower ethanol conversion values at intermediate reaction temperatures (Fig. 6.3-b). This result may be related to the higher amount of acidic sites displayed by NA in the TPD curves (Fig. 6.2-b), as these sites favour the formation of ethylene through the dehydration of ethanol (eq. 6.3), which is then transformed to coke (eq. 6.11). The decomposition of methane (eq. 6.8) can also occur at these sites. In comparison, MgNA presents a lower amount of carbon deposition mainly due to its higher alkalinity, although the DTA peak related to combustion reveals that coke is heavier than the other samples, which makes the regeneration process more critical for MgNA. The low amount of carbonaceous deposit formation together with the high water consumption observed for MoNA and CoNA could indicate that the steam reforming of coke (eq. 6.12) is more favoured for these samples compared to other samples such as ZnNA. Additionally, the DTA peak of CoNA is shifted towards lower temperatures, corresponding to a milder regeneration step.

6.4 Conclusions

The substitution of 11% of Ni by a third element provides a slight decrease in surface area, except for MoNA. Additionally, a higher weight loss was noted for the modified samples, as well as a decrease in the crystallinity, although MgNA showed similar a XRD pattern to that of NA. In fact, the MgNA and NA samples revealed a reduction peak located at higher temperatures, which indicates a more difficult reduction of NiO to Ni^0. The catalytic evaluation revealed that the dehydration and dehydrogenation of ethanol occurs at lower temperatures, while higher temperatures favoured the formation of hydrogen and synthesis gas. CoNA, MoNA and ZnNA samples exhibited higher water consumption and conversion of ethanol at intermediate temperatures. The TPO-DTA data for samples after the reaction presented a high coke formation on NA, which is expected due to its higher acidity, as verified by TPD. Despite having a lower deactivation due to coke deposition associated with its higher alkalinity content, MgNA exhibited a DTA peak at higher temperatures than the other catalysts, which indicates that the regeneration process would be more severe for this sample.

ACKNOWLEDGEMENTS

The authors are grateful for financial support from MCT/CNPq and CAPES.

References

[1] Tuti S, Pepe F. On the catalytic activity of cobalt oxide for the steam reforming of ethanol. *Catal Lett* 2008;**122**:196-203.

[2] Vizcaíno AJ, Carrero A, Calles JA. Hydrogen production by ethanol steam reforming over Cu–Ni supported catalysts. *Int J Hydrogen Energy* 2007;**32**: 1450-1461.

[3] Huber GW, Chheda JN, Barrett CJ, Dumesic JA. Production of liquid alkanes by aqueous-phase processing of biomass-derived carbohydrates. *Science* 2005;**308**: 1446-1450.

[4] Rostrup-Nielsen JR. Making fuels from biomass. *Science* 2005;**308**: 1421-2.

[5] Rostrup-Nielsen JR, Nielsen R. Fuels and energy for the future: The role of catalysis. *Catal. Rev.* 2004;**46**: 247-270.

[6] Zhang B, Cai W, Li Y, Xu Y, Shen W. Hydrogen production by steam reforming of ethanol over an Ir/CeO_2 catalyst: Reaction mechanism and stability of the catalyst. *Int J Hydrogen Energy* 2008;**33**: 4377-4386.

[7] Deluga GA, Salge JR, Schmidt LD, Verykios XE. Renewable hydrogen from ethanol by autothermal reforming. *Science* 2004;**303**: 993-7.

[8] Galvita VV, Semin GL, Belyaev VD, Semikolenov VA, Tsiakaras P, Sobyanin VA. Synthesis gas production by steam reforming of ethanol. *Appl.Catal., A Gen*. 2001;**220**: 123-7.

[9] Lima SM, Silva AM, Costa LOO, Graham UM, Jacobs G; Davis BH et al. Study of catalyst deactivation and reaction mechanism of steam reforming, partial oxidation, and oxidative steam reforming of ethanol over Co/CeO_2 catalyst. *J.Catal.* 2009;**268**: 268-281.

[10] Llorca J, de la Piscina PR, Dalmon JA, Sales J, Homs N. CO-free hydrogen from steam-reforming of bioethanol over ZnO-supported cobalt catalysts - Effect of the metallic precursor. *Appl Catal B* 2003;**43**: 355-369.

[11] Wang F, Li Y, Cai W, Zhan E, Mu X, Shen W. Ethanol steam reforming over Ni and Ni-Cu catalysts. *Catal. Today* 2009;**146**: 31-6.

[12] Liguras DK, Goundani K, Verykios XE. Production of hydrogen for fuel cells by catalytic partial oxidation of ethanol over structured Ni catalysts. *J. Power Sources* 2004;**130**: 30–7.

[13] Busca G, Costantino U, Montanari T, Ramis G, Resini C, Sisani M. Nickel versus cobalt catalysts for hydrogen production by ethanol steam reforming: Ni-Co-Zn-Al catalysts from hydrotalcite-like precursors. *Int J Hydrogen Energy* 2010;**35**: 5356-5366.

[14] Muroyama H, Nakase R, Matsui T, Eguchi K. Ethanol steam reforming over Ni-based spinel oxide. *Int J Hydrogen Energy* 2010;**35**: 1575-1581.

[15] Más V, Dieuzeide ML, Jobbágy M, Baronetti G, Amadeo N, Laborde M. Ni(II)-Al(III) layered double hydroxide as catalyst precursor for ethanol steam reforming: Activation treatments and kinetic studies. *Cat. Today* 2008;**133**: 319-323.

[16] Holgado MJ, Rives V, San Román MS. Characterization of Ni–Mg–Al mixed oxides and their catalytic activity in oxidative dehydrogenation of n-butane and propene. *Appl. Catal., A Gen*. 2001;**214**: 219-228.

[17] Vaccari A. Preparation and catalytic properties of cationic and anionic clays. *Cat. Today* 1998;**41**: 53-71.

[18] Vaccari A. Clays and catalysis: a promising future. *Appl. Clay Sci.* 1999;**14**: 161-198.

[19] Kovanda F, Rojka T, Bezdicka P, Jiratova K, Obalova L, Pacultova K et al. Effect of hydrothermal treatment on properties of Ni-Al layered double hydroxides and related mixed oxides. *J. Solid State Chem*. 2009;**182**: 27-36.

[20] Martinez R, Romero E, Guimon C, Bilbao R. CO_2 reforming of methane over coprecipitated Ni-Al catalysts modified with lanthanum. *Appl. Catal., A Gen*. 2004; **274**: 139-149.

[21] Montoya JA, Romero-Pascual E, Gimon C, Del Angel P, Monzon A. Methane reforming with CO_2 over Ni/ZrO_2-CeO_2 catalysts prepared by sol-gel. *Catal. Today* 2000;**63**: 71-85.

[22] Guo JJ, Lou H, Zhao H, Chai DF, Zheng XM. Dry reforming of methane over nickel catalysts supported on magnesium aluminate spinels. *Appl. Catal., A Gen*. 2004;**273**: 75-82.

[23] Daza CE, Gallego J, Moreno JA, Mondragon F, Moreno S, Molina R. CO_2 reforming of methane over Ni/Mg/Al/Ce mixed oxides. *Catal. Today* 2008;**133**: 357-366.

[24] Resini C, Montanari T, Barattini L, Ramis G, Busca G, Presto S et al. Hydrogen production by ethanol steam reforming over Ni catalysts derived from hydrotalcite-like precursors: Catalyst characterization, catalytic activity and reaction path. *Appl. Catal., A Gen*. 2009;**355**: 83-93.

Capítulo 7

Synthesis, characterisation and catalytic performance of Cu- and Co-modified Fe-Al co-precipitated catalysts for the steam reforming of ethanol

Artigo aceito para publicação no periódico: *Global NEST Journal*, em outubro de 2014.

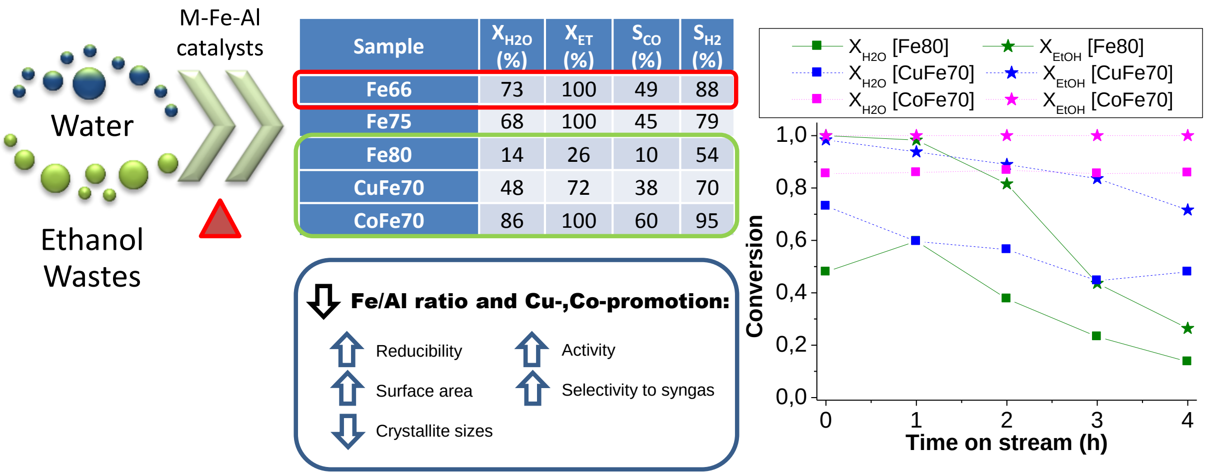

Sample	X_{H2O} (%)	X_{ET} (%)	S_{CO} (%)	S_{H2} (%)
Fe66	73	100	49	88
Fe75	68	100	45	79
Fe80	14	26	10	54
CuFe70	48	72	38	70
CoFe70	86	100	60	95

SYNTHESIS, CHARACTERISATION AND CATALYTIC PERFORMANCE OF CU- AND CO-MODIFIED FE-AL CO-PRECIPITATED CATALYSTS FOR THE STEAM REFORMING OF ETHANOL

G. SOUZA[1,2], C. RUOSO[1], N.R. MARCILIO[1] AND O.W. PEREZ-LOPEZ[1,*]

[1] *Department of Chemical Engineering, Federal University of Rio Grande do Sul - UFRGS, R. Eng. Luiz Englert S/N° - Build. 12204, 90040-040 Porto Alegre, Brazil*

[2] *Fundação de Ciência e Tecnologia do Estado do Rio Grande do Sul - CIENTEC, Av. das Indústrias, 2270, Distrito Industrial, 94930-230 Cachoeirinha, Brazil.*

[*] Corresponding author: O. W. Perez-Lopez. UFRGS, Rua Eng. Luiz Englert S/N°, Build. 12204. Zip Code: 90040-040 - Porto Alegre, Brazil. Phone: +55 51 3308 3953. Fax: +55 51 3308 3277. Email: perez@enq.ufrgs.br

Abstract

This paper reports the synthesis and the investigation of the properties and performance of Fe-Al catalysts modified with Cu or Co for the steam reforming of ethanol. The materials were prepared by the precipitation method with different Fe/Al ratios. The samples were characterised by the S_{BET}, TG/DTG, XRD, H_2-TPR and TPO/DTA analyses. The increase in the Fe/Al ratio leads to a decrease in the specific surface area and shifts the reduction peaks towards higher temperatures. The partial substitution of Fe by Co or Cu modifies the structure of the materials because higher specific surface areas and crystallites of iron oxides with smaller sizes are formed. The promotion also improves the reducibility of the iron species. These changes provide higher activity and selectivity towards H_2 and CO for the modified samples and for the samples with lower Fe/Al ratio. The Co-containing catalyst showed the best performance because this sample exhibited the highest conversions and selectivity towards both H_2 and CO and the lowest formation of coke according to the TPO analysis.

Keywords: Iron catalyst, precipitation method, mixed oxides, steam reforming, cobalt, copper, coke.

7.1. Introduction

The processes involving wastes derived from biomass feedstock arise as interesting alternatives taking into account the needs for the minimisation of landfill disposal and the depletion of the crude petroleum reserves and consequently oscillation on its price (de Souza *et al.*, 2012a; Ponton Lozano *et al.*, 2014). The steam reforming of bio-wastes is a promising route because it can originates hydrogen and synthesis gas (a mixture of H_2 and CO) from renewable resources. The use of hydrogen for fuel cells still requires greater efforts in terms of research and development before large scale application of this technology. The questions related to the cost of this new infrastructure and the efficiency matters that would be required for a future hydrogen society could lead to the production of synthetic liquid fuels instead of only hydrogen (Huber *et al.*, 2005; Rostrup-Nielsen, 2005). Hydrocarbons and a wide range of other chemicals can be produced from the conversion of synthesis gas originated from biomass resources (such as rich ethanol wastes) through the Fischer-Tropsch Synthesis (FTS) or processes involving the synthesis and further transformation of methanol. Moreover, the FTS technology produces ultra clean diesel oil fraction with high cetane number and without any sulfur and aromatic compounds (Lira *et al.*, 2008), thus preventing the emission of pollutants such as particulates, benzene, toluene, polycyclic aromatic hydrocarbons (PAH) and SO_x.

The development of catalysts is crucial for the feasibility of the steam reforming of ethanol for commercial scale. Several catalysts have already been studied, mostly based on Ni (Zhang *et al.*, 2009a; Wang and Wang, 2010), Co (Song *et al.*, 2011; Espinal *et al.*, 2012; Davidson *et al.*, 2013) or noble metals such as Ir, Rh and Pd (Galvita *et al.*, 2001; Zhang *et al.*, 2008a; González Vargas *et al.*, 2013; Coronel *et al.*, 2014). However, nickel is still the preferred option because of its high activity for the reforming reaction and lower price (Dias and Assaf, 2003; Jones *et al.*, 2008). The literature does not report results for steam reforming of ethanol over Fe-based catalysts. However, its' much cheaper price (Dry, 2002), apparently moderate activity for reforming (Jones *et al.*, 2008) and interesting results involving the decomposition of ethanol (Li *et al.*, 2008; Wang *et al.*, 2011) are incentives to the investigation of Fe-bulk materials for the steam reforming of ethanol reaction.

This paper reports the study of Fe-Al catalysts for the steam reforming of ethanol, herein representing rich ethanol wastes. The samples were prepared by the precipitation method with different Fe/Al ratios. Also, the modifications on the structure and catalytic performance provided by the partial substitution of Fe^{3+} by a divalent metal (Cu^{2+} or Co^{2+}) was investigated in this work.

7.2. Methods

7.2.1 Preparation of samples

The samples were synthesised with different Fe/Al molar ratios by the continuous co-precipitation method described earlier (de Souza *et al.*, 2012a). The Fe-Al samples were prepared from an aqueous solution containing the Fe(III) and Al(III) nitrates. The aqueous solutions for the modified samples also contained the Co(II) or Cu(II) nitrates. An aqueous solution containing NaOH and Na_2CO_3 (1:1 v/v) was used as the precipitant. The solutions were continuously fed into a continuous stirred tank reactor (CSTR) kept at constant temperature (60 ± 1°C) and pH (9 ± 0.1). After crystallisation at 60°C for 1 h, the precipitate was filtered and washed with distilled and deionised water. After drying at 80°C for 24 h in an oven, the samples were crushed and sieved. The fraction with particle sizes between 355 and 500 µm was taken. The thermal treatment was conducted under an air flow of 50 mL min^{-1} at 600°C for 6 h.

7.2.2 Catalytic evaluation

The catalysts were reduced in situ under 100 mL min^{-1} of pure H_2 flow for 1 h at 600°C prior to the catalytic evaluation. The steam reforming reactions were performed in a quartz tubular fixed bed reactor (6 mm i.d.) loaded with 100 mg of catalyst. The tests were performed under atmospheric pressure at 600°C. The flow rate of nitrogen was adjusted to 100 mL min^{-1} through a mass flow controller. The ethanol-water mixture (1:1 molar ratio) was fed by a syringe-type micro-pump at a flow rate of 0.5 mL h^{-1}. The products were analysed by gas chromatography. The ethanol conversion and the water consumption (X_{react}) were defined based on the concentration in the inlet ($[React]_{IN}$) and outlet ($[React]_{OUT}$) streams:

$$X_{react}(\%) = \frac{[\mathrm{Re}\,act]_{IN} - [\mathrm{Re}\,act]_{OUT}}{[\mathrm{Re}\,act]_{IN}} x100 \tag{7.1}$$

The selectivity for hydrogen (S_{H2}) and C-containing products (S_{Ci}) was evaluated as follows:

$$S_{H2} = \frac{[H_2]}{\sum \nu_j . [H_{2j}]} \tag{7.2}$$

$$S_{Ci} = \frac{\nu_i . [C_i]}{\sum \nu_j . [C_j]} \tag{7.3}$$

Where [C_j] and [H_{2j}] is respectively the number of moles of C-containing and H_2-containing *j* product in the outlet stream and *uj* is the ratio of stoichiometric reaction coefficients.

7.2.3 Characterisation

The uncalcined samples were characterised by thermogravimetry (TG/DTG). The specific surface area (S_{BET}), X-ray diffraction (XRD) and temperature-programmed reduction (H_2-TPR) was performed for the calcined catalysts. The spent catalysts were investigated by the temperature-programmed oxidation coupled with differential thermal analyses (TPO/DTA).

The TG/DTG and TPO/DTA experiments were conducted using a thermobalance (TA Model SDT600). Approximately 10 mg each of the uncalcined (TG/DTG) or the spent sample (TPO/DTA) was purged with 1000 mL min^{-1} of nitrogen at 30°C for 10 min before the tests. Then the samples were heated at 10°C min^{-1} to 850°C under a synthetic air flow rate of 100 mL min^{-1}.

The S_{BET} and H_2-TPR data were collected using a multipurpose system equipped with a thermal conductivity detector (TCD). A quartz “U-type” reactor was loaded with 100 mg of the calcined sample and placed in a temperature-controlled oven. A pretreatment step under nitrogen flow at 250°C was conducted for 1 h before the measures. For the H_2-TPR analysis, the temperature was increased at a rate of 10°C min^{-1} from 40°C to 900°C. The heating was carried out under 30 mL min^{-1} of a diluted H_2/N_2 mixture (10% v/v). The S_{BET} data was recorded using the N_2 dynamic adsorption method at -196°C.

The XRD patterns were obtained using the powder method for the calcined catalysts. The patterns were collected for 2θ between 10 and 70° with a Bruker D2 Phaser X-ray diffractometer. The spectra were collected at ambient temperature using CuKα radiation.

7.3 Results and discussion

Table 7.1 exhibits the nominal molar composition and the S_{BET} measurements for the calcined catalysts.

Table 7.1. Nominal composition and S_{BET} measurements for the calcined samples.

Sample	Composition (mol. %)				S_{BET} (m^2 g^{-1})
	Cu	Co	Fe	Al	
Fe66	0.0	0.0	66.7	33.3	79
Fe75	0.0	0.0	75.0	25.0	46
Fe80	0.0	0.0	80.0	20.0	37
CuFe70	10.0	0.0	70.0	20.0	78
CoFe70	0.0	10.0	70.0	20.0	78

Table 7.1 shows that the specific surface area strongly decreases with decreasing Al content for samples with different Fe/Al ratios. This trend highlights the role of aluminium as a structural promoter for the precipitated samples. Despite involving another metal with different oxidation state, the same behaviour was observed for Co-Al precipitated catalysts (Hermes, 2010). The substitution of 10 mol. % of iron by copper or cobalt significantly increases the specific surface area. The combination of both trivalent elements (Fe^{3+} and Al^{3+}) probably does not provide the formation of mixed oxides, which are known to possess high specific surface area. On the other hand, the presence of the divalent metals (Cu^{2+} or Co^{2+}) would allow the formation of mixed oxides, thus the increment on the specific surface area provided by referred metals. Additionally, the presence of copper was told to lead to smaller crystallites of Fe_2O_3, which could also contribute to increase the specific surface area (Wan *et al.*, 2008).

Figure 7.1 exhibits the curves related to the thermal decomposition of the uncalcined Fe-Al samples.

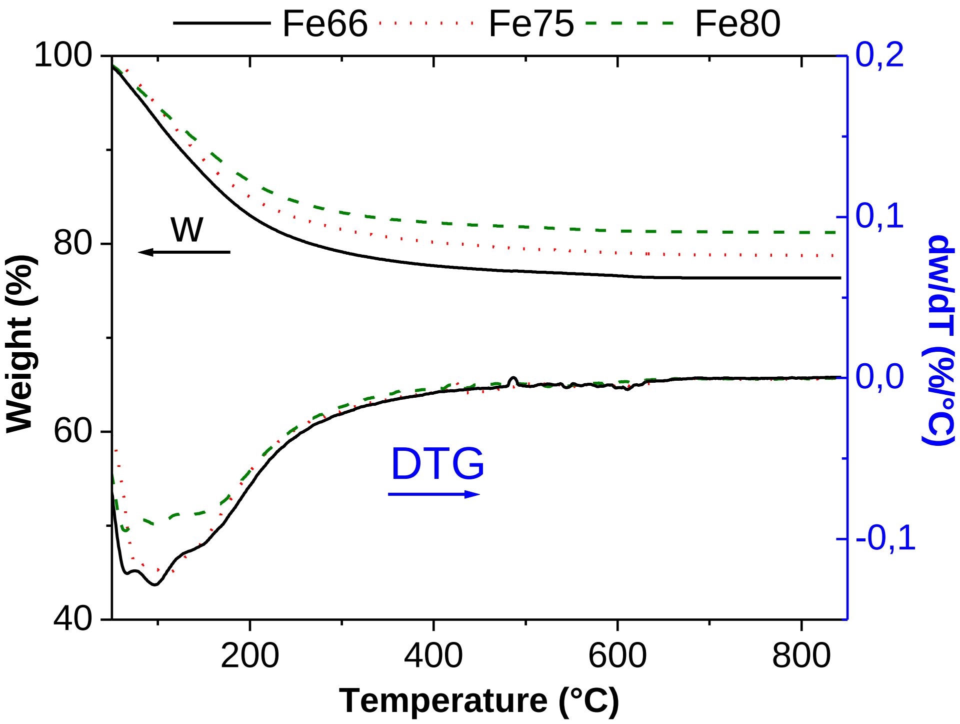

Figure 7.1. TG/DTG curves for uncalcined samples.

The DTG peaks related to the decomposition of the precursors are observed at temperatures below 400°C. The decomposition phenomena might include the water removal at lower temperatures, followed by the release of the NO, OH^- and CO_3^{2-} compounds generated from the decomposition of the precursors (Crepaldi *et al.*, 2000; Frost *et al.*, 2005; Palmer *et al.*, 2009; Hermes *et al.*, 2011). The total weight loss in Figure 7.1 varied with the content of iron and aluminium on samples. However, the DTG peaks end at similar temperatures, suggesting that the thermal stability of the Fe-Al samples might be approximately the same. Other materials synthesised by the precipitation method with metal nitrates and sodium precursors also exhibited the thermal decomposition ending at temperatures below 400°C (Zhang *et al.*, 2008b; Hermes *et al.*, 2011).

The X-ray diffractograms and the H_2-TPR profiles for the calcined samples are showed in Figure 7.2-a and 7.2-b, respectively. The XRD patterns in Figure 7.2-a present diffraction reflections located at 2θ = 24.2, 33.2, 35.6, 40.9, 49.5, 54.0, 57.6, 62.4 and 64.0° for all the samples. These diffraction peaks can be ascribed to the hematite phase (Fe_2O_3). The X-ray diffraction patterns did not point to the formation of the hercynite phase ($FeAl_2O_4$). The diffractograms are similar to those reported by Zhang *et al.* (2009b) for Fe-Al materials prepared by the sol-gel method.

The CoFe70 present an additional reflection with weak intensity at 2θ = 36.9° that indicates the presence of the Co_3O_4 phase. Regarding the CuFe70 catalyst, the stronger peak ascribed to the tenorite phase (CuO) at 2θ = 38.7° was not identified in Figure 2-a, neither the reflections associated to Cu-containing mixed oxides. The additional phases expected for the CoFe70 and CuFe70 catalysts could not be precisely identified due to the low content of cobalt or copper on these samples. However, the absence of the aluminium ferrite is in agreement with the specific surface area measurements (Table 7.1), because the partial substitution of Fe by Cu or Co might form the mixed oxides that would lead to the increase in the surface area.

Based on the width at half the maximum intensity for the reflection at 2θ = 35.6°, a decrease in the crystallinity of the Fe_2O_3 phase is noted for both the Cu- and Co-modified catalysts compared to the Fe80 sample. This peak could also suggest that the partial substitution of Fe by Cu or Co originates Fe_2O_3 crystallites with smaller diameters, which would also be expected by the mixed oxides that might be formed for these modified samples.

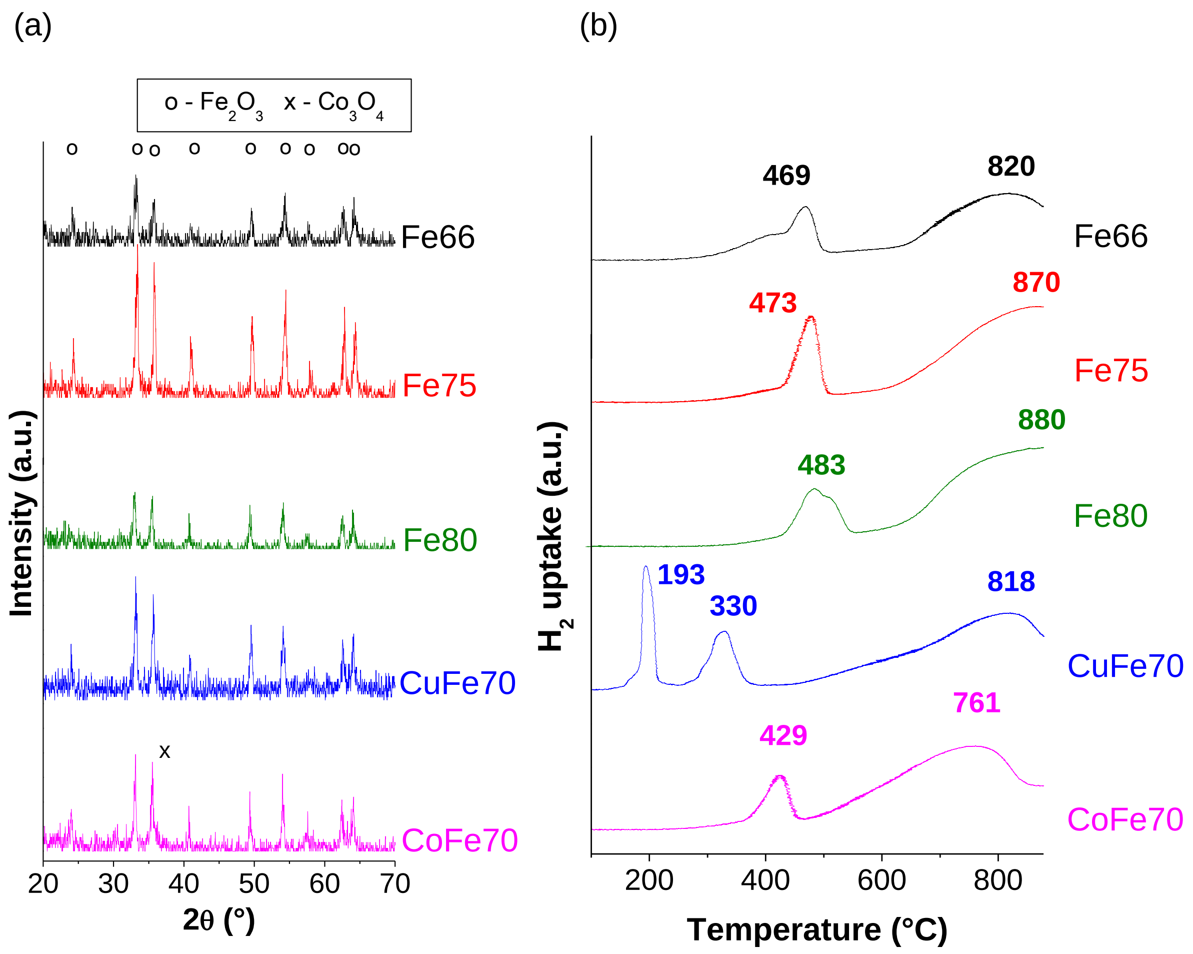

Figure 7.2. (a) XRD patterns and (b) H_2-TPR profiles for calcined samples.

The H_2-TPR curves are shown in Figure 7.2-b. Two main reduction peaks can be seen for all the Fe-Al samples. The peaks located at temperatures in the range 300-550°C can be ascribed to the reduction of the Fe_2O_3 phase to the Fe_3O_4 phase and possibly its subsequent reduction to FeO. The overlapped peaks starting at 600°C are related to further transformations of the iron oxides to metallic iron. This peak at higher temperatures could also be related to the reduction of the $FeAl_2O_4$ spinel phase because the mixed oxides are told to be thermally more stable and therefore more difficult to be reduced (Vaccari, 1998; Hermes *et al.*, 2011). Nonetheless, this Fe-Al mixed oxide phase was not identified by the XRD analysis (Figure 7.2-a) and is not expected from the iron precursor adopted (Fe^{3+}). The peak at higher temperatures does not finish due to the limit of the equipment for the upper temperature. However, it can be seen that the reduction peaks shift towards higher temperatures with increasing Fe/Al ratio. The reduction profile found for the Fe-Al samples is similar to that reported for other bulk iron (Hayakawa *et al.*, 2006) and Fe-Al materials (Oliveira and Rangel, 2003).

For the CoFe70 catalyst, two main peaks are also observed. The first one takes place at approximately the same temperature compared to the unpromoted Fe-Al samples. This peak is ascribed to the reduction of the Fe_2O_3 and the bulk cobalt oxides to metallic cobalt. The reduction of Co_3O_4 to Co^0 is known to takes place at these temperatures. Additionally to the further reduction of the iron oxides to metallic iron, the hydrogen consumption at higher temperatures might also include the reduction of the $CoAl_2O_4$ phase identified by the XRD analysis (Figure 7.2-a) (Hermes *et al.*, 2011; Cai *et al.*, 2013; Escobar and Perez-Lopez, 2014; Fakeeha *et al.*, 2014).

The copper-promoted catalyst show a different reduction profile compared to the other catalysts. An additional peak is noted at temperatures in the range 135 - 230°C. This TPR peak is assigned to the reduction CuO to Cu^0. The peak attributed to the initial reduction of the Fe_2O_3 phase occurs at lower temperatures for the CuFe70 sample. As showed in other papers, the presence of copper shifts the reduction of the iron oxides towards lower temperatures. The Cu crystallites nucleate during reduction of CuO at lower temperatures, providing H_2 dissociation sites capable of reducing iron oxides at significantly lower temperatures (Zhang *et al.*, 2006; Wan *et al.*, 2008). The addition of copper also shifts significantly towards lower temperatures the further reduction of the iron oxides to Fe^0 and possibly the reduction of the Cu-containing mixed oxides. For example, this broad reduction peak starts at *ca*. 100°C lower temperatures compared to the Fe66 sample. The same behaviour was observed for the Cu-Co-Al mixed oxides reported by Escobar and Perez-Lopez (2014).

Figure 7.3 exhibits the variation of the distribution of products and water consumption with time on stream for the steam reforming of ethanol over the Fe66 catalyst. The conversion of ethanol was complete during all the reaction.

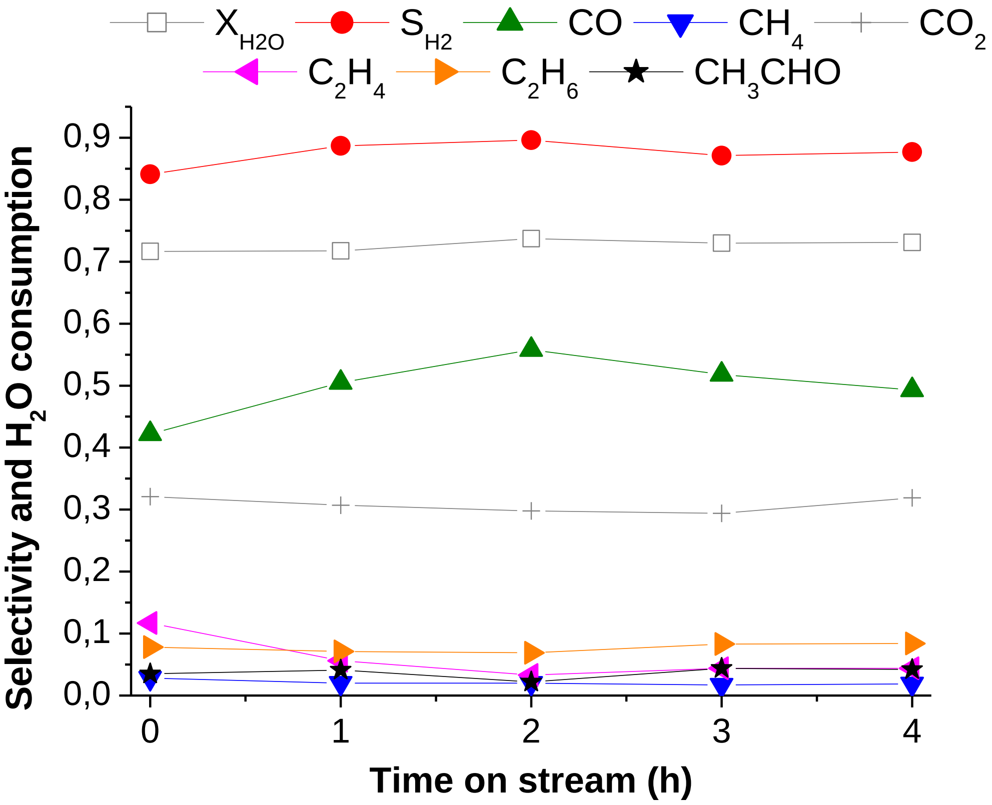

Figure 7.3. Distribution of products and water consumption with time on stream for the steam reforming of ethanol over the Fe66 catalyst.

As illustrated in Figure 7.3 for the Fe66 catalyst, the distribution of products and the water consumption did not change significantly during the catalytic evaluation. For the Fe66 catalyst, the highest selectivity values towards hydrogen and carbon monoxide and consumption of water was observed after 2 h, although it remains almost at the same level in the period range 2 – 4 h. The main products formed during the reaction are H_2, CO and CO_2. This result highlights the steam reforming of ethanol reactions (eq. 7.4 and eq. 7.5) that are favoured during all the catalytic evaluation.

$$C_2H_5OH + H_2O \rightarrow 2CO + 4H_2 \qquad \Delta H_{298K} = 256 \text{ kJ mol}^{-1} \tag{7.4}$$

$$C_2H_5OH + 3H_2O \rightarrow 2CO_2 + 6H_2 \qquad \Delta H_{298K} = 174 \text{ kJ mol}^{-1} \tag{7.5}$$

On the other hand, other products are observed in Figure 7.3 because the consumption of water does not follow the complete conversion of ethanol. This phenomenon points to reactions involving the decomposition of ethanol. The decomposition of ethanol can also form the synthesis gas (eq. 7.6). The methane produced in eq. 7.6 can be further decomposed to hydrogen and carbon (eq. 7.7). The ethane and ethylene can be produced from the dehydration of ethanol (eq. 7.8), while oxygenates such as acetaldehyde might be formed from the dehydrogenation of ethanol (eq. 7.9).

$$C_2H_5OH \rightarrow CH_4 + CO + H_2 \qquad \Delta H_{298K} = 49\ kJ\ mol^{-1} \tag{7.6}$$

$$CH_4 \rightarrow C_{(S)} + 2H_2 \qquad \Delta H_{298K} = 75\ kJ\ mol^{-1} \tag{7.7}$$

$$C_2H_5OH \rightarrow C_2H_4 + H_2O \qquad \Delta H_{298K} = 45\ kJ\ mol^{-1} \tag{7.8}$$

$$C_2H_5OH \rightarrow CH_3CHO + H_2 \qquad \Delta H_{298K} = 68\ kJ\ mol^{-1} \tag{7.9}$$

Table 7.2 summarises the results collected after 4 h of the steam reforming of ethanol at 600°C. The DTA peaks related to the oxidation of carbon and the mass of carbon formed per mass of catalyst ($m_C\ m_{cat}^{-1}$) estimated by the TPO/DTA analyses of spent catalysts are also shown in Table 7.2.

Table 7.2. Results of the steam reforming of ethanol after 4 h and TPO/DTA data.

Sample	X_{H2O} (%)	X_{ET} (%)	S_{CO} (%)	S_{H2} (%)	H_2/CO ratio (mol mol^{-1})	TPO/DTA analysis	
						$m_C\ m_{cat}^{-1}$ ($g_C\ g_{cat}^{-1}$)	DTA Peak (°C)
Fe66	73	100	49	88	2.7	0.08	581
Fe75	68	100	45	79	2.7	0.27	561
Fe80	14	26	10	54	6.0	0.04	514
CuFe70	48	72	38	70	2.6	0.05	528
CoFe70	86	100	60	95	2.6	0.01	539

(EtOH:H_2O = 1 mol mol^{-1}; W_{CAT} = 0.1 g; T_{REA} = 600°C, F_{LIQ} = 0.5 mL h^{-1}).

The selectivity towards both the components of the synthesis gas and the water consumption decreases with increasing Fe/Al ratio. Therefore, the performance of these Fe-Al samples followed the specific surface area measurements in this reaction (Table 7.1). This worsening in the performance for samples with increasing Fe/Al ratio is more evident taking into account the results collected for the Fe80 catalyst. This sample exhibited low conversion of ethanol in addition to the lowest values for water consumption and selectivity.

The TPO/DTA analysis revealed lower amount of coke on the Fe66 sample compared to the Fe75 catalyst. This result is in agreement with the higher consumption of water and selectivity towards H_2 and CO observed for the Fe66 sample because coke might be gasified by water to generate synthesis gas (eq. 7.10). However, this sample might require approximately 20°C higher temperatures for its regeneration compared to the Fe75 catalyst.

$$C_{(S)} + H_2O \rightarrow CO + H_2 \qquad \Delta H_{298K} = 131\ \mathrm{kJ\ mol^{-1}} \qquad (7.10)$$

Regarding the samples in which 10 mol. % of iron was substituted by copper or cobalt, Table 7.2 shows that the modification leads to a significant improvement on the activity and the selectivity towards the synthesis gas after 4 h of reaction. This improvement on the performance is expected from the changes on the structure of the materials provided by the divalent metal (Cu^{2+} and Co^{2+}), which leaded to an increase in the specific surface area (Table 7.1), crystallites of iron oxides with smaller diameters (Figure 7.2-a) and higher thermal stability ascribed to the mixed oxides (Vaccari, 1998). Moreover, it is expected from previous results collected for the decomposition of ethanol (Souza *et al.*, 2012) and to the higher activity for the reforming reactions of Co compared to Fe (Jones *et al.*, 2008). The H_2/CO ratio of the synthesis gas is the same for the CuFe70 and CoFe70 samples and is almost at the same level compared to the Fe66 and Fe75 catalysts. The low formation of carbon on the modified samples compared to the other samples with different Fe/Al is remarkable. The CoFe70 catalyst exhibited the best performance because this sample showed the highest consumption of water, selectivity towards both the H_2 and CO products and formed the lowest quantity of coke.

Figure 7.4-a shows the evolution of the conversion of ethanol and consumption of water with time on stream for the Fe80, CuFe70 and CoFe70 catalysts. The corresponding selectivity towards H_2 and CO with time on stream is showed in Figure 7.4-b. Figure 7.4-a depicts the deactivation phenomenon that takes place on the Fe80 catalyst. The conversion of ethanol and the water consumption decrease continuously after 1 h of reaction for the Fe80 catalyst, thus revealing low thermal stability for this sample. The selectivity towards H_2 and CO in Figure 7.4-b follows this behaviour for the Fe80 catalyst.

As previously showed in Table 7.2, the overall performance is enhanced when Fe is partly substituted by Cu or Co. Comparing to the Fe80 sample, the modification with copper enhances the activity (Figure 7.4-a) and the selectivity towards H_2 and CO (Figure 7.4-b) of the sample with time on stream. Despite exhibiting the same trend, the decrease on the activity during the reaction is less dramatically for the CuFe70 sample compared to the Fe80 catalyst. The performance for the CuFe70 might be affected by the sintering of the Cu^0 phase, because the reduction of the CuO phase takes place at low temperatures (Figure 7.2-b), as this phenomenon was observed after decomposition of ethanol over Cu-Ni-Al samples (de Souza *et al.*, 2012b). In addition to the higher values, the Figure 7.4-a and Figure 7.4-b show that both the conversions and the distribution of products remain at the same level with time on stream for the CoFe70 catalyst. Therefore, Figure 7.4-a and Figure 7.4-b point to the high thermal stability for this sample in addition to its best activity and selectivity results.

(a)

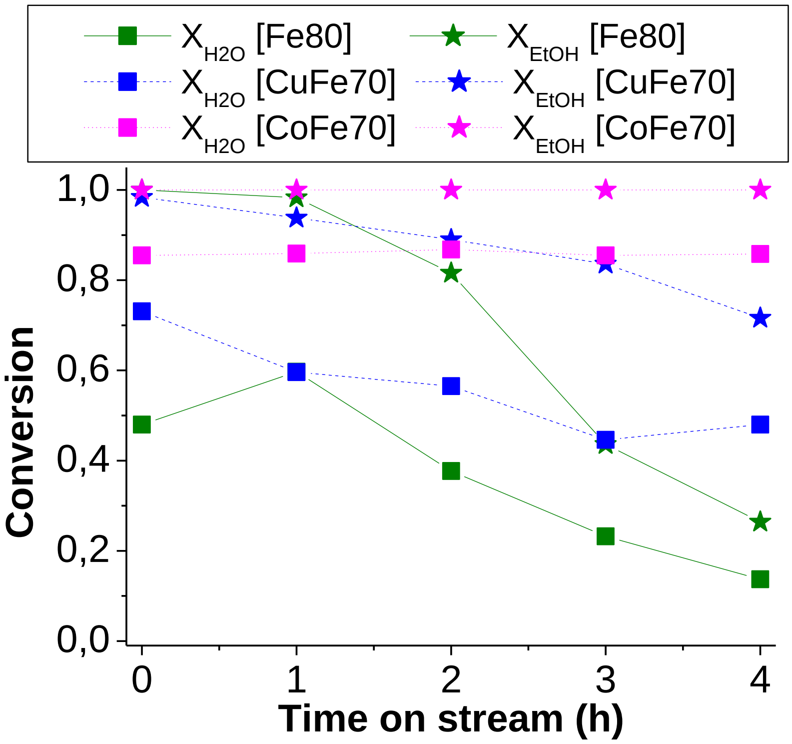

(b)

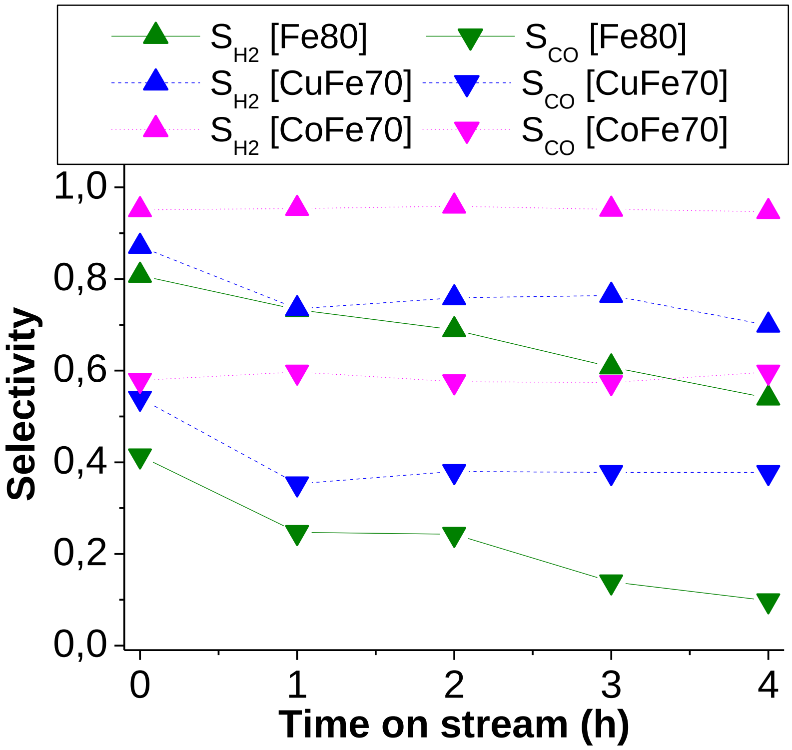

Figure 7.4. Evolution of (a) the ethanol conversion and water consumption and (b) the selectivity towards H_2 and CO with time on stream for the steam reforming of ethanol over the Fe80 (solid line), CuFe70 (dash) and CoFe70 (dot) catalysts.

7.4 Conclusions

A series of Fe-Al samples with different Fe/Al ratios and modified with Cu or Co was prepared by the precipitation method, characterised and evaluated for the steam reforming of ethanol. Higher specific surface areas and easier reducible iron species were observed for samples with lower Fe/Al ratio and for samples modified with Cu or Co. The former samples also exhibited smaller crystallites of iron oxides. These changes on the structure provided higher conversions of ethanol and water consumption and higher selectivity towards H_2 and CO for the samples with lower Fe/Al ratios and for the modified catalysts. The Co-loaded sample showed the best performance in terms of activity, selectivity and formation of coke. The results obtained point to the investigation of Cu- or Co-promoted samples with lower Fe/Al ratios.

ACKNOWLEDGEMENTS

The authors wish to thank the financial support and scholarships granted by the “Conselho Nacional de Desenvolvimento Científico e Tecnológico – CNPq” and by the “Coordenação de Aperfeiçoamento de Pessoal de Nível Superior – CAPES”.

References

Cai W.-J., Qian L.-P., Yue B., Chen X.-Y. and He H.-Y. (2013), Reforming of CH_4 with CO_2 over Co/Mg–Al oxide catalyst, *Chinese Chemical Letters*, **24**, 777-779.

Coronel L., Múnera J.F., Tarditi A.M., Moreno M.S. and Cornaglia L.M. (2014), Hydrogen production by ethanol steam reforming over Rh nanoparticles supported on lanthana/silica systems, *Applied Catalysis B: Environmental*, **160–161**, 254-266.

Crepaldi E.L., Pavan P.C. and Valim J.B. (2000), Comparative study of the coprecipitation methods for the preparation of Layered Double Hydroxides, *Journal of the Brazilian Chemical Society*, **11**, 64-70.

Davidson S., Sun J. and Wang Y. (2013), Ethanol Steam Reforming on Co/CeO_2: The Effect of ZnO Promoter, *Topics in Catalysis*, **56**, 1651-1659.

de Souza G., Ávila V.C., Marcílio N.R. and Perez-Lopez O.W. (2012a), Synthesis Gas Production by Steam Reforming of Ethanol over M-Ni-Al Hydrotalcite-type Catalysts; M = Mg, Zn, Mo, Co, *Procedia Engineering*, **42**, 1805-1815.

de Souza G., Balzaretti N.M., Marcílio N.R. and Perez-Lopez O.W. (2012b), Decomposition of Ethanol Over Ni-Al Catalysts: Effect of Copper Addition. *Procedia Engineering*, **42**, 335-345.

Dias J.A.C. and Assaf J.M. (2003) Influence of calcium content in Ni/CaO/γ-Al_2O_3 catalysts for CO_2-reforming of methane, *Catalysis Today*, **85**, 59-68.

Dry, M.E. (2002), The Fischer-Tropsch process: 1950-2000, *Catalysis Today*, **71**, 227-241.

Escobar C. and Perez-Lopez O. (2014), Hydrogen Production by Methane Decomposition Over Cu–Co–Al Mixed Oxides Activated Under Reaction Conditions, *Catalysis Letters*, **144**, 796-804.

Espinal R., Taboada E., Molins E., Chimentao R.J., Medina F. and Llorca J. (2012), Cobalt hydrotalcites as catalysts for bioethanol steam reforming. The promoting effect of potassium on catalyst activity and long-term stability, *Applied Catalysis B: Environmental*, **127**, 59-67.

Fakeeha A.H., Naeem M.A., Khan W.U. and Al-Fatesh A.S. (2014), Syngas production via CO_2 reforming of methane using Co-Sr-Al catalyst, *Journal of Industrial and Engineering Chemistry*, **20**, 549-557.

Frost R.L., Musumeci A.W., Bostrom T., Adebajo M.O., Weier M.L. and Martens W. (2005), Thermal decomposition of hydrotalcite with chromate, molybdate or sulphate in the interlayer, *Thermochimica Acta*, **429**, 179-187.

Galvita V.V., Semin G.L., Belyaev V.D., Semikolenov V.A., Tsiakaras P. and Sobyanin V.A. (2001), Synthesis gas production by steam reforming of ethanol, *Applied Catalysis A-General*, **220**, 123-127.

González Vargas O.A., de los Reyes Heredia J.A., Wang J.A., Chen L.F., Montesinos Castellanos A. and Llanos M.E. (2013), Hydrogen production over Rh/Ce-MCM-41 catalysts via ethanol steam reforming, *International Journal of Hydrogen Energy*, **38**, 13914-13925.

Hayakawa H., Tanaka H. and Fujimoto K. (2006), Studies on precipitated iron catalysts for Fischer-Tropsch synthesis, *Applied Catalysis A-General*, **310**, 24-30.

Hermes, N.A. (2010), *Hidrogênio e nanotubos de carbono por decomposição catalítica do metano: desempenho de catalisadores à base de cobalto e alumínio*. MSc. Thesis. UFRGS, Porto Alegre.

Hermes N.A., Lansarin M.A. and Perez-Lopez O.W. (2011), Catalytic Decomposition of Methane Over M-Co-Al Catalysts (M = Mg, Ni, Zn, Cu), *Catalysis Letters*, **141**, 1018-1025.

Huber G.W., Chheda J.N., Barrett C.J. and Dumesic J.A. (2005), Production of liquid alkanes by aqueous-phase processing of biomass-derived carbohydrates, *Science*, **308**, 1446-1450.

Jones G., Jakobsen J.G., Shim S.S., Kleis J., Andersson M.P., Rossmeisl J., Abild-Pedersen F., Bligaard T., Helveg S., Hinnemann B., Rostrup-Nielsen J.R., Chorkendorff I., Sehested J. and Nørskov J.K. (2008), First principles calculations and experimental insight into methane steam reforming over transition metal catalysts, *Journal of Catalysis*, **259**, 147-160.

Li W., Wang H., Ren Z., Wang G. and Bai J. (2008), Co-production of hydrogen and multi-wall carbon nanotubes from ethanol decomposition over Fe/Al_2O_3 catalysts, *Applied Catalysis B-Environmental*, **84**, 433-439.

Lira E., Lopez C.M., Oropeza F., Bartolini M., Alvarez J., Goldwasser M., Linares F.L., Lamonier J.-F. and Zurita M.J.P. (2008), HMS mesoporous silica as cobalt support for the Fischer-Tropsch Synthesis: Pretreatment, cobalt loading and particle size effects, *Journal of Molecular Catalysis A-Chemical*, **281**, 146-153.

Oliveira A.C. and Rangel M.d.C. (2003), Desidrogenação do etilbenzeno sobre compostos de ferro e alumínio, *Química Nova*, **26**, 170-176.

Palmer S.J., Spratt H.J. and Frost R.L. (2009), Thermal decomposition of hydrotalcites with variable cationic ratios, *Journal of Thermal Analysis and Calorimetry*, **95**, 123-129.

Ponton Lozano S., Montoya Gómez N.Y., Martínez Sepúlveda J.A., Cañizares Cañizares P. and Fernández Morales F.J. (2014), Study of pre-treatments for an enhanced bio-ethanol production from the organic fraction of municipal solid wastes, *Global NEST Journal*, **16**

Rostrup-Nielsen J.R. (2005), Making fuels from biomass, *Science*, **308**, 1421-1422.

Song L.X., Chen J., Zhu L.H., Xia J. and Yang J. (2011), Modification in Structure, Phase Transition, and Magnetic Property of Metallic Gallium Driven by Atom–Molecule Interactions, *Inorganic Chemistry*, **50**, 7988-7996.

Souza G., Ruoso C., Balzaretti N.M., Marcilio N.R. and Perez-Lopez O.W. (2012), Synthesis gas and carbon nanotubes production from catalytic decomposition of renewable resources. *Proceedings Venice 2012, Fourth International Symposium on Energy from Biomass and Waste* (ed by, p. PG09. San Servolo - Venice.

Vaccari A. (1998), Preparation and catalytic properties of cationic and anionic clays, *Catalysis Today*, **41**, 53-71.

Wan H., Wu B., Zhang C., Xiang H. and Li Y. (2008), Promotional effects of Cu and K on precipitated iron-based catalysts for Fischer-Tropsch synthesis, *Journal of Molecular Catalysis A-Chemical*, **283**, 33-42.

Wang G., Wang H., Li W., Ren Z., Bai J. and Bai J. (2011), Efficient production of hydrogen and multi-walled carbon nanotubes from ethanol over Fe/Al_2O_3 catalysts, *Fuel Processing Technology*, **92**, 531-540.

Wang W. and Wang Y. (2010), Steam reforming of ethanol to hydrogen over nickel metal catalysts, *International Journal of Energy Research*, **34**, 1285-1290.

Zhang B., Cai W., Li Y., Xu Y. and Shen W. (2008a), Hydrogen production by steam reforming of ethanol over an Ir/CeO_2 catalyst: Reaction mechanism and stability of the catalyst, *International Journal of Hydrogen Energy*, **33**, 4377-4386.

Zhang C.H., Yang Y., Teng B.T., Li T.Z., Zheng H.Y., Xiang H.W. and Li Y.W. (2006), Study of an iron-manganese Fischer-Tropsch synthesis catalyst promoted with copper, *Journal of Catalysis*, **237**, 405-415.

Zhang L., Li W., Liu J., Guo C., Wang Y. and Zhang J. (2009a), Ethanol steam reforming reactions over $Al_2O_3 \cdot SiO_2$-supported Ni–La catalysts, *Fuel*, **88**, 511-518.

Zhang L., Millet J.-M.M. and Ozkan U.S. (2009b), Effect of Cu loading on the catalytic performance of Fe-Al-Cu for water-gas shift reaction, *Applied Catalysis A-General*, **357**, 66-72.

Zhang L.H., Xiang X., Zhang L., Li F., Zhu J., Evans D.G. and Duan X. (2008b), Influence of iron substitution on formation and structure of Cu-based mixed oxides derived from layered double hydroxides, *Journal of Physics and Chemistry of Solids*, **69**, 1098-1101.

Capítulo 8

Dry reforming of methane at moderate temperatures over modified Co-Al co-precipitated catalysts

Artigo publicado no periódico: *Materials Research – Ibero-american Journal of Materials*, em julho de 2014.

Dry reforming of methane at moderate temperatures over modified Co-Al co-precipitated catalysts

Guilherme de Souza[a], Nilson R. Marcilio[a], Oscar W. Perez-Lopez[*,a]

[a] *Department of Chemical Engineering, UFRGS - Federal University of Rio Grande do Sul, R. Eng. Luiz Englert s/n, 90040-040 Porto Alegre, RS, Brazil*

[*] Corresponding author: Tel.: +55 (51) 3308.3953; fax: +55 (51) 3308.3277. E-mail address: perez@enq.ufrgs.br (O.W. Perez-Lopez).

Abstract

M-Co-Al (M = Ca, La, Li or Mg) materials were synthesised by co-precipitation and investigated for dry reforming of methane. Thermogravimetry, temperature-programmed oxidation, reduction and CO_2 desorption, specific area and X-ray diffraction were utilised for characterisation. Activity tests were conducted at atmospheric pressure, temperatures between 400-550°C , CH_4/CO_2 molar ratio of 1 and GHSV of 6000 NmL $CH_4 \cdot g^{-1} \cdot h^{-1}$. The partial substitution of Co by a third element increased the area and changed the acid/base properties, reducibility and crystallinity of the oxides. These modifications resulted in higher activity for dry reforming of methane, mainly related to the decrease in the acidity of the promoted materials and, consequently, lower carbon formation. The Li-modified sample presented the lowest coke deposition due to the increase in stronger basic sites. The Mg-promoted catalyst exhibited the best activity performance. This depicts the enhancement in the reducibility and acid/base properties found in the MgCoAl sample.

Keywords: Dry reforming of methane; Co-based catalyst; carbon deposition; precipitation method, mixed oxides.

8.1. Introduction

Carbon dioxide reforming of methane is an interesting route for converting natural gas into synthesis gas (or syngas), which can generate a wide range of products such as clean transportation fuels and other chemicals. The increase in the known reserves of natural gas and the feasibility of exploring natural reserves in remote locations several kilometres from the coast and in small fields stimulate the development of Gas-To-Liquids (GTL) technology. These reserves usually cannot be monetised by using conventional technologies such as pipelines or liquefied natural gas [1, 2], promoting the conversion in loco of the gas. The process is also environmentally friendly because fuels are being produced from both greenhouse gases in this case.

The transition metals from group VIII of the periodic table are active for reforming processes. Among the referred elements, the literature points to Ru and Rh as the most active metals, followed by Ni, Ir, Pt, Pd and Co [3, 4]. The catalysts based on noble metals exhibit a lower carbon formation rate compared to Ni- and Co-samples, leading to less dissolution of carbon into these metals [4]. However, the lower price is an incentive for the use of Ni- and Co-based catalysts, mainly Ni-samples. Nickel presents very high activity for methanation, so its fines could possibly promote this reaction for the downstream tail gas. Therefore, cobalt catalysts could be an interesting alternative that avoids this drawback [5]. Moreover, related papers reported higher activity for Co-based catalysts compared to Ni-based samples that were prepared either by the precipitation or impregnation methods [6, 7].

So far, most of the studies for dry reforming of methane over cobalt materials in the literature explore supported catalysts [5, 8, 9]. For dry reforming of methane over Co-supported catalysts, previous works showed that the presence of alkalis or small quantities of noble metals could slow down the reoxidation of metallic cobalt and the formation of coke [5, 10, 11]. For example, Bouarab et al. showed that the addition of

La_2O_3 or MgO to Co/SiO_2 could change the acid-base properties of this material [5]. As a result, this material inhibits coke formation by the adsorption of CO_2 species on the surface and hence promotes CO_2 reaction with deposited carbon by the reverse of the Boudouard reaction [5]. In the same way, Fakeeha and co-workers revealed that addition of Sr leads to coke suppression by improving the interaction between Co and the support and the Lewis basicity of the samples [12]. Similar results for alkali promotion were observed for Ni-based catalysts, which included K, Li, La, Mg, Ba and Ca [13-19]. Moreover, this promotion can be performed by adding the alkali directly during the synthesis of co-precipitated samples. This preparation method can originate mixed oxides, which have desirable properties such as high surface area, high thermal stability and small crystallite sizes [20, 21]. Indeed, several nickel-spinel oxides have shown excellent results for dry reforming of methane [22-28]. According to Bhattacharyya et al., the mixed oxide materials derived from a hydrotalcite-type (HT) structure might provide a random distribution of the divalent metal ions (M^{2+}) in the layered structure. The active metal ions should be surrounded by other ions that might minimise aggregation and thus prevent sintering and coke formation [26]. Additionally, promising results have been achieved by similar mixed oxide materials based on cobalt in different processes [29-31], and these results lead to the investigation of dry reforming of CH_4 on Co-mixed oxide catalysts.

The present work investigates the two mentioned strategies, i.e., the CO_2 reforming of methane over Co-Al mixed oxide materials modified with alkali elements such as Ca, La, Li or Mg. The third element was chosen based on the effect of slowing down the reoxidation of metallic Ni or Co described earlier. The different charges and ionic radii, which increase in the order $Li^+ < Mg^{2+} < Co^{2+} < Ca^{2+} < La^{3+}$, were also taken into account for selecting the metal because these properties can lead to different structures of the mixed oxides.

8.2. Experimental

The catalysts were synthesised by the co-precipitation method using two aqueous solutions. The first solution contained an aqueous mixture of aluminium nitrate and cobalt nitrate, and for the modified Co-Al samples a third nitrate salt was added (Ca, Li, La or Mg). An aqueous solution of Na_2CO_3 was used as the precipitant. Both solutions were continuously added into a continuous stirred-tank reactor (CSTR) at a constant temperature (50°C) and pH (8 ± 0.1). The precipitate was collected and kept under stirring at 50°C for 1 h. After crystallisation, the precipitate was vacuum filtered and washed with deionised water. This process was conducted until the conductivity value of the filtrate was lower than 50 $\mu S \cdot cm^{-1}$. This value ensures that the ions from the precursors (mostly Na^+) were almost completely removed. Then, the material was dried at 80°C for 24 h in an oven. The obtained solids were crushed and sieved to the desired particle sizes ($355 < d_p < 500$ µm) and calcined under a continuous air flow (50 $mL \cdot min^{-1}$) at 600°C for 6 h.

The materials were characterised by surface area measurements (S_{BET}), thermogravimetry (TG/DTA), X-ray diffraction (XRD), temperature-programmed reduction (H_2-TPR), temperature-programmed desorption of dioxide carbon (CO_2-TPD) and temperature-programmed oxidation (TPO/DTA). The XRD patterns were collected with a Bruker D2 Phaser X-ray diffractometer using CuKα radiation. The Co^0 apparent crystallite sizes were calculated by the Scherrer equation from the reflection at 44.3°. The TG/DTA and TPO/DTA analysis were performed in a TA thermobalance (Model SDT Q600). After pretreatment at room temperature with N_2 flow, 10 mg of uncalcined (TG/DTA) or spent sample (TPO/DTA) was heated to approximately 850°C at a rate of 10°C·min^{-1} under an air flow rate of 100 $mL \cdot min^{-1}$. The S_{BET} were obtained by the N_2 dynamic adsorption method at the normal boiling point of N_2 (-196°C). The CO_2-TPD curves were collected using a multipurpose system (SAMP3). Approximately 100 mg of the calcined sample was placed in a quartz tube located in a temperature-controlled oven. After being outgassed at 250°C under N_2 flow for 1 h, the sample was saturated with CO_2 at 100°C for 30 min followed by a purge with He for 30 min. The desorption curves were recorded with a thermal conductivity detector (TCD) by increasing the temperature form 100°C to 600°C (10°C·min^{-1}) under a 30 mL·min^{-1} He flow. The H_2-TPR analysis was carried out in the same multipurpose system, where the temperature was increased to *ca.* 900°C (10°C·min^{-1}) using 30 mL·min^{-1} of a reduction mixture containing 10% H_2/N_2 (v/v).

The dry reforming of methane tests were performed under atmospheric pressure in a fixed-bed quartz reactor (½ in. diameter) loaded with 100 mg of catalyst diluted with quartz (1:2 v/v) and using quartz wool as the support for the catalytic bed. The samples were reduced in situ for 1 h at 700°C (5°C·min^{-1}) under 50 mL·min^{-1} of a 10%H_2/N_2 (v/v) mixture prior to the reactions. The runs were carried out at temperatures between 400 and 550°C using a CO_2/CH_4 molar ratio of 1. These operational conditions might coincide with regions of increased thermodynamic potential for carbon formation [32, 33], which is a more interesting condition to investigate the effect of alkali promotion on the deactivation of catalyst due to coke deposition. The gas hourly space velocity (GHSV) was approximately 6000 mL CH_4·g^{-1}·h^{-1}. The CH_4 and CO_2 conversions were calculated using an on-line gas chromatograph equipped with a TCD. The reactor exit gas mixture was injected three times at each reaction temperature value (average standard deviation < 1). The conversion values were obtained by the difference between the measured area and the corresponding area collected in blank injections, which was performed by bypassing the reactor. The reaction was also kept at 500°C for 5 h to evaluate the thermal stability and the coke deposition.

8.3 Results and discussion

The catalyst nomenclature, the nominal composition and the TGA/DTA results are summarised in Table 8.1. The thermogravimetric curves obtained for the LiCoAl sample are presented in Fig. 8.1, which includes the derivative thermogravimetric analysis (DTG) and the differential thermal analysis (DTA).

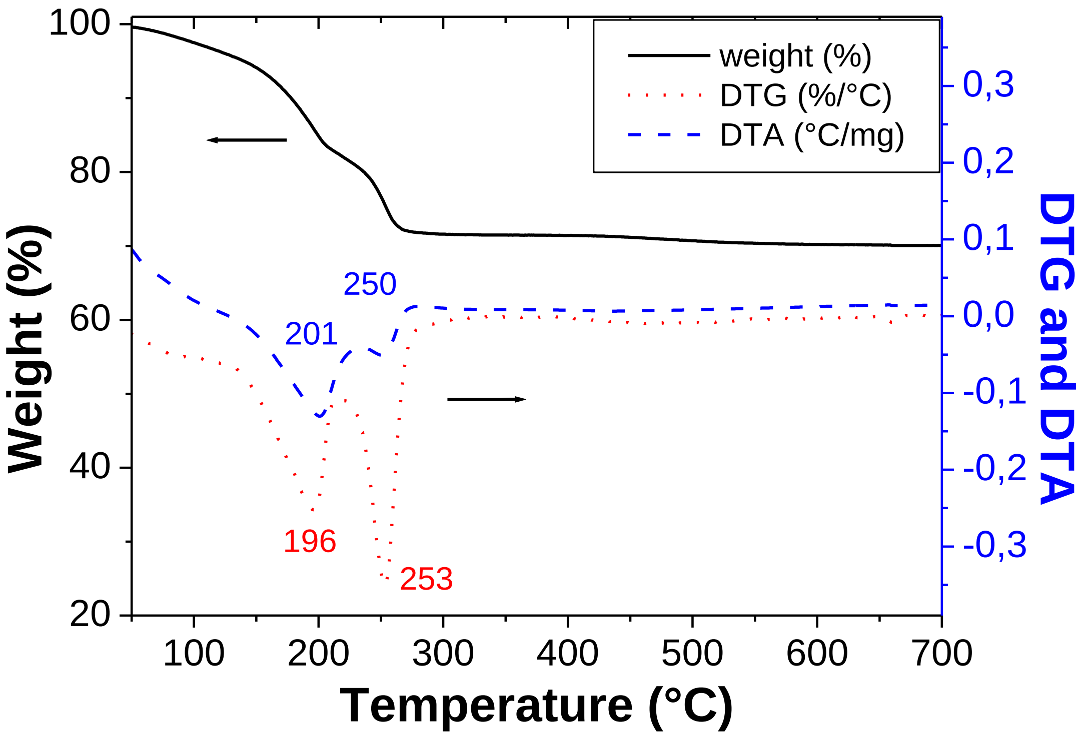

Figure 8.1. Thermogravimetric curves collected for the LiCoAl sample: weight (solid line), derivative thermogravimetry (dotted line) and differential thermal analysis (dashed line).

Table 8.1. Weight loss and DTA data obtained from thermogravimetry for uncalcined samples.

Sample	Third element (M)	Composition (mol %)			Total weight loss (%)	DTA peak temperature (°C)		
		M	Co	Al		1st peak	2nd peak	3rd peak
CoAl	-	0.0	66.7	33.3	27.1	209	248	-
CaCoAl	Ca	11.1	55.6	33.3	34.9	206	249	-
LaCoAl	La	11.1	55.6	33.3	27.3	200	248	441
LiCoAl	Li	11.1	55.6	33.3	29.8	201	250	-
MgCoAl	Mg	11.1	55.6	33.3	31.0	211	268	-

As illustrated in Figure 8.1, two major weight losses and endothermic peaks are observed. The first weight loss (approximately 15 to 20%) is an endothermic event that takes place at temperatures between 200 and 211°C. This transition is related to the release of interlayer water molecules from the structure. The second DTG-DTA peak occurs at temperatures between 248 and 268°C and is commonly ascribed to the removal of hydroxyl host-layers and CO_3^{2-} from the structure [34], although this peak might include the release of NO provided by the decomposition of nitrates from the precursors. Table 8.1 shows that the second peak is shifted towards higher temperatures for the MgCoAl sample, which suggests a higher thermal stability for this material [35]. The endothermic effects are typically observed in the thermal decomposition of anionic clays [36-38]. These peaks indicate that the layered structure collapses below 400°C, yielding the mixed metal oxides [39]. Nonetheless, the LaCoAl sample exhibits an additional endothermic DTA peak located at 441°C, which is followed by a small weight loss (not showed). This phenomenon should be related to changes in the oxidative state of La. The total weight loss varies between 27.1 and 34.9%. The position and the relative intensity of the DTG peaks are similar to the results reported by Wang et al. [40] for Co-Al catalysts synthesised with a similar method.

The measurements of the BET specific surface area are shown in Table 8.2.

Table 8.2. BET surface area, degree of reduction (%) and Co^0 apparent crystallite diameter by XRD for calcined and reduced samples, respectively.

Sample	S_{BET} (m^2/g)	Degree of reduction (%)	d by XRD (nm)
CoAl	54	73	22
CaCoAl	64	69	34
LaCoAl	68	73	26
LiCoAl	56	73	25
MgCoAl	67	94	29

The standard sample (CoAl) exhibits a surface area value of 54 $m^2 \cdot g^{-1}$. The specific surface area reported herein is the same value that was previously obtained for similar precipitated Co-Al materials calcined at 600°C [41]. The partial substitution of Co by a third element with alkaline character increases the surface area. Although the modification with La gives the highest area, high areas (between 64 and 67 $m^2 \cdot g^{-1}$) are clearly achieved when Co is partly substituted by another divalent element because the M^{2+}/M^{3+} ratio is kept at the same value claimed to form pure phases of HT compounds [20]. Indeed, the partial substitution of Co^{2+} by Li^+ minimally changes the surface area. The results suggest that the changes in the specific surface area might be related to the formation of different mixed oxide phases rather than the electronic aspects or ionic radii of the elements.

The XRD patterns of the calcined catalysts are shown in Fig. 8.2.

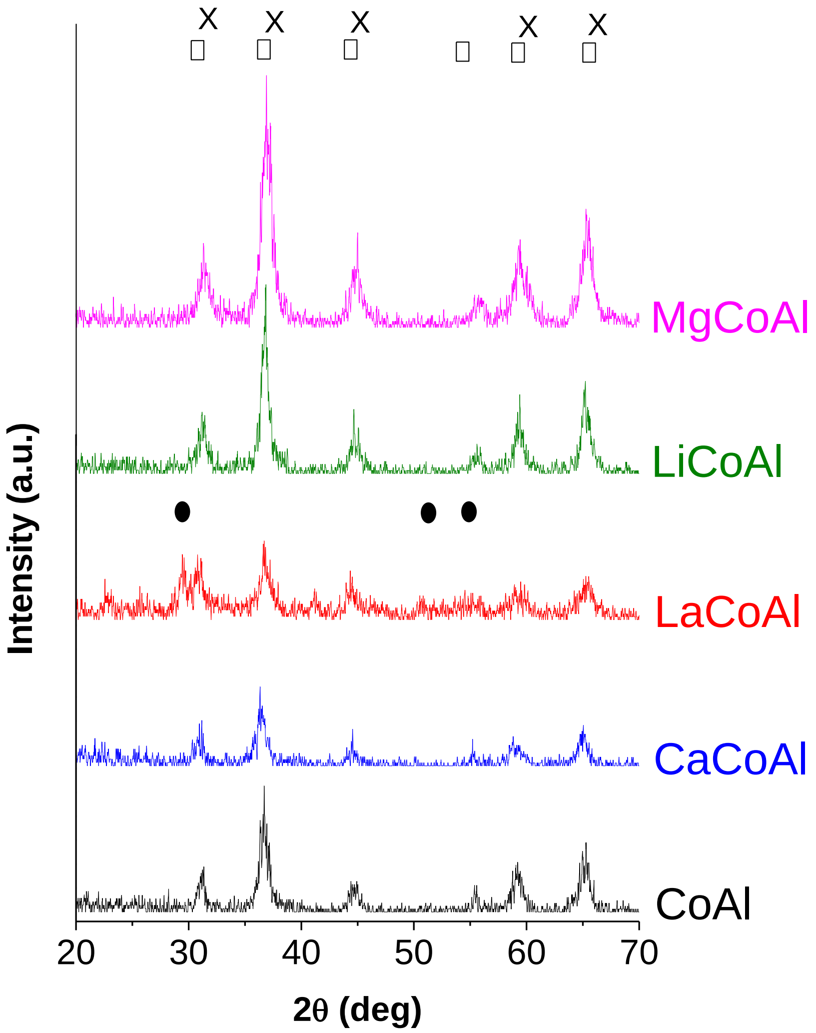

Figure 8.2. XRD patterns for calcined samples.
Identified crystalline phases: (□) Co_3O_4; (X) $CoAl_2O_4$; (●) La_2O_3.

The catalysts exhibit similar patterns, with poorly crystalline structures, where the diffraction reflections assigned to the Co_3O_4 and the $CoAl_2O_4$ crystalline phases were detected for all the samples. Our group found the same cobalt oxide phases for the Cu-Co-Al catalysts, in which the promoter oxide also could not be observed, mostly due to the lower amount of this oxide [42]. Similar results regarding the formation of a lesser crystalline structure for the supported La-Co/Al_2O_3 catalyst was also reported by Hu & Lu (2010)[43]. For the LaCoAl catalyst, additional reflections indicate the presence of a segregated La_2O_3 phase. The Co_3O_4 crystallite sizes cannot be accurately estimated by XRD because of the low peak intensities and the overlapping of diffraction peaks from both the identified Co oxide phases. However, changes in the crystallinity are caused by the presence of a third element. Indeed, the MgCoAl and LiCoAl samples show an increase in crystallinity, indicating the formation of a higher ordered mixed oxide structure.

The H_2-TPR curves of the calcined samples are presented in Figure 8.3.

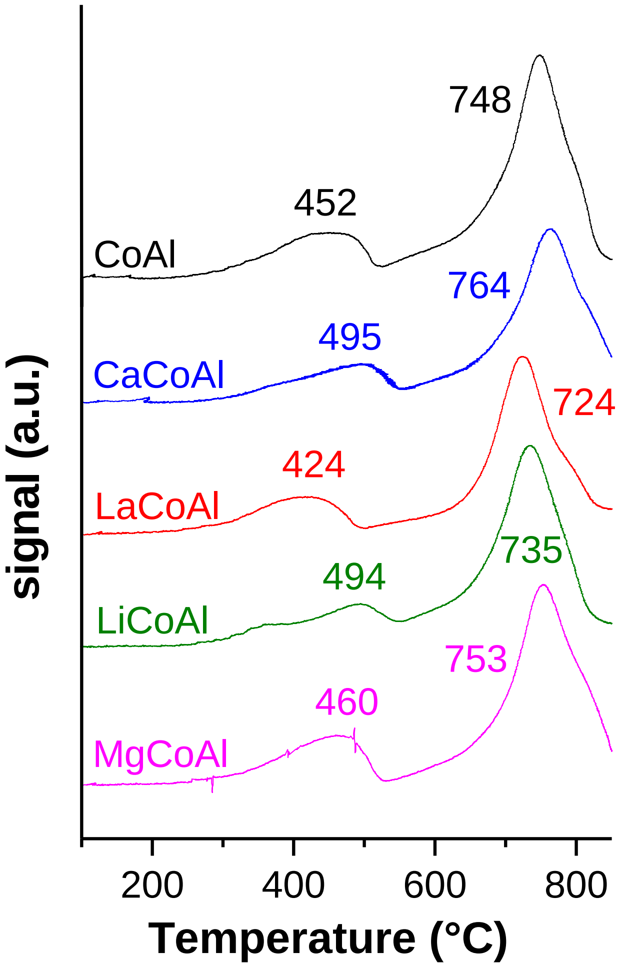

Figure 8.3. H_2-TPR profiles.

The reduction peak centred at 424 – 495°C corresponds to the reduction of bulk cobalt oxide identified by XRD (i.e., $Co_3O_4 \rightarrow CoO \rightarrow Co^0$) [30, 44, 45]. Additionally, the peak centred at higher temperatures (724 – 764°C) can be ascribed to the reduction of $CoAl_2O_4$ phase, which should occur at higher temperatures due to the increased stabilisation of the Co^{2+} ions by the Al^{3+} ions in the spinel phase [8, 30, 46, 47]. Furthermore, the uptake of H_2 at higher temperatures might include the reduction of other mixed oxide phases containing the promoters. Thereby, the reduction of mixed oxides such as $LaCoO_3$ [48] and $Co_4Mg_2Al_2$ [49] should take place at these temperatures. Although the referred mixed oxides cannot be identified by XRD due to the small peak intensities (Figure 8.2), the existence of such phases cannot be disregarded.

The overall shape of curves does not change significantly with the addition of a third element, but the reducibility of the phases and the degree of reduction are modified. Except for the MgCoAl samples, the area of peaks decreases for the modified catalysts, mostly because there is a lower content of Co oxide to be reduced to the metallic phase. Indeed, the surface area measurements (Table 8.2) and the XRD patterns (Fig. 8.2) reveal an influence of alkali content on crystallinity, while the TPR highlights that these modifications impact the reduction of the Co species. The partial substitution of Co by Li or La increases the reducibility of the $CoAl_2O_4$ phase, whereas an opposite trend is observed when Co is partly substituted by Mg or Ca. The latter behaviour depicts a stronger interaction between the Co oxide and the MgO- or CaO-modified support, which requires higher temperatures to be reduced. These results follow the same trend observed for other Mg-Co-Al and for CaO-Ni/Al_2O_3 catalysts with similar loadings for the promoters [14, 16, 29]. Among the M-Co-Al catalysts, the LaCoAl sample exhibits well-defined behaviour, because both reduction peaks are located at significantly lower temperatures. This change in the reduction temperatures for LaCoAl might be caused by the presence of the segregated La_2O_3 phase (see the XRD pattern in Fig. 8.2). The La oxide was found to promote the reduction of the Co species at lower temperatures [48], which might weaken the interaction of Co with the Al oxide. Aside from the effect on the reduction temperatures, Table 8.2 shows that the alkalis do not change the degree of reduction with respect to the CoAl sample, except for the MgCoAl catalyst. This latter material exhibited an enhanced degree of reduction compared to the other samples (20% higher). Apparently, magnesium causes changes in the properties of the material so that a higher fraction of the Co in the mixed oxides could be reduced to metallic cobalt.

Table 8.2 also shows the apparent Co^0 crystallite size estimated from the XRD patterns for the reduced samples. Higher Co^0 diameters are observed for the modified catalysts. The Co^0 average size increases in the following order: CoAl < LiCoAl ≈ LaCoAl < MgCoAl < CaCoAl.

The CO_2 desorption curves are exhibited in Figure 8.4.

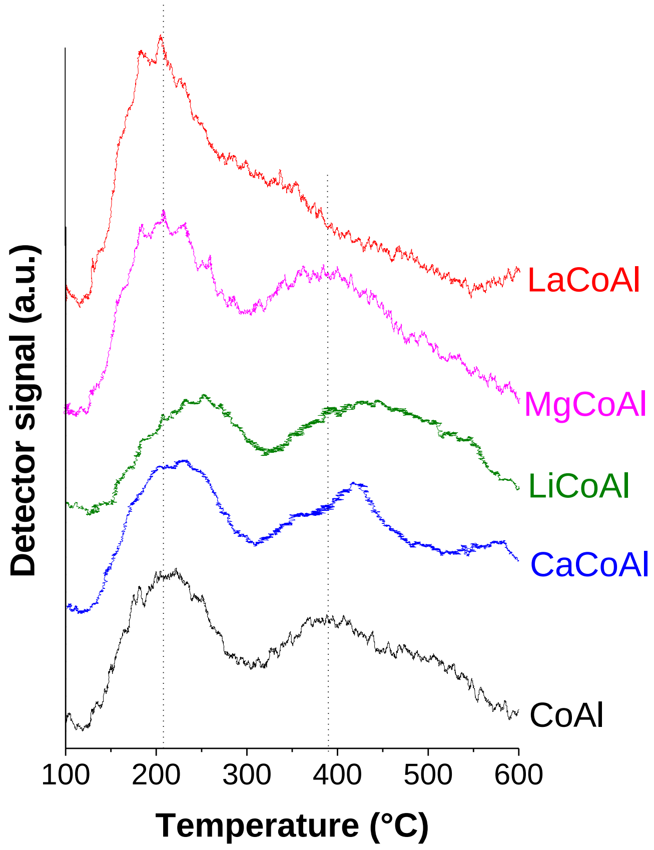

Figure 8.4. CO_2-TPD curves.

There are at least two peaks overlapped for all samples. The first peak in the range 150 – 300°C represents sites with weak alkalinity, while the peaks at higher temperatures (in the range 300 – 600°C) are related to the desorption of CO_2 from stronger basic sites. Additionally, Table 8.3 presents the estimated temperature for the different types of sites by deconvolution of the peaks.

Table 8.3. CO_2-TPD data for calcined samples.

Sample	Sites with weaker alkalinity		Sites with stronger alkalinity			
	1st peak (°C)	Area (a.u.)	1st peak (°C)	2nd peak (°C)	3rd peak (°C)	Area (a.u.)
CoAl	209	286	381	503	-	455
CaCoAl	218	345	352	418	579	534
LaCoAl	196	202	307	536	-	641
LiCoAl	233	140	454	-	-	400
MgCoAl	204	345	382	551	-	797

The total area of the sites with weaker and stronger alkalinity provides an idea about the amount of each type of site. From Figure 8.4, the curves have different shapes according to the promoter added to the sample. The LaCoAl catalyst exhibits a different profile because the peaks are predominantly shifted towards lower temperatures. This behaviour indicates that the strength of the basic sites is weaker for this material. The TPD profile for LaCoAl might be related to its different structure, mainly to the segregated La_2O_3 phase observed by XRD (Figure 8.2) for this sample. The areas related to CO_2 uptake in Table 8.3 reveal an increase in the amount of sites with higher alkalinity for all the modified samples, except for LiCoAl. Thus, the overall CO_2-TPD profiles depict the enhancement in the Lewis basicity of samples. Fakeeha et al. (2014) observed the same trend for Sr-promoted Co-Al catalysts [12]. However, Figure 8.4 highlights that the peaks are shifted towards higher temperatures for the LiCoAl material, thus providing evidence of the role of Li in the strength of the alkaline sites for this catalyst. The MgCoAl catalyst exhibited the highest amount of both the weaker and the stronger basic sites according to the area values showed in Table 8.3. This result is in agreement with the different structure that led to the higher degree of reduction displayed by MgCoAl (see Table 8.2).

The catalytic performance at different reaction temperatures is shown in Figure 8.5 and Figure 8.6.

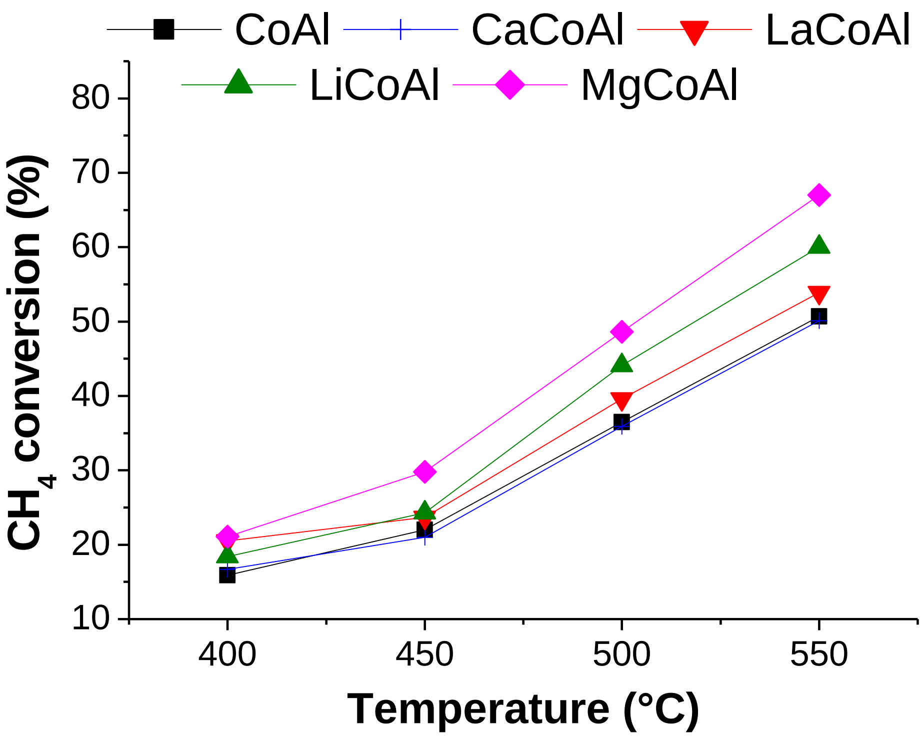

Figure 8.5. CH_4 conversion vs. reaction temperature.

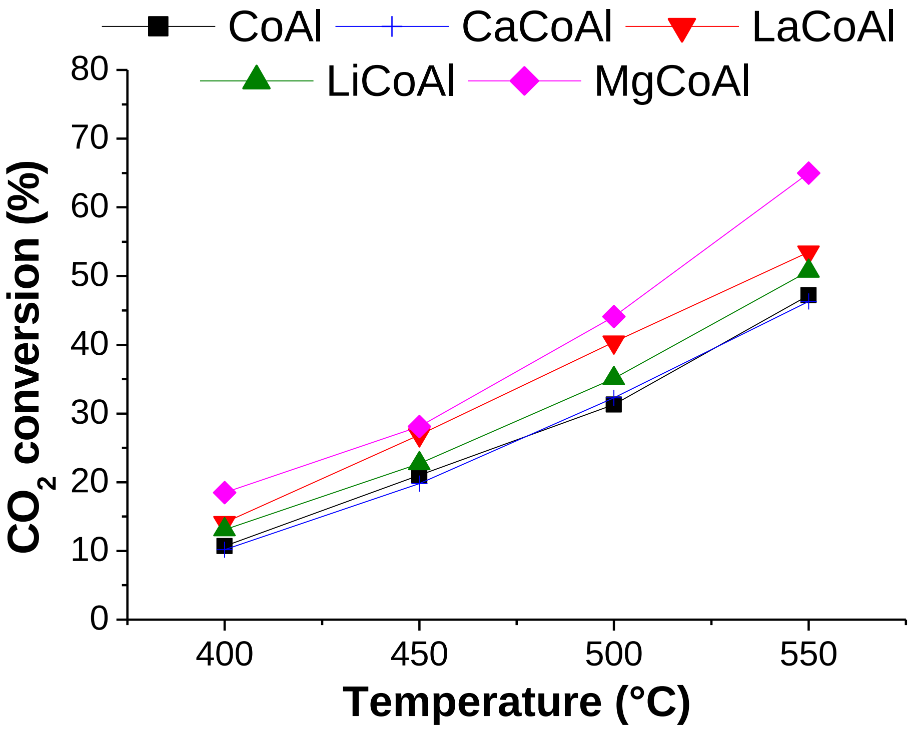

Figure 8.6. CO_2 conversion vs. reaction temperature.

Higher conversions of CH_4 and CO_2 are observed using the MgCoAl catalyst at all the reaction temperatures. The catalytic performance of both the LaCoAl and the LiCoAl catalysts also improves at higher temperatures, while the other two catalysts (i.e., CoAl and CaCoAl) exhibit similar results. Therefore, the activity tests in Figure 8.5 cannot be correlated to the surface area and Co^0 crystallite diameters (Table 8.2). Higher conversions of both gases is exhibited by the LaCoAl, LiCoAl and MgCoAl catalysts, and this result is possibly related to the significant changes in the number (MgCoAl and LaCoAl) and strength (LiCoAl) of the basic sites in these samples, as shown in the TPD curves (see Table 8.3 and Figure 8.4). The alkali promotion might minimise carbon formation and hence favour the accessibility of reactants to the active sites. The same effect on activity was also reported by Fakeeha and co-workers (2014) for Sr-promoted cobalt catalysts [12]. Additionally, the higher degree of reduction exhibited by MgCoAl (Table 8.2) also contributes to higher activity because the metallic Co phase is more active than the Co oxide species for the reforming reaction. The increase in the performance of Co-based catalysts promoted with small amounts of Mg was also observed for the partial oxidation of methane [50, 51], as well as for Mg-Ni-Al catalysts for dry reforming [22]. The best activity of the Mg-promoted sample was also found for supported Co-based catalysts promoted with earth metals for combined partial oxidation and CO_2 reforming of methane to produce synthesis gas [52, 53]. For the mixed oxides herein reported, the increase in the performance appears to be mostly related to the changes in the basicity of the active sites provided by the interaction between the alkali and Co oxides because the modified samples exhibit larger Co^0 crystallite diameters compared to CoAl. As postulated elsewhere for Ni-supported samples [15], the increase in the conversion of CO_2 by the promotion of an alkali might be due to the formation of strongly ionic oxides. These oxides may attract the CO_2 to the surface, increasing the conversion of methane as well. However, by adding a more electropositive alkali (Ca), the cobalt electron density tends to increase significantly. The change in the electronic density should decrease the adsorption of methane and carbon dioxide. The decrease in adsorption could explain the lower effect of Ca promotion on the activity found for CaCoAl.

The data for stability runs and carbon deposition on spent catalysts after 5 h at 500°C is summarised in Figures 8.7 and 8.8, respectively.

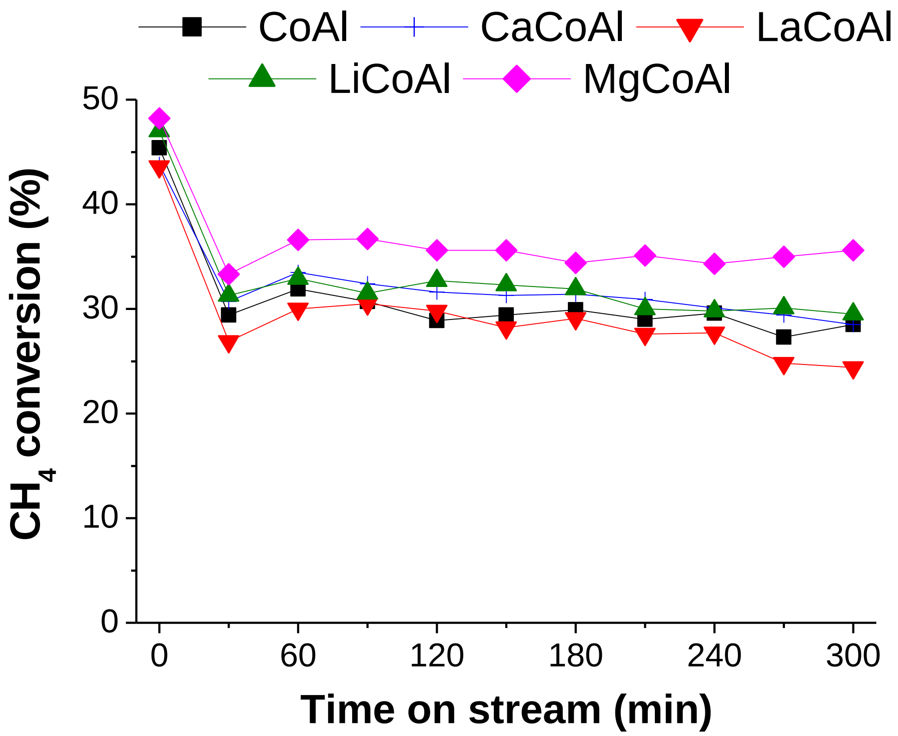

Figure 8.7. Evolution of CH_4 conversion with time on stream.

Figure 8.7 shows a rapid decrease in the conversion of methane at the beginning of the reaction. As reported elsewhere, the three major phenomena that cause catalyst deactivation during dry reforming of methane are sintering, metal oxidation and coking [8, 9]. Initially, Co^0 reoxidation might take place due to the presence of oxygen from the dissociation of CO_2 because the coke accumulation and metal sintering mechanisms deactivate the catalyst more steadily and hence should require larger periods to affect the activity. After the aforementioned decrease in the methane conversion, catalysts show a stable activity profile, except for LaCoAl. Apparently, this sample has smaller CH_4 conversions at the end of reaction, which could suggest that LaCoAl could deactivate faster due to sintering for longer runs. Among the investigated catalysts, LaCoAl appears to be the most susceptible to sintering because the TPR profiles (as shown in Figure 8.3) show that these Co oxide species reduce at the lowest temperatures, especially the segregated Co_3O_4 phase. While the performance of CoAl, CaCoAl and LiCoAl is similar during the stability runs, the enhanced performance for the MgCoAl is remarkable. This performance follows the improved results found for this sample during tests at different reaction temperatures (see Figure 8.5 and Figure 8.6).

Figure 8.8 displays the DTA peaks associated with the combustion of carbon and the relative amount of coke formed compared to the standard Co-Al sample (in parenthesis).

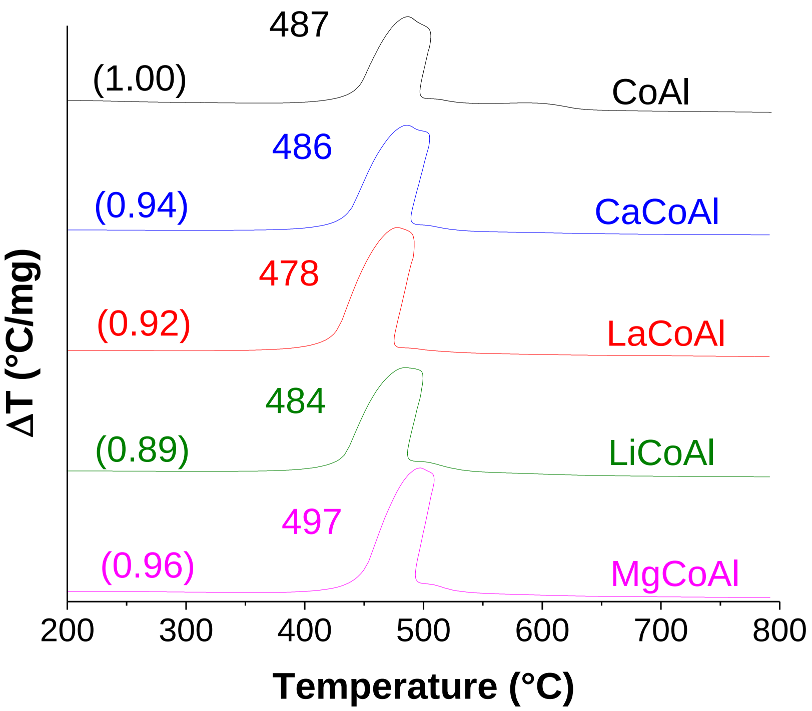

Figure 8.8. TPO/DTA curves for spent catalysts.

For these materials, the major drawback of adding the alkali is the growth in the size of the Co^0 sites (Table 8.2). For the reforming processes, larger crystallites of the active metal are believed to promote coke formation, which is mainly observed for Ni-based catalysts [26]. However, Figure 8.8 shows that the carbon formation is lower for the modified catalysts because the addition of an alkali provides an increase in the number or strength of the basic sites (see the CO_2-TPD results in Table 8.3 and Figure 8.4). Among the modified catalysts, the amount of carbon formed following the conversion of CH_4 is displayed in Figure 8.5, except for LiCoAl. Indeed, this material experienced the lowest amount of carbon deposition. This result highlights the role of increased strength of the basic sites because the LiCoAl catalyst displayed the highest increase in strength for both the sites with weak and intermediate alkalinity while maintaining a high conversion of methane and carbon dioxide. Moreover, the Co^0 crystallite size for LiCoAl is similar to the standard CoAl catalyst (Table 8.2) and might contribute to lower carbon deposition on this catalyst. Significantly less carbon forms using the LaCoAl catalyst compared to CoAl. This result is expected because of the higher amount of basic sites found on this material (Table 8.3). Moreover, the conversion of methane with time on stream after 4 h is lower for this sample (Figure 8.7), which would also be related to the low carbon deposition for the LaCoAl catalysts.

On the other hand, the DTA peaks associated with the combustion of carbon indicate that the temperature required for regeneration is similar. However, the coke formed by MgCoAl is oxidised at a temperature only 10°C higher than the standard CoAl catalyst.

Pronounced accumulation of carbon is known to occur for reforming of methane over cobalt catalysts with large crystallite sizes because small particles favour carbon gasification by CO_2 [54]. However, the overall stability of the catalysts in Figure 8.7 suggests that the carbon deposits do not cover all the active sites, and some of the sites are still available for the chemisorption and dissociation of methane and carbon dioxide. The literature reports that amorphous carbon could easily cover all the active sites, while filamentous carbon can grow without covering the metal surface [8]. Amorphous carbon oxidises at approximately 400°C, while the DTA peaks in Figure 8.8 are centred at ca. 490°C, which could be assigned to carbon nanotubes or nanofibres [27, 29, 42]. Therefore, the TPO/DTA analysis suggests that filamentous carbon is formed for the Co-Al samples investigated herein. This affirmation is also supported by scanning electronic microscopy (SEM) and Raman spectra collected by our group for the decomposition of methane or ethanol over similar Co-Al mixed oxides [29, 55]. For both cases, the SEM images show filamentous tubes that cover the particle surface for the spent catalysts. Specifically, the ratio between the D- and G-bands from the Raman spectra suggest that multi-walled carbon nanotubes (MWCNT) or nanofibres are deposited on catalyst surface after ethanol decomposition. De Sousa et al. observed the same MWCNT structure for dry reforming of methane over Ni-spinel oxides [27]. The $CoAl_2O_4$ species are also ascribed to prevent carbon deposition that could lead to deactivation after coking [9]. Based on previous results and on a review of the literature for the relationship between the carbonaceous material and crystalline structure referred above, the catalyst stability in the conversion of methane (Figure 8.7) can be ascribed mostly to the formation of carbon filaments that do not encapsulate the active metal sites and thus keep the activity stable, which is favoured by the presence of cobalt aluminate species.

8.4 Conclusions

A series of Co-based materials promoted with alkalis was synthesised and evaluated for dry reforming of methane at moderate temperatures. The partial substitution of small quantities of Co by Ca, La, Li or Mg modifies the reducibility of the Co species and the crystallinity of the oxides in the structure. A small increase in the specific area and an increase in the alkaline properties of the materials were also noted. These changes in the material influence the catalytic properties for dry reforming of methane and for carbon formation, mostly for the Mg- and Li-promoted samples.

Despite having shown smaller metallic Co crystallite sizes, the unpromoted catalyst (CoAl) exhibited the lowest activity (conversions of CO_2 and CH_4) for all the reaction temperature range. This result might be due to the higher coke formation rate attributed to the higher acidity of the catalyst. On the other hand, all the alkali-promoted catalysts exhibited lower carbon deposition after a decrease in the acidity or an increase in the strength of the alkaline sites for these materials.

The Li-containing sample presented the highest strength of both the weak and the strong basic sites. These properties provided the lowest carbon formation for the LiCoAl catalyst.

Among all the samples, the sample modified with Mg showed the best performance for dry reforming of methane. This result can be attributed to the commitment between textural properties (surface area), reducibility and acid/base properties. The best activity was achieved at 550°C, which is a moderate temperature for this reaction. The mixed oxides might favour the formation of non-deactivating coke, thus the stable activity observed in the stability experiments.

ACKNOWLEDGEMENTS

The authors thank the financial support granted by CAPES (Coordenação de Aperfeiçoamento de Pessoal de Pessoal de Nível Superior) and CNPq (Conselho Nacional de Desenvolvimento Científico e Tecnológico) to carry out this work.

References

1. Dry ME. The Fischer-Tropsch process: 1950-2000. *Catalysis Today.* 2002; 71:227-241.

2. Feio LSF, Hori CE, Mattos LV, Zanchet D, Noronha FB, Bueno JMC. Partial oxidation and autothermal reforming of methane on Pd/CeO_2-Al_2O_3 catalysts. *Applied Catalysis A-General.* 2008; 348:183-192.

3. Jones G, Jakobsen JG, Shim SS, Kleis J, Andersson MP, Rossmeisl J, Abild-Pedersen F, Bligaard T, Helveg S, Hinnemann B, Rostrup-Nielsen JR, Chorkendorff I, Sehested J, Nørskov JK. First principles calculations and experimental insight into methane steam reforming over transition metal catalysts. *Journal of Catalysis.* 2008; 259:147-160.

4. Rostrup-Nielsen JR, Hansen JHB. CO_2-reforming of methane over transition metals. *Journal of Catalysis.* 1993; 144:38-49.

5. Bouarab R, Akdim O, Auroux A, Cherifi O, Mirodatos C. Effect of MgO additive on catalytic properties of Co/SiO_2 in the dry reforming of methane. *Applied Catalysis A: General*. 2004; 264:161-168.

6. Luisetto I, Tuti S, Di Bartolomeo E. Co and Ni supported on CeO_2 as selective bimetallic catalyst for dry reforming of methane. *International Journal of Hydrogen Energy.* 2012; 37:15992-15999.

7. San-José-Alonso D, Juan-Juan J, Illán-Gómez MJ, Román-Martínez MC. Ni, Co and bimetallic Ni–Co catalysts for the dry reforming of methane. *Applied Catalysis A: General.* 2009; 371:54-59.

8. Ewbank JL, Kovarik L, Kenvin CC, Sievers C. Effect of preparation methods on the performance of Co/Al_2O_3 catalysts for dry reforming of methane. *Green Chemistry.* 2014; 16:885-896.

9. Budiman A, Song S-H, Chang T-S, Shin C-H, Choi M-J. Dry Reforming of Methane Over Cobalt Catalysts: A Literature Review of Catalyst Development. *Catalysis Surveys from Asia.* 2012; 16:183-197.

10. Nagaoka K, Takanabe K, Aika K-I. Modification of Co/TiO_2 for dry reforming of methane at 2 MPa by Pt, Ru or Ni. *Applied Catalysis A: General*. 2004; 268:151-158.

11. Nagaoka K, Takanabe K, Aika K-I. Influence of the reduction temperature on catalytic activity of Co/TiO_2 (anatase-type) for high pressure dry reforming of methane. *Applied Catalysis A: General*. 2003; 255:13-21.

12. Fakeeha, A. H.; Naeem, M. A.; Khan, W. U.; Al-Fatesh, A. S., Syngas production via CO2 reforming of methane using Co-Sr-Al catalyst. *Journal of Industrial and Engineering Chemistry* **2014,** 20, (2), 549-557.

13. Ruckenstein E, Hu YH. Carbon dioxide reforming of methane over nickel/alkaline earth metal oxide catalysts. *Applied Catalysis A: General*. 1995; 133:149-161.

14. Quincoces CE, Dicundo S, Alvarez AM, González MG. Effect of addition of CaO on Ni/Al_2O_3 catalysts over CO_2 reforming of methane. *Materials Letters*. 2001; 50:21-27.

15. Dias JAC, Assaf JM. Influence of calcium content in $Ni/CaO/\gamma\text{-}Al_2O_3$ catalysts for CO_2-reforming of methane. *Catalysis Today*. 2003; 85:59-68.

16. Hou Z, Yokota O, Tanaka T, Yashima T. Characterization of Ca-promoted $Ni/\alpha\text{-}Al_2O_3$ catalyst for CH_4 reforming with CO_2. *Applied Catalysis A: General*. 2003; 253:381-387.

17. Jing Q, Lou H, Mo L, Fei J, Zheng X. Combination of CO_2 reforming and partial oxidation of methane over Ni/BaO-SiO_2 catalysts to produce low H_2/CO ratio syngas using a fluidized bed reactor. *Journal of Molecular Catalysis A: Chemical*. 2004; 212:211-217.

18. Juan-Juan J, Román-Martínez MC, Illán-Gómez MJ. Effect of potassium content in the activity of K-promoted Ni/Al_2O_3 catalysts for the dry reforming of methane. *Applied Catalysis A: General*. 2006; 301:9-15.

19. Barroso-Quiroga MM, Castro-Luna AE. Catalytic activity and effect of modifiers on Ni-based catalysts for the dry reforming of methane. *International Journal of Hydrogen Energy*. 2010; 35:6052-6056.

20. Vaccari A. Clays and catalysis: A promising future. *Applied Clay Science*. 1999; 14:161-198.

21. Trifiró F, Vaccari A: Hydrotalcite-like anionic clays (layer double hydroxides); Comprehensive supramolecular chemistry. Oxford, Pergamon, 1996, pp 251, vol. 257.

22. Perez-Lopez OW, Senger A, Marcilio NR, Lansarin MA. Effect of composition and thermal pretreatment on properties of Ni-Mg-Al catalysts for CO_2 reforming of methane. *Applied Catalysis A-General*. 2006; 303:234-244.

23. Guo JJ, Lou H, Zhao H, Chai DF, Zheng XM. Dry reforming of methane over nickel catalysts supported on magnesium aluminate spinels. *Applied Catalysis A-General*. 2004; 273:75-82.

24. Daza CE, Gallego J, Moreno JA, Mondragon F, Moreno S, Molina R. CO_2 reforming of methane over Ni/Mg/Al/Ce mixed oxides. *Catalysis Today*. 2008; 133:357-366.

25. Hou Z, Yashima T. Meso-porous Ni/Mg/Al catalysts for methane reforming with CO_2. *Applied Catalysis A: General*. 2004; 261:205-209.

26. Bhattacharyya A, Chang VW, Schumacher DJ. CO_2 reforming of methane to syngas: I: Evaluation of hydrotalcite clay-derived catalysts. *Applied Clay Science*. 1998; 13:317-328.

27. de Sousa FF, de Sousa HAS, Oliveira AC, Junior MCC, Ayala AP, Barros EB, Viana BC, Filho JM, Oliveira AC. Nanostructured Ni-containing spinel oxides for the dry reforming of methane: Effect of the presence of cobalt and nickel on the deactivation behaviour of catalysts. *International Journal of Hydrogen Energy.* 2012; 37:3201-3212.

28. Serrano-Lotina A, Martin AJ, Folgado MA, Daza L. Dry reforming of methane to syngas over La-promoted hydrotalcite clay-derived catalysts. *International Journal of Hydrogen Energy.* 2012; 37:12342-12350.

29. Hermes NA, Lansarin MA, Perez-Lopez OW. Catalytic decomposition of methane over M-Co-Al catalysts (M = Mg, Ni, Zn, Cu). *Catalysis Letters*. 2011; 141:1018-1025.

30. Khassin AA, Yurieva TM, Kustova GN, Itenberg IS, Demeshkina MP, Krieger TA, Plyasova LM, Chermashentseva GK, Parmon VN. Cobalt-aluminum co-precipitated catalysts and their performance in the Fischer-Tropsch synthesis. *Journal of Molecular Catalysis A-Chemical*. 2001; 168:193-207.

31. Reshetenko TV, Avdeeva LB, Khassin AA, Kustova GN, Ushakov VA, Moroz EM, Shmakov AN, Kriventsov VV, Kochubey DI, Pavlyukhin YT, Chuvilin AL, Ismagilov ZR. Coprecipitated iron-containing catalysts (Fe-Al_2O_3, Fe-Co-Al_2O_3, Fe-Ni-Al_2O_3) for methane decomposition at moderate temperatures i. Genesis of calcined and reduced catalysts. *Applied Catalysis A-General*. 2004; 268:127-138.

32. Ross JRH. Natural gas reforming and CO_2 mitigation. *Catalysis Today.* 2005; 100:151-158.

33. Serrano-Lotina A, Daza L. Influence of the operating parameters over dry reforming of methane to syngas. *International Journal of Hydrogen Energy.* 2014; 39:4089-4094.

34. Yu X-P, Chu W, Wang N, Ma F. Hydrogen production by ethanol steam reforming on NiCuMgAl catalysts derived from hydrotalcite-like precursors. *Catalysis Letters.* 2011; 141:1228-1236.

35. Palmer SJ, Spratt HJ, Frost RL. Thermal decomposition of hydrotalcites with variable cationic ratios. *Journal of Thermal Analysis and Calorimetry*. 2009; 95:123-129.

36. Vaccari A. Preparation and catalytic properties of cationic and anionic clays. *Catalysis Today*. 1998; 41:53-71.

37. Holgado MJ, Rives V, San Roman MS. Characterization of Ni-Mg-Al mixed oxides and their catalytic activity in oxidative dehydrogenation of n-butane and propene. *Applied Catalysis A-General*. 2001; 214:219-228.

38. de Souza G, Ávila VC, Marcílio NR, Perez-Lopez OW. Synthesis Gas Production by Steam Reforming of Ethanol over M-Ni-Al Hydrotalcite-type Catalysts; M = Mg, Zn, Mo, Co. *Procedia Engineering.* 2012; 42:1805-1815.

39. Lopez-Salinas E, Garcia-Sanchez M, Luisa Ramon-Garcia M, Schifter I. New gallium-substituted hydrotalcites: $[Mg_{1-x}Ga_x(OH)_2](CO_3)_{x/2}\cdot mH_2O$. *Journal of Porous Materials*. 1996; 3:169-174.

40. Wang D-Y, Leuteritz A, Wagenknecht U, Heinrich G. Self-assembling organomodified Co/Al based layered double hydroxides (LDH) via one-step route. *Transactions of Nonferrous Metals Society of China*. 2009; 19:1479-1482.

41. Xu W, Liu X, Ren J, Liu H, Ma Y, Wang Y, Lu G. Synthesis of nanosized mesoporous Co–Al spinel and its application as solid base catalyst. *Microporous and Mesoporous Materials*. 2011; 142:251-257.

42. Escobar C, Perez-Lopez OW. Hydrogen Production by Methane Decomposition Over Cu–Co–Al Mixed Oxides Activated Under Reaction Conditions. *Catalysis Letters.* 2014; 144:796-804.

43. Hu X, Lu G. Acetic acid steam reforming to hydrogen over Co–Ce/Al_2O_3 and Co–La/Al_2O_3 catalysts—the promotion effect of Ce and La addition. *Catalysis Communications*. 2010; 12:50-53.

44. Ribet S, Tichit D, Coq B, Ducourant B, Morato F. Synthesis and activation of Co-Mg-Al layered double hydroxides. *Journal of Solid State Chemistry*. 1999; 142:382-392.

45. Gabrovska M, Edreva-Kardjieva R, Tenchev K, Tzvetkov P, Spojakina A, Petrov L. Effect of Co-content on the structure and activity of Co–Al hydrotalcite-like materials as catalyst precursors for CO oxidation. *Applied Catalysis A: General*. 2011; 399:242-251.

46. Benito R, Herrero M, Labajos FM, Rives V, Royo C, Latorre N, Monzon A. Production of carbon nanotubes from methane use of Co-Zn-Al catalysts prepared by microwave-assisted synthesis. *Chemical Engineering Journal*. 2009; 149:455-462.

47. Bialas A, Niebrzydowska P, Dudek B, Piwowarska Z, Chmielarz L, Michalik M, Kozak M, Kuśtrowski P. Coprecipitated Co–Al and Cu–Al oxide catalysts for toluene total oxidation. *Catalysis Today*. 2011; 176:413-416.

48. Nudel JN, Umansky BS, Lombardo EA. Bulk, surface and catalytic characterization of the Co_3O_4-La_2O_3-Al_2O_3 system. *Applied Catalysis A: General*. 1987; 31:275-289.

49. Gennequin C, Kouassi S, Tidahy L, Cousin R, Lamonier J-F, Garcon G, Shirali P, Cazier F, Aboukaïs A, Siffert S. Co–Mg–Al oxides issued of hydrotalcite precursors for total oxidation of volatile organic compounds. Identification and toxicological impact of the by-products. *Comptes Rendus Chimie*. 2010; 13:494-501.

50. Sokolovskii VD, Coville NJ, Parmaliana A, Eskendirov I, Makoa M. Methane partial oxidation. Challenge and perspective. *Catalysis Today*. 1998; 42:191-195.

51. Choudhary VR, Sansare SD, Mamman AS. Low-temperature selective oxidation of methane to carbon monoxide and hydrogen over cobalt-MgO catalysts. *Applied Catalysis A: General.* 1992; 90:L1-L5.

52. Ruckenstein E, Wang HY. Combined catalytic partial oxidation and CO_2 reforming of methane over supported cobalt catalysts. *Catalysis Letters.* 2001; 73:99-105.

53. Wang HY, Ruckenstein E. Partial oxidation of methane to synthesis gas over alkaline earth metal oxide supported cobalt catalysts. *Journal of Catalysis.* 2001; 199:309-317.

54. Segner J, Campbell CT, Doyen G, Ertl G. Catalytic oxidation of CO on Pt(111): The influence of surface defects and composition on the reaction dynamics. *Surface Science.* 1984; 138:505-523.

55. Ruoso C, Souza G, Balzaretti NM, Marcilio NR, Perez-Lopez OW. Nanotubos de carbono a partir da decomposição do etanol sobre catalisadores Co-Al. *In: Proceedings of the COBEQ - Brazilian Congress on Chemical Engineering*; 2012; Búzios, Brazil. ABEQ; 2012. p. 8846-8854.

Capítulo 9

Dry reforming of methane over Mg-Co-Al mixed oxides catalysts: effect of Mg content and reduction conditions

Artigo submetido para publicação no periódico: *Chemical Engineering Communications*, em junho de 2014.

Dry reforming of methane over Mg-Co-Al mixed oxides catalysts: effect of Mg content and reduction conditions

GUILHERME DE SOUZA[1,2], CÁSSIA RUOSO[1],
NILSON R. MARCILIO[1] AND OSCAR W. PEREZ-LOPEZ[1,*]

[1] *Department of Chemical Engineering, Federal University of Rio Grande do Sul, Eng. Luiz Englert St. S/N°, 90040-040 Porto Alegre - RS, Brazil. Phone: +55 51 3308 3953. Fax: +55 51 3308 3277. Email: [gdesouza; cassiar; nilson; perez]@enq.ufrgs.br*

[2] *Fundação de Ciência e Tecnologia do Estado do Rio Grande do Sul - CIENTEC, das Indústrias Av., No. 2270, Distrito Industrial, 94930-230 Cachoeirinha - RS, Brazil. Phone: +55 51 3439 6352. Email: guilherme-souza@cientec.rs.gov.br*

* Corresponding author: Oscar William Perez-Lopez. Department of Chemical Engineering, Federal University of Rio Grande do Sul, Eng. Luiz Englert St. S/N°, 90040-040 Porto Alegre - RS, Brazil. Phone: +55 51 3308 3953. Fax: +55 51 3308 3277. Email: perez@enq.ufrgs.br

Abstract

Mg-Co-Al mixed oxides were synthesised by the precipitation method and evaluated for dry reforming of methane. Samples were characterised by thermal techniques (TGA/DTA, NH_3-TPD, H_2-TPR and TPO), specific surface area and X-ray diffraction. Activity runs were conducted at atmospheric pressure, temperatures between 400-550°C, CH_4/CO_2 molar ratio of 1 and space velocity of 6000 NmL CH_4/g/h. The partial substitution of Co by Mg increased the surface area and the thermal stability and changed the reducibility and the acid-base properties of samples. These modifications led to a higher activity for dry reforming of methane for the catalyst with Mg/Co = 0.5, mainly due to its enhanced thermal stability. However, its higher activity was followed by higher amounts of coke. The different activation procedures highlighted Co_3O_4 as the main active phase rather than the Co-mixed oxides. Therefore, milder activation temperatures are required in order to properly reduce the Co_3O_4 phase and to avoid sintering.

Keywords: Dry reforming of methane; Cobalt catalyst; Mixed oxides; Magnesium; Coke; Precipitation method.

9.1. Introduction

As methane and carbon dioxide contributes to 4-9% and 9-26% of the total greenhouse effect, the mitigation of their emission is a major challenge (Chattanathan et al., 2012). Among different processes suggested to deal with this concern, CO_2-reforming of CH_4 (also referred as “dry reforming”) is a promising route for producing CO-rich synthesis gas from both greenhouse gases that arise from different processes. After the cleaning steps, the synthesis gas can feed an internal combustion engine or undergo to liquid fuels and other valuable chemicals through processes such as the Fischer-Tropsch synthesis, the Methanol-To-Gasoline process, etc. The main reaction is shown in equation 9.1.

$$CH_4 + CO_2 \rightarrow 2CO + 2H_2 \qquad \Delta H_{298K} = 246 \text{ kJ/mol} \qquad (9.1)$$

From a thermodynamic point of view, it is desirable to operate the dry reforming of methane at high temperatures and with CO_2/CH_4 ratios above unity in order to avoid regions with a thermodynamic potential for carbon formation. However, operation at lower temperatures with CO_2/CH_4 ratios around unity might be more attractive for industrial purposes (Gadalla and Bower, 1988; Chen et al., 2001).

The metals from group VIII of the periodic table are known to be active for reforming processes, but the lower price makes the use of nickel- and cobalt-based catalysts attractive (Rostrup-Nielsen and Hansen, 1993). Literature on this process refers to nickel as the preferred choice for industrial steam reforming catalysts (Daza et al., 2008; Jones et al., 2008; Aasberg-Petersen et al. 2011). However, Ni presents very high activity for methanation, so its fines could possibly promote this reaction for the downstream tail gas. The Co-catalysts are less active for the methanation reaction. Therefore, cobalt is a good option to avoid this drawback observed for nickel catalysts (Bouarab et al., 2004).

San-José-Alonso and co-workers (2009) showed much higher activity for alumina-supported Co-catalyst compared to similar Ni-based catalyst for dry reforming of methane. However, this is followed by a significant increase in carbon formation (San-José-Alonso et al., 2009). A previous work showed that catalyst deactivation by coking could be minimised with the presence of alkalis (Bouarab et al., 2004). The alkali promotion is usually performed by an additional impregnation step. Nonetheless, this modification can also be performed by preparing materials through the co-precipitation method. This preparation method favours the synthesis of mixed oxides, which has desirable properties such as high surface area, high thermal stability and small crystallite sizes (Trifiró and Vaccari, 1996; Vaccari, 1999). Interesting results achieved by Co-mixed oxides in different processes (Khassin, et al., 2001; Reshetenko, et al. 2004; de Souza et al., 2012) are also an incentive for its investigation for dry reforming of CH_4 on these catalysts.

Among a group of alkalis previously evaluated for the promotion of Co-mixed oxides samples, our group showed that addition of Mg gives the most interesting results (Souza et al., 2013). This work extends the previous study by evaluating the effect of the different contents of Mg over the structural and catalytic properties of Mg-Co-Al mixed oxides for dry reforming of methane. The activation method was also investigated for this catalytic system.

9.2. Experimental

9.2.1 Preparation of samples

The Mg-Co-Al samples were prepared by the continuous co-precipitation method. For the precipitation process, an aqueous solution containing a mixture of aluminium nitrate, cobalt nitrate and magnesium nitrate was prepared. An aqueous solution of Na_2CO_3 was used as precipitant. The nitrate solution was continuously added at a constant flow rate to a continuous stirred tank reactor (CSTR) kept at 50°C (± 0.5). The alkaline solution containing sodium carbonate was fed at a variable flow rate in order to maintain the pH values at 8.0 (± 0.1). The precipitate was collected and continued to be stirred at 50°C for 1 h. After crystallisation, the slurry was filtered and washed thoroughly with deionised water in order to remove the ions from the precursors. Then, the solids were dried at 80°C for 24 h in an oven. The dried solids were crushed and sieved and he fraction with the desired particle sizes (355 < dp < 500 µm) was collected. The oxides were obtained by thermal treatment with synthetic air (50 mL/min) at 600°C for 6 h.

9.2.2 Characterisation

In order to investigate the structural properties of the solids, different techniques were employed. The characterisation techniques included surface area measurements (S_{BET}), thermogravimetry (TG/DTA), X-ray diffraction (XRD), temperature-programmed ammonia desorption (NH_3-TPD), temperature-programmed reduction (H_2-TPR) and temperature-programmed oxidation (TPO/DTA).

The XRD patterns were collected with a Bruker D2 Phaser X-ray diffractometer using CuKα radiation. The patterns for reduced samples were recorded after activation at the same conditions adopted for the activity tests, followed by passivation under diluted oxygen flow (1.4% v/v). The apparent Co^0 crystallite diameters were estimated by the Scherrer equation from the reflection at 44.3°. A thermobalance equipment (TA, Model SDT Q600) was used for the TG/DTA and TPO/DTA analysis. Approximately 10 mg of uncalcined (TG/DTA) or spent sample (TPO/DTA) was used in all experiments. The pretreatment for both analyses was carried out at room temperature under nitrogen flow. The sample was heated to 850°C at a rate of 10°C/min under a 100 mL/min air flow. The S_{BET} data were obtained by the nitrogen dynamic adsorption method at the normal boiling point of N_2 (-196°C).

The H_2-TPR curves were acquired in a multipurpose system. Approximately 0.1 g of the calcined catalyst was placed in a quartz tube located in a temperature-controlled electric oven. An in situ thermal treatment under N_2 flow was performed at 250°C for 1 h prior to the reduction step. The temperature was cooled to room temperature and then increased to ca. 900°C (10°C/min) using 30 mL/min of a diluted 10% H_2 (v/v) mixture. The data was recorded by a thermal conductivity detector (TCD). The NH_3-TPD curves were obtained using the same multipurpose system used for the H_2-TPR analysis. After the thermal treatment under N_2 flow, the calcined sample was saturated with a NH_3/He mixture (10% v/v) at 100°C for 30 min. After a purge step at a flow rate of 30 mL/min of He during 30 min, the desorption curves were recorded while increasing the temperature from 100°C to 600°C (10°C/min) under 30 mL/min of He.

9.2.3 Catalytic runs

The reforming of methane with carbon dioxide was performed under atmospheric pressure in a tubular fixed-bed quartz reactor (½ in. diameter). The reactor was loaded with 0.1 g of diluted catalyst (quartz, 1:2 v/v). Quartz wool was used as the support for the catalytic bed. The activation was performed in situ at 700°C for 1 h, although one sample was reduced at 500°C for 4 h. For both cases, the catalysts were heated at 5°C/min under 50 mL/min of a 10% H_2/N_2 (v/v) reduction mixture. The runs were carried out at temperatures between 400 and 550°C using a

CO_2/CH_4 molar ratio of 1. The gas hourly space velocity (GHSV) adopted was 6000 mL CH_4/g/h. The products were analysed on-line by gas chromatography.

9.3 Results and discussion

9.3.1 Characterisation

The molar composition (as prepared) and S_{BET} data for calcined samples are displayed in Table 9.1.

Table 9.1. Nominal composition and S_{BET} data for the calcined samples.

Sample	Composition (mol %)			Mg/Co ratio	S_{BET} (m^2/g)
	Mg	Co	Al		
Mg11CA	11	55	33	0.2	67
Mg22CA	22	44	33	0.5	77
Mg33CA	33	33	33	1.0	114

The materials were prepared maintaining the M^{II}/M^{III} molar ratio at 2, in order to favour the synthesis of mixed oxides (Vaccari, 1998). The surface area observed for the standard sample (Mg11CA) is close to that reported for similar Mg-Co-Al catalyst calcined at 500°C (Gennequin et al., 2010). Table 9.1 shows that the partial substitution of Co by higher contents of Mg increases the specific surface area. The same trend was observed by Gennequin et al. (2010). The increase is more significant for the catalyst synthesised with the highest content of magnesium. Indeed, an increase of 70% in the surface area value can be seen for Mg33CA compared to the catalyst with lower Mg content (Mg11CA). The decrease in the content of Co might favour the formation of $CoAl_2O_4$ instead of Co_3O_4. Therefore, the increase in the surface area with increasing Mg/Co ratio might be related to the mixed oxide because this phase presents higher specific surface area (Xu et al., 2011). Similarly, the $MgAl_2O_4$ species might also be favoured with increasing Mg/Co ratio, which could also contribute to form a material with higher specific surface area.

The TG/DTA curves for the uncalcined samples are presented in Figure 9.1.

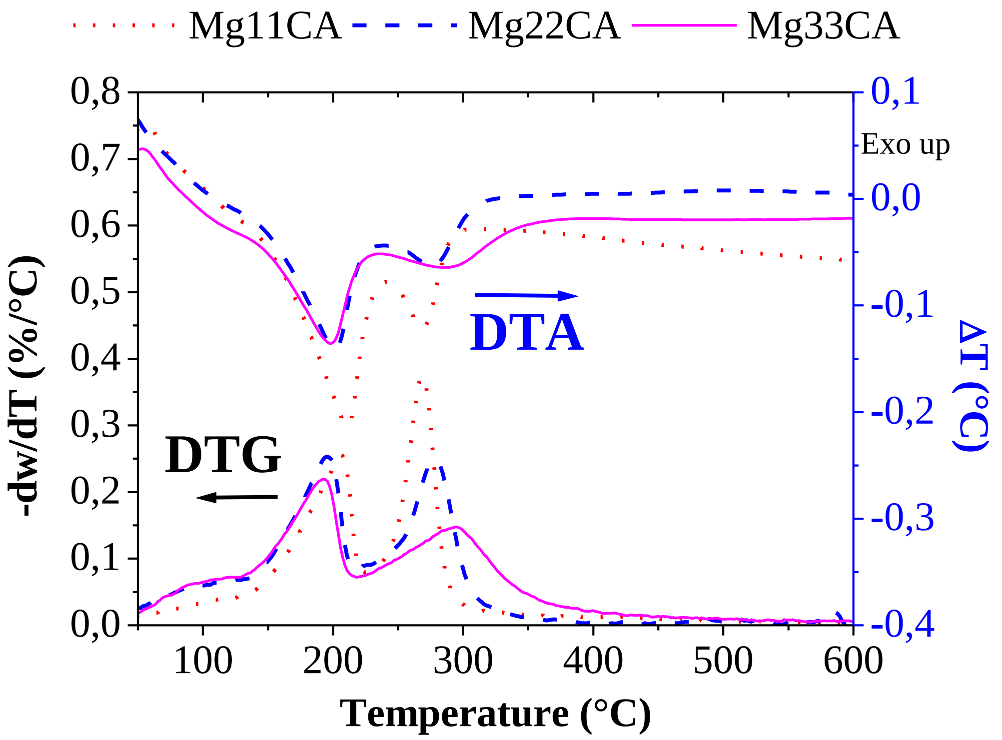

Figure 9.1. TG/DTA curves for uncalcined samples.

Figure 9.1 shows two major DTG/DTA endothermic peaks for the three samples. The peak at ca. 200°C is typically ascribed to the loss of interlayer water, while the peak at ca. 270°C is related to the decomposition of nitrates and release of the OH^- and CO_3^{2-} anions. As expected for these materials, it can be noticed that the structure collapses in temperatures below 400°C, yielding the mixed oxides (Holgado et al., 2001; de Souza et al., 2012).

The thermal decomposition behaviour varies according to the Mg/Co ratio. The first peak shifted towards lower temperatures, while the peak at ca. 270°C shifted towards higher temperatures with decreasing Mg/Co ratio. Moreover, this last DTG peak also became weaker and broader. Based on this peak at higher temperatures, it reveals that materials with higher thermal stability are formed for samples with higher Mg/Co ratio. Indeed, the Mg33CA sample exhibits these later DTG/DTA peaks ending at temperatures approximately 80°C higher when comparing to Mg11CA. Therefore, the DTG/DTA curves support the S_{BET} measurements (Table 9.1) because the mixed oxides are known to generally exhibit high thermal stability (Vaccari, 1998, 1999).

Figure 9.2 displays the XRD patterns for calcined catalysts.

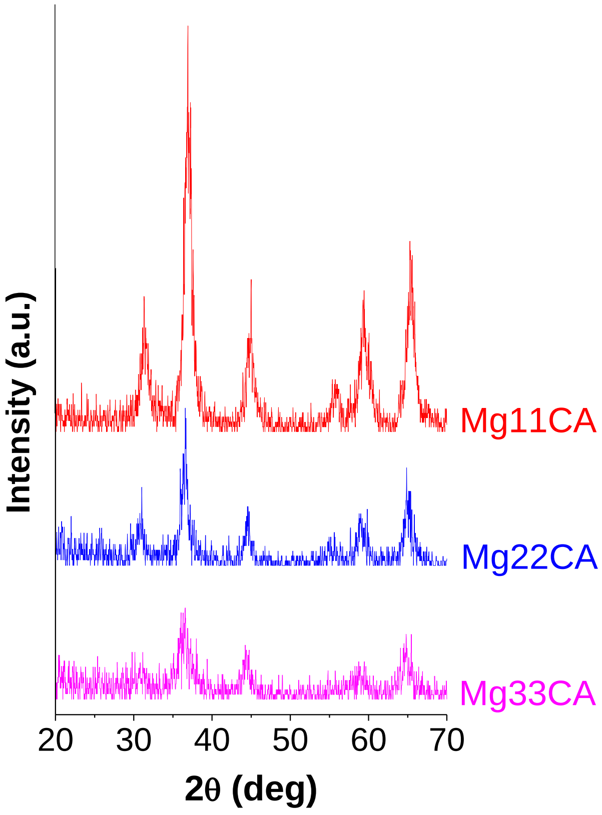

Figure 9.2. XRD patterns for calcined catalysts.

Figure 9.2 shows diffraction reflections that suggest the presence of the Co_3O_4 and the $CoAl_2O_4$ crystalline phases for the Mg11CA catalyst, because both the phases have very similar reflections (Li et al., 2005). The same cobalt oxide phases were identified for precipitated Cu-Co-Al catalysts (Escobar and Perez-Lopez, 2014). The partial substitution of Co by higher levels of Mg might lead to lesser crystalline structures. It was not possible to estimate the Co_3O_4 crystallite sizes because of the low intensities of the reflections for the Mg22CA and Mg33CA catalysts, as well as to the coincidence of the reflections for the identified phases. Apparently, based on the diffraction peaks with higher intensity, the three materials present the same crystalline phases.

H_2-TPR profiles are shown in Figure 9.3.

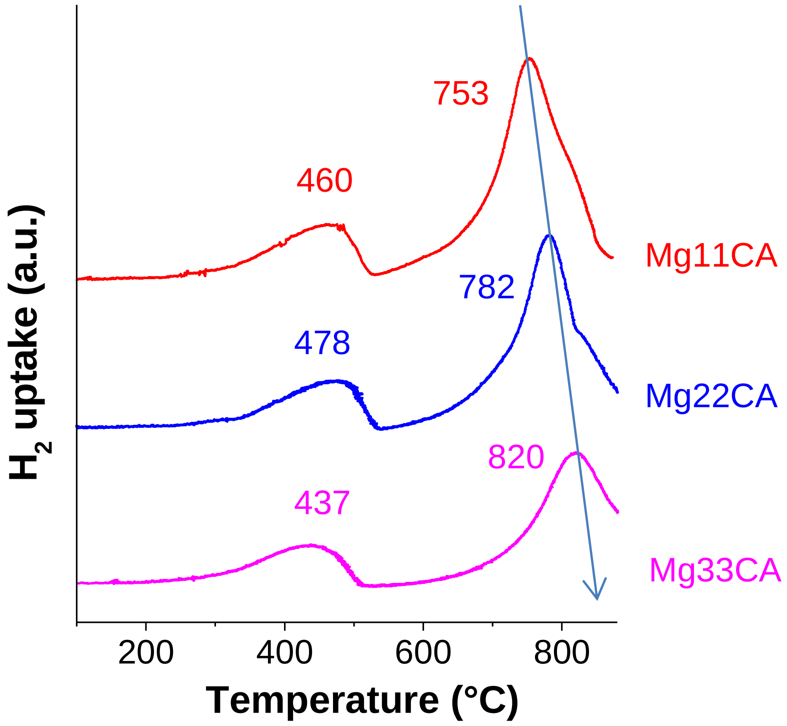

Figure 9.3. H_2-TPR profiles for the calcined samples.

The reduction peak centred at temperatures between 250 – 530°C corresponds to the reduction of the segregated Co_3O_4 phase, which was identified by XRD (Figure 9.2). Other references also reported the same transformation for this temperature range (Khassin et al., 2001; Gabrovska et al., 2011; Hermes et al., 2011). The shape of this peak suggests two curves overlapped for all the samples, pointing to the transformation $Co_3O_4 \rightarrow CoO \rightarrow Co^0$. The peak located at higher temperatures can be ascribed to the reduction of Co in $CoAl_2O_4$ phase, which is known to occur at higher temperatures due to a strong stabilisation of Co^{2+} that is surrounded by Al^{3+} in the spinel phase (Benito et al., 2009; Bialas et al., 2011; Escobar and Perez-Lopez, 2014).

It can be noted that the area and position of peaks vary according to the Mg/Co ratio. The peaks ascribed to the reduction of the $CoAl_2O_4$ mixed oxides shift towards higher temperatures with increasing Mg/Co ratio. Although the magnesium aluminate phase was not identified by XRD (Figure 9.2), the shift on the reduction temperature of the $CoAl_2O_4$ phase might be promoted by the $MgAl_2O_4$ mixed oxide suggested by S_{BET} (Table 9.1), which would be favoured by the higher Mg content. The higher stability of this phase could also minimise the aggregation phenomenon of the Co-mixed oxides. This would lead to crystallites with smaller diameters obtained for this phase and hence requiring higher temperatures to be reduced (Hong et al., 2010). This hypothesis could explain the higher temperatures needed for the reduction of the samples with higher contents of magnesium. Furthermore, this observation is in agreement with the higher thermal stability expected for samples with higher Mg/Co ratios (see the TG/DTA data in Figure 9.1). The area of the reduction peak assigned to the Co_3O_4 oxide (peak at lower temperatures) decreases in the following order: Mg11CA (100%) > Mg22CA (91%) > Mg33CA (79%). The Mg22CA sample showed the reduction of the Co_3O_4 oxide at the highest temperature (478°C), suggesting its increased thermal stability.

The ammonia desorption curves are displayed in Figure 9.4. Three types of sites can be observed from the major peak related to desorption of ammonia. The deconvolution of peaks provides a better insight about the strength and amount of each acid site. The first peak is centred at 145 - 235°C and represents sites with weaker acidity. The peak with maximum in the range 330 - 389°C is related to intermediate acid sites. The peak located at higher temperatures indicates a strong interaction of ammonia with these sites, which means that these sites possess the strongest acidity.

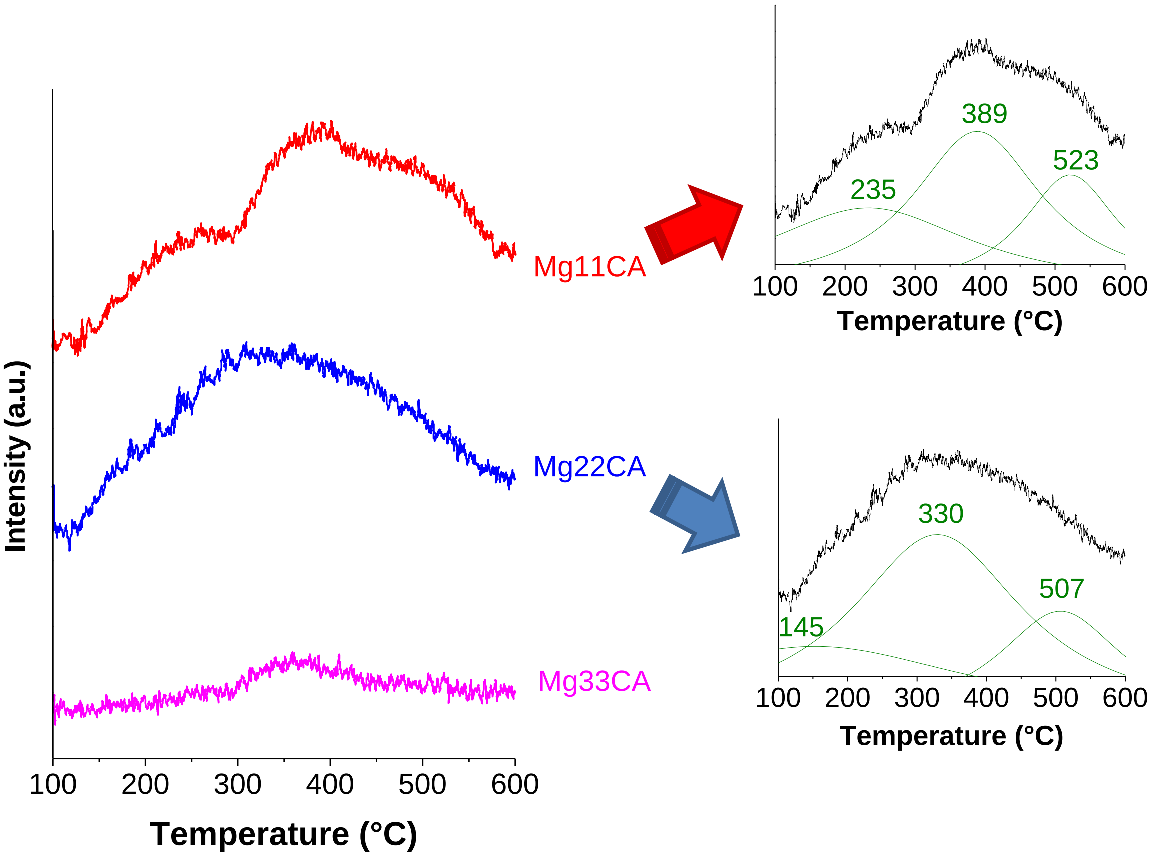

Figure 9.4. NH_3-TPD profiles for the calcined samples.

The NH_3-TPD results revealed significant differences in the acid-basic properties according to the Mg/Co ratio adopted. The Table 9.2 exhibits numeric data for the NH_3-TPD peaks shown in Figure 9.4.

Table 9.2. NH_3-TPD data for calcined samples.

NH_3-TPD peak	Mg11CA		Mg22CA		Mg33CA	
	T (°C)	Area (%)	T (°C)	Area (%)	T (°C)	Area (%)
1st peak	235	35	145	33	301	12
2nd peak	389	42	330	47	361	30
3rd peak	523	23	507	20	512	58
Total area (a.u.)		1300		1800		200

Comparison of the desorption curves of Mg11CA to Mg22CA shows that the total area of peaks does not vary significantly. It means that both the samples exhibit similar total acidity, although the acidity of the Mg22CA is the highest among the three samples. On the other hand, the partial substitution of 22 mol. % of Co by Mg changed the profile by shifting the desorption peaks towards lower temperatures and hence decreasing the strength of these sites. It leads to higher amounts of intermediate acid sites for the Mg22CA catalyst rather than the stronger acid sites exhibited by Mg11CA. The substitution of Co by higher contents of Mg (i.e., the Mg33CA sample) resulted in significantly lesser amounts of acid sites. It reveals that a decrease in the overall acidity of the mixed oxide is obtained only for Mg/Co molar ratios around 1.

9.3.2 Catalytic activity

The variation of CH_4 and CO_2 conversion with reaction temperature for the different Mg-Co-Al catalysts is presented in Figure 9.5-a and 5-b, respectively.

(a)

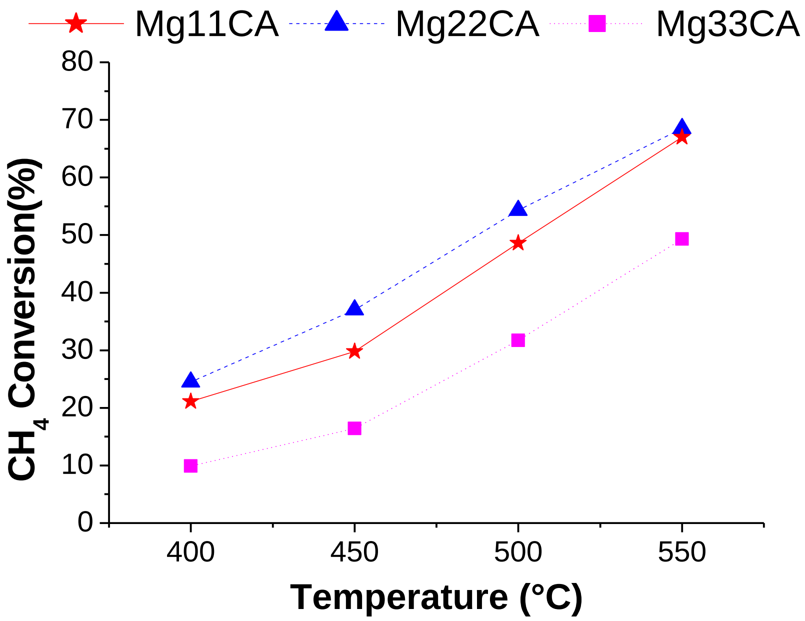

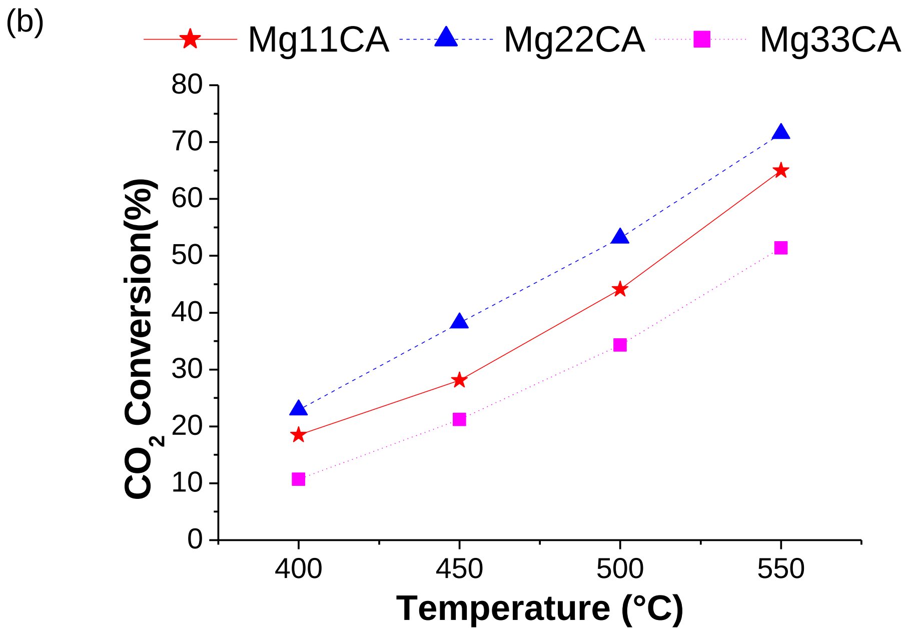

Figure 9.5. Variation of (a) CH_4 and (b) CO_2 conversion with reaction temperature for dry reforming of methane on different Mg-Co-Al catalysts (T_{red} = 700°C / 1 h; CO_2/CH_4 = 1; GHSV = 6000 mL CH_4/g/h).

The conversion of both the CO_2 and CH_4 gases increases with reaction temperature when Co is substituted by 22 mol. % of Mg (Mg22CA catalyst). Despite possessing a lower content of the active metal (Co) compared to the Mg11CA catalyst, the increased thermal stability seems to be crucial for the higher activity for the Mg22CA sample. The aforementioned S_{BET} (Table 9.1), TG/DTA (Figure 9.1) and TPR (Figure 9.3) analyses pointed to the Mg22CA catalyst as more thermally stable compared to Mg11CA. Moreover, the activity data also highlighted the role of the Co_3O_4 phase for the performance, because the Mg22CA sample presented this oxide phase with the highest thermal stability. It suggests that the Co_3O_4 phase is the main phase that promotes the reforming reaction. The Mg33CA catalyst exhibits the lowest activity among the Mg-Co-Al samples investigated herein. This might be explained by its lowest amount of Co and its NH_3-TPD profile (Figure 9.4), which revealed a much lesser amount of acid sites for this sample. The activity results are quite interesting when compared to Co-supported samples tested at similar space velocities (Bouarab et al., 2004; Takanabe et al., 2005) because high conversions were achieved at significantly lower reaction temperatures.

After the catalytic evaluation, the spent catalysts with different Mg/Co ratios were investigated by TPO/DTA. The DTA curves collected for this analysis are exhibited in Figure 9.6.

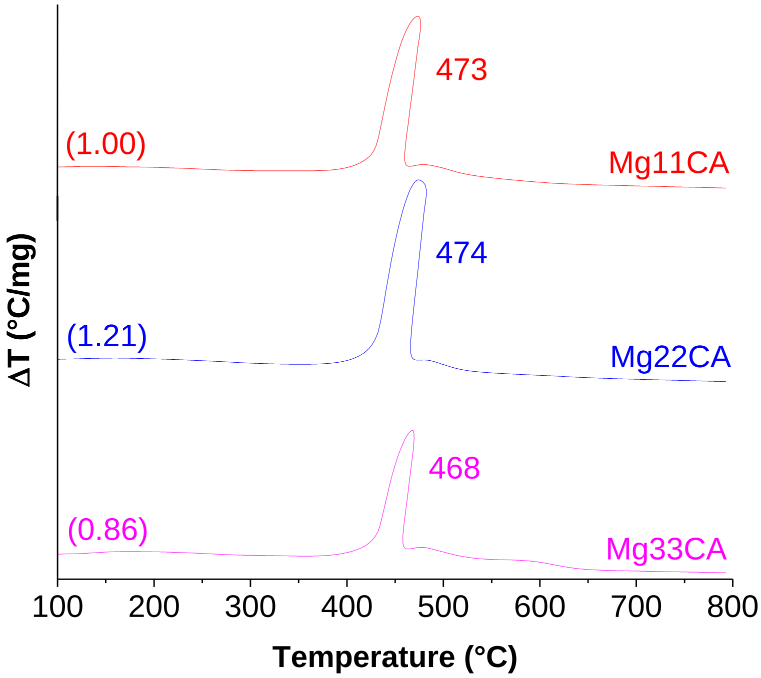

Figure 9.6. TPO/DTA curves for spent catalysts after dry reforming of methane (T_{red} = 700°C / 1 h; CO_2/CH_4 = 1; GHSV = 6000 mL CH_4/g/h).

The values in parenthesis express the relative amount of coke formed compared to the Mg11CA sample, which is obtained from the difference between the initial and final sample weight.

The exothermic DTA peak in Figure 9.6 occurs at temperatures between 400 - 600°C and is related to the oxidation of carbon that is formed during the reaction. The shape of this DTA peak is similar for the three samples. Moreover, the maxima temperatures are the same, being centred at 470°C. This result suggests that the type of coke formed is very similar and hence is not influenced by the Mg/Co ratio. Amorphous carbon typically oxidises at approximately 400°C or even lower. Thus, the peaks in Figure 9.6 might be related to the combustion of carbon nanotubes or nanofibres that do not encapsulate the active metal sites and thus keep the activity stable (Hermes et al. 2011; de Sousa et al., 2012; Escobar and Perez-Lopez, 2014). Therefore, the TPO/DTA analysis suggests that filamentous carbon is formed for the reported Mg-Co-Al catalysts, which could be related to the $CoAl_2O_4$ species that is told to prevent the deposition of carbon that deactivates reforming catalysts (Budiman et al., 2012).

On the other hand, the amount of coke formed during reaction varied according to the acid properties of the samples and activity for the reforming process showed in Figure 9.4 and Figure 9.5, respectively. The carbon formation is related to the density of acid sites, because these sites favour the cracking reactions. Indeed, the Mg33CA catalyst exhibited the lowest amount of carbon covering its surface because this sample revealed the lowest acidity.

9.3.3 Influence of the activation conditions

Results for the catalytic tests conducted at different activation conditions are displayed in Figure 9.7.

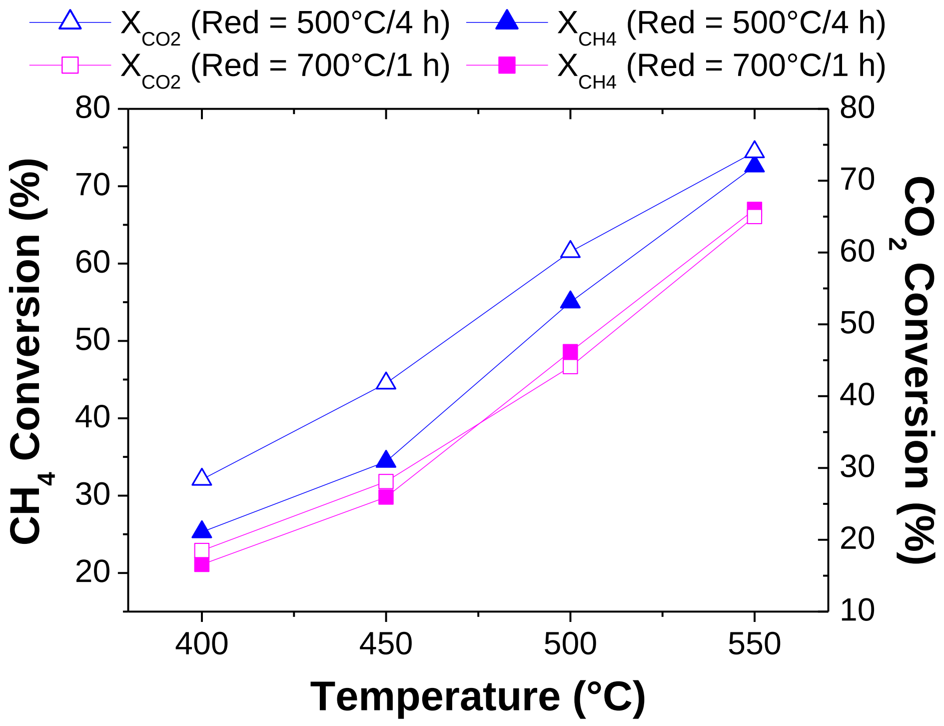

Figure 9.7. Variation of CH_4 (solid symbols) and CO_2 (open) conversion with reaction temperature for dry reforming of methane over Mg11CA reduced at 500°C/4 h and 700°C/1 h (CO_2/CH_4 = 1; GHSV = 6000 mL CH_4/g/h).

The conversions for CO_2 and CH_4 increase when the reduction temperature was decreased from 700°C to 500°C. Based on the TPR profiles (Figure 9.3), the activation at 700°C could provide the reduction of Co in the Co_3O_4 and $CoAl_2O_4$ phases. However, the activation at the highest temperature conducted to lower conversions for all reaction temperatures compared to the sample activated at 500°C for 4 h. Therefore, this behaviour might be related to changes in the crystalline structure due to 700°C. This higher activation temperature seems to be a severe condition for the activation of Co_3O_4, because the reduction of this phase occurs at approximately 450°C. The higher temperature could lead to crystallites with larger diameters. In order to investigate if this phenomenon actually occurs, XRD patterns for the reduced Mg11CA catalysts were collected. The results are shown in Figure 9.8.

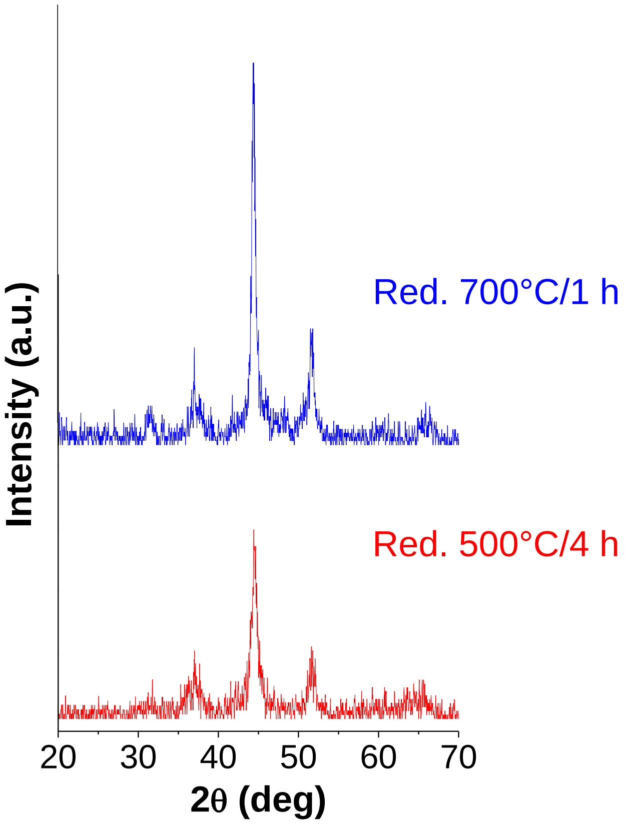

Figure 9.8. XRD patterns for the Mg11CA catalyst reduced under hydrogen flow at 500°C/4 h and 700°C/1 h.

The XRD patterns in Figure 9.8 show lower crystallinity for the Mg11CA sample reduced at 500°C for 4 h. Based on the reflections at 2θ = 44.2° and 51.5°, it can be noted the formation of Co^0 for both the reduction procedures. Other diffraction peaks ascribed to Co_3O_4 and $CoAl_2O_4$ could be related to the passivation step or to the incomplete reduction of the Co oxide species to metallic cobalt under these conditions. The line broadening at half the maximum intensity of the peaks related to Co^0 evidence that the crystallite size for the Mg11CA catalyst reduced at 500°C for 4 h is smaller compared to sample reduced at 700°C. As mentioned above, the activation at milder conditions might prevent the sintering of active metal sites and thus provides smaller crystallites. It should give higher area for the active metal available for the reaction. This might increase the turnover frequency and hence the higher CO_2 and CH_4 conversions achieved by the sample reduced at 500°C for 4 h (shown in Figure 9.7).

Finally, results in Figure 9.7 and Figure 9.8 support the previous discussion on Figure 9.5. It reveals that the Co_3O_4 is the active phase for the dry reforming of methane rather than Co-mixed oxides, thus the highest conversions observed for the Mg22CA catalyst. This catalyst was found to possess the Co_3O_4 phase with enhanced thermal stability in TPR curves (Figure 9.3). As also highlighted by the TG/DTA (Figure 9.1) and the S_{BET} (Table 9.1) analyses, the overall increased stability caused by the mixed oxides with increasing Mg/Co ratio might also contribute to its enhanced catalytic performance. However, the low content for the active metal and the significant change in the number of acid sites (see Figure 9.4) leads to low activity for samples with the Mg/Co ratio = 1.

9.4 Conclusions

A series of Mg-Co-Al samples was synthesised, characterised and evaluated for the dry reforming of methane. The structural properties of samples varied according to the Mg/Co ratio. The increase in the surface area and the shift towards higher temperatures for the thermogravimetric and for the reduction peaks revealed an increase in the thermal stability with increasing Mg/Co ratio. This phenomenon is ascribed to the formation of the mixed oxides rather than the Co_3O_4. All the samples exhibited XRD reflections attributed to the Co_3O_4 and $CoAl_2O_4$ phases. The acid-basic properties also changed. The NH_3-TPD results showed that the acidity decreases with increasing Mg/Co ratio, being almost completely eliminated for the Mg/Co ratio = 1. The Mg22CA sample showed the highest activity for dry reforming of methane thanks to the increased thermal stability, especially for its Co_3O_4 phase. This phase appeared to be the main active phase for the reforming reaction. Thus, milder activation temperatures are desirable in order to properly reduce these Mg-Co-Al catalysts. The coke formation followed the conversions observed for the dry reforming runs.

ACKNOWLEDGEMENTS

The authors wish to thank the financial support and scholarships granted by the “Conselho Nacional de Desenvolvimento Científico e Tecnológico – CNPq” and by the “Coordenação de Aperfeiçoamento de Pessoal de Nível Superior – CAPES”.

References

Aasberg-Petersen, K., Dybkjær, I., Ovesen, C. V., Schjødt, N. C., Sehested, J., and Thomsen, S.G. (2011). Natural gas to synthesis gas – Catalysts and catalytic processes. J. Nat. Gas Sci. Engin., 3, 423-459.

Benito, R., Herrero, M., Labajos, F. M., Rives, V., Royo, C., Latorre, N., and Monzon, A. (2009). Production of carbon nanotubes from methane: Use of Co-Zn-Al catalysts prepared by microwave-assisted synthesis. Chem. Eng. J. (Amsterdam, Neth.), 149, 455-462.

Bialas, A., Niebrzydowska, P., Dudek, B., Piwowarska, Z., Chmielarz, L., Michalik, M., Kozak, M., Kuśtrowski, P. (2011). Coprecipitated Co–Al and Cu–Al oxide catalysts for toluene total oxidation. Catal. Today, 176, 413-416.

Bouarab, R., Akdim, O., Auroux, A., Cherifi, O., Mirodatos, C. (2004). Effect of MgO additive on catalytic properties of Co/SiO2 in the dry reforming of methane. Appl. Catal., A Gen., 264, 161-168.

Budiman, A., Song, S.-H., Chang, T.-S., Shin, C.-H., Choi, M.-J. (2012). Dry Reforming of Methane Over Cobalt Catalysts: A Literature Review of Catalyst Development. Catal. Surv. Asia, 16, 183-197.

Chattanathan, S. A., Adhikari, S., Taylor, S. (2012). Conversion of carbon dioxide and methane in biomass synthesis gas for liquid fuels production. Int. J. Hydrog. Energy, 37, 18031-18039.

Chen, D., Lødeng, R., Anundskås, A., Olsvik, O., Holmen, A. (2001). Deactivation during carbon dioxide reforming of methane over Ni catalyst: microkinetic analysis. Chem. Eng. Sci., 56, 1371-1379.

Daza, C. E., Gallego, J., Moreno, J. A., Mondragon, F., Moreno, S., Molina, R. (2008). CO2 reforming of methane over Ni/Mg/Al/Ce mixed oxides. Catal. Today, 133, 357-366.

de Sousa, F. F., de Sousa, H. S. A., Oliveira, A. C., Junior, M. C. C., Ayala, A. P., Barros, E. B., Viana, B. C., Filho, J. M., Oliveira, A. C. (2012). Nanostructured Ni-containing spinel oxides for the dry reforming of methane: Effect of the presence of cobalt and nickel on the deactivation behaviour of catalysts. Int. J. Hydrog. Energy, 37, 3201-3212.

de Souza, G., Ávila, V. C., Marcílio, N. R., Perez-Lopez, O. W. (2012). Synthesis Gas Production by Steam Reforming of Ethanol over M-Ni-Al Hydrotalcite-type Catalysts; M=Mg, Zn, Mo, Co. Proc. Engin., 42, 1805-1815.

Escobar, C., Perez-Lopez, O. W. (2014). Hydrogen Production by Methane Decomposition Over Cu–Co–Al Mixed Oxides Activated Under Reaction Conditions. Catal. Lett., 144, 796-804.

Gabrovska, M., Edreva-Kardjieva, R., Tenchev, K., Tzvetkov, P., Spojakina, A., Petrov, L. (2011). Effect of Co-content on the structure and activity of Co–Al hydrotalcite-like materials as catalyst precursors for CO oxidation. Appl. Catal., A Gen., 399, 242-251.

Gadalla, A. M., Bower, B. (1988). The role of catalyst support on the activity of nickel for reforming methane with CO2. Chem. Eng. Sci., 43, 3049-3062.

Gennequin, C., Kouassi, S., Tidahy, L., Cousin, R., Lamonier, J.-F., Garcon, G., Shirali, P., Cazier, F., Aboukaïs, A., Siffert, S. (2010). Co–Mg–Al oxides issued of hydrotalcite precursors for total oxidation of volatile organic compounds. Identification and toxicological impact of the by-products. C. R. Chim., 13, 494-501.

Hermes, N. A., Lansarin, M. A., Perez-Lopez, O. W. (2011). Catalytic Decomposition of Methane Over M-Co-Al Catalysts (M = Mg, Ni, Zn, Cu). Catal. Lett., 141, 1018-1025.

Holgado, M. J., Rives, V., San Roman, M. S., 2001. Characterization of Ni-Mg-Al mixed oxides and their catalytic activity in oxidative dehydrogenation of n-butane and propene. Appl. Catal., A Gen., 214, 219-228.

Hong, J., Chu, W., Chernavskii, P. A., Khodakov, A. Y. (2010). Effects of zirconia promotion on the structure and performance of smaller and larger pore silica-supported cobalt catalysts for Fischer–Tropsch synthesis. Appl. Catal., A Gen., 382, 28-35.

Jones, G., Jakobsen, J. G., Shim, S. S., Kleis, J., Andersson, M. P., Rossmeisl, J., Abild-Pedersen, F., Bligaard, T., Helveg, S., Hinnemann, B., Rostrup-Nielsen, J. R., Chorkendorff, I., Sehested, J., Nørskov, J. K. (2008). First principles calculations and experimental insight into methane steam reforming over transition metal catalysts. J. Catal., 259, 147-160.

Khassin, A. A., Yurieva, T. M., Kustova, G. N., Itenberg, I. S., Demeshkina, M. P., Krieger, T. A., Plyasova, L. M., Chermashentseva, G. K., Parmon, V. N. (2001). Cobalt-aluminum co-precipitated catalysts and their performance in the Fischer-Tropsch synthesis. J. Mol. Catal. A: Chem., 168, 193-207.

Li, F., Tan, Q., Evans, D., Duan, X. (2005). Synthesis of carbon nanotubes using a novel catalyst derived from hydrotalcite-like Co–Al layered double hydroxide precursor. Catal. Lett., 99, 151-156.

Reshetenko, T. V., Avdeeva, L. B., Khassin, A. A., Kustova, G. N., Ushakov, V. A., Moroz, E. M., Shmakov, A. N., Kriventsov, V. V., Kochubey, D. I., Pavlyukhin, Y. T., Chuvilin, A. L., Ismagilov, Z. R. (2004). Coprecipitated iron-containing catalysts (Fe-Al2O3, Fe-Co-Al2O3, Fe-Ni-Al2O3) for methane decomposition at moderate temperatures I. Genesis of calcined and reduced catalysts. Appl. Catal., A Gen., 268, 127-138.

Rostrup-Nielsen, J. R., Hansen, J. H. B. (1993). CO2-Reforming of Methane over Transition Metals. J. Catal., 144, 38-49.

San-José-Alonso, D., Juan-Juan, J., Illán-Gómez, M. J., Román-Martínez, M. C. (2009). Ni, Co and bimetallic Ni–Co catalysts for the dry reforming of methane. Appl. Catal., A Gen., 371, 54-59.

Souza, G., Marcilio, N. R., Perez-Lopez, O. W. (2013). Reforma a seco do metano em temperaturas moderadas sobre catalisadores Co-Al co-precipitados modificados com metal alcalino. In: Proceedings of the 17° Congresso Brasileiro de Catálise e VII Congresso de Catálise do Mercosul. SBCat, Gramado, pp. OR2-65.

Takanabe, K., Nagaoka, K., Nariai, K., Aika, K.-I. (2005). Titania-supported cobalt and nickel bimetallic catalysts for carbon dioxide reforming of methane. J. Catal., 232, 268-275.

Trifiró, F., Vaccari, A. (1996). Hydrotalcite-like anionic clays (layer double hydroxides). In, Comprehensive Supramolecular Chemistry. Pergamon, Oxford, pp. 251, vol. 257.

Vaccari, A. (1998). Preparation and catalytic properties of cationic and anionic clays. Catal. Today, 41, 53-71.

Vaccari, A. (1999). Clays and catalysis: a promising future. Appl. Clay Sci., 14, 161-198.

Xu, W., Liu, X., Ren, J., Liu, H., Ma, Y., Wang, Y., Lu, G. (2011). Synthesis of nanosized mesoporous Co–Al spinel and its application as solid base catalyst. Microporous Mesoporous Mater., 142, 251-257.

Capítulo 10

Conclusões e sugestões para trabalhos futuros

Conforme apresentado nos capítulos precedentes, a proposta da tese era a de avaliar catalisadores do tipo óxidos mistos à base de ferro, cobalto ou níquel em diferentes processos para a geração do gás de síntese.

A partir dos resultados obtidos neste trabalho, pode-se concluir:

- Para o grupo de catalisadores Ni-Al preparado por co-precipitação, com razões molares Ni/Al entre 0,5 e 9, foi observado que as características dos materiais sofrem forte influência da razão Ni/Al adotada. Na amostra com razão Ni/Al < 1, o material apresentou características típicas de Al_2O_3, indicando estar, o óxido de níquel segregado, bem disperso sobre a alumina. Associada à sua maior quantidade de sítios ácidos fortes, essa amostra apresentou maior formação de eteno na reação de decomposição do etanol. Além disso, revelou a formação de coque na forma amorfa, a qual a literatura aponta como sendo mais propensa a encapsular o metal ativo e promover a desativação do catalisador. A amostra com maior razão Ni/Al apresentou características da fase NiO *bulk*, em que o excesso de Ni resultou no colapso da fase espinélio, permanecendo, a maior parte do níquel, na forma NiO segregado. As análises *TG-DTA*, *TPO-DTA* e *XRD* do catalisador após a reação indicaram que o material com esta composição possui menor estabilidade térmica, conduzindo à sinterização do metal ativo e maior tendência à desativação por formação de coque. Nas amostras com razão Ni/Al entre 1 e 3 $mol \cdot mol^{-1}$, foi observada a formação de óxidos mistos, apresentando elevada área específica, moderada acidez, alta estabilidade térmica e alta resistência à desativação por formação de coque. Dentre as amostras com razões Ni/Al intermediárias, os catalisadores com razão molar Ni/Al de 2 e 3 apresentaram as caraterísticas mais promissoras na reação de decomposição do etanol. As referidas amostras exibiram maior seletividade a H_2 e CO e baixa formação de eteno e de coque. O melhor desempenho destas amostras pode ser atribuído à formação do óxido misto $NiAl_2O_4$ com moderada acidez e maior estabilidade térmica.

- A partir da determinação de composição adequada para os materiais precipitados, foram sintetizadas amostras à base de Fe, Co ou Ni. A análise *XRD* dos precursores dos catalisadores contendo níquel e cobalto revelou reflexões características de materiais do tipo hidrotalcita, a qual foi corroborada pelas curvas de decomposição térmica. Nos catalisadores calcinados, o difratogramas de raios X e a análise de *TPR* também se alinharam aos resultados obtidos para os precursores catalíticos. A caracterização dos catalisadores contendo Co ou Ni revelou a presença dos óxidos mistos $CoAl_2O_4$ e $NiAl_2O_4$, respectivamente. Por outro lado, o catalisador Fe-Al não apresentou características de óxidos mistos, formando apenas a fase Fe_2O_3 segregada. Em decorrência do metal ativo e das características associadas aos óxidos mistos, os catalisadores contendo Co ou Ni exibiram melhor desempenho para a formação de gás de síntese e conversão estável de etanol na reação da decomposição do etanol. Por outro lado, a amostra contendo Fe apresentou maior seletividade para compostos de maior cadeia (eteno e acetaldeído). As caracterizações dos catalisadores após os testes revelaram a deposição de carbono predominantemente na forma de filamentos, o que justificou a manutenção da conversão de etanol de 100% para os testes de atividade catalítica, à exceção do teste conduzido a 500°C sobre catalisador à base de ferro.

- A substituição de 11 mol% de níquel por um terceiro elemento proporcionou modificações nas propriedades estruturais e catalíticas dos catalisadores Ni-Al co-precipitados. As alterações mais significativas foram observadas no perfil de redução e nas características ácidas das amostras. O pico de redução se deslocou para temperaturas menores para os catalisadores contendo Mo, Zn ou Co, sugerindo que um maior percentual do níquel acomodou-se na forma de NiO segregado para estas amostras. Além disso, foi observada uma diminuição na acidez das amostras com a substituição parcial de níquel por um terceiro elemento. Dentre as amostras modificadas, o catalisador contendo magnésio apresentou características similares ao catalisador padrão Ni-Al, em termos de propriedades morfológicas e catalíticas. Por outro lado, nos testes de reforma a vapor do etanol, os catalisadores modificados com Zn, Mo ou Co apresentaram maior consumo de água e maiores conversões de etanol para temperaturas de reação intermediárias. O catalisador contendo cobalto apresentou o melhor desempenho.

- A avaliação de amostras Fe-Al com diferentes razões Fe/Al revelou a importância do alumínio como promotor estrutural, proporcionando área específica mais elevada. Também foram observados picos de *TPR* deslocados para temperaturas mais baixas nas amostras com razão Fe/Al mais baixa. Foi observado melhor desempenho na reação de reforma a vapor do etanol do catalisador com razão Fe/Al mais baixa. Comportamentos similares foram observados quando ocorreu a substituição parcial de Fe por Cu ou Co, na amostra com maior razão Fe/Al. Neste caso, a presença do metal divalente possibilitaria a formação de estruturas do tipo óxidos mistos. A amostra contendo cobalto apresentou maiores conversões e seletividade para gás de síntese, além de ter exibido desempenho constante durante a reação de reforma. A amostra contendo cobre apresentou melhores resultados nos testes de reforma, porém também apresentou desativação durante a reação. A sua menor estabilidade térmica provavelmente se relacione à sinterização da fase ativa, conforme sugerido pelos picos de redução em temperaturas significativamente inferiores à temperatura da reação de reforma. Desta forma, o estudo envolvendo as amostras Fe-Al modificadas apontou para catalisadores com menor razão Fe/Al e modificada com cobalto.

- Na investigação de amostras Ca-, La-, Li- e Mg-Co-Al para a reforma do metano com CO_2, similarmente ao verificado para as amostras Fe-Al modificadas, foram observadas mudanças na redutibilidade e aumento na área específica com a substituição parcial do metal ativo (Co) por um terceiro elemento. Apesar da formação de cristais de Co^0 com menores diâmetros, o catalisador padrão Co-Al exibiu a menor atividade. Este resultado pôde ser relacionado com a maior formação de coque observada sobre este catalisador, o qual deve estar relacionado à maior acidez apresentada por este material na análise de *TPD-NH_3*. O aumento na quantidade e na força dos sítios alcalinos das amostras modificadas conduziu a uma menor deposição de coque nos testes de atividade, sobretudo para a amostra contendo Li. O desempenho do catalisador Mg-Co-Al foi superior em termos de conversões de CH_4 e CO_2 e de seletividade a H_2. Este resultado pode ser atribuído ao melhor compromisso entre as propriedades texturais, a redutibilidade e o caráter ácido/base exibido por esta amostra. Os melhores resultados de atividade foram obtidos na maior temperatura de reação, ou seja, em 550°C. Os resultados dos óxidos mistos nesta temperatura, moderada para as reações de reforma, forneceu resultados promissores quando comparados ao reportado na literatura para condições de velocidades espaciais (*GHSV*) similares.

- No estudo de catalisadores Mg-Co-Al co-precipitados em diferentes razões Mg/Co, entre 0,2 e 1,0, foi possível otimizar o sistema catalítico e definir as condições adequadas para a sua ativação. Medidas de caracterização indicaram maior estabilidade térmica para amostras com maior razão Mg/Co em decorrência do favorecimento da formação de óxidos mistos para esta composição. As propriedades ácido/base também foram influenciadas pela composição das amostras. Enquanto a amostra com razão Mg/Co intermediária apresentou sítios ácidos com menor força e maior proporção de sítios com menor (moderada) acidez, a amostra com maior razão Mg/Co exibiu significativamente menor acidez total. Os experimentos de atividade catalítica na reação de reforma a seco do metano mostraram melhor desempenho para a amostra com razão molar Mg/Co = 0,5, em decorrência da maior estabilidade térmica dos óxidos formados nesta amostra. Os resultados também apontaram para a importância da fase Co_3O_4 para a atividade catalítica, uma vez que o referida fase óxida apresentou maior estabilidade para o catalisador com razão Mg/Co = 0,5 $mol \cdot mol^{-1}$. Este resultado foi evidenciado pelos testes de atividade precedidos por diferentes condições de ativação, ou seja, com redução em 700°C por 1 h e em 500°C por 4 h. A redução em temperatura mais baixa, embora fosse insuficiente para a redução da fase $CoAl_2O_4$, proporcionou a formação de menores cristais de Co^0, minimizando o fenômeno de sinterização e conduzindo a maiores conversões de CH_4 e CO_2. A menor atividade apresentada pelo catalisador com a razão Mg/Co mais elevada relacionou-se com a fraca acidez revelada por esta amostra, bem como ao menor teor de metal ativo na reação de reforma (Co).

Desta forma, foi possível verificar a pertinência da utilização de catalisadores do tipo óxidos mistos, com os metais ativos cobalto, ferro ou níquel, em diferentes processos associados à obtenção de gás de síntese. O presente trabalho determinou as composições que proporcionam características e propriedades catalíticas adequadas para os processos, bem como explorou modificações dos sistemas catalíticos inicialmente propostos, visando à sua otimização. Em geral, os óxidos mistos apresentaram alta área específica, elevada estabilidade térmica e moderada acidez que conduziram a melhores desempenhos nos diferentes processos.

No estudo das amostras com diferentes razões Ni/Al, melhores resultados foram observados para catalisadores com razão molar Ni/Al de 2 e 3. Para a decomposição do etanol, foram avaliados ferro, níquel e cobalto como metais ativos, dos quais o cobalto forneceu maior rendimento em gás de síntese e razão H_2/CO próxima a 2. Para a reforma a vapor do etanol, os promotores cobalto e molibdênio forneceram os resultados mais promissores nos catalisadores baseados em níquel, enquanto que a promoção com cobalto conduziu aos melhores resultados na reforma do etanol sobre catalisadores Fe-Al. Maior atividade para a reforma a seco do metano sobre catalisadores Co-Al modificados com álcalis foi observada para a amostra Mg-Co-Al com razão molar Mg/Co de 0.5.

Entretanto, estudos posteriores ainda serão necessários para avaliar, com maior rigor, a possibilidade dos óxidos mistos propostos serem empregados comercialmente para os processos investigados neste trabalho. Especialmente, para a avaliação da viabilidade dos catalisadores do tipo óxidos mistos propostos, ainda são demandados testes de desempenho destes materiais em unidades de maior escala, empregando-se maiores tempos de reação e comparando os resultados com os observados para catalisadores comerciais.

Além dos desafios supramencionados, outras sugestões para a realização de trabalhos futuros, relacionados aos resultados obtidos nesta tese, são feitas a seguir:

- Realização de testes com maior tempo de reação, para a avaliação da estabilidade dos catalisadores aos mecanismos de desativação tais como sinterização e crescimento dos cristais do metal ativo, deposição de coque e oxidação da fase metálica.

- Estudo de estratégias para a regeneração *in situ* dos catalisadores, especialmente no que se refere à deposição de coque.

- Avaliação das propriedades catalíticas do sistema Co-Fe-Al, com razão Fe/Al próxima de 2 mol·mol^{-1}, na reação de reforma a vapor do etanol.

- Avaliação do desempenho do sistema catalítico Mg-Co-Al na reação de reforma combinada do metano (H_2O + CO_2) sobre o catalisador selecionado, uma vez que este processo proporcionaria uma razão H_2/CO mais adequada e menor formação de coque.

Referências Bibliográficas

AASBERG-PETERSEN, K.; DYBKJÆR, I.; OVESEN, C. V.; SCHJØDT, N. C.; SEHESTED, J.; THOMSEN, S. G. Synthesis gas production for FT synthesis. In: STEYNBERG, A.; DRY, M. (Eds.). **Studies in Surface Science and Catalysis**, 1. ed. Amsterdan: Elsevier, 2004. v. 152, cap. 4, p. 258-405.

______. Natural gas to synthesis gas – Catalysts and catalytic processes. **Journal of Natural Gas Science and Engineering,** v. 3, n. 2, p. 423-459, maio 2011.

ABDELKADER, A.; DALY, H.; SAIH, Y.; MORGAN, K.; MOHAMED, M. A.; HALAWY, S. A.; HARDACRE, C. Steam reforming of ethanol over Co_3O_4–Fe_2O_3 mixed oxides. **International Journal of Hydrogen Energy**, v. 38, n. 20, p. 8263-8275, jul. 2013.

ABELLÓ, S.; BOLSHAK, E.; MONTANÉ, D. Ni–Fe catalysts derived from hydrotalcite-like precursors for hydrogen production by ethanol steam reforming. **Applied Catalysis A: General,** v. 450, n. 2, p. 261-274, jan. 2013.

ALLMANN, R.; JEPSEN, H. P. Die struktur des hydrotalkits. **Neues Jahrbuch für Mineralogie**, Monatshefte, 1969.

ARMOR, J. N. The multiple roles for catalysis in the production of H_2. **Applied Catalysis A: General,** v. 176, n. 2, p. 159-176, jan. 1999.

BALZARETTI, N. M.; GALLAS, M. R.; COSTA, T. M. H.; STEFANI, V.; PEROTTONI, C. A.; DA JORNADA, J. A. H. Raman investigation of 2,5-bis(benzoxazol-2 '-yl)4-methoxyphenol under high pressure. **Journal of Raman Spectroscopy,** v. 34, n. 3, p. 244-247, mar 2003.

BARROSO-QUIROGA, M. M.; CASTRO-LUNA, A. E. Catalytic activity and effect of modifiers on Ni-based catalysts for the dry reforming of methane. **International Journal of Hydrogen Energy,** v. 35, n. 11, p. 6052-6056, jun. 2010.

BARTHOS, R.; SZÉCHENYI, A.; KOÓS, Á.; SOLYMOSI, F. The decomposition of ethanol over Mo_2C/carbon catalysts. **Applied Catalysis A: General**, v. 327, n. 1, p. 95-105, jul. 2007.

BAYRAM, B.; SOYKAL, I. I.; VON DEAK, D.; MILLER, J. T.; OZKAN, U. S. Ethanol steam reforming over Co-based catalysts: Investigation of cobalt coordination environment under reaction conditions. **Journal of Catalysis**, v. 284, n. 1, p. 77-89, nov. 2011.

BENITO, R.; HERRERO, M.; LABAJOS, F. M.; RIVES, V.; ROYO, C.; LATORRE, N.; MONZON, A. Production of carbon nanotubes from methane Use of Co-Zn-Al catalysts prepared by microwave-assisted synthesis. **Chemical Engineering Journal,** v. 149, n. 1-3, jul. 2009.

BHATTACHARYYA, A.; CHANG, V. W.; SCHUMACHER, D. J. CO_2 reforming of methane to syngas: I: evaluation of hydrotalcite clay-derived catalysts. **Applied Clay Science,** v. 13, n. 5–6, p. 317-328, nov. 1998.

BIALAS, A.; NIEBRZYDOWSKA, P.; DUDEK, B.; PIWOWARSKA, Z.; CHMIELARZ, L.; MICHALIK, M.; KOZAK, M.; KUŚTROWSKI, P. Coprecipitated Co–Al and Cu–Al oxide catalysts for toluene total oxidation. **Catalysis Today,** v. 176, n. 1, p. 413-416, nov. 2011.

BOLSHAK, E.; ABELLÓ, S.; MONTANÉ, D. Ethanol steam reforming over Ni–Fe-based hydrotalcites: Effect of iron content and reaction temperature. **International Journal of Hydrogen Energy**, v. 38, n. 14, p. 5594-5604, maio 2013.

BORG, Ø.; HAMMER, N.; ENGER, B. C.; MYRSTAD, R.; LINDVÅG, O. A.; ERI, S.; SKAGSETH, T. H. Effect of biomass-derived synthesis gas impurity elements on cobalt Fischer–Tropsch catalyst performance including in situ sulphur and nitrogen addition. **Journal of Catalysis,** v. 279, n. 1, p. 163-173, abr. 2011.

BOUARAB, R.; AKDIM, O.; AUROUX, A.; CHERIFI, O.; MIRODATOS, C. Effect of MgO additive on catalytic properties of Co/SiO_2 in the dry reforming of methane. **Applied Catalysis A: General,** v. 264, n. 2, p. 161-168, jun. 2004.

BP STATISTICAL REVIEW OF WORLD ENERGY. London: BP, 2003. Disponível em: <www.bp.com/worldenergy>. Acesso em 16 de maio de 2013.

BSHISH, A.; YAKOOB, Z.; NARAYANAN, B.; RAMAKRISHNAN, R.; EBSHISH, A. Steam-reforming of ethanol for hydrogen production. **Chemical Papers,** v. 65, n. 3, p. 251-266, jun. 2011.

BUDIMAN, A.; SONG, S.-H.; CHANG, T.-S.; SHIN, C.-H.; CHOI, M.-J. Dry Reforming of Methane Over Cobalt Catalysts: A Literature Review of Catalyst Development. **Catalysis Surveys from Asia**, v. 16, n. 4, p. 183-197, dez. 2012.

BUSCA, G.; COSTANTINO, U.; MONTANARI, T.; RAMIS, G.; RESINI, C.; SISANI, M. Nickel versus cobalt catalysts for hydrogen production by ethanol steam reforming: Ni-Co-Zn-Al catalysts from hydrotalcite-like precursors. **International Journal of Hydrogen Energy,** v. 35, n. 11, p. 5356-5366, jun. 2010.

BUSSI, J.; MUSSO, M.; VEIGA, S.; BESPALKO, N.; FACCIO, R.; ROGER, A.-C. Ethanol steam reforming over NiLaZr and NiCuLaZr mixed metal oxide catalysts. **Catalysis Today**, v. 213, n. 0, p. 42-49, set. 2013.

CAI, W.-J.; QIAN, L.-P., YUE, B., CHEN, X.-Y.; HE, H.-Y. Reforming of CH_4 with CO_2 over Co/Mg–Al oxide catalyst. **Chinese Chemical Letters**, v. 24, n. 9, p. 777-779, set. 2013.

CARVALHO, D. L.; DE AVILLEZ, R. R.; RODRIGUES, M. T.; BORGES, L. E. P.; APPEL, L. G. Mg and Al mixed oxides and the synthesis of n-butanol from ethanol. **Applied Catalysis A: General**, v. 415–416, n. 0, p. 96-100, fev. 2012.

CARVALHO, D. C.; DE SOUZA, H. S. A.; FILHO, J. M.; OLIVEIRA, A. C.; CAMPOS, A.; MILET, É. R. C.; DE SOUSA, F. F.; PADRON-HERNANDEZ, E.; OLIVEIRA, A. C. A study on the modification of mesoporous mixed oxides supports for dry reforming of methane by Pt or Ru. **Applied Catalysis A: General**, v. 473, n. 0, p. 132-145, mar. 2014.

CASEY RESEARCH. Disponível em: <http://www.caseyresearch.com/articles/oil-price-differentials-caught-between-sands-and-pipelines>. Acesso em: 11 jun. 2013.

CAVANI, F.; TRIFIRO, F.; VACCARI, A. Hydrotalcite-type anionic clays: preparation, properties and applications. **Catalysis Today**, v. 11, n. 2, p. 173-301, dec 1991.

CHATTANATHAN, S. A.; ADHIKARI, S.; TAYLOR, S. Conversion of carbon dioxide and methane in biomass synthesis gas for liquid fuels production. **International Journal of Hydrogen Energy,** v. 37, n. 23, p. 18031-18039, dez. 2012.

CHEN, D.; LØDENG, R.; ANUNDSKÅS, A.; OLSVIK, O.; HOLMEN, A. Synthesis of carbon nanofibers: effects of Ni crystal size during methane decomposition. **Journal of Catalysis,** v. 229, n. 1, p. 82-96, jan. 2005.

CHEN, J.; ZHANG, X.; ARANDIYAN, H.; PENG, Y.; CHANG, H.; LI, J. Low temperature complete combustion of methane over cobalt chromium oxides catalysts. **Catalysis Today**, v. 201, n. 0, p. 12-18, mar. 2013.

CHEN, R.; XIE, Y.; ZHOU, Y.; WANG, J.; WANG, H. Production of hydrogen-rich gas and multi-walled carbon nanotubes from ethanol decomposition over molybdenum modified Ni/MgO catalysts. **Journal of Energy Chemistry**, v. 23, n. 2, p. 244-250, mar. 2014.

CHOUDHARY, V. R.; MONDAL, K. C. CO_2 reforming of methane combined with steam reforming or partial oxidation of methane to syngas over $NdCoO_3$ perovskite-type mixed metal-oxide catalyst. **Applied Energy,** v. 83, n. 9, p. 1024-1032, set. 2006.

CHOUDHARY, V. R.; SANSARE, S. D.; MAMMAN, A. S. Low-temperature selective oxidation of methane to carbon monoxide and hydrogen over cobalt-MgO catalysts. **Applied Catalysis A: General**, v. 90, n. 1, p. L1-L5, out. 1992

COELHO, M.G. **Influência do íon trivalente nas propriedades catalíticas do sistema Cu/Zn/M (M = Al ou Cr) para as reações de hidrogenação do monóxido de carbono e transformação do etanol.** 1994. Tese (Doutorado em Engenharia química)-Programa de Pós-Graduação em Engenharia Química, Universidade Federal de São Carlos, São Carlos, 1994.

COLEMAN, L. J. I.; EPLING, W.; HUDGINS, R. R.; CROISET, E. Ni/Mg–Al mixed oxide catalyst for the steam reforming of ethanol. **Applied Catalysis A: General**, v. 363, n. 1–2, p. 52-63, jul. 2009.

COMPACT GTL Disponível em: <http://www.compactgtl.com/about/petrobras-commercial-demonstration-plant/>. Acesso em: 11 jun. 2013.

CORONEL, L.; MÚNERA, J. F.; TARDITI, A. M.; MORENO, M. S.; CORNAGLIA, L. M. Hydrogen production by ethanol steam reforming over Rh nanoparticles supported on lanthana/silica systems. **Applied Catalysis B: Environmental**, v. 160–161, n. 0, p. 254-266, nov. 2014.

CREPALDI, E. L.; PAVAN, P. C.; VALIM, J. B. Comparative study of the coprecipitation methods for the preparation of Layered Double Hydroxides. **Journal of the Brazilian Chemical Society**, v. 11, p. 64-70, 2000.

CRISAFULLI, C.; SCIRÈ, S.; MINICÒ, S.; SOLARINO, L. Ni–Ru bimetallic catalysts for the CO_2 reforming of methane. **Applied Catalysis A: General,** v. 225, n. 1–2, p. 1-9, fev. 2002.

DA SILVA, A. M.; DE SOUZA, K. R.; JACOBS, G.; GRAHAM, U. M.; DAVIS, B. H.; MATTOS, L. V.; NORONHA, F. B. Steam and CO_2 reforming of ethanol over Rh/CeO_2 catalyst. **Applied Catalysis B: Environmental,** v. 102, n. 1–2, p. 94-109, fev. 2011.

DAUENHAUER, P. J.; DREYER, B. J.; DEGENSTEIN, N. J.; SCHMIDT, L. D. Millisecond reforming of solid biomass for sustainable fuels. **Angew. Chem. Int. Ed. Engl.,** v. 46, n. 31, p. 5864-5867, jan. 2007.

DAVIDSON, S.; SUN, J.; WANG, Y. Ethanol Steam Reforming on Co/CeO_2: The Effect of ZnO Promoter. **Topics in Catalysis**, v. 56, n. 18-20, p. 1651-1659, dez. 2013.

DAZA, C. E.; GALLEGO, J.; MORENO, J. A.; MONDRAGON, F.; MORENO, S.; MOLINA, R. High stability of Ce-promoted Ni/Mg–Al catalysts derived from hydrotalcites in dry reforming of methane. **Fuel,** v. 89, n. 3, p. 592-603, mar. 2010.

______. CO_2 reforming of methane over Ni/Mg/Al/Ce mixed oxides. **Catalysis Today,** v. 133, p. 357-366, abr.-jun. 2008.

DE JONG, K. P. **Synthesis of Solid Catalysts.** 1. ed. Utrecht: Wiley, 2009.

DE LIMA, S. M.; DA SILVA, A. M.; DA COSTA, L. O. O.; GRAHAM, U. M.; JACOBS, G.; DAVIS, B. H.; MATTOS, L. V.; NORONHA, F. B. Study of catalyst deactivation and reaction mechanism of steam reforming, partial oxidation, and oxidative steam reforming of ethanol over Co/CeO_2 catalyst. **Journal of Catalysis**, v. 268, n. 2, p. 268-281, dez. 2009.

DE SOUSA, F. F.; DE SOUSA, H. S. A.; OLIVEIRA, A. C.; JUNIOR, M. C. C.; AYALA, A. P.; BARROS, E. B.; VIANA, B. C.; FILHO, J. M.; OLIVEIRA, A. C. Nanostructured Ni-containing spinel oxides for the dry reforming of methane: Effect of the presence of cobalt and nickel on the deactivation behaviour of catalysts. **International Journal of Hydrogen Energy**, v. 37, n. 4, p. 3201-3212, fev. 2012.

DE SOUZA, G.; ÁVILA, V. C.; MARCÍLIO, N. R.; PEREZ-LOPEZ, O. W. Synthesis Gas Production by Steam Reforming of Ethanol over M-Ni-Al Hydrotalcite-type Catalysts; M = Mg, Zn, Mo, Co. **Procedia Engineering**, v. 42, n. 0, p. 1805-1815, 2012.

DE SOUZA, G.; BALZARETTI, N. M.; MARCÍLIO, N. R.; PEREZ-LOPEZ, O. W. Decomposition of Ethanol Over Ni-Al Catalysts: Effect of Copper Addition. **Procedia Engineering**, v. 42, n. 0, p. 335-345, 2012.

DELUGA, G. A.; SALGE, J. R.; SCHMIDT, L. D.; VERYKIOS, X. E. Renewable hydrogen from ethanol by autothermal reforming. **Science**, v. 303, n. 5660, p. 993-997, fev. 2004.

DEMIRBAS, A. Progress and recent trends in biofuels. **Progress in Energy and Combustion Science,** v. 33, n. 1, p. 1-18, fev. 2007.

DI BLASI, C.; SIGNORELLI, G.; DI RUSSO, C.; REA, G. Product Distribution from Pyrolysis of Wood and Agricultural Residues. **Industrial & Engineering Chemistry Research,** v. 38, n. 6, p. 2216-2224, jan. 1999.

DI COSIMO, J. I.; DÍEZ, V. K.; XU, M.; IGLESIA, E.; APESTEGUÍA, C. R. Structure and Surface and Catalytic Properties of Mg-Al Basic Oxides. **Journal of Catalysis**, v. 178, n. 2, p. 499-510, set. 1998.

DIAS, J. A. C.; ASSAF, J. M. Influence of calcium content in Ni/CaO/γ-Al_2O_3 catalysts for CO_2-reforming of methane. **Catalysis Today,** v. 85, n. 1, p. 59-68, set. 2003.

DRY, M. E. The Fischer-Tropsch process: 1950-2000. **Catalysis Today,** v. 71, n. 3-4, p. 227-241, jan. 2002.

______. Chemical concepts used for engineering purposes. In: STEYNBERG, A.; DRY, M. (Eds.). **Studies in Surface Science and Catalysis**, 1. ed. Amsterdan: Elsevier, 2004a. v. 152, cap. 3, p. 196-257.

______. FT catalysts. In: STEYNBERG, A.; DRY, M. (Eds.). **Studies in Surface Science and Catalysis**, 1. ed. Amsterdan: Elsevier, 2004b. v. 152, cap. 7, p. 533-600.

DRY, M. E.; STEYNBERG, A. P. Commercial FT Process Applications. In: STEYNBERG, A.; DRY, M. (Eds.). **Studies in Surface Science and Catalysis**, 1. ed. Amsterdan: Elsevier, 2004. v. 152, cap. 5, p. 406-481.

DUFOUR, A.; GIRODS, P.; MASSON, E.; ROGAUME, Y.; ZOULALIAN, A. Synthesis gas production by biomass pyrolysis: Effect of reactor temperature on product distribution. **International Journal of Hydrogen Energy,** v. 34, n. 4, p. 1726-1734, fev. 2009.

ENGER, B. C.; LØDENG, R.; HOLMEN, A. A review of catalytic partial oxidation of methane to synthesis gas with emphasis on reaction mechanisms over transition metal catalysts. **Applied Catalysis A: General,** v. 346, n. 1–2, p. 1-27, ago. 2008.

______. Modified cobalt catalysts in the partial oxidation of methane at moderate temperatures. **Journal of Catalysis,** v. 262, n. 2, p. 188-198, mar. 2009.

ESCOBAR, C. Decomposição do metano sobre catalisadores Co-Al modificados com cobre. 2012. Dissertação (Mestrado em Engenharia Química)-Programa de Pós-Graduação em Engenharia Química, Universidade Federal do Rio Grande do Sul, Porto Alegre, 2012.

ESCOBAR, C.; PEREZ-LOPEZ, O. Hydrogen Production by Methane Decomposition Over Cu–Co–Al Mixed Oxides Activated Under Reaction Conditions. **Catalysis Letters**, v. 114, n. 5, p. 796-804, mar. 2014.

ESPINAL, R.; TABOADA, E.; MOLINS, E.; CHIMENTAO, R. J.; MEDINA, F.; LLORCA, J. Cobalt hydrotalcites as catalysts for bioethanol steam reforming. The promoting effect of potassium on catalyst activity and long-term stability. **Applied Catalysis B: Environmental**, v. 127, n. 0, p. 59-67, out. 2012a.

ESPINAL, R.; TABOADA, E.; MOLINS, E.; CHIMENTAO, R. J.; MEDINA, F.; LLORCA, J. Cobalt hydrotalcite for the steam reforming of ethanol with scarce carbon production. **RSC Advances**, v. 2, n. 7, p. 2946-2956, 2012.

ESPINOZA, R. L.; STEYNBERG, A. P.; JAGER, B.; VOSLOO, A. C. Low temperature Fischer–Tropsch synthesis from a Sasol perspective. **Applied Catalysis A: General,** v. 186, n. 1–2, p. 13-26, out. 1999.

EUROPEAN BIOFUELS TECHNOLOGY PLATFORM. Disponível em: <http://www.biofuelstp.eu/btl.html>. Acesso em: 11 jun. 2013.

EWBANK, J. L.; KOVARIK, L.; KENVIN, C. C.; SIEVERS, C. Effect of preparation methods on the performance of Co/Al_2O_3 catalysts for dry reforming of methane. **Green Chemistry**, v. 16, n. 2, p. 885-896, jan. 2014.

FAJARDO, H.; LONGO, E.; MEZALIRA, D.; NUERNBERG, G.; ALMERINDO, G.; COLLASIOL, A.; PROBST, L. D.; GARCIA, I. T. S.; CARREÑO, N. V. Influence of support on catalytic behavior of nickel catalysts in the steam reforming of ethanol for hydrogen production. **Environmental Chemistry Letters**, v. 8, n. 1, p. 79-85, mar. 2010.

FAKEEHA, A. H.; NAEEM, M. A.; KHAN, W. U.; AL-FATESH, A. S. Syngas production via CO_2 reforming of methane using Co-Sr-Al catalyst. **Journal of Industrial and Engineering Chemistry**, v. 20, n. 2, p. 549-557, mar. 2014.

FARRELL, A. E.; BRANDT, A. R. Risks of the oil transition. **Environmental Research Letters,** v. 1, n. 1, p. 1-6, out. 2006.

FEIO, L. S. F.; HORI, C. E.; MATTOS, L. V.; ZANCHET, D.; NORONHA, F. B.; BUENO, J. M. C. Partial oxidation and autothermal reforming of methane on

Pd/CeO_2-Al_2O_3 catalysts. **Applied Catalysis A: General,** v. 348, n. 2, p. 183-192, out. 2008.

FROST, R. L.; MUSUMECI, A. W.; BOSTROM, T.; ADEBAJO, M. O.; WEIER, M. L.; MARTENS, W. Thermal decomposition of hydrotalcite with chromate, molybdate or sulphate in the interlayer. **Thermochimica Acta**, v. 429, n. 2, p. 179-187, maio 2005.

GABROVSKA, M.; EDREVA-KARDJIEVA, R.; TENCHEV, K.; TZVETKOV, P.; SPOJAKINA, A.; PETROV, L. Effect of Co-content on the structure and activity of Co–Al hydrotalcite-like materials as catalyst precursors for CO oxidation. **Applied Catalysis A: General,** v. 399, n. 1–2, p. 242-251, maio 2011.

GADALLA, A. M.; BOWER, B. The role of catalyst support on the activity of nickel for reforming methane with CO_2. **Chemical Engineering Science**, v. 43, n. 11, p. 3049-3062, 1988.

GALLEGO, J.; MONDRAGON, F.; BATIOT-DUPEYRAT, C. Simultaneous production of hydrogen and carbon nanostructured materials from ethanol over $LaNiO_3$ and $LaFeO_3$ perovskites as catalyst precursors. **Applied Catalysis A: General**, v. 450, n. 0, p. 73-79; jan. 2013.

GALLEGO, J.; SIERRA, G.; MONDRAGON, F.; BARRAULT, J.; BATIOT-DUPEYRAT, C. Synthesis of MWCNTs and hydrogen from ethanol catalytic decomposition over a Ni/La_2O_3 catalyst produced by the reduction of $LaNiO_3$. **Applied Catalysis A: General,** v. 397, n. 1-2, p. 73-81, abr. 2011.

GALVITA, V. V.; SEMIN, G. L.; BELYAEV, V. D.; SEMIKOLENOV, V. A.; TSIAKARAS, P.; SOBYANIN, V. A. Synthesis gas production by steam reforming of ethanol. **Applied Catalysis A: General,** v. 220, n. 1-2, p. 123-127, out. 2001.

GAO, F.; ZHANG, L.; YANG, Y.; HUANG, S. Quality of horizontally aligned single-walled carbon nanotubes: Is methane as carbon source better than ethanol? **Applied Surface Science**, v. 256, n. 11, p. 3357-3360, mar. 2010.

GENNEQUIN, C.; KOUASSI, S.; TIDAHY, L.; COUSIN, R.; LAMONIER, J.-F.; GARCON, G.; SHIRALI, P.; CAZIER, F.; ABOUKAÏS, A.; SIFFERT, S. Co–Mg–Al oxides issued of hydrotalcite precursors for total oxidation of volatile organic compounds. Identification and toxicological impact of the by-products. **Comptes Rendus Chimie**, v. 13, n. 5, p. 494-501, maio 2010.

GENNEQUIN, C.; SAFARIAMIN, M.; SIFFERT, S.; ABOUKAÏS, A.; ABI-AAD, E. CO_2 reforming of CH_4 over Co–Mg–Al mixed oxides prepared via hydrotalcite like precursors. **Catalysis Today**, v. 176, n. 1, p. 139-143, nov. 2011.

GOLDWASSER, M. R.; RIVAS, M. E.; LUGO, M. L.; PIETRI, E.; PÉREZ-ZURITA, J.; CUBEIRO, M. L.; GRIBOVAL-CONSTANT, A.; LECLERCQ, G. Combined methane reforming in presence of CO_2 and O_2 over $LaFe_{1-x}Co_xO_3$ mixed-oxide perovskites as catalysts precursors. **Catalysis Today,** v. 107–108, s/n., p. 106-113, out. 2005.

GONZÁLEZ VARGAS, O. A.; DE LOS REYES HEREDIA, J. A.; WANG, J. A.; CHEN, L. F.; MONTESINOS CASTELLANOS, A.; LLANOS, M. E. Hydrogen production over

Rh/Ce-MCM-41 catalysts via ethanol steam reforming. **International Journal of Hydrogen Energy**, v. 38, n. 32, p. 13914-13925, out. 2013.

GUO, J. J.; LOU, H.; ZHAO, H.; CHAI, D. F.; ZHENG, X. M. Dry reforming of methane over nickel catalysts supported on magnesium aluminate spinels. **Applied Catalysis A: General,** v. 273, n. 1-2, p. 75-82, out. 2004.

HAGEN, J. **Industrial Catalysis: A Practical Approach.** 2. ed. Weinheim: Wiley-VCH, 2006.

HAMELINCK, C. N.; FAAIJ, A. P. C.; DEN UIL, H.; BOERRIGTER, H. Production of FT transportation fuels from biomass; technical options, process analysis and optimisation, and development potential. **Energy,** v. 29, n. 11, p. 1743-1771, set. 2004.

HAYAKAWA, H.; TANAKA, H.; FUJIMOTO, K. Studies on precipitated iron catalysts for Fischer-Tropsch synthesis. **Applied Catalysis A: General,** v. 310, p. 24-30, ago. 2006.

HERMES, N. A. **Hidrogênio e nanotubos de carbono por decomposição catalítica do metano: desempenho de catalisadores à base de cobalto e alumínio**. 2010. 93 f. Dissertação (Mestrado em Engenharia Química)-Programa de Pós-Graduação em Engenharia Química, Universidade Federal do Rio Grande do Sul, Porto Alegre, 2010.

HERMES, N. A.; LANSARIN, M. A.; PEREZ-LOPEZ, O. W. Catalytic Decomposition of Methane Over M-Co-Al Catalysts (M = Mg, Ni, Zn, Cu). **Catalysis Letters,** v. 141, n. 7, p. 1018-1025, jul. 2011.

HOLGADO, M. J.; RIVES, V.; SAN ROMAN, M. S. Characterization of Ni-Mg-Al mixed oxides and their catalytic activity in oxidative dehydrogenation of n-butane and propene. **Applied Catalysis A: General,** v. 214, n. 2, p. 219-228, jun. 2001.

HONG, J.; CHU, W.; CHERNAVSKII, P. A.; KHODAKOV, A. Y. Impact of sorbitol addition on the structure and performance of silica-supported cobalt catalysts for Fischer–Tropsch synthesis. **Catalysis Today,** v. 175, n. 1, p. 528-533, out. 2011.

HOU, Z.; YASHIMA, T. Meso-porous Ni/Mg/Al catalysts for methane reforming with CO_2. **Applied Catalysis A: General,** v. 261, n. 2, p. 205-209, abr. 2004.

HOU, Z.; YOKOTA, O.; TANAKA, T.; YASHIMA, T. Characterization of Ca-promoted Ni/α-Al_2O_3 catalyst for CH_4 reforming with CO_2. **Applied Catalysis A: General,** v. 253, n. 2, p. 381-387, out. 2003.

HU, X.; LU, G. Syngas production by CO_2 reforming of ethanol over Ni/Al_2O_3 catalyst. **Catalysis Communications,** v. 10, n. 13, p. 1633-1637, jul. 2009.

HUBER, G. W.; CHHEDA, J. N.; BARRETT, C. J.; DUMESIC, J. A. Production of liquid alkanes by aqueous-phase processing of biomass-derived carbohydrates. **Science**, v. 308, n. 5727, p. 1446-1450, jun. 2005.

HYDROCARBON PROCESSING. Disponível em: <http://www.hydrocarbonprocessing.com/>. Acesso em: 10 jul. 2013.

IGARASHI, H.; MURAKAMI, H.; MURAKAMI, Y.; MARUYAMA, S.; NAKASHIMA, N. Purification and characterization of zeolite-supported single-walled carbon nanotubes catalytically synthesized from ethanol. **Chemical Physics Letters**, v. 392, n. 4–6, p. 529-532, jul. 2004.

ILGAZ-SOYKAL, I.; BAYRAM, B.; SOHN, H.; GAWADE, P.; MILLER, J. T.; OZKAN, U. S. Ethanol steam reforming over Co/CeO_2 catalysts: Investigation of the effect of ceria morphology. **Applied Catalysis A: General**, v. 449, n. 0, p. 47-58, dez. 2012.

JING, Q.; LOU, H.; MO, L.; FEI, J.; ZHENG, X. Combination of CO_2 reforming and partial oxidation of methane over Ni/BaO-SiO_2 catalysts to produce low H_2/CO ratio syngas using a fluidized bed reactor. **Journal of Molecular Catalysis A: Chemical,** v. 212, n. 1–2, p. 211-217, abr. 2004.

JONES, G.; JAKOBSEN, J. G.; SHIM, S. S.; KLEIS, J.; ANDERSSON, M. P.; ROSSMEISL, J.; ABILD-PEDERSEN, F.; CHORKENDORFF, I.; SEHESTED, J.; NØRSKOV, J. K. First principles calculations and experimental insight into methane steam reforming over transition metal catalysts. **Journal of Catalysis,** v. 259, n. 1, p. 147-160, out. 2008.

JUAN-JUAN, J.; ROMÁN-MARTÍNEZ, M. C.; ILLÁN-GÓMEZ, M. J. Effect of potassium content in the activity of K-promoted Ni/Al_2O_3 catalysts for the dry reforming of methane. **Applied Catalysis A: General,** v. 301, n. 1, p. 9-15, fev. 2006.

JUN, K.-W.; ROH, H.-S.; KIM, K.-S.; RYU, J.-S.; LEE, K.-W. Catalytic investigation for Fischer–Tropsch synthesis from bio-mass derived syngas. **Applied Catalysis A: General,** v. 259, n. 2, p. 221-226, mar. 2004.

KABE, T. Liquefaction of coal. In: KABE, T.; ISHIHARA, A.; QIAN, E. W.; SUTRISNA, I. P.; KABE, Y. (Eds.). **Studies in Surface Science and Catalysis**. Amsterdan: Elsevier, 2004. v. 150, p.181-267.

KHASSIN, A. A.; YURIEVA, T. M.; KUSTOVA, G. N.; ITENBERG, I. S.; DEMESHKINA, M. P.; KRIEGER, T. A.; PLYASOVA, L. M. Cobalt-aluminum co-precipitated catalysts and their performance in the Fischer-Tropsch synthesis. **Journal of Molecular Catalysis A: Chemical,** v. 168, n. 1-2, mar 2001.

KIM, D. K.; STÖWE, K.; MÜLLER, F.; MAIER, W. F. Mechanistic study of the unusual catalytic properties of a new NiCe mixed oxide for the CO_2 reforming of methane. **Journal of Catalysis,** v. 247, n. 1, p. 101-111, abr. 2007.

KOIKE, M.; ISHIKAWA, C.; LI, D.; WANG, L.; NAKAGAWA, Y.; TOMISHIGE, K. Catalytic performance of manganese-promoted nickel catalysts for the steam reforming of tar from biomass pyrolysis to synthesis gas. **Fuel,** v. 103, n. 0, p. 122-129, jan. 2013.

KOVANDA, F.; ROJKA, T.; BEZDICKA, P.; JIRATOVA, K.; OBALOVA, L.; PACULTOVA, K.; BASTL, Z. Effect of hydrothermal treatment on properties of Ni-Al layered double hydroxides and related mixed oxides. **Journal of Solid State Chemistry,** v. 182, n. 1, p. 27-36, jan. 2009.

LEE, H. H. **Heterogeneous Reactor Design.** 1. Ed. Stoneham: Butterworth Publishers, 1985.

LI, W.; WANG, H.; REN, Z.; WANG, G.; BAI, J. Co-production of hydrogen and multi-wall carbon nanotubes from ethanol decomposition over Fe/Al_2O_3 catalysts. **Applied Catalysis B-Environmental,** v. 84, n. 3-4, p. 433-439, dez. 2008.

LI, W. Z.; ZHANG, H.; WANG, C. Y.; ZHANG, Y.; XU, L. W.; ZHU, K.; XIE, S. S. Raman characterization of aligned carbon nanotubes produced by thermal decomposition of hydrocarbon vapor. **Applied Physics Letters,** v. 70, n. 20, p. 2684-2686, maio 1997.

LIGURAS, D. K.; GOUNDANI, K.; VERYKIOS, X. E. Production of hydrogen for fuel cells by catalytic partial oxidation of ethanol over structured Ni catalysts. **Journal of Power Sources**, v. 130, n. 1-2, p. 30-37, maio 2004

LIRA, E.; LOPEZ, C. M.; OROPEZA, F.; BARTOLINI, M.; ALVAREZ, J.; GOLDWASSER, M.; LINARES, F. L.; LAMONIER, J.-F.; ZURITA, M. J. P. HMS mesoporous silica as cobalt support for the Fischer-Tropsch Synthesis: Pretreatment, cobalt loading and particle size effects. **Journal of Molecular Catalysis a-Chemical,** v. 281, n. 1-2, p. 146-153, fev. 2008.

LIU, G.; LARSON, E. D.; WILLIAMS, R. H.; KREUTZ, T. G.; GUO, X. Making Fischer−Tropsch Fuels and Electricity from Coal and Biomass: Performance and Cost Analysis. **Energy & Fuels,** v. 25, n. 1, p. 415-437, jan. 2011.

LIU, Q.; OUYANG, Y.; ZHANG, L.; XU, Y.; FANG, Y. Effects of argon flow rate and reaction temperature on synthesizing single-walled carbon nanotubes from ethanol. **Physica E: Low-dimensional Systems and Nanostructures,** v. 41, n. 7, p. 1204-1209, jun. 2009.

LLORCA, J.; DE LA PISCINA, P. R.; DALMON, J. A.; SALES, J.; HOMS, N. CO-free hydrogen from steam-reforming of bioethanol over ZnO-supported cobalt catalysts - Effect of the metallic precursor. **Applied Catalysis B-Environmental,** v. 43, n. 4, p. 355-369, jul. 2003.

LÖGDBERG, S.; TRISTANTINI, D.; BORG, Ø.; ILVER, L.; GEVERT, B.; JÄRÅS, S.; BLEKKAN, E. A.; HOLMEN, A. Hydrocarbon production via Fischer–Tropsch synthesis from H_2-poor syngas over different Fe-Co/γ-Al_2O_3 bimetallic catalysts. **Applied Catalysis B: Environmental,** v. 89, n. 1–2, p. 167-182, jul. 2009.

LOPEZ-SALINAS, E.; GARCIA-SANCHEZ, M.; LUISA RAMON-GARCIA, M.; SCHIFTER, I. New Gallium-Substituted Hydrotalcites: $[Mg_{1-x}Ga_x(OH)_2](CO_3)_{x/2}\cdot mH_2O$. **Journal of Porous Materials,** v. 3, n. 3, p. 169-174, set. 1996.

LU, Y.; LEE, T. Influence of the Feed Gas Composition on the Fischer-Tropsch Synthesis in Commercial Operations. **Journal of Natural Gas Chemistry,** v. 16, n. 4, p. 329-341, dez. 2007.

LUISETTO, I.; TUTI, S.; DI BARTOLOMEO, E. Co and Ni supported on CeO_2 as selective bimetallic catalyst for dry reforming of methane. **International Journal of Hydrogen Energy**, v. 37, n. 21, p. 15992-15999, nov. 2012.

LUNSFORD, J. H. Catalytic conversion of methane to more useful chemicals and fuels: a challenge for the 21st century. **Catalysis Today,** v. 63, n. 2–4, p. 165-174, dez. 2000.

MACHEJ, T.; SERWICKA, E. M.; ZIMOWSKA, M.; DULA, R.; MICHALIK-ZYM, A.; NAPRUSZEWSKA, B.; ROJEK, W.; SOCHA, R. Cu/Mn-based mixed oxides derived from hydrotalcite-like precursors as catalysts for methane combustion. **Applied Catalysis A: General**, v. 474, n. 0, p. 87-94, mar. 2014.

MANFRO, R. L.; SOUZA, M. M. V. M. Production of Renewable Hydrogen by Glycerol Steam Reforming Using Ni–Cu–Mg–Al Mixed Oxides Obtained from Hydrotalcite-like Compounds. **Catalysis Letters,** v. 144, n. 0, p. 867-877, fev. 2014.

MANTRIPRAGADA, H. C.; RUBIN, E. S. Techno-economic evaluation of coal-to-liquids (CTL) plants with carbon capture and sequestration. **Energy Policy,** v. 39, n. 5, p. 2808-2816, maio 2011.

MARTINEZ, R.; ROMERO, E.; GUIMON, C.; BILBAO, R. CO_2 reforming of methane over coprecipitated Ni-Al catalysts modified with lanthanum. **Applied Catalysis A-General,** v. 274, n. 1-2, p. 139-149, out. 2004.

MARTONO, E.; VOHS, J. M. Support effects in cobalt-based ethanol steam reforming catalysts: Reaction of ethanol on Co/CeO_2/YSZ(100) model catalysts. **Journal of Catalysis,** v. 291, p. 79-86, maio 2012.

MAS, V.; BERGAMINI, M. L.; BARONETTI, G.; AMADEO, N.; LABORDE, M. A Kinetic Study of Ethanol Steam Reforming Using a Nickel Based Catalyst. **Topics in Catalysis,** v. 51, p. 39-48, nov. 2008a.

MAS, V.; DIEUZEIDE, M. L.; JOBBAGY, M.; BARONETTI, G.; AMADEO, N.; LABORDE, M. Ni(II)-Al(III) layered double hydroxide as catalyst precursor for ethanol steam reforming: Activation treatments and kinetic studies. **Catalysis Today,** v. 133, p. 319-323, abr.-jun. 2008b.

MEZALIRA, D. Z.; PROBST, L. D.; PRONIER, S.; BATONNEAU, Y.; BATIOT-DUPEYRAT, C. Decomposition of ethanol over Ni/Al_2O_3 catalysts to produce hydrogen and carbon nanostructured materials. **Journal of Molecular Catalysis a-Chemical,** v. 340, n. 1-2, p. 15-23, abr. 2011.

MME – MINISTÉRIO DE MINAS E ENERGIA. **Balanço Energético Nacional 2014: Ano base 2013.** Empresa de Pesquisa Energética. Rio de Janeiro: EPE, 2014. p.121.

MIYAZAWA, T.; KIMURA, T.; NISHIKAWA, J.; KUNIMORI, K.; TOMISHIGE, K. Catalytic properties of Rh/CeO_2/SiO_2 for synthesis gas production from biomass by catalytic partial oxidation of tar. **Science and Technology of Advanced Materials,** v. 6, n. 6, p. 604-614, set. 2005.

MOHANTY, S.; KUNZRU, D.; SARAF, D. N. Hydrocracking: a review. **Fuel,** v. 69, n. 12, p. 1467-1473, dez. 1990.

MONTOYA, J. A.; ROMERO-PASCUAL, E.; GIMON, C.; DEL ANGEL, P.; MONZON, A. Methane reforming with CO_2 over Ni/ZrO_2-CeO_2 catalysts prepared by sol-gel. **Catalysis Today,** v. 63, n. 1, p. 71-85, dez. 2000.

MUROYAMA, H.; NAKASE, R.; MATSUI, T.; EGUCHI, K. Ethanol steam reforming over Ni-based spinel oxide. **International Journal of Hydrogen Energy,** v. 35, n. 4, p. 1575-1581, fev. 2010.

NAGAOKA, K.; TAKANABE, K.; AIKA, K.-I. Influence of the reduction temperature on catalytic activity of Co/TiO_2 (anatase-type) for high pressure dry reforming of methane. **Applied Catalysis A: General,** v. 255, n. 1, p. 13-21, nov. 2003.

______. Modification of Co/TiO_2 for dry reforming of methane at 2 MPa by Pt, Ru or Ni. **Applied Catalysis A: General,** v. 268, n. 1–2, p. 151-158, ago. 2004.

NAKAMURA, K.; FUJITSUKA, M.; KITAJIMA, M. Disorder-induced line broadening in 1st-order Raman-scattering from graphite. **Physical Review B,** v. 41, n. 17, p. 12260-12263, jun. 1990.

NUDEL, J. N.; UMANSKY, B. S.; LOMBARDO, E. A. Bulk, surface and catalytic characterization of the Co_3O_4-La_2O_3-Al_2O_3 system. **Applied Catalysis**, v. 31, n. 2, p. 275-289, jun. 1987.

OLIVEIRA, A. C.; RANGEL, M. D. C. Desidrogenação do etilbenzeno sobre compostos de ferro e alumínio. **Química Nova**, v. 26, p. 170-176, 2003.

PACHECO, L. D. C.; PESSOA, F. L. P.; FALCÃO, P. W. D. C. Utilização do CO_2 na reforma do glicerol para a obtenção de hidrogênio e gás de síntese. In: CONGRESSO BRASILEIRO DE P&D EM PETRÓLEO E GÁS, 5., 2009, Fortaleza. **Anais**.

PALMER, S. J.; SPRATT, H. J.; FROST, R. L. Thermal decomposition of hydrotalcites with variable cationic ratios. **Journal of Thermal Analysis and Calorimetry,** v. 95, n. 1, p. 123-129, jan. 2009.

PAWELEC, B.; DAMYANOVA, S.; ARISHTIROVA, K.; FIERRO, J. L. G.; PETROV, L. Structural and surface features of PtNi catalysts for reforming of methane with CO_2. **Applied Catalysis A: General,** v. 323, n. 0, p. 188-201, abr. 2007.

PEÑA, M. A.; GÓMEZ, J. P.; FIERRO, J. L. G. New catalytic routes for syngas and hydrogen production. **Applied Catalysis A: General,** v. 144, n. 1–2, p. 7-57, set. 1996.

PEREZ-LOPEZ, O.W.; SENGER, A.; MARCILIO, N.R.; LANSARIN, M.A. Effect of composition and thermal pretreatment on properties of Ni–Mg–Al catalysts for CO_2 reforming of methane**. Applied Catalysis A: General**, v. 303, p. 234-244, abr. 2006.

POGGIO-FRACCARI, E.; IRIGOYEN, B.; BARONETTI, G.; MARIÑO, F. Ce-Pr mixed oxides as active supports for Water-gas Shift reaction: Experimental and density functional theory characterization, **Applied Catalysis A: General**, v. 485, n. 0, p. 123-132, set. 2014.

POMPEO, F.; NICHIO, N. N.; FERRETTI, O. A.; RESASCO, D. Study of Ni catalysts on different supports to obtain synthesis gas. **International Journal of Hydrogen Energy,** v. 30, n. 13–14, p. 1399-1405, out. 2005.

QUINCOCES, C. E.; DICUNDO, S.; ALVAREZ, A. M.; GONZÁLEZ, M. G. Effect of addition of CaO on Ni/Al_2O_3 catalysts over CO_2 reforming of methane. **Materials Letters,** v. 50, n. 1, p. 21-27, ago. 2001.

RĂCIULETE, M.; LAYRAC, G.; TICHIT, D.; MARCU, I. C. Comparison of Cu_xZnAlO mixed oxide catalysts derived from multicationic and hybrid LDH precursors for methane total oxidation. **Applied Catalysis A: General**, v. 477, n. 0, p. 195-204, maio 2014.

RAPAGNÁ, S.; PROVENDIER, H.; PETIT, C.; KIENNEMANN, A.; FOSCOLO, P. U. Development of catalysts suitable for hydrogen or syn-gas production from biomass gasification. **Biomass and Bioenergy,** v. 22, n. 5, p. 377-388, maio 2002.

REGALBUTO, J. **Catalyst Preparation: Science and Engineering.** 1. ed. London: CRC Press, 2006.

RENNARD, D. C.; FRENCH, R.; CZERNIK, S.; JOSEPHSON, T.; SCHMIDT, L. Production of synthesis gas by partial oxidation and steam reforming of biomass pyrolysis oils. **International Journal of Hydrogen Energy,** v. 35, n. 9, p. 4048-4059, maio 2010.

RENNARD, D. C.; DAUENHAUER, P. J.; TUPY, S. A.; SCHMIDT, L. D.. Autothermal Catalytic Partial Oxidation of Bio-Oil Functional Groups: Esters and Acids. **Energy & Fuels,** v. 22, n. 2, p. 1318-1327, jan. 2008.

RENNARD, D. C.; KRUGER, J. S.; SCHMIDT, L. D. Autothermal Catalytic Partial Oxidation of Glycerol to Syngas and to Non-Equilibrium Products. **ChemSusChem,** v. 2, n. 1, p. 89-98, 2009.

RESHETENKO, T. V.; AVDEEVA, L. B.; KHASSIN, A. A.; KUSTOVA, G. N.; USHAKOV, V. A.; MOROZ, E. M.; SHMAKOV, A. N. Coprecipitated iron-containing catalysts (Fe-Al_2O_3, Fe-Co- Al_2O_3, Fe-Ni- Al_2O_3) for methane decomposition at moderate temperatures I. Genesis of calcined and reduced catalysts**. Applied Catalysis A-General**, v. 268, n. 1-2, p. 127-138, ago. 2004.

RESINI, C.; MONTANARI, T.; BARATTINI, L.; RAMIS, G.; BUSCA, G.; PRESTO, S.; RIANI, P.; MARAZZA, R.; SISANI, M.; MARMOTTINI, F.; COSTANTINO, U. Hydrogen production by ethanol steam reforming over Ni catalysts derived from hydrotalcite-like precursors: Catalyst characterization, catalytic activity and reaction path. **Applied Catalysis A: General,** v. 355, n. 1-2, p. 83-93, fev. 2009.

RIBET, S.; TICHIT, D.; COQ, B.; DUCOURANT, B.; MORATO, F. Synthesis and activation of Co-Mg-Al layered double hydroxides. **Journal of Solid State Chemistry,** v. 142, n. 2, fev. 1999.

ROH, H.-S.; POTDAR, H. S.; JUN, K.-W. Carbon dioxide reforming of methane over co-precipitated Ni–CeO_2, Ni–ZrO_2 and Ni–Ce–ZrO_2 catalysts. **Catalysis Today,** v. 93–95, n. 0, p. 39-44, set. 2004.

ROMERO, A.; JOBBÁGY, M.; LABORDE, M.; BARONETTI, G.; AMADEO, N. Ni(II)–Mg(II)–Al(III) catalysts for hydrogen production from ethanol steam reforming: Influence of the Mg content**, Applied Catalysis A: General**, v. 470, n. 0, p. 398-404, jan. 2014.

ROSS, J. R. H. Natural gas reforming and CO_2 mitigation. **Catalysis Today**, v. 100, n. 1–2, p. 151-158, fev. 2005.

ROSTRUP-NIELSEN, J. R. Activity of nickel catalysts for steam reforming of hydrocarbons. **Journal of Catalysis,** v. 31, n. 2, p. 173-199, nov. 1973.

______. Production of synthesis gas. **Catalysis Today,** v. 18, n. 4, p. 305-324, dez. 1993.

______. Making fuels from biomass. **Science**, v. 308, n. 5727, p. 1421-1422, jun. 2005.

ROSTRUP-NIELSEN, J. R.; HANSEN, J. H. B. CO_2-Reforming of Methane over Transition Metals. **Journal of Catalysis,** v. 144, n. 1, p. 38-49, nov. 1993.

RUCKENSTEIN, E.; HU, Y. H. Carbon dioxide reforming of methane over nickel/alkaline earth metal oxide catalysts. **Applied Catalysis A: General,** v. 133, n. 1, p. 149-161, dez. 1995.

RUCKENSTEIN, E.; WANG, H. Y. Combined catalytic partial oxidation and CO_2 reforming of methane over supported cobalt catalysts. **Catalysis Letters**, v. 73, n. 2-4, p. 99-105, 2001.

RUOSO, C.; SOUZA, G.; BALZARETTI, N. M.; MARCILIO, N. R.; PEREZ-LOPEZ, O. W. Nanotubos de carbono a partir da decomposição do etanol sobre catalisadores Co-Al. In: Congresso Brasileiro de Engenharia Química, 19., 2012, Búzios, p.8846-8854. **Anais**.

SAITO, Y.; YOSHIKAWA, T.; BANDOW, S.; TOMITA, M.; HAYASHI, T. Interlayer spacings in carbon nanotubes. **Physical Review B**, v. 48, n. 3, 1993.

SAN-JOSÉ-ALONSO, D.; JUAN-JUAN, J.; ILLÁN-GÓMEZ, M. J.; ROMÁN-MARTÍNEZ, M. C. Ni, Co and bimetallic Ni–Co catalysts for the dry reforming of methane. **Applied Catalysis A: General**, v. 371, n. 1–2, p. 54-59, dez. 2009.

SANTOS, A. C. S. F. **Efeito do teor de CeO_2 em catalisadores de Pt/CeO_2-Al_2O_3 para as reações de oxidação parcial e reforma do metano**. 2005. 162 f. Tese (Doutorado em Engenharia Química)-Programa de Pós-Graduação em Engenharia Química, Universidade Federal de São Carlos, São Carlos, 2005.

SATTERFIELD, C. N. **Heterogeneous Catalysis in Industrial Practice.** 2. ed. New York: McGraw-Hill, Inc., 1991.

SEGNER, J.; CAMPBELL, C. T.; DOYEN, G.; ERTL, G. Catalytic oxidation of CO on Pt(111): The influence of surface defects and composition on the reaction dynamics. **Surface Science**, v. 138, n. 2–3, p. 505-523, mar. 1984.

SERRANO-LOTINA, A.; DAZA, L. Influence of the operating parameters over dry reforming of methane to syngas. **International Journal of Hydrogen Energy**, v. 39, n. 8, p. 4089-4094, mar. 2014.

SERRANO-LOTINA, A.; MARTIN, A. J., FOLGADO, M. A.; DAZA, L. Dry reforming of methane to syngas over La-promoted hydrotalcite clay-derived catalysts. **International Journal of Hydrogen Energy**, v. 37, n. 17, p. 12342-12350, set. 2012.

SLAGTERN, Å.; SWAAN, H. M.; OLSBYE, U.; DAHL, I. M.; MIRODATOS, C. Catalytic partial oxidation of methane over Ni-, Co- and Fe-based catalysts. **Catalysis Today,** v. 46, n. 2–3, p. 107-115, nov. 1998.

SOKOLOVSKII, V. D.; COVILLE, N. J.; PARMALIANA, A.; ESKENDIROV, I.; MAKOA, M. High yield syngas formation by partial oxidation of methane over Co-alumina catalysts. In: DE PONTES, M. et al.(Eds.). **Studies in Surface Science and Catalysis**: Amsterdan: Elsevier, 1997. v. 107, p.461-465.

SONG, L. X.; CHEN, J.; ZHU, L. H.; XIA, J.; YANG, J. Modification in Structure, Phase Transition, and Magnetic Property of Metallic Gallium Driven by Atom–Molecule Interactions. **Inorganic Chemistry**, v. 50, n. 17, p. 7988-7996, set. 2011.

SOUSA-AGUIAR, E. F. **Aplicação de reatores de microcanais à engenharia química**. In: CONGRESSO BRASILEIRO DE ENGENHARIA QUÍMICA, 18., 2010, Foz do Iguaçú. Palestra proferida em: 21/09/2010.

SOUZA, G. **Preparação, caracterização e desempenho de catalisadores à base de ferro na Síntese de Fischer-Tropsch**. 2010. 158 f. Dissertação (Mestrado em Engenharia Química)-Programa de Pós-Graduação em Engenharia Química, Universidade Federal do Rio Grande do Sul, Porto Alegre, 2010.

SOUZA, G.; MARCILIO, N. R.; PEREZ-LOPEZ, O. W. Reforma a seco do metano em temperaturas moderadas sobre catalisadores Co-Al co-precipitados modificados com metal alcalino. In: 17° Congresso Brasileiro de Catálise e VII Congresso de Catálise do Mercosul, 2013, Gramado. SBCat. **Anais**. p.OR2-65.

SOUZA, G.; RUOSO, C.; BALZARETTI, N. M.; MARCÍLIO, N. R.; PEREZ-LOPEZ, O. W. Synthesis gas and carbon nanotubes production from catalytic decomposition of renewable resources. In: Proceedings of Venice 2012 - International Symposium on Energy from Biomass and Waste, 4., 2012, San Servolo - Venice. CISA Publisher. **Anais**, p.PG09.

STEINHAUER, B.; KASIREDDY, M. R.; RADNIK, J.; MARTIN, A. Development of Ni-Pd bimetallic catalysts for the utilization of carbon dioxide and methane by dry reforming. **Applied Catalysis A: General,** v. 366, n. 2, p. 333-341, set. 2009.

STEYNBERG, A. P.; ESPINOZA, R. L.; JAGER, B.; VOSLOO, A. C. High temperature Fischer–Tropsch synthesis in commercial practice. **Applied Catalysis A: General,** v. 186, n. 1–2, p. 41-54, out. 1999.

TAKANABE, K.; NAGAOKA, K.; NARIAI, K.; AIKA, K.-I. Titania-supported cobalt and nickel bimetallic catalysts for carbon dioxide reforming of methane. **Journal of Catalysis**, v. 232, n. 2, p. 268-275, jun. 2005.

THEVENOT, F.; SZYMANSKI, R.; CHAUMETTE, P. Preparation and characterization of Al-rich Zn-Al hydrotalcite-like compounds**. Clays and Clay Material**, v. 37, p. 396-402, 1989.

TIAN, R.; WANG, X.; LI, M.; HU, H.; CHEN, R.; LIU, F.; ZHENG, H.; WAN, L. An efficient route to functionalize singe-walled carbon nanotubes using alcohols. **Applied Surface Science**, v. 255, n. 5, Part 2, p. 3294-3299, dez. 2008.

TOSCANI, H.; MALDONADO, L.; KUNZLER, J. A.; GÉA, C.; RECH, R. L.; SOBREIRO, L. E. L.; SAFFER, M.; LAY, M. L. Projeto CIGÁS: Gaseificação de carvão em leito fluidizado sob pressão. In: 3° Congresso Brasileiro de Energia, 1984, Rio de Janeiro. **Anais**. p.254.

TRANE-RESTRUP, R.; DAHL, S.; JENSEN, A. D. Steam reforming of ethanol: Effects of support and additives on Ni-based catalysts. **International Journal of Hydrogen Energy,** v. 38, p. 15105-15118, out. 2013.

TRIFIRÓ, F.; VACCARI, A. Hydrotalcite-like anionic clays (layer double hydroxides). In ATWOOD, J. S.; DAVIES, J. E. D.; MACNICOL, D. D.; VÖGTLE, F. (Eds.). **Comprehensive Supramolecular Chemistry**. Oxford: Pergamon, 1996. v. 7, p.251.

TUTI, S.; PEPE, F. On the catalytic activity of cobalt oxide for the steam reforming of ethanol. **Catalysis Letters,** v. 122, n. 1-2, p. 196-203, abr 2008.

TZOMPANTZI, F.; MENDOZA-DAMIÁN, G.; RICO, J. L.; MANTILLA, A. Enhanced photoactivity for the phenol mineralization on ZnAlLa mixed oxides prepared from calcined LDHs. **Catalysis Today**, v. 220–222, n. 0, p. 56-60, mar. 2014.

URDĂ, A.; POPESCU, I.; CACCIAGUERRA, T.; TANCHOUX, N.; TICHIT, D.; MARCU, I.-C. Total oxidation of methane over rare earth cation-containing mixed oxides derived from LDH precursors. **Applied Catalysis A: General**, v. 464–465, n. 0, p. 20-27, ago. 2013.

VACCARI, A. Preparation and catalytic properties of cationic and anionic clays. **Catalysis Today,** v. 41, n. 1-3, p. 53-71, maio 1998.

______. Clays and catalysis: a promising future. **Applied Clay Science,** v. 14, n. 4, p. 161-198, abr. 1999.

VAIDYA, P. D.; RODRIGUES, A. E. Insight into steam reforming of ethanol to produce hydrogen for fuel cells. **Chemical Engineering Journal**, v. 117, n. 1, p. 39-49, mar. 2006.

VELASCO, J. A.; LOPEZ, L.; VELÁSQUEZ, M.; BOUTONNET, M.; CABRERA, S.; JÄRÅS, S. Gas to liquids: A technology for natural gas industrialization in Bolivia. **Journal of Natural Gas Science and Engineering,** v. 2, n. 5, p. 222-228, nov. 2010.

VIZCAINO, A. J.; CARRERO, A.; CALLES, J. A. Hydrogen production by ethanol steam reforming over Cu-Ni supported catalysts. **International Journal of Hydrogen Energy,** v. 32, n. 10-11, p. 1450-1461, jul.-ago. 2007.

VOSLOO, A. C. Fischer-Tropsch: a futuristic view. **Fuel Processing Technology,** v. 71, n. 1-3, p. 149-155, jun. 2001.

WAN, H.; WU, B.; ZHANG, C.; XIANG, H.; LI, Y. Promotional effects of Cu and K on precipitated iron-based catalysts for Fischer-Tropsch synthesis. **Journal of Molecular Catalysis A: Chemical,** v. 283, n. 1-2, p. 33-42, mar. 2008.

WANG, D.-Y.; LEUTERITZ, A.; WAGENKNECHT, U.; HEINRICH, G. Self-assembling organomodified Co/Al based layered double hydroxides (LDH) via one-step route. **Transactions of Nonferrous Metals Society of China,** v. 19, n. 6, p. 1479-1482, dez. 2009.

WANG, F.; LI, Y.; CAI, W.; ZHAN, E.; MU, X.; SHEN, W. Ethanol steam reforming over Ni and Ni-Cu catalysts. **Catalysis Today,** v. 146, n. 1-2, p. 31-36, ago. 2009.

WANG, G.; WANG, H.; LI, W.; REN, Z.; BAI, J.; BAI, J. Preparation of hydrogen and carbon nanotubes over cobalt-containing catalysts via catalytic decomposition of ethanol. **Rsc Advances,** v. 1, n. 8, p. 1585-1592, 2011a.

______. Efficient production of hydrogen and multi-walled carbon nanotubes from ethanol over Fe/Al_2O_3 catalysts. **Fuel Processing Technology,** v. 92, n. 3, p. 531-540, mar. 2011b.

______. Simultaneous production of hydrogen and multi-walled carbon nanotubes by ethanol decomposition over Ni/Al_2O_3 catalysts. **Applied Catalysis B: Environmental,** v. 88, n. 1–2, p. 142-151, abr. 2009.

WANG, H. Y.; RUCKENSTEIN, E. Conversions of Methane to Synthesis Gas over Co/γ-Al_2O_3 by CO_2 and/or O_2. **Catalysis Letters,** v. 75, n. 1-2, p. 13-18, jan. 2001.

WANG, L.; HISADA, Y.; KOIKE, M.; Li, D.; WATANABE, H.; NAKAGAWA, Y.; TOMISHIGE, K. Catalytic performance and characterization of Ni-Fe catalysts for the steam reforming of tar from biomass pyrolysis to synthesis gas. **Applied Catalysis A: General,** v. 392, n. 1–2, p. 248-255, jan. 2011.

______. Catalytic performance and characterization of Ni–Co catalysts for the steam reforming of biomass tar to synthesis gas. **Fuel,** v. 112, n. 0, p. 654-661, out. 2013.

WANG, S.; LU, G. Q.; MILLAR, G. J. Carbon Dioxide Reforming of Methane To Produce Synthesis Gas over Metal-Supported Catalysts: State of the Art. **Energy & Fuels,** v. 10, n. 4, p. 896-904, jan. 1996.

WANG, W.; WANG, Y. Steam reforming of ethanol to hydrogen over nickel metal catalysts. **International Journal of Energy Research**, v. 34, n. 14, p. 1285-1290, 2010.

WANG, W.; WANG, Y. Q. Thermodynamic analysis of steam reforming of ethanol for hydrogen generation. **International Journal of Energy Research**, v. 32, n. 15, p. 1432-1443, 2008.

WORLD COAL ASSOCIATION. Disponível em: <http://www.worldcoal.org/>. Acesso em: 11 jun. 2013.

XU, W.; LIU, X.; REN, J.; LIU, H.; MA, Y.; WANG, Y.; LU, G. Synthesis of nanosized mesoporous Co–Al spinel and its application as solid base catalyst**. Microporous and Mesoporous Materials**, v. 142, n. 1, p. 251-257, jun. 2011.

YU, X.-P.; CHU, W.; WANG, N.; MA, F. Hydrogen Production by Ethanol Steam Reforming on NiCuMgAl Catalysts Derived from Hydrotalcite-Like Precursors. **Catalysis Letters**, v. 141, n. 8, ago. 2011.

ZHANG, B.; CAI, W.; LI, Y.; XU, Y.; SHEN, W. Hydrogen production by steam reforming of ethanol over an Ir/CeO_2 catalyst: Reaction mechanism and stability of the catalyst. **International Journal of Hydrogen Energy,** v. 33, p. 4377-4386, 2008.

ZHANG, C. H.; YANG, Y.; TENG, B. T.; LI, T. Z.; ZHENG, H. Y.; XIANG, H. W.; LI, Y. W. Study of an iron-manganese Fischer-Tropsch synthesis catalyst promoted with copper. **Journal of Catalysis,** v. 237, n. 2, p. 405-415, jan. 2006.

ZHANG, L.; LI, W.; LIU, J.; GUO, C.; WANG, Y.; ZHANG, J. Ethanol steam reforming reactions over Al_2O_3•SiO_2-supported Ni–La catalysts. **Fuel**, v. 88, n. 3, p. 511-518, mar. 2009.

ZHANG, L.; MILLET, J.-M. M.; OZKAN, U. S. Effect of Cu loading on the catalytic performance of Fe-Al-Cu for water-gas shift reaction. **Applied Catalysis A: General,** v. 357, n. 1, p. 66-72, mar. 2009.

ZHANG, L. H.; XIANG, X.; ZHANG, L.; LI, F.; ZHU, J.; EVANS, D. G.; DUAN, X. Influence of iron substitution on formation and structure of Cu-based mixed oxides derived from layered double hydroxides. **Journal of Physics and Chemistry of Solids**, v. 69, n. 5-6, p. 1098-1101, maio-jun. 2008.

ZHANG, W. Automotive fuels from biomass via gasification. **Fuel Processing Technology,** v. 91, n. 8, p. 866-876, ago. 2010.